Modelling spherical flame propagation in a closed volume

by Ian Stefanes Scott

April 2014

A dissertation submitted in fulfilment of the academic requirements for the degree of Master of Science in Engineering in the Department of Chemical Engineering

Dedicated to all the educators throughout my life.

Declarations

I am presenting this dissertation in fulfilment of the requirements for the degree of Master of Science in Engineering.

I know the meaning of plagiarism and declare that all of the work in this dissertation, save for that which is properly acknowledged, is my own.

I hereby grant the University of Cape Town free licence to reproduce for the purpose of research either the whole or any portion of the contents, in any manner whatsoever, of this dissertation.

_____

Ian Scott

7 April 2014

Acknowledgements

Firstly, I want to thank my supervisor, Prof. Klaus Möller, for his guidance and insights. Also, Dr. Chris Woolard, my co-supervisor, for his motivation and support of my work.

The staff and students at the SAFL should also be acknowledged, since that was the incubation chamber for this work. Thank you for all the opportunities to share my ideas with you and your honest replies. It was an exciting, stimulating and fun work environment.

Moving to Cape Town, I knew very few people there. However, the UCT Mountain and Ski Club changed this. The spectacular trips grew my love and appreciation for the natural world we live in. Thank you for the many great adventures that filled most of my weekends, and recharged my energy levels. A great club!

Finally, thanks to my family for your ongoing support during the long stretch of this work. Thank you for your encouragement and for understanding my commitment to this work.

The financial assistance of the National Research Foundation (NRF) and Sasol towards this research is acknowledged. Opinions expressed and conclusions arrived at, are those of the author and should not necessarily be attributed to the NRF or Sasol.

Synopsis

The highly exothermic reaction of fuel combustion is the most common source of usable energy in the world. The fuel itself originates almost entirely from fossil fuels, such as crude oil and natural gas. The use of these fuels for energy production is under pressure in recent times due to environmental and availability concerns. This then sets the stage for combustion research aimed at providing more efficient combustion processes and characterising the combustion behaviour of alternative fuels. The laminar flame speed of a combustible mixture is a well defined combustion characteristic that influences the efficiency and performance of many combustion processes. An example of where flame speed has a strong impact on the performance of a combustion process, is the blow-out and relight ability in flight applications of gas turbine engines. A very common experimental setup to obtain laminar flame speed data is the constant volume combustion bomb, where the laminar flame speed is calculated from the measured flame speed of a spherical flame, propagating outwards inside a usually spherical combustion chamber.

In this work, a model is developed with the aim of describing the behaviour of an outwardly propagating spherical flame in a closed spherical volume for the purpose of modelling experimentally observed flame behaviours. This model is then used, firstly to predict the laminar flame speed and Markstein length[1] of an iso-octane and air flame at 370 K and 1 bar for the fuel equivalence ratios of 0.8, 0.9, 1.0, 1.1 and 1.2. A sensitivity study for the effects of the fuel, oxygen and intermediate molecule diffusion, as well as the thermal conductivity and the reaction kinetics, on the flame behaviour and flame characteristics, is carried out. The model is used to predict the flame behaviour in different constant volume combustion bomb sizes, to show the effect that the choice of combustion chamber size has.

The process of flame propagation is a complex interaction between different thermo-physical and chemical properties of the fuel-oxidiser mixture. Early attempts to describe the laminar flame speed of a mixture in one equation showed promise, where the reaction kinetics, thermal conductivity and adiabatic flame temperature were among the most prominent fundamental properties included. A vast amount of experimental and modelling work has been done on laminar flame speed and other combustion characteristics, and the effects of temperature, pressure, gas composition, flame geometry and reaction kinetics on flame speed were shown. Experimental flame speed studies, where the a constant

[1] Markstein length indicates the sensitivity of the flame speed to flame geometry effects.

volume combustion bomb is used, are also abundant. These studies show complex behaviours for the interaction of pressure, temperature and fuel to air ratios for the effects on Markstein length and laminar flame speed.

For an outwardly propagating, spherical flame in a closed volume, the changing curvature of the flame strongly influences the flame speed. Further, the accumulation of hot combustion products causes an increase in pressure in the entire combustion chamber, which also adiabatically heats the burned and unburned gases. This then indicates some of the challenges in modelling the experimental setup, since the flame in a constant volume combustion bomb is constantly exposed to changing conditions. In literature, different approaches to calculating the laminar fame speed from the experimental constant volume combustion bomb data are aimed at increased accuracy. However, the accuracy improvements are seldom significant when compared to the inherent experimental errors.

The model developed in this work is based on the conservation of species, energy and momentum, and for each of these a partial differential equation is derived. The conservation of momentum is specifically included to describe the convective velocity field of the gas, that would enable the system to have a uniform pressure across the spatial domain while this pressure increases with time. Several assumptions are made to simplify the system, where the assumption of symmetry around the centre of the spherical flame is the most significant, since it simplifies the partial differential equations to one dimension in space and one dimension in time. These partial differential equations include terms to describe the convective flow of gas, the diffusion of species, thermal conduction of heat and production of species at certain reaction rates. The mathematical system is solved using BACOL (B-spline Adaptive COLlocation), a numerical procedure, while several functions and routines are created to describe the mathematical system and populate the terms in the partial differential equations.

The model produces flame position data over time, at the conditions mentioned above, for a combustion chamber with an inside diameter of 10 cm, where the increase in the spatially uniform pressure is achieved. Comparison of the model-derived flame speed and pressure data with experimental data from previous studies does not show good agreement and therefore adjustments to parameters in the model are considered. The oxygen diffusion coefficient used in this model is reduced by 75% for this reason and results in more accurate local oxygen to fuel ratios across the flame front. This yields the final model that succeeds in describing most of the experimentally observed flame speed behaviour, such as influence of the ignition event on flame speed, the increase in flame speed due to the increase in

spherical flame radius, decrease in flame speed due to increase in pressure, and the effect of the fuel to air ratio on the flame speed trends. A comparison for the same conditions modelled for a 5 cm and 19 cm inside radius combustion chamber showed that the flame speed behaviour is the same for the first part of the flame propagation. However, the pressure in the smaller combustion chamber increases faster, and at a flame radius of approximately 1.7 cm, the pressure in the smaller combustion chamber has increased by 0,05 bar. At this point the two flame speed trends start to deviate from each other.

The flame speed data produced by the model is then used to derive the laminar flame speeds and Markstein lengths at the specific conditions for iso-octane and air, by following both linear and nonlinear regression strategies used in experimental calculations. It is clear that the laminar flame speeds derived from the model data are lower than those obtained from experimental studies, with differences as high as 15 $\mathbf{cm.s^{-1}}$. The laminar flame speed values display the correct effect of the fuel air ratio, as observed for experimental data, and the Markstein lengths derived from the model data show very good agreement with experimental values. A sensitivity study on the effects of fundamental properties of the fuel and air mixture on the laminar flame speed and Markstein length, shows several interesting effects. The laminar flame speed and Markstein length show sensitivity to fuel diffusion in conditions where the fuel is stoichiometrically limited, whereas the sensitivity to oxygen diffusion is more pronounced in conditions where oxygen is stoichiometrically limited. Further, the thermal conductivity is shown to have the same effect on the laminar flame speed, but the opposite effect on the Markstein length when compared to the effect of fuel and oxygen diffusion. The reaction kinetics is shown to have a strong effect, where lower reaction kinetics significantly decreases the laminar flame speed and increases the Markstein length.

Some of the modelled effects from the sensitivity study agree with experimental results from other studies. The effect that the addition of dimethyl ether to a methane and air flame has on the Markstein length, was studied experimentally by Chen (2009) and is given here as an example of such a case. It was found in the above mentioned study that the addition of dimethyl ether causes the Markstein length to increase continually for mixtures where fuel is stoichiometrically limited. This then is explained by the decrease in fuel diffusion caused by the increased dimethyl ether content of the fuel mixture, which is similar to the effect modelled in the current study for a decrease in fuel diffusion.

The result of this work is a working model that captures much of the experimental flame behaviour of an outwardly propagating spherical flame in a closed volume. This ability

is due to the implementation of accurate descriptions of fundamental properties and the successful integration of complex interactions. The model therefore provides insights into the effects of the fundamental properties and how they interact to result in experimentally observed phenomena. Further improvement of the model is possible by incorporating a more complex and realistic reaction kinetic scheme. It is recommended to base this on high temperature combustion kinetics. The developed model can be employed to model an extended list of conditions for different fuels or fuel mixtures. It is also recommended that the model is used for predicting the effect of ignition differences on the flame behaviour, as the capacity to describe this has also been demonstrated. Another possible use for the model is the comparison of different experimental setups, such as different combustion chamber sizes, in order to optimise experimental setups and data interpretation, and to have a basis for comparison of results from different experimental setups.

Contents

1. Introduction

The burning of hydrocarbon fuels for energy utilisation is an age old practice (e.g. wood fires to cook food), and is a very common practice in the modern world of today. Electricity generation, internal combustion engines and gas turbine engines for transportation, furnaces, and boilers for industrial energy and residential heating are some of the major application fields where hydrocarbon fuels are burned to utilise the energy release. These application fields are faced with two significant challenges:

- A growing concern for the global environmental impact of continual burning of hydrocarbon fuels. The focus here is on carbon dioxide emissions which is, at this stage, unavoidable when burning hydrocarbons.
- The diversification of the hydrocarbon source. With an ever growing global population, the demand for energy requires use of previously under-utilised hydrocarbon sources, such as natural gas and biofuels.

According to the International Energy Agency (2012), transportation accounted for 27.3% of the world's energy consumption in 2010, where 96.6% of this energy was supplied directly from fossil fuel sources[1]. The transportation sector relies heavily on oil-derived fuels for energy, as is shown in Figure 1.1.

Note that the value of energy consumption for transportation from oil products[2] is divided by 10 in Figure 1.1, to enhance the smaller contributions of the other energy sources. The energy source category in Figure 1.1, labeled as "Other", includes geothermal, solar, wind, electricity, heat, etc. Figure 1.1 shows that energy consumption for transportation increased for all energy sources from 1973 to 2010, except for coal and peat. This then shows the diversification of energy sources for transportation, where new fuel products are entering the market.

[1] Fossil fuels refer to coal/peat, oil and natural gas.
[2] Oil products includes liquefied petroleum gas (LPG), gasoline, kerosene, diesel and marine diesel.

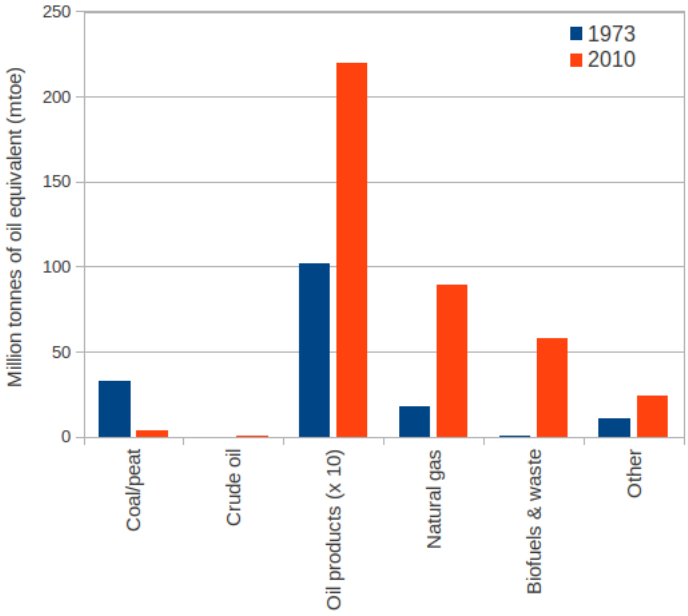

Figure 1.1.: Energy sources for the world's transportation energy use in 1973 and 2010. Adapted from International Energy Agency (2012).

There is currently no mature technology available which will enable the meaningful reduction of carbon dioxide emissions when burning hydrocarbon fuels. There are also no sufficient clean alternative energy sources available to replace hydrocarbons as a source of energy. Liquid hydrocarbon fuels dominate the transportation sector and are preferred since they have a high energy density and are easy to transport (Hui and Sung, 2013). In the study of Höök et al. (2012) it was concluded that: "*even if new energy systems undergo a rapid 'oil boom'-development - i.e. they mimic the most extreme historical events - their contribution to global energy supply by 2050 will be marginal.*" For these reasons, there is a strong focus on more efficiently utilising energy from burning hydrocarbons, thereby emitting less carbon dioxide for each unit of energy effectively utilised.

Understanding the way hydrocarbons burn enables improved engine designs and fuel choices aimed at increasing efficiencies. It is here where combustion research plays an important role. The burn rate or burn duration in an internal combustion engine influences the efficiency and pollutant formation of the internal combustion engine and is strongly influenced by combustion characteristics (Marshall et al., 2011, Johnston and Farrell, 2005). Another aspect of engine performance where combustion characteristics of the fuel and air mixture is important, is the blowout and relight behaviour in gas turbine

engines. This is of particular importance in flight applications, where the engine is submitted to extreme weather conditions (Lefebvre, 1999). In both the above examples, the laminar flame speed of the combustible mixture is an important parameter in determining engine performance.

1.1. Motivation

Laminar flame speed is considered a fundamental combustion property of a fuel, since it depends only on the mixture composition, pressure and temperature for a given fuel oxidiser system (Farrell et al., 2004). The laminar flame speed (also laminar burning velocity) of a fuel oxidiser mixture is defined as the velocity of the unburned gas normal to the surface of a stationary flame at steady state conditions. There are several experimental approaches to measuring the laminar flame speed of a mixture, including the flat flame burner setup, the opposed-jet burner setup and the constant volume combustion bomb (Glassman and Yetter, 2008). Each of these experimental setups has advantages and disadvantages and, in general, the data interpretation is not trivial. This has led to discrepancies in laminar flame speed results reported in different studies. However, this has improved significantly over the years, as shown in Figure 1.2.

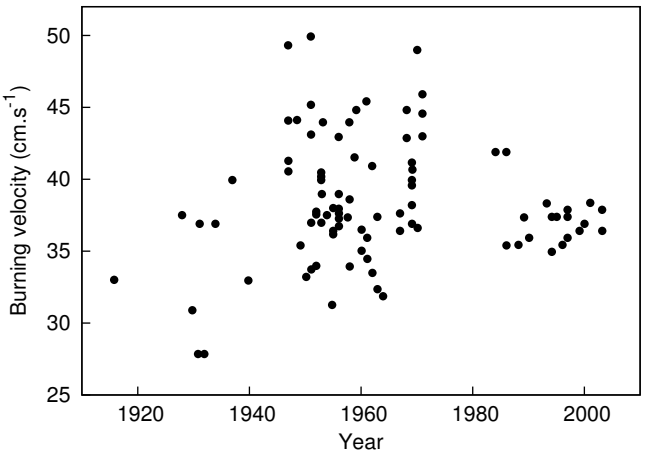

Figure 1.2.: Reported maximum laminar flame speeds for methane and air mixtures at 298 K and 1 atm versus the year of publication. (Law, 2011)

The maximum laminar flame speeds for methane and air reported before 1980 in Figure 1.2 shows high variation. However, as more appropriate methods for interpreting the experimental data were developed, the discrepancies between values reported from differ-

ent studies decreased (Law, 2011). Since the experimental approaches for determining laminar flame speed differ fundamentally, there are still significant discrepancies among recent results from different studies (Kelley et al., 2011).

Enormous effort goes into the development of detailed reaction mechanisms that describe the combustion of several fuels. Since these mechanisms are elaborate, they are often reduced to less descriptive models to improve their computational expense. These models are then used in numerical models such as PREMIX (Kee et al., 1985) to calculate laminar flame speeds. The PREMIX software produces a steady state, planar flame and forms part of the commercially available CHEMKIN package (Kee et al., 2000). There are fewer non-steady state flame models available, which are capable of describing flame propagation. The recently developed A-SURF (Chen, 2009) model is capable of describing spherical flame propagation, but is not commercially or publicly available.

This study will focus on the specific experimental setup of a constant volume combustion bomb, used to determine the laminar flame speed of a fuel oxidiser mixture. A model that is capable of describing the basic flame behaviour, that is experimentally observed for these setups, is a very valuable tool for the combustion researcher. Such a model can be used to compare different constant volume combustion bomb setups in order to gain insight into the discrepancies in the experimental data from different sources. A further application could be to predict the type of experimental setup, such as combustion chamber volume, that is best suited for specific experimental programs. A model like this can also be used to obtain a better understanding of the role that fundamental fuel properties play in complex flame propagation processes.

1.2. Aim and scope

It is the aim of this work to develop a one dimensional reacting flow model for the specific purpose of describing an outwardly propagating, spherical flame that should simulate the flame propagation in a constant volume combustion bomb. The experimental setup in most cases consists of a spherical cavity or combustion chamber filled with the combustible mixture of interest. This mixture is ignited in the centre of the sphere, resulting in a spherical flame that propagates outwards until it reaches the combustion chamber wall and all the gas in the spherical cavity is consumed by the flame. In Figure 1.3, a shadowgraph of a spherical, outwardly propagating flame in a spherical combustion chamber is shown. The time lapse, at which each shadowgraph in Figure 1.3 is taken from the ignition event

in the centre, is given in the bottom left corner of each shadowgraph.

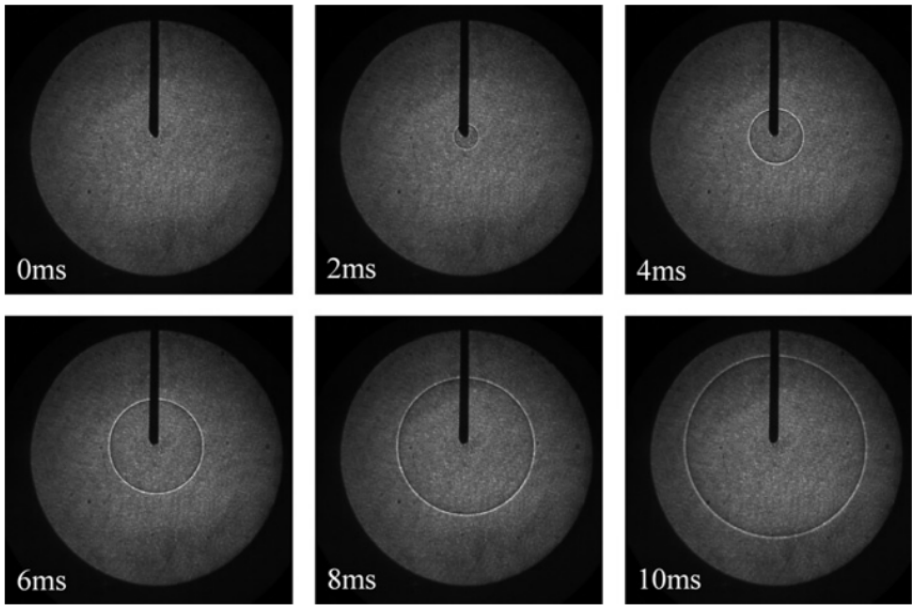

Figure 1.3.: Shadowgraphs of an expanding spherical flame of a stoichiometric mixture of iso-octane and air with initial conditions of 423 K and 1 bar. (Galmiche et al., 2012)

This study produces a model that describes the flame behaviour seen in Figure 1.3, by calculating the condition of the gas at all radial points inside such a spherical cavity as time progresses. To achieve this a one-dimensional system of partial differential equations is derived, that describes the change in species concentrations, temperature and convective velocity of the gas at any radial point. The model includes reaction kinetics, thermal conduction and diffusion of species. In the mathematical system, the radial position and time are two independent variables. A numerical solver is implemented to solve the system of partial differential equations. The numerical solver chosen for this work is BACOL (Wang et al., 2004a), which has several useful features and succeeds in solving the elaborate system of equations.

The conditions modelled in this work are limited to a mixture of iso-octane and air at initial conditions of 370 K and 1 bar for different fuel to air ratios. One drawback of the developed model is its complexity, leading to a long time required to solve the system for one condition and therefore the number of conditions modelled is limited. To model a flame that progresses through a closed spherical space with a 50 mm radius takes

approximately 44 hours per CPU in this study[3].

1.3. Research objectives

The purpose of this modelling exercise is to produce a model that is capable of predicting combustion characteristics of a fuel oxidiser mixture, such as the laminar flame speed and Markstein length, by describing the flame behaviour in the constant volume combustion bomb experimental environment. The value of the model is then demonstrated by comparing different experimental setups under similar conditions and by showing the sensitivity of flame characteristics to certain fuel properties. The model also provides insights into the initial flame behaviour in combustion bombs where only the pressure is measured, since the behaviour cannot be derived from the initial pressure data. A list of objectives for the development of this model is provided below:

1. To obtain an ignition strategy that will initiate flame propagation at a radius close to zero.
2. The total pressure should increase as a result of the increasing hot burned gas, while remaining spatially uniform.
3. To predict experimental flame speed behaviour as the flame stretch rate decreases.
4. To predict the trend of flame speed with increasing pressure.
5. To compare predicted laminar flame speeds and Markstein lengths with literature values.
6. To predict the sensitivity of laminar flame speeds and Markstein lengths to oxygen, fuel and intermediate species diffusion, as well as thermal conductivity and reaction kinetics.

Some of the objectives listed above pose challenges that are ignored in many earlier studies, such as including strategies to describe the uniform pressure increase. The above objectives are chosen in order to develop a model that provides a realistic description of the complete flame propagation in a spherical cavity, similar to that of the constant volume combustion bomb experimental setup.

[3] A 3.3 GHz Core i7 processor is used in this study.

1.4. Dissertation layout

This dissertation consists of five chapters: an introduction, literature review, theory and methods, results and discussion and a conclusion. In the current chapter, the introduction, the background and motivation for the work is given, followed by the aim, scope and research objectives. In the literature review, Chapter 2, some literature related to fundamental fuel properties and how it influences laminar flame speed is referenced and discussed, followed by an extensive description of constant volume combustion bomb experiments, its data interpretation and findings. Chapter 3 is dedicated to the theory and methods followed to derive the partial differential equations and all their inputs, as well as the numerical solver and additional coded procedures required to solve the mathematical system. The results and discussions in Chapter 4 contains initial model results and the approach followed to improve these results, followed by the results for the derived combustion characteristics which are compared to experimental findings. The sensitivity analyses of the combustion characteristics to several fuel properties are also included in the results and discussion chapter. Finally, the conclusions of this study are summarised in Chapter 5, where some recommendations for further development of this work are made. There are also several appendices at the back of this dissertation, containing supplementary methods and findings, as well as the commented code for important segments of the model.

The nomenclature for this document is given in Appendix A, while some of the conventions often used in this dissertation are briefly mentioned below. When referring to the fuel equivalence ratio, this indicates the molar ratio of fuel to oxygen, divided by the stoichiometric molar ratio of fuel to oxygen. The stoichiometric molar ratio of fuel to oxygen is defined as the stoichiometric coefficient of fuel divided by the stoichiometric coefficient of oxygen in a balanced reaction equation for complete combustion. Further, with regards to the flame speeds of a spherical flame in a closed volume, four different speeds are referred to in this dissertation. The flame propagation speed (S_n) is the true speed at which the flame propagates, while the unstretched flame propagation speed (S_s) is extrapolated from the flame propagation speed data and represents the speed at which burned gas flows away from a flat, steady-state flame. In this work, the laminar flame speed (S_L) is calculated from the unstretched flame propagation speed (S_s) and is a derived quantity that is widely reported. The stretched normal flame speed (u_n) is mentioned in this study, and refers to an estimated speed where the flame position is adjusted to a situation where remaining unburned gas is at the initial pressure.

2. Literature review

Flame speeds for many different fuel oxidiser mixtures have been extensively studied, both theoretically and experimentally, over the last decades. The aim of this chapter is firstly to establish the fundamental mixture properties that interact in the flame propagation process and then discuss each of these properties. Secondly, the effect of each of these properties on flame speed properties is shown. Finally, different experimental techniques for obtaining laminar flame data are described and evaluated.

A simple approach discussed in Section 2.1 shows that a flame is a complex process and that the laminar flame speed is dependent on several other fundamental combustion properties of the mixture. Different fuels show differences in these combustion properties and therefore different laminar flame speeds are observed. Modelling the process of flame propagation requires a comprehensive mathematical description of fundamental mixture properties such as reaction kinetics and molecular transport. In literature, one dimensional models for laminar flame speed in a steady-state open system are used widely. In particular, the software PREMIX as part of CHEMKIN (Kee et al., 1985) is commonly used. However, modelling transient flame propagation in a closed combustion bomb is less common and presents several challenges.

2.1. Fundamentals

A flame is the region of combustion in a mixture of fuel and oxidiser, where the combustion reactions and therefore heat release occurs. Different flame types can be identified, depending on the nature of mixing (premixed or non-premixed) and flow dynamics (laminar or turbulent). In non-premixed flames, combustion and mixing of the fuel and oxidiser takes place simultaneously, which implies that propagation of a flame front is not possible. Flame speed is a characteristic of premixed flames where laminar flame speeds and turbulent flame speeds are defined. In the case of turbulent premixed flames, the flame front propagates into turbulent fluid flow, resulting in curved flame fronts (Warnatz et al.,

2001).

The spark ignition engine is a common example of a combustion system where turbulent premixed flames govern the combustion process. The fluid flow of a turbulent premixed flame is much more complex than that of a laminar premixed flame and therefore more difficult to predict. If the intensity of turbulence is not too high, a turbulent premixed flame can be described as a collection of many laminar premixed flames by the so-called "flamelet model". This then serves as motivation to study the laminar flame speed of different combustion systems as it gives more insight and predictive capabilities for turbulent premixed flame combustion systems (Warnatz et al., 2001).

Figure 2.1 shows the structure of a flame from which the governing processes for propagation can be identified as the rate of heat release and transport processes, such as thermal conduction and diffusion of radicals. These processes cause a wave of chemical reaction that is thermally induced and is called deflagration. The flame front can be divided into three zones: a preheat zone, a reaction zone, and a recombination zone as depicted in the simple temperature profile schematic shown in Figure 2.1 (Glassman and Yetter, 2008).

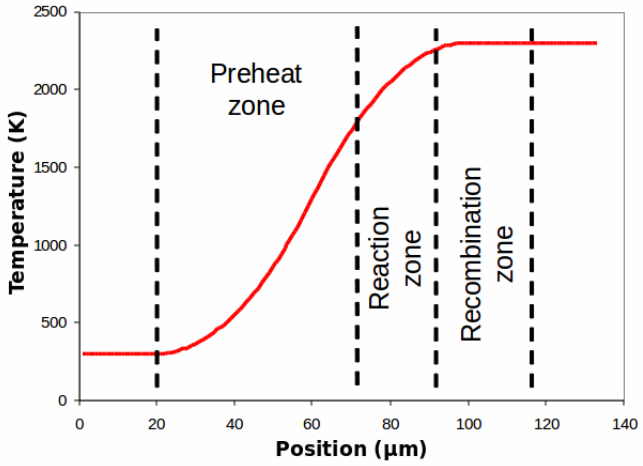

Figure 2.1.: Schematic temperature profile of flame indicating the structure of the flame front.

In the reaction zone, reactions cause heat release which then heats the unburned gas by thermal conduction due to a temperature gradient. In the first stage of the reaction zone, pyrolysis of the fuel molecules take place to form intermediates and in a following stage the intermediates are consumed. This behaviour causes different hydrocarbon fuels to produce similar flame structures and flame speeds, since the fuels first undergo pyrolysis producing intermediate species which are similar for different hydrocarbon fuels. The

heat generated in the reaction zone is transferred to the unburned gas in the preheat zone causing more reaction and hence the propagation of the flame front (Glassman and Yetter, 2008).

Initial theoretical analyses of laminar flame speeds consisted of three categories: thermal limited models, diffusion limited models, and comprehensive models. The thermal limited model postulates that the flame propagation is driven by the conduction of heat from the reaction region to the unburned gas whereas the diffusion limited model postulates that the diffusion of free radicals is the main driver for flame propagation (Glassman and Yetter, 2008). It was later, after studying flames where no intermediates are involved, concluded that thermal conduction alone is able to drive flame propagation and therefore thermal limited models are sufficient to estimate laminar flame speeds (Glassman and Yetter, 2008). The comprehensive models include both thermal conduction and diffusion of all species together with chemical kinetic mechanisms to calculate laminar flame speeds (Glassman and Yetter, 2008).

The thermal limited model, initially developed by Le Chatelier and Mallard (1883), used a concept where the flame is divided into two regions: the region of burning and the region of thermal conduction. At the boundary between these regions the gas temperature is at its ignition temperature and heat is conducted through this boundary to the region of conduction. This concept is shown in the schematic temperature profile of Figure 2.2.

It is assumed that thermal energy conducted back from the region of burning is equal to the energy required to heat the unburned gas to the ignition temperature in the region of conduction. From this the expression in Equation 2.1 for laminar flame speed is obtained (Glassman and Yetter, 2008).

$$S_L = \sqrt{\frac{\lambda\,(T_f - T_i)}{\rho c_p\,(T_i - T_0)}\,\frac{\dot{\omega}}{\rho}} \tag{2.1}$$

In Equation 2.1, S_L is the laminar flame speed, λ is the thermal conductivity, ρ is the density, c_p is the constant pressure heat capacity, $\dot{\omega}$ specifies the reaction rate and T_f, T_i and T_0 are the final, ignition and initial temperature respectively. Further developments were aimed at obtaining a more representative term for the temperature ratio containing the unknown ignition temperature (T_i). They followed the standard procedure of narrow reaction zone asymptotics and arrived at Equation 2.2 (Glassman and Yetter, 2008).

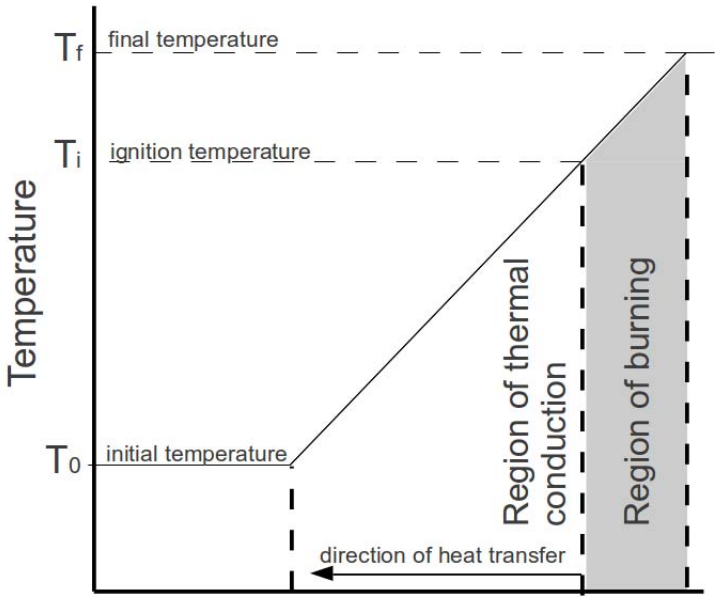

Figure 2.2.: Schematic temperature profile showing the concept of a thermal conduction driven flame.

$$\frac{T_i - T_0}{T_f - T_i} = \frac{RT_f^2}{E\,(T_f - T_0)} = \beta \tag{2.2}$$

In Equation 2.2, R is the universal gas constant, E is an activation energy and the reciprocal of the temperature ratio term is presented as β. The expression for laminar flame speed is now given by Equation 2.3.

$$S_L = \sqrt{\frac{\lambda}{\rho c_p \beta}\frac{\dot{\omega}}{\rho}} \tag{2.3}$$

The generic expression for reaction rate ($\dot{\omega}$) is given in Equation 2.4, where A_{RR} is the pre-exponential constant.

$$\dot{\omega} = A_{RR} \exp\left(\frac{-E}{RT}\right) \tag{2.4}$$

Glassman and Yetter (2008) stated that, by assuming general hydrocarbon flame conditions in Equation 2.3, the flame thickness is in the order of 1 mm while the thickness of the region of reaction is of the order of a tenth of a millimetre. It was also shown

from Equation 2.3 that the dependence of laminar flame speed on the pressure (P) of the system can be presented by Equation 2.5.

$$S_L \propto \left(P^{g-2}\right)^{1/2} \tag{2.5}$$

This pressure dependence is due to the density terms (ρ) in Equation 2.3 and the order of the reaction rate, which is represented by g in Equation 2.5. Although the reaction rate for hydrocarbon combustion can be approximated as second-order, it has been found that the laminar flame speed decreases with an increase in pressure. This is due to the increasing role of the third-order reaction (Reaction 2.6) which decreases the rate of heat release (Glassman and Yetter, 2008).

$$H + O_2 + M \rightarrow HO_2 + M \tag{2.6}$$

The symbol M, in Reaction 2.6 represents a third body species and this concept is discussed in Section 3.4.2. It is also noted that the dependence of the mass burning rate or mass flow rate ($\dot{m}$) on pressure is given by Equation 2.7.

$$\dot{m} \propto P^{g/2} \tag{2.7}$$

Therefore the mass burning rate will increase with an increase in pressure. The dependence of laminar flame speed on temperature is dominated by the exponential in the rate expression ($\dot{\omega}$) in Equation 2.4. Therefore the relation in Equation 2.8 is assumed for the temperature dependence of laminar flame speed.

$$S_L \propto \sqrt{\exp\left(\frac{-E}{RT_f}\right)} \tag{2.8}$$

The temperature term in Equation 2.8 is taken as the final temperature (T_f) since it is argued that most of the reaction takes place close to the highest temperature. Thus, an increase in the initial temperature will cause an increase of a lesser degree in the final flame temperature, which will cause the laminar flame speed to increase according to the relation shown in Equation 2.8. The approach of the thermal limited model gives valuable insight into the thermal influences on laminar flame speed and from this simple approach, explanations for observed flame phenomena can be suggested.

The comprehensive model takes a more holistic approach and includes thermal and diffusive effects in its calculations. This approach utilises numerical computations to solve the energy and species conservation equations for a steady-state flame. By including a detailed chemical kinetic mechanism, the temperature and species profiles across the flame front can be accurately predicted. The PREMIX (Kee et al., 1985) code is used widely to solve one-dimensional adiabatic premixed steady-state flames by calculating the transport, thermochemical and reaction properties of the system. This approach then provides a much more detailed description of the flame, including the laminar flame speed. Because of its higher complexity it is more difficult to identify the fundamental causes of observed trends, but sensitivity analyses are incorporated in the PREMIX code for this purpose.

Equation 2.1 then shows that the laminar flame speed is a function of several fundamental properties of the fuel oxidiser mixture, namely: thermal conductivity (λ), reaction rate ($\dot{\omega}$), density (ρ), heat capacity (c_p) and the initial, ignition and final temperatures ($T_0,\ T_i,\ T_f$). The following sections will look at some of these fundamental properties to establish expected trends and to gain a better understanding of the influences of properties such as pressure and temperature on them. Some approaches for implementing these properties into a combustion model are discussed in Chapter 3.

2.1.1. Adiabatic flame temperature

The flame temperature is a characteristic property of the equilibrium state of a combustion event and is an important property when considering flame propagation in a gas. This is due to the fact that the molecular transport of energy, or heat transfer, enables flame propagation and is a function of the temperature gradient over the flame front. In this section the parameters influencing the adiabatic flame temperature of a gas will be discussed followed by a brief overview of the adiabatic flame temperatures of different gas mixtures of relevance.

The flame temperature for a constant pressure system is calculated from a reactants-products energy balance, which is shown in Equation 2.9 (Glassman and Yetter, 2008).

$$\sum_{i\,prod} n_i \left[\{(h_{T_2} - h_0) - (h_{T_0} - h_0)\} + h_{f(T_0)}\right]_i \quad = \quad \sum_{j\,reac} n_j \left[\{(h_{T_1} - h_0) - (h_{T_0} - h_0)\} + h_{f(T_0)}\right]_j \tag{2.9}$$

In Equation 2.9, the molar heat of formation $\left(h_{f(T_0)}\right)$ of the fuel reactant at standard conditions is an important factor in determining the temperature of the flame product mixture (T_2). Since larger reactant molecules consist of more carbon, hydrogen and other atoms, the heat of formation per unit mass is considered when comparing reactant fuel molecules to normalise the effect of number of product moles (n_i). The heat of formation of the reactants based on mass, varies little among most hydrocarbon fuels (Glassman and Yetter, 2008). However, in comparing the flame temperature of different fuels of higher molecular weights (liquid fuels), it is seen that the heat of formation is the determining factor for the observed differences.

The composition of the combustion product mixture is a direct result of the atoms present in the reactants and in what ratios they are present, as well as the initial temperature and pressure. In a C-H-O system, the combustion products will be CO_2, H_2O and their dissociation products. These dissociation products are produced via reversible reaction paths which have a significant effect on the flame temperature. Two common reversible reactions associated with combustion products are given by Reactions 2.10 and 2.11.

$$H_2O \rightleftarrows H_2 + \frac{1}{2}O_2 \tag{2.10}$$

$$CO_2 \leftrightarrows CO + \frac{1}{2}O_2 \tag{2.11}$$

The adiabatic flame temperature of a stoichiometric mixture of methane and air was calculated from initial conditions of 273 K and 1 bar by Law et al. (2006). It was shown that by omitting the dissociation reactions, the adiabatic flame temperature decreases from 2 325 K to 2 224 K. Other less significant reactions are also possible and may become more significant at elevated temperatures, such as the dissociation of H_2 and O_2. A complex mixture of many different molecules is therefore possible for a combustion product mixture. The composition of this combustion product mixture is dependent on the atoms available from the reactant mixture and the equilibrium states of the reactions,

which are again dependent on the pressure and temperature as discussed by Glassman and Yetter (2008).

In a system where air is the oxidiser, the effect of the mostly inert nitrogen gas (N_2) plays an important role in the flame temperatures. The unreacted nitrogen gas makes up a large fraction of the combustion product, therefore much of the energy released by the combustion reactions is used to heat up this unreacted nitrogen. However, nitrogen gas will react with oxygen at high temperatures. As a rule of thumb, nitrogen monoxide (NO) will start forming in minute amounts at temperatures above 1 700 K. It has also been found that nitrogen reactions only start affecting the system thermodynamically at temperatures above 3 000 K (Glassman and Yetter, 2008).

From a practical point of view, it has been observed that the flame temperature of a given fuel reaches a maximum when the reactant mixture is close to the stoichiometric mole fractions. This effect is simply because at non-stoichiometric conditions, there will either be unreacted oxidiser (O_2) or fuel left which must be heated by the available heat of combustion. Conditions where the oxidiser is in excess are referred to as fuel lean reactant mixtures and conditions where the fuel is in excess are referred to as a fuel rich reactant mixture. The fuel equivalence ratio (ϕ) of a reactant mixture is the ratio of fuel to oxidiser in the mixture, divided by the stoichiometric ratio of fuel to oxidiser. The flame temperature of many fuels reaches a maximum between equivalence ratios of 1.0 and 1.1. The adiabatic flame temperature of iso-octane and n-heptane from initial conditions of 298 K and 1 atm for different fuel equivalence ratios is shown in Figure 2.3 (Huang et al., 2004).

From Figure 2.3 it is clear that the equivalence ratio of the reactant mixture is an important determining factor of the flame temperature. Another important factor determining the adiabatic flame temperature is the H/C mole ratio in the reactant mixture. This ratio directly determines the ratio of water vapour and carbon dioxide formed in the product mixture. The combustion products from the hydrogen atoms is water vapour and its dissociation products, which have lower heat capacities than those of carbon dioxide and its dissociation products. Therefore a higher ratio of hydrogen combustion products to carbon combustion products will result in higher flame temperatures (Glassman and Yetter, 2008).

Pressure also affects the flame temperature due to its influence on the equilibrium states of the dissociation reactions. For this reason pressure variations have the greatest effect on combustion systems with a high degree of dissociation. The pressure effect is more

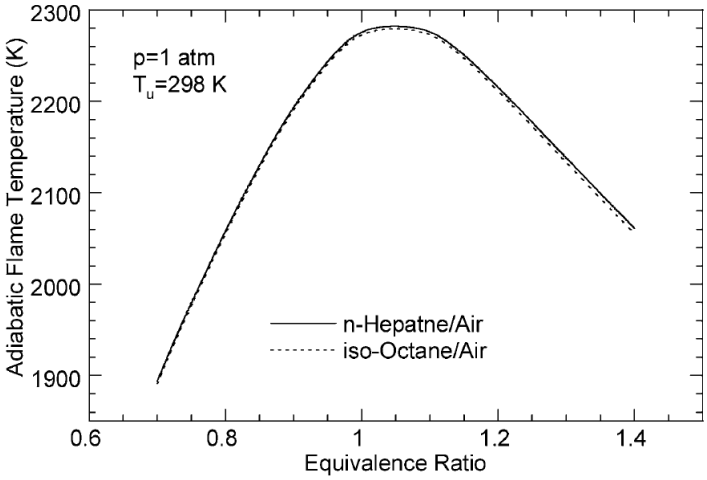

Figure 2.3.: Adiabatic flame temperature of n-heptane and iso-octane in air for different fuel equivalence ratios. (Huang et al., 2004)

significant at stoichiometric conditions, for example, since the degree of dissociation is higher. An increase in pressure results in an increase of the flame temperature. This is explained by Le Chatelier's principle where an increase in pressure favours a system with fewer molecules. The result is a shift in the equilibrium state of the dissociation reactions, to form fewer molecules and thus fewer dissociation products are produced from the reversible reactions given in Reactions 2.10 and 2.11. It was also shown that the pressure effect is much more significant for combustions systems with pure oxygen, since the presence of inert nitrogen gas dampens the degree of dissociation leading to a less significant pressure effect on the flame temperature (Glassman and Yetter, 2008).

The adiabatic flame temperatures for several pure hydrocarbon fuels and air are available from literature. In most cases these are calculated values, since the experimental setup for adiabatic conditions is not easily achieved. Glassman and Yetter (2008) reported calculated values for the adiabatic flame temperatures of several hydrocarbons. These values, some of which are given in Table 2.1, were calculated for a constant pressure, stoichiometric, adiabatic system with an initial temperature of 298 K and a constant pressure of 1 atm, and the above mentioned dissociation reactions were taken into account.

Table 2.1 shows some notable trends. Firstly, the adiabatic flame temperature for alkanes shows little variation between fuel molecules of different sizes. Also, the adiabatic flame temperature of aromatic fuel molecules, such as toluene, is significantly higher considering the small difference between that of the alkanes. This is explained by the difference in

Table 2.1.: Constant pressure adiabatic flame temperatures of selected pure hydrocarbons in air. (Glassman and Yetter, 2008)

Name	Chemical formula	T_{ad} (K)
Heptane	C_7H_{16}	2 265
Octane	C_8H_{18}	2 266
n-Decane	$C_{10}H_{22}$	2 267
n-Dodecane	$C_{12}H_{26}$	2 268
n-Hexadecane	$C_{16}H_{34}$	2 269
Methylcyclohexane	C_7H_{14}	2 269
Propylcyclohexane	C_9H_{18}	2 271
Propylbenzene	C_9H_{12}	2 306
Toluene	C_7H_8	2 317

the mass-based heat of formation for alkanes and aromatics. The constant pressure adiabatic flame temperatures in Table 2.1 are lower than the constant volume adiabatic flame temperatures, since no energy is lost through expansion in the constant volume system.

It can therefore be concluded that the equivalence ratio of the reactant mixture is a key factor influencing the flame temperature along with the H/C ratio in the mixture and the heat of formation of the fuel. Further, the presence of an inert diluent such as nitrogen gas in the oxidiser mixture has a significant decreasing effect on the flame temperature. Finally it was also found that the pressure of the reactant system has a significant effect on the flame temperature if the conditions are such that at a low pressure, a high degree of dissociation is present in the system.

The adiabatic flame temperature of a given fuel oxidiser mixture at certain conditions, describes the final equilibrium state after a combustion process. It is a measure of the magnitude of the heat release that occurred during combustion and the heating of the combustion products, taking into account reaction equilibrium. This final temperature of the combustion products plays an important role in flame propagation. For this reason it is essential to obtain an accurate description of the final equilibrium state of the combustion products in order to obtain an accurate description of the burning velocity.

2.1.2. Chemical reactions

As mentioned before, a flame can be described as a reaction wave, where fuel and oxidiser is converted to combustion products via chemical reaction. Although a reactant-to-product approach gives the impression that these reactions are very simple, that is not the case. A simple combustion system such as that of hydrogen and oxygen requires of the order of 40 elementary reactions to describe the complete reaction mechanism (Warnatz et al., 2001). Chemical kinetic mechanisms have been developed to describe these reaction mechanisms in a model. These chemical kinetic mechanisms are validated against experimental data such as auto-ignition delay times and jet stirred reactor data (Dagaut, 2002).

A well known phenomena in combustion research is the auto-ignition delay, where the fuel oxidiser mixture, at auto-ignition conditions, shows no significant heat release for a specific time before rapid reaction takes place and heat release is observed. This time delay is then called the auto-ignition delay time or just ignition delay time and is a widely studied parameter for many different fuels and under many different conditions. In this section, the underlying chemistry responsible for the auto-ignition delay is discussed, followed by models describing this chemistry. Since the auto-ignition delay time serves as a good overall description of the reaction kinetics and ignition time, it is used as the basis for the discussion of chemical reaction rates of a propagating flame, in this work.

Radical-chain explosions, where chemical reactions are governed by a chain-branching mechanism, are responsible for this delayed ignition. A chain-branching step in a mechanism is defined as a reaction where one radical reacts to form two or more radicals. During the ignition delay time, radicals are formed via chemical reactions that consume a small amount of fuel molecules and result in insignificant heat release. At the point where the radical concentration is high enough to consume a significant amount of the fuel molecules, rapid reaction and therefore significant heat release will occur, resulting in the observed ignition of the mixture (Warnatz et al., 2001).

Since the rates of the underlying reactions are temperature dependent, the ignition delay time of a fuel oxidiser mixture is strongly dependent on the temperature. The relation between the auto-ignition delay time and temperature for a given fuel oxidiser mixture can be represented by a simple Arrhenius relation where the ignition delay time is directly proportional to the exponential of the reciprocal temperature as shown in Equation 2.12 (Warnatz et al., 2001).

$$\tau_{ign} \propto \exp\left(\frac{1}{T_i}\right) \tag{2.12}$$

In Equation 2.12, τ_{ign} is the ignition delay time and T_i is the initial temperature. However, the auto-ignition delay times of many fuel components show a more complex dependence on temperature, such as negative temperature coefficient (NTC) and cool flame behaviour. NTC refers to the phenomena where the auto-ignition delay time for a certain fuel oxidiser mixture increases with an increase in temperature over a specific temperature range. Cool flame behaviour refers to the phenomena where after an initial time delay a smaller heat release occurs followed by a further time delay before the main heat release occurs. Fuel components that displays cool flame behaviour are referred to as two-stage fuels. The fuel component n-heptane is an example of a two-stage fuel that shows strong NTC behaviour as seen in Figure 2.4. These complexities are a consequence of more complex reaction mechanisms for the radical-chain explosions.

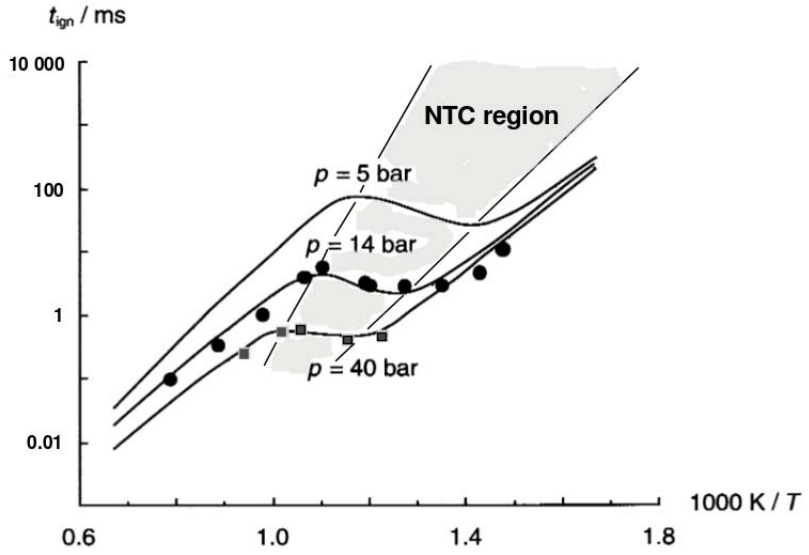

Figure 2.4.: Ignition delay times for stoichiometric n-heptane-air mixture where the NTC region is indicated. Adapted from Warnatz et al. (2001)

Figure 2.4 also shows that the ignition delay times are significantly influenced by the initial pressure of the system. These observed effects are consequences of the chemical reaction mechanisms and the influence of temperature and pressure on each of the individual reactions. A schematic of the chemical pathways dominant at different temperatures follows.

2.1.2.1. Chemistry

Due to complex reaction mechanisms for the combustion of fuel components, different reaction pathways are dominant under different conditions. This then results in different reaction pathways being dominant at higher and lower temperatures and therefore the complex dependence of auto-ignition delay times on temperature. What is regarded as high temperature and low temperature is not clearly defined and can differ between different fuel components. In the reactions below, R, R′ and R″ represent different alkyl groups, while M represent a third body molecule that acts as an activation point for reactants in the chemical reaction, as explained in Section 3.4.2.

High temperature (above 1 200K)
As mentioned previously, the reaction mechanisms responsible for hydrocarbon combustion are governed by chain-branching steps. At very high temperatures, the dominant chain-branching step is simply (Warnatz et al., 2001):

$$H\bullet + O_2 \rightarrow O\bullet + OH\bullet \tag{2.13}$$

However, at lower temperatures Reaction 2.13 is too slow.

Intermediate temperature (900 K < T < 1 200 K)
It was determined that at intermediate temperatures the $HO_2\bullet$ radical also takes part in a chain-branching step as shown in Reaction 2.14 (Warnatz et al., 2001).

$$\begin{aligned} HO_2\bullet + RH &\rightarrow H_2O_2 + R\bullet \\ H_2O_2 + M &\rightarrow OH\bullet + OH\bullet + M \end{aligned} \tag{2.14}$$

The $HO_2\bullet$ radical can be produced from the $OH\bullet$ radicals as shown:

$$\begin{aligned} OH\bullet + H_2 &\rightarrow H_2O + H\bullet \\ H\bullet + O_2 + M &\rightarrow HO_2\bullet + M \end{aligned} \tag{2.15}$$

Low temperature (below 900 K)
At lower temperatures, the decomposition of H_2O_2 is much slower and therefore the chain-branching step is driven by other mechanisms which are fuel specific and thus more complicated. Peroxy radicals are the main radicals responsible for chain-branching steps

here. The peroxy radical ($RO_2\bullet$) is formed via a reversible oxygen addition reaction, as seen in Reaction 2.16 (Warnatz et al., 2001).

$$\begin{array}{rcrcrcl} R\bullet & + & O_2 & \rightleftarrows & RO_2\bullet & & \\ RO_2\bullet & + & RH & \rightarrow & ROOH & + & R\bullet \\ ROOH & & & \rightarrow & RO\bullet & + & HO\bullet \\ RO_2\bullet & & & \rightarrow & HOOR'\bullet & & \\ HOOR'\bullet & & & \rightarrow & R'O & + & HO\bullet \end{array} \tag{2.16}$$

The reaction mechanism in Reaction 2.16 shows that the $RO_2\bullet$ radical can follow two paths of which the second ($RO_2\bullet \rightarrow HOOR'\bullet$, internal H-atom abstraction) is the faster and thus dominant path. The $HOOR'\bullet$ radical formed in Reaction 2.16 further takes part in another reversible reaction with oxygen as seen in Reaction 2.17.

$$\begin{array}{rcrcrcl} HO_2R'\bullet & + & O_2 & \rightleftarrows & HO_2R'O_2\bullet & & \\ HO_2R'O_2\bullet & + & RH & \rightarrow & HO_2R'O_2H & + & R\bullet \\ HO_2R'O_2H & & & \rightarrow & HO_2R'O\bullet & + & HO\bullet \\ HO_2R'O\bullet & & & \rightarrow & OR'O & + & HO\bullet \\ HO_2R'O_2\bullet & & & \rightarrow & \overset{\bullet}{H}O_2R''O_2H & & \\ \overset{\bullet}{H}O_2R''O_2H & & & \rightarrow & HO_2R''O & + & HO\bullet \\ HO_2R''O & & & \rightarrow & OR''O\bullet & + & HO\bullet \end{array} \tag{2.17}$$

The product of the second oxygen addition reaction ($HO_2R'O_2\bullet$) can again react via two different pathways. Following these pathways the chain-branching is achieved as shown in Reaction 2.17, resulting in low temperature chain-branching. The two oxygen addition reactions are reversible and at lower temperatures will favour the forward reaction. This mechanism causes the observed cool flame effect, where the low temperature kinetics cause some heat release via the two oxygen addition reactions. The temperature will therefore increase due to the heat release and when it reaches a certain point, the equilibriums of the two oxygen addition reactions shift and the backward reactions are favoured. Therefore, at higher temperatures, the pathways from Reactions 2.16 and 2.17 are "shut down". After the initial smaller temperature rise, another ignition delay is observed before the main heat release. This second "ignition delay" is again governed by the high temperature kinetics (Warnatz et al., 2001).

This then gives an overview of the reactions that govern the ignition delay time and

therefore combustion kinetics. When these mechanisms are applied to real fuels, it results in much larger mechanisms, including all probable elementary reactions. These large reaction mechanisms form the basis for numerical modelling of combustion systems, as is discussed in the next section.

2.1.2.2. Chemical kinetic models

In order to accurately model combustion processes for a given system, the reaction mechanism and rate of each reaction is required. However, the number of possible species present in the combustion chemistry drastically increases with an increase in carbon number of the fuel component. With an increase in species, the number of possible reactions increases even more drastically. This effect is shown in Figure 2.5.

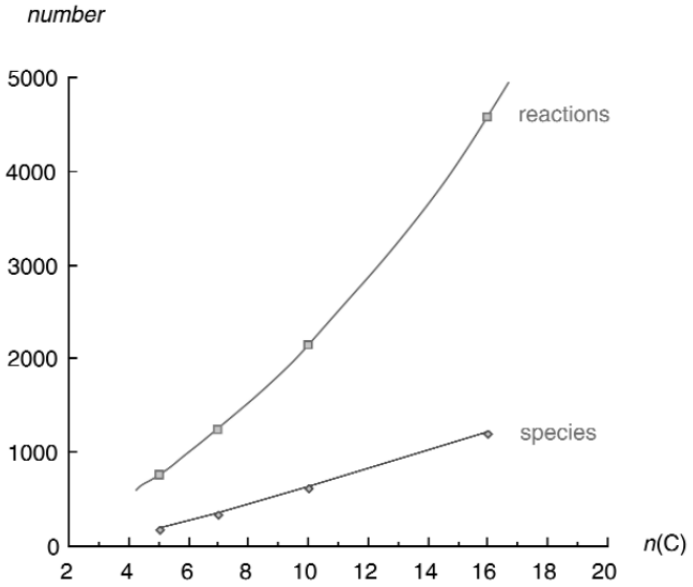

Figure 2.5.: Number of species and reactions involved in low temperature oxidation for different carbon number alkanes. (Warnatz et al., 2001)

Kinetic mechanisms that include all relevant species and reactions are referred to as detailed chemical kinetic mechanisms. Given the large amount of species to keep track of, these detailed chemical kinetic mechanisms for higher carbon number fuel components are computationally very expensive. For this reason, the implementation of a detailed chemical kinetic mechanism in models of more complex systems, such as engine models, is not practically justifiable if the required computational power is not available. This has led to the development of reduced, skeletal and global reaction mechanisms, which are

simpler, but less accurate. A simple classification of these models is given in Table 2.2, taken directly from Zheng et al. (2004).

Table 2.2.: Categories of chemical kinetic models. (Zheng et al., 2004)

Category	Description	Species	Reactions
Detailed	The latest "comprehensive" reaction set.	100's	1 000's
Lumped	Uses a lumped description for larger species.	100's	1 000's
Reduced	A subset of the detailed model.	10's	10's - 100's
Skeletal	Employs class chemistry and lumping concepts.	10's	10's
Global	Utilise global reactions to minimise reaction set.	<10	<10

Note that Table 2.2 does not give the definite classification of chemical mechanism models, but indicates the differences between the models. It should also be noted that development of these models are focused on fuel components generally used in models and are not available for a large range of fuel components. The simpler chemical kinetic models, such as skeletal and global models, are mostly validated against simulated data using detailed models, since experimental data from different researchers usually do not show good agreement with each other (Griffiths, 1995).

Westbrook et al. (2011) developed a single detailed chemical kinetic model to describe combustion of primary reference fuels (PRF) for both gasoline and diesel, i.e. for mixtures of n-heptane, n-hexadecane, iso-octane and iso-cetane. This model basically consists of a mechanism for n-hexadecane and iso-cetane combustion, where n-heptane and iso-octane are intermediate products of n-hexadecane and iso-cetane combustion respectively. This comprehensive model shows good agreement with experimental data. However, it is noted that additional experimental data for iso-cetane combustion is required for sufficient validation. Westbrook et al. (2011) also noted that for stoichiometric fuel air mixtures, the auto-ignition delay times for all four components in this model are very similar over the whole calculated temperature range except for the NTC region. It was then concluded that it was this differing behaviour in the NTC region that causes the difference in cetane number for these fuel components (Westbrook et al., 2011).

As mentioned before, a detailed chemical kinetic model enables accurate predictions of a large number of intermediate species in simple combustion systems such as a homogeneous autoignition experiment. However, for a more complex system such as the constant volume combustion bomb in this study, a simplified chemical kinetic model is required. Detailed chemical kinetic mechanisms such as the one discussed above are often used to

produce lumped, reduced and sometimes skeletal models. Global models are very simple chemical kinetic models that are based on an overall reaction schematic, as given in Section 2.1.2.1, and are optimised with and validated against detailed chemical kinetic models.

A global chemical kinetic model with 5 reactions was developed by Schreiber et al. (1994) to describe the ignition delay of n-heptane and iso-octane, the primary reference fuels for gasoline. This particular model is fitted to ignition delay data for different mixtures of n-heptane and iso-octane, to be able to model the ignition time of any PRF mixture in an internal combustion engine simulation. The correct ignition delay time response to pressure was achieved by including pressure dependence of certain reaction rates. The reaction scheme for primary reference fuels developed by Schreiber et al. (1994) is given in Table 2.3.

Table 2.3.: Schreiber global model reaction rate parameters.

	Reaction	A_{RR} (mol m s)	E/R (K)	Reaction heat ($\frac{\text{kJ}}{\text{mol}}$)
1	$F \rightarrow X$	5.0×10^8	18 050	709.9
2	$X + 12.5O_2 \rightarrow P$	7.0×10^6	7 200	-4 709.9
3^+	$F + 2O_2 \rightarrow I$	3.5×10^9	19 500	-53.9
3^-	$I \rightarrow F + 2O_2$	6.0×10^{27}	37 500	53.9
4	$I \rightarrow 2Y$	6.0×10^7	5 000	-60.0
5	$Y + 0.5F + 11.5O_2 \rightarrow P$	1.0×10^9	16 500	-3 913.1

The X, I and Y in Table 2.3 are collective representations of intermediate species forming as a result of either high or low temperature chemical pathways. Reaction 1 and 2 in Table 2.3 describes the simpler high temperature kinetics while the rest of the reactions in Table 2.3 describes the more complex intermediate and low temperature kinetics. The two stage ignition observed for alkanes is captured by Reaction 3 in Table 2.3, which has a forward and backward reaction rate. This reversible step then represents the reversible low temperature oxygen addition steps discussed in Section 2.1.2.1. In Equation 2.18, the reaction rate constant (k_i) for each reaction rate (RR_i) is calculated from the pre-exponential constant (A_{RR}) and normalised activation energy ($\frac{E}{R}$) given in Table 2.3.

$$k = A_{RR}\, exp\left(-\frac{E}{RT}\right) \tag{2.18}$$

It should be noted that the units of the reaction rate constant (k_i) and the pre-exponential constant (A_{RR}) are not fixed and vary as the rate equations vary. However, the base units

for these constants are taken as moles, metres and seconds, as indicated in Table 2.3. The reaction rate for each reaction in Table 2.3 is given in Equation 2.19.

$$\begin{aligned} RR_1 &= k_1 [\mathrm{F}] \left(\frac{P}{P_0}\right)^{0.5} \\ RR_2 &= k_2 [\mathrm{X}] [\mathrm{O_2}] [M] \\ RR_{3^+} &= k_{3^+} [\mathrm{F}] [\mathrm{O_2}] [M] \left(\frac{P}{P_0}\right)^{-2.2} C_{3^+} \\ RR_{3^-} &= k_{3^-} [\mathrm{I}] \left(\frac{P}{P_0}\right)^{-3.5} \\ RR_4 &= k_4 [\mathrm{I}] C_4 \\ RR_5 &= k_5 [\mathrm{O_2}] [Y] \end{aligned} \tag{2.19}$$

Equation 2.19 then gives the reaction rates for each of the reactions in this global reaction model. The concentration of a certain species is represented by [F], which is the concentration of the fuel (F) in this case. The pressure dependence of the model is described by the $\frac{P}{P_0}$ terms, where P is the pressure of the system and P_0 is the reference pressure, 10 bar. The terms C_{3^+} and C_4 are introduced to enable the model to describe the combustion thermal response of an iso-octane and n-heptane mixture, based on its octane number, according to Equation 2.20.

$$\begin{aligned} C_{3^+} &= \frac{110 - ON}{10} \\ C_4 &= \left(\frac{110 - ON}{10}\right)^{\frac{1}{2}} \end{aligned} \tag{2.20}$$

In Equation 2.20, ON is the octane number for the mixture. In the case where iso-octane and n-heptane are mixed, the octane number is simply the volume fraction of iso-octane in the mixture. This reaction model is very simple, yet has the ability to describe important combustion parameters such as the ignition delay time and the NTC behaviour. This then enables the prediction of ignition delay times for different iso-octane and n-heptane mixtures, as seen in Figure 2.6 taken from Schreiber et al. (1994).

Figure 2.6 shows that this model shows reasonable agreement with experimental data. However, it was reported by Schreiber and co-workers (1994) that the model showed

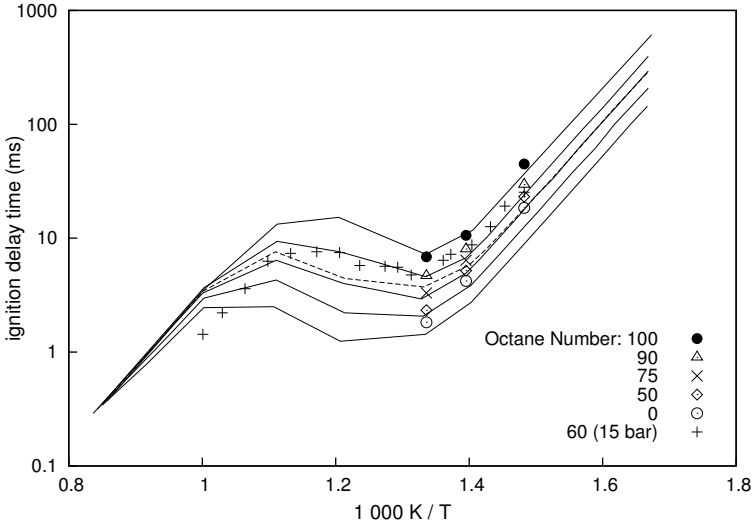

Figure 2.6.: Ignition delay times for different Octane Number fuels. (Replotted from Schreiber et al. (1994))

excellent agreement with the detailed chemical kinetic model of Griffiths et al. (1994). The Schreiber model (1994) is a very useful tool for combustion models of complex systems, but has some drawbacks. It is only validated against iso-octane, n-heptane mixtures and its accuracy in describing the ignition delay times of other fuel mixtures or pure components with equivalent octane numbers, is unknown. The reaction enthalpies provided by Schreiber et al. (1994) for the high and low temperature reaction pathways also defy Hess' law[1], since these pathways have the same reactants and products, but result in different overall reaction enthalpies.

The potential of this global reaction model as a tool in complex simulations has prompted its further development to produce a more reliable version (Bourdon et al., 2004). The simplicity of the global model, developed by Schreiber et al. (1994), provides the opportunity to increase its accuracy for a certain combustible mixture by optimising the parameters for that particular case. Bourdon et al. (2004) did this for two cases; one for a near stoichiometric mixture of n-heptane and air with a large fraction of exhaust gas recirculation (EGR) and one for a mixture of n-heptane and air at very lean conditions. The accuracy for ignition delay times of the first case, when compared to detailed chemical kinetic simulations, was greatly improved . The improvements for the second case were less severe, yet as expected the accuracy was improved. Although this approach

[1] Hess' law: "The overall energy change in going from reactants to products does not depend on the route taken." (Daintith, 2004)

ensures a simple, accurate global reaction model, it is a time consuming task to optimise the model for each specific case.

As discussed above, there are several chemical kinetic models available to describe the combustion chemistry of a fuel. These models vary in complexity, accuracy and in what they are developed to model, as seen for the case of the global model developed by Schreiber et al. (1994), which aimed to describe the ignition delay times for a PRF fuel. For the modelling of a propagating flame, the first attempt should be a simple chemical kinetic model. However, this will render the model unable to accurately describe certain effects present in a propagating flame, such as the diffusion of small intermediates. Whether the diffusion of these intermediate species has a significant effect on flame speed is questionable and will be addressed in the sensitivity analyses in Chapter 4.

2.2. Physical and chemical effects on laminar flame speed

In Section 2.1 the thermal limited model of Le Chatelier and Mallard (1883) gives a good indication of what response to expect from the laminar flame speed behaviour for different chemical and physical effects in a fuel oxidiser mixture. Physical effects that will be discussed are the fuel equivalence ratio, unburned gas temperature, pressure, inert dilution, the flame stretch rate and flame instability. The effect of fuels with different ignition delay time behaviour will also be discussed to shed some light on chemical effects on laminar flame speed.

2.2.1. Fuel equivalence ratio effect

The effect of fuel equivalence ratio on the laminar flame speed follows that of the adiabatic flame temperature, which peaks near stoichiometric mixture under slightly fuel rich conditions ($1.05 < \phi < 1.1$), as shown in Figure 2.3. Since the adiabatic flame temperature itself has a significant effect on laminar flame speed, the observed behaviour is expected (Glassman and Yetter, 2008). This effect is shown in Figure 2.7 where the laminar flame speed of iso-octane at different fuel equivalence ratios from three different experimental studies (Davis and Law, 1998, Huang et al., 2004, Kumar et al., 2007) are shown along with the model prediction (solid line) of Jerzembeck et al. (2009).

In Figure 2.7 the laminar flame speed of iso-octane peaks at a fuel equivalence ratio of approximately 1.05 and at a maximum value of approximately 35 $\mathrm{cm.s^{-1}}$. The data from

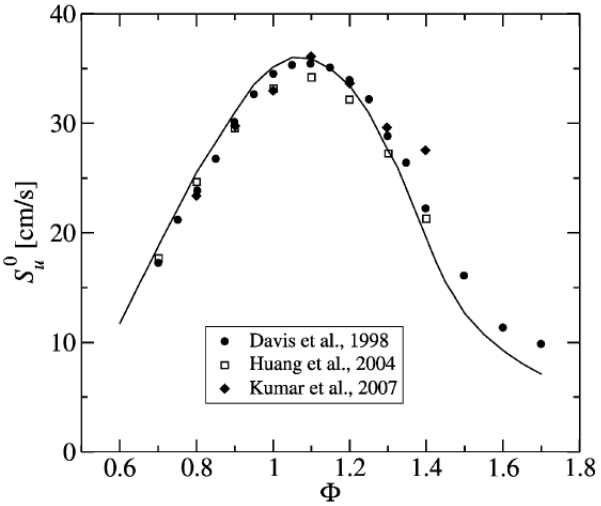

Figure 2.7.: Laminar flame speed of iso-octane at 298 K and 1 atm for different fuel equivalence ratios. (Jerzembeck et al., 2009)

different studies shows reasonable agreement and the modelling of the laminar flame speed by Jerzembeck et al. (2009) shows very good agreement with the experimental data.

This behaviour is seen for all hydrocarbon fuels in air, just as the adiabatic flame temperature for all hydrocarbon fuels shows this behaviour (Glassman and Yetter, 2008). In contrast to this is hydrogen and air mixtures which has a maximum laminar flame speed of 325 $\mathbf{cm.s^{-1}}$ which occurs well on the rich side ($\phi \approx 1.7$) at ambient conditions. This phenomena, where the maximum occurs far on the rich side, is explained by the substantial increase in thermal conductivity caused by an increase in hydrogen concentration in the premixed gas. This strong thermal conductivity effect on the laminar flame speed of hydrogen shows the importance of thermal conduction in the flame propagation process (Glassman and Yetter, 2008).

2.2.2. Pressure and temperature effect

The pressure effect for laminar flame speed can be estimated from Equation 2.5 and it has been reported that the overall order of reaction is in the range of 1.5 to 2, causing a decrease in laminar flame speed as pressure increases. At lower pressures, Reaction 2.6 has less of an effect and the decrease in laminar flame speed due to a rise in pressure is less severe. At higher oxygen concentrations the temperature rise, due to lack of dissociation, dominates the effect of Reaction 2.6. The result of this is an increase of laminar flame

speed with an increase in pressures for pure oxygen fuel mixtures (Glassman and Yetter, 2008).

Glassman and Yetter (2008) also evaluated the effects of pressure by conducting a computational study on a stoichiometric methane air flame with initial temperature of 298 K and pressures of 0.25 atm, 1 atm and 8 atm. It was found that the laminar flame speed decreases as pressure increases and that the mass burn rate increases as expected from the thermal limited model. The temperature profiles and heat release rates are shown in Figure 2.8.

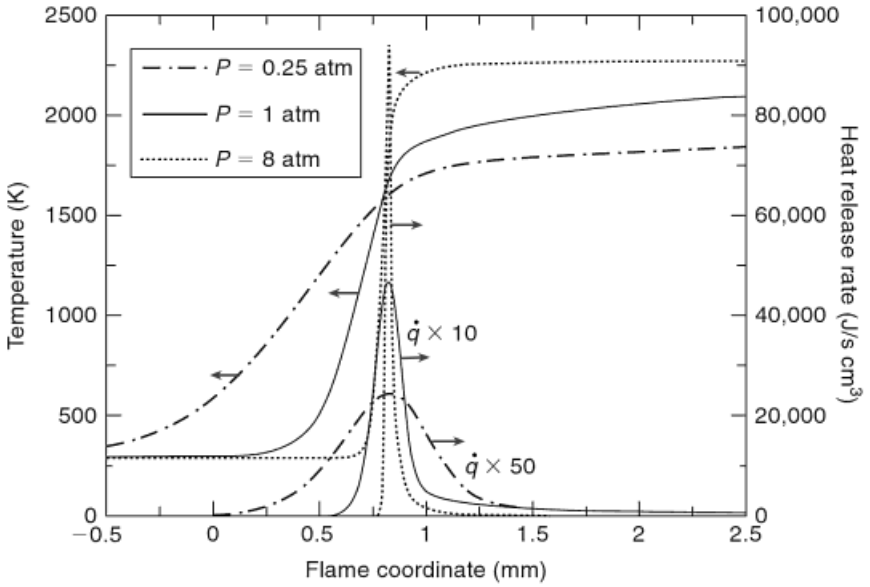

Figure 2.8.: Pressure effect on temperature profile and heat release rate of a stationary methane air flame. (Glassman and Yetter, 2008)

Figure 2.8 shows that at higher pressures the temperature gradient is steeper, accompanied by a higher heat release rate. This observation shows that as pressure increases, the laminar flame speed and the flame thickness decreases resulting in similar residence times for the gas in the flame. Experimentally the pressure effect on the laminar flame speed of iso-octane was shown by Bradley et al. (1998) in a constant volume combustion bomb for fuel equivalence ratios of 0.8 and 1.0 and initial temperatures of 358 K, 400 K and 450 K and initial pressures of 1 bar, 5 bar and 10 bar. In these experiments the pressure was varied by simply changing the initial pressure in the combustion bomb. The results for different laminar flame speeds at different temperatures and pressures are shown in Figure 2.9.

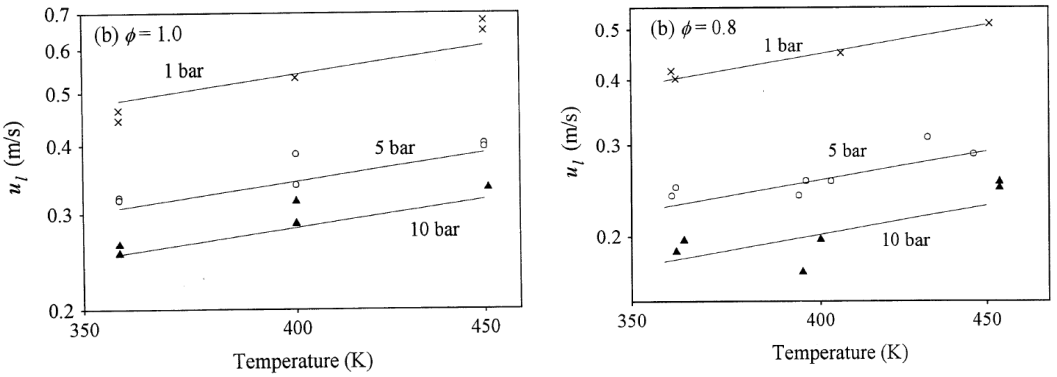

Figure 2.9.: Temperature effect on laminar flame speed of a iso-octane and air mixture with fuel equivalence ratio of 1.0 (a) and 0.8 (b).(Bradley et al., 1998)

Figure 2.9 shows the decrease in laminar flame speed as pressure increases for different temperatures and fuel equivalence ratios. The dependence of the laminar flame speed on the pressure in Figure 2.9 is represented by an overall fit of the empirical Equation 2.21.

$$S_L = S_{L,0} \left(\frac{T_u}{T_0}\right)^{\beta_T} \left(\frac{P}{P_0}\right)^{\beta_P} \tag{2.21}$$

In Equation 2.21, $S_{L,0}$, T_0 and P_0 are the reference laminar flame speed, temperature and pressure respectively. This reference laminar flame speed ($S_{L,0}$) was found to be 0.48 $\mathrm{m.s^{-1}}$ for $\phi = 1$ and 0.4 $\mathrm{m.s^{-1}}$ for $\phi = 0.8$ at 358 K and 1 bar. S_L is the predicted laminar flame speed at the unburned gas temperature (T_u) and system pressure (P). The temperature and pressure dependence is characterised by the exponential coefficients β_T and β_P respectively. This empirical fit did produce different exponential coefficients of the pressure dependence (β_P) for the stoichiometric ($\phi = 1$) and lean ($\phi = 0.8$) fuel air mixtures as is shown in Table 2.4.

Table 2.4.: Empirical temperature and pressure fit parameters for Equation 2.21. (Bradley et al., 1998)

ϕ	β_T	β_P
0.8	1.07	-0.348
1.0	1.01	-0.282

Table 2.4 shows the significant difference in pressure dependence for the two different fuel equivalent ratios tested, where the temperature effect is approximately the same in

both cases. This almost linear dependence of the laminar flame speed on the unburned gas temperature is also shown in Figure 2.9.

The lines in Figure 2.9 are again from the empirical fit of Equation 2.21 and show good agreement with the data. This data clearly shows the laminar flame speed of iso-octane increasing with an increase in unburned gas temperature. According to Glassman and Yetter (2008), an approximation for the activation energy term in Equation 2.2 for hydrocarbon oxidation is of the order of 160 $\mathbf{kJ.mol^{-1}}$, which indicates that the laminar flame speeds of hydrocarbons are very sensitive to temperature. Therefore, one might expect a stronger unburned gas temperature effect, since an increase in reaction rates and thermal conductivity is expected. However, it should be noted that the bulk of the reactions take place at higher temperatures in the flame, which is also true for thermal conduction, taking place where a strong temperature gradient exists. Therefore the unburned gas temperature has a small effect on the adiabatic flame temperature, which in turn causes an increase in laminar flame speed.

2.2.3. Inert gas dilution

Air, the oxidiser used in most combustion processes, is a mixture of mostly nitrogen and oxygen with small amounts of argon, carbon dioxide and other components. In this mixture of gases it is only the oxygen that takes part in the combustion of the fuel, while the rest of the components in air remain mostly inert.

The effect of an inert gas on the laminar flame speed of a fuel oxidiser mixture is therefore of importance and can mostly be attributed to its effect on the adiabatic flame temperature and molecular transport (thermal conduction and diffusion). Figure 2.10 shows the effect of replacing nitrogen with argon and helium respectively, on the burning velocity of methane in "air" (Clingman and Pease, 1956). This burning velocity was measured with an outdated Bunsen burner experimental setup, but it is equivalent to laminar flame speed.

The difference between laminar flame speed in nitrogen and argon in Figure 2.10 is explained by a difference in the heat capacity of these two gases. Although nitrogen and argon have similar thermal conductivities, nitrogen has a higher heat capacity than argon. This then results in higher adiabatic flame temperatures for the argon flame and therefore higher laminar flame speeds. However, the heat capacities of argon and helium are very similar, but in this case helium gas has a higher thermal conductivity than argon gas

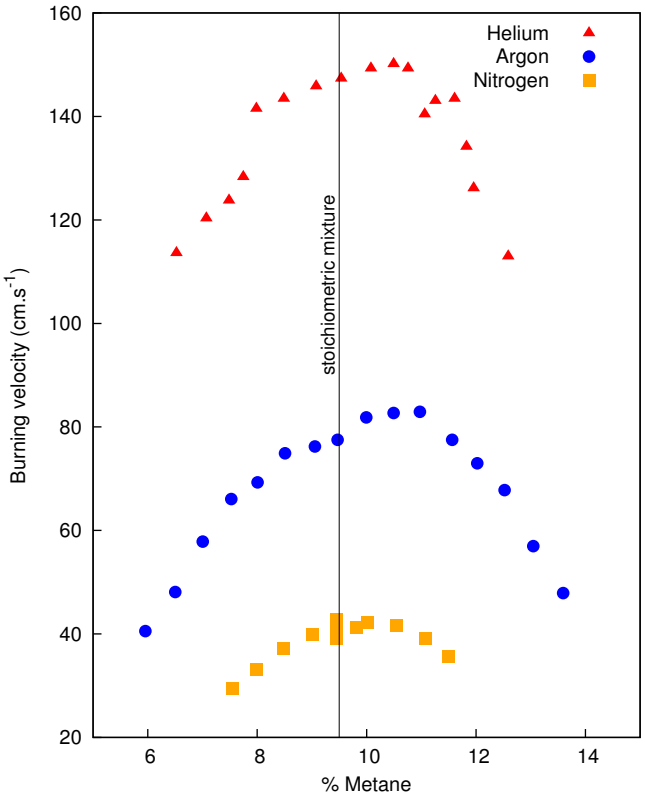

Figure 2.10.: Effect of different inert gases on the laminar flame speed of methane at 298 K and 1 atm. Replotted from Clingman and Pease (1956).

and therefore the helium flame has a higher laminar flame speed (Glassman and Yetter, 2008). This again emphasises the importance of both the flame temperature and thermal conduction on the flame propagation process.

2.2.4. The effect of flame stretch rate

The flame stretch rate at a specific point on the flame surface is defined as the rate of change of an infinitesimal small surface element area surrounding the point, normalised to that area as shown in Equation 2.22 (Bradley et al., 1996). Flame stretch is present in many laminar flame speed measurement methods, such as constant volume combustion bomb and opposed-jet experimental setups. Therefore the effect of the stretch rate on the flame speed should be well characterised in order to obtain accurate values for laminar flame speeds, free of flame stretch rate. It was postulated by Bradley et al. (1996) that the variation in laminar flame speed data from different experimental studies is caused

by inadequate incorporation of the flame stretch rate in experimental calculations. The flame stretch rate describes the non-laminar behaviour of the flame. A flame stretch rate of zero represents laminar conditions.

$$\alpha = \frac{1}{A}\frac{dA}{dt} \tag{2.22}$$

In Equation 2.22, α is the flame stretch rate as defined and A is the area of the infinitesimal small surface element, with $\frac{dA}{dt}$ the rate of change of A over time (t). This flame stretch rate is also expressed in terms of the aerodynamic flow field strain (α_s) and the flame stretch due to the curvature of the cold front of the propagating flame (α_c) as shown in Equation 2.23 (Bradley et al., 1996).

$$\alpha = \alpha_s + \alpha_c \tag{2.23}$$

The aerodynamic flow field strain (α_s) is caused by the gas velocity ahead of the flame, which has an effect on the molecular transport governing flame propagation. The flame stretch due to curvature of the cold flame front (α_c) is caused by the geometric effect of the finite flame thickness of a curved flame. A curved flame is called positively stretched if it is convex towards the unburned gas, as opposed to a negatively stretched flame, which is concave towards the unburned gas. The curvature results in either greater (positive stretch) or smaller (negative stretch) contact area between the flame and unburned gas per unit volume of the flame, as compared to a flat flame. In an outwardly propagating spherical flame, both these flame stretch rate sources are present. However, they can be accounted for as a whole by the overall stretch rate from Equation 2.22. For an outwardly propagating spherical flame this overall flame stretch rate is given by Equation 2.24 (Bradley et al., 1996).

$$\alpha = \frac{2}{r_u}S_n \tag{2.24}$$

In Equation 2.24, r_u is the radius of the cold flame front and S_n is the speed at which this cold flame front propagates or $S_n = \frac{dr_u}{dt}$ (Bradley et al., 1996). Note that the flame propagation speed (S_n) differs from the laminar flame speed (S_L), since it is influenced by the flame stretch rate and the expanding gases in the flame.

Since the flame stretch rate has a physical influence on the molecular transport processes

essential to flame propagation, it affects the flame propagation speed. It is almost intuitive that a positively stretched flame will propagate slower than a flat flame, since the reaction zone in a positively stretched flame is in contact with more cold unburned gas and therefore more thermal conduction is required to heat up the unburned gas layer next to the flame. The effect of the flame stretch rate on the flame propagation speed of an outwardly propagating spherical stoichiometric flame (positive stretch) shows this behaviour. Here the flame propagation speed is lower at higher flame stretch rates (lower radius flames) and increases as the flame stretch rate decreases. Figure 2.11 shows the effect of the overall flame stretch rate (α), as calculated from Equation 2.24, on the flame propagation speed (S_n) (Bradley et al., 1998).

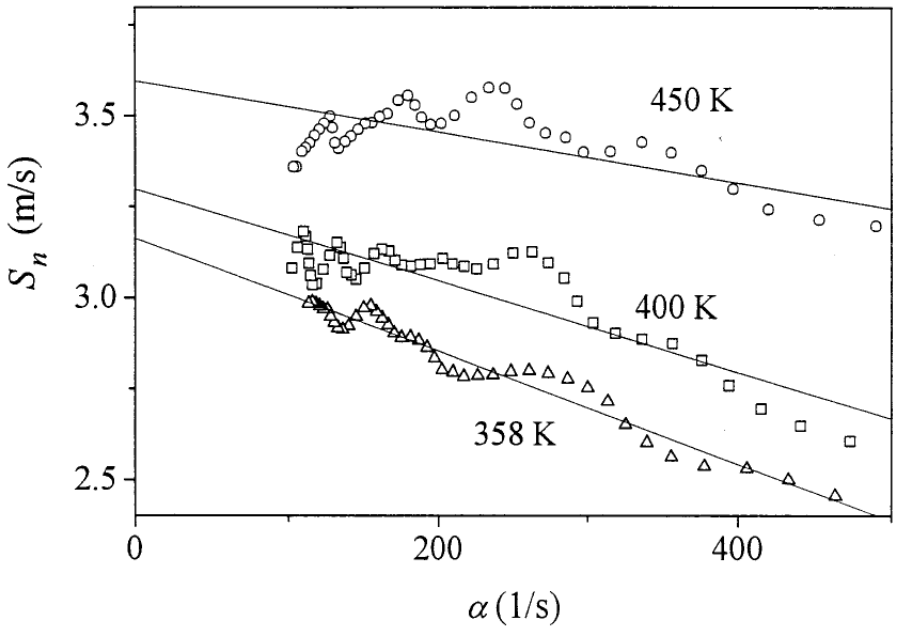

Figure 2.11.: The effect of flame stretch rate on the flame propagation speed of a stoichiometric iso-octane, air mixture at 1 bar . (Bradley et al., 1998)

It should be noted that high flame stretch rates occur at a low flame radius and as the flame propagates to higher flame radii, the flame stretch rate decreases and the flame approaches a laminar flame geometry. Figure 2.11 shows an approximately linear relation between the flame propagation speed and the flame stretch rate. The solid lines represent linear regression lines that fit the data best. These linear regression lines then show an unstretched flame propagation speed (S_s) at zero stretch rate and produces the burned gas Markstein length (L_b), which is defined as the negative value of the gradient. The

Markstein length is an indication of the sensitivity of the flame propagation speed to the flame stretch rate for specific conditions. The unstretched flame propagation speed (S_s) still differs from the laminar flame speed (S_L), since the expanding gases in the flame front contribute to it. Figure 2.11 also shows that the effect of the flame stretch rate becomes less severe at higher temperatures of the unburned gas and therefore the Markstein length decreases as the temperature of the unburned gas increases.

The fuel equivalence ratio has a strong effect on the sensitivity of the flame speed to the flame stretch rate. This is due to the variation in importance of the fuel and oxygen molecular transport parameters with changes in the fuel equivalence ratio. In Figure 2.12, the variation of the sensitivity of the flame propagation speed (S_n) to the flame stretch rate (α) at different fuel equivalence ratios is shown.

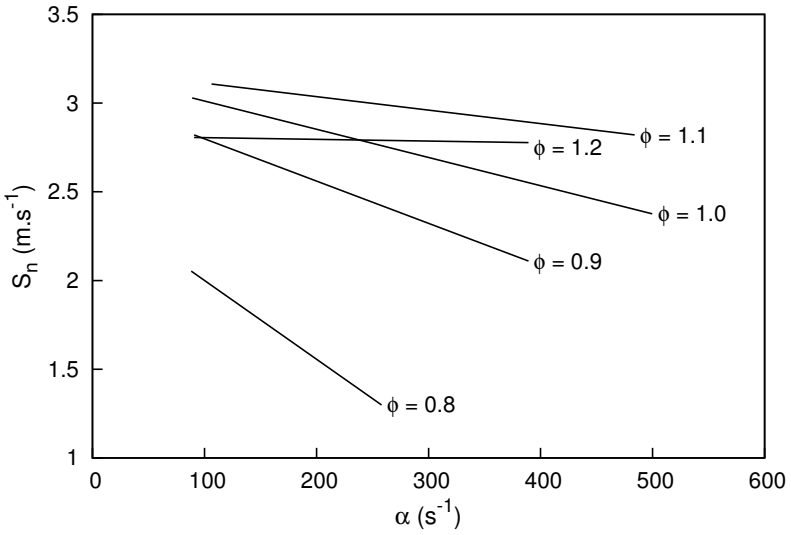

Figure 2.12.: The effect of flame stretch rate on iso-octane and air flame speeds at 358 K and 1 bar for different equivalence ratios. (Bradley et al., 1998)

Figure 2.12 is adapted from Bradley et al. (1998) to only show the linear regressions of the experimental data as solid lines, with the experimental data points omitted. The trend of the stretch rate effect on flame propagation speed is of importance here; therefore the solid lines in Figure 2.12 only show the fitted linear variation of the flame propagation speed (S_n) with flame stretch rate (α). The gradients of the solid lines in Figure 2.12 represent the Markstein lengths, which indicate the sensitivity of the flame speed to the flame stretch rate.

In Figure 2.12, it is clear that as the fuel air mixture becomes more fuel rich (fuel equiva-

lence ratio increases) the Markstein length decreases and therefore the flame propagation speed sensitivity to flame stretch rate decreases. At a fuel equivalence ratio of 1.2, there seems to be a negligible effect of flame stretch rate on the flame propagation speed as the flame propagation speed does not show significant acceleration nor deceleration. As the trend in Figure 2.12 indicates, at higher fuel equivalence ratios the flame propagation speed will show deceleration as the spherical flame propagates outwards, resulting in a negative Markstein length (positive gradient in Figure 2.12) (Bradley et al., 1998).

A possible explanation for the behaviour of the flame propagation speed sensitivity to the stretch rate at higher fuel equivalence ratios, is that at fuel rich conditions, the flame speed becomes more sensitive to oxygen diffusion. Bechtold and Matalon (1999) showed that flame propagation speed is sensitive to oxygen diffusion and more so at fuel rich conditions. Oxygen molecules diffuses faster than the larger fuel molecules and at low flame radii the flame is in contact with more unburned gas containing oxygen. Therefore, as the flame propagates and the flame radius increases, the oxygen in proximity to the flame per unit flame area decreases. Thus, as the flame radius increases and the flame stretch rate decreases, the flame propagation speed decreases. This then shows interesting flame speed behaviour where thermal conductivity and diffusion causes opposing flame stretch rate effects. A similar argument is followed in the later work of Bechtold and Matalon (2001).

2.2.5. Flame instability

In the case of outwardly propagating spherical flames, it is observed, under conditions of high pressure and low flame stretch rate, that the flame will become unstable. This refers to the phenomena where the flame is no longer a smooth spherical flame, but shows a multitude of cracks and cross-cracks across the flame surface. A flame displaying this behaviour is referred to as a cellular flame and the difference between a smooth, stable flame and a cellular, unstable flame is shown in the shadowgraphs in Figure 2.13 (Far et al., 2010).

Figure 2.13 shows the shadowgraphs of two flames with approximately the same flame radius, where (a) is smooth and stable while (b) is cellular and unstable. The cellularity of the flame has a significant influence on the flame propagation speed, since it significantly increases the flame area. In Figure 2.14 the increase of the flame propagation speed due to cellularity at a certain flame stretch rate is seen.

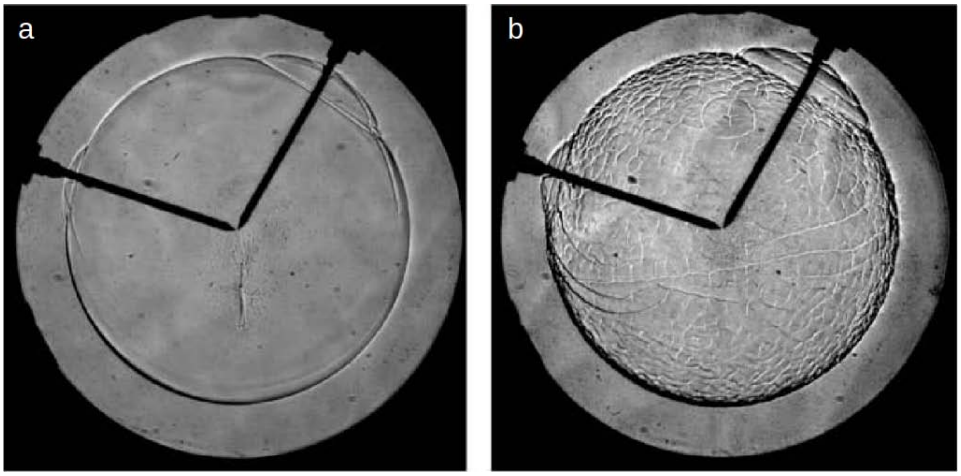

Figure 2.13.: Shadowgraphs of spherical flames for a stoichiometric mixture of jet fuel and air with initial temperature of 500 K, showing (a) the stable flame with initial pressure of 2 atm and (b) the unstable cellular flame with initial pressure of 3 atm. (Far et al., 2010)

In Figure 2.14, the flame propagation speed appears stable and increasing as the flame stretch rate decreases for the spherical flame at 1 bar, but at higher pressures the flame becomes unstable where a clear increase in flame propagation speed is seen. Flame instability appears once the flame stretch rate is lower than a critical value, at which time the flame surface becomes cellular, increasing the flame area and resulting in an increased burning rate. Figure 2.14 also shows that the critical flame stretch rate increases as the pressure increases. This same effect is seen for an increasing fuel equivalence ratio in the work of Bradley et al. (1998) and is related to the sensitivity of the flame propagation speed to the flame stretch rate. The reason for this is that outwardly propagating spherical flames are intrinsically unstable in the absence of the stabilising influence of thermo diffusive effects (Bradley et al., 1998). Thus, under conditions where the flame stretch rate has a less significant influence on the flame propagation speed (high pressures and fuel rich conditions), the stabilising thermo diffusive effects are much smaller. Under such conditions the flame becomes unstable at higher flame stretch rates. Bradley et al. (1998) attempted to characterise the flame radius where an iso-octane air flame becomes unstable and found that the flame thickness is an important parameter, since it plays an important role in the flame stretch rate effect.

In this section, the effect of several physical conditions on flame speed is summarised. In the case of a constant volume combustion bomb, the expanding spherical flame will be subject to changes in flame stretch rate and pressure as well as changes in the temperature

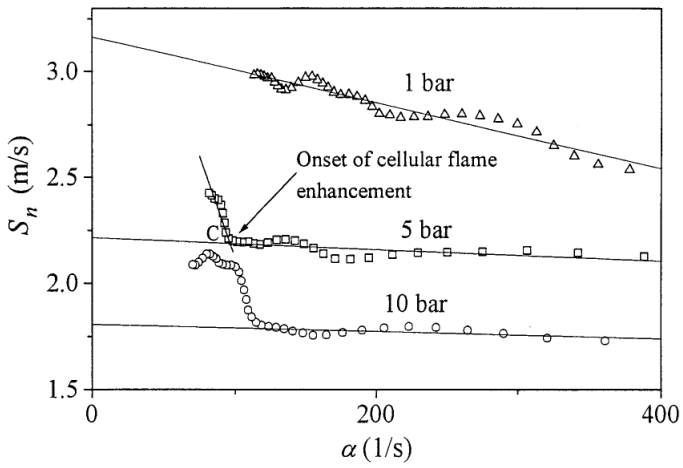

Figure 2.14.: Effect of cellular flame structure on the spherical flame propagation speed of an iso-octane and air flame. (Bradley et al., 1998)

of the unburned gas due to adiabatic heating. For this reason it is essential that the influence of these physical conditions on flame speed is well understood in order to account for them in the determination of laminar flame speed from constant volume combustion bomb experiments.

2.2.6. The effect of the chemical structure of the fuel

Most hydrocarbon fuels display similar yet different laminar flame speeds and these small differences are caused mostly their by different chemical structures. The unburned gas mixture of fuel and air consists mostly of air, especially for heavier fuel components. Therefore molecular transport, such as the thermal conductivity, is not influenced significantly by the smaller fraction of fuel. Different fuels, however, do show different reaction kinetics, as seen in the ignition delay time data of different fuels (Floweday, 2010), and result in different adiabatic flame temperatures. The laminar flame speeds of a wide range of fuel components were determined qualitatively by Farrell et al. (2004) in a constant volume combustion bomb.

Experimental measurements of laminar flame speeds for 45 different hydrocarbons were done by Farrell et al. (2004) to determine the effect of molecular structure on laminar flame speed. It was mentioned earlier that the difference in laminar flame speeds for different fuels is largely described by the differences in adiabatic flame temperatures. However, Farrell et al. (2004) showed that differences in reaction kinetics also plays an

important role. Figure 2.15 shows the highest measured laminar flame speed for a range of fuel equivalence ratios of several hydrocarbons versus their adiabatic flame temperature.

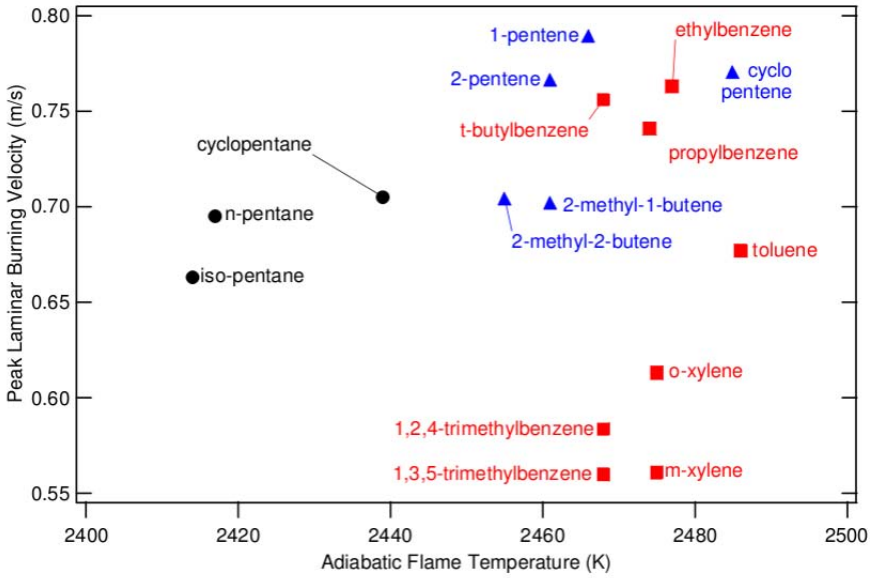

Figure 2.15.: Peak laminar flame speed of various hydrocarbons at 450 K and 304 kPa versus the adiabatic flame temperature. (Farrell et al., 2004)

From Figure 2.15 it is clear that certain similar hydrocarbon fuels with adiabatic flame temperatures close to each other, but different molecular structures, show different laminar flame speeds, as is observed for the case of o-xylene (ortho-xylene) and m-xylene (meta-xylene). This then serves as clear evidence that reaction kinetics have a significant influence on the laminar flame speed of a fuel. This can also be seen from Equation 2.1, where faster reaction kinetics will cause faster ignition at a lower temperature, resulting in a higher laminar flame speed. To obtain the final laminar flame speed results of Farrell et al. (2004), the flame stretch rate effect was ignored and the data was extrapolated back to the initial condition in the constant volume combustion bomb of 450 K and 304 kPa. Farrell et al. (2004) showed that their derivation method produced flame speeds that were approximately 10% higher than data from other authors. Nevertheless, the results from their study are used for comparison of laminar flame speeds of different hydrocarbon fuels, as shown in Figure 2.16.

Interesting trends are identified from Figure 2.16, such as the fastest laminar flame speed for paraffins is that of ethane while the slowest is that of methane. Although ethane has a higher adiabatic flame temperature than methane, analysis of the chemical kinetic

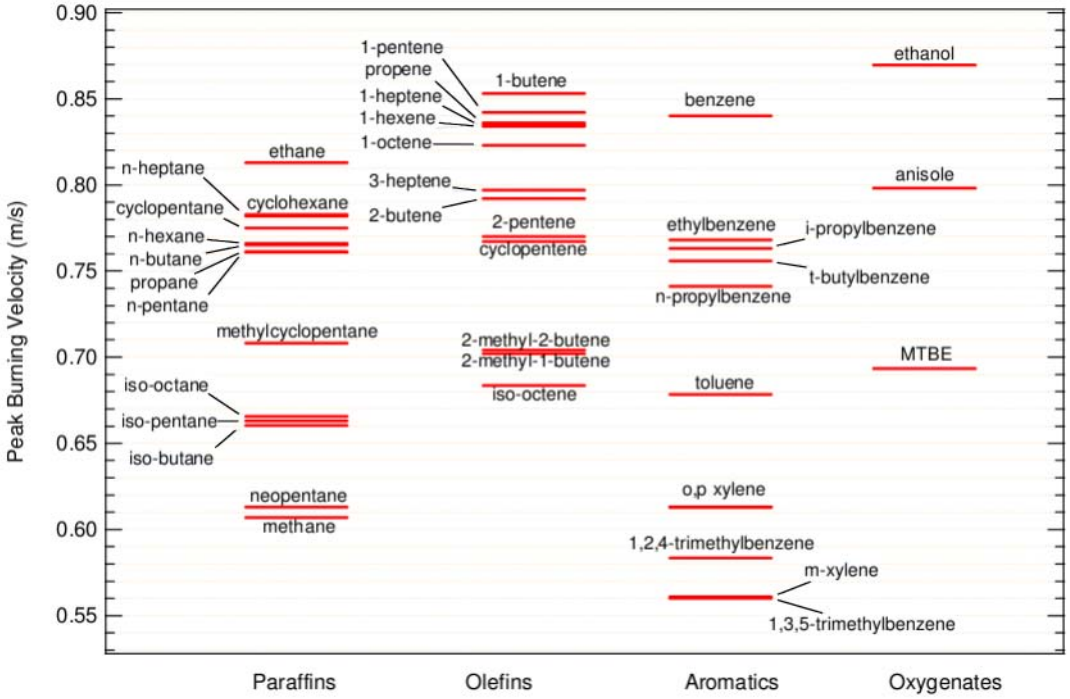

Figure 2.16.: Peak laminar flame speeds of different hydrocarbons at 450 K and 304 kPa determined by Farrell et al. (2004).

pathways shows that more methyl radicals form during methane oxidation and more ethyl radicals during ethane oxidation. The methyl radical has a low reactivity and produces few H• radicals, which promote chain branching. The ethyl radical decomposes rapidly to form H• and other radicals, promoting chain branching and therefore increasing the overall rate of combustion. This same effect explains the difference in laminar flame speeds of branched alkanes compared to equivalent linear alkanes. Branched alkanes have the propensity to form more methyl radicals (Farrell et al., 2004).

Figure 2.16 also shows that for aromatics, benzene has the highest laminar flame speed, while the branched aromatics, such as toluene, have lower laminar flame speeds. Analysis of the chemical kinetics again shows significant differences in the major chemical pathways. Most of the benzene decomposes to phenyl radicals, while most of the toluene decomposes into benzyl radicals. The benzyl radicals are resonantly stabilised and therefore less reactive than the phenyl radicals. Although the pathways of benzene and toluene both funnel through cyclopentadienyl, the decomposition pathway of toluene comprises more steps, which includes the less reactive benzyl radical. Therefore the combustion kinetics of

toluene are slower than that of benzene. The influence of the length of the alkyl branches on the aromatics is the same as that observed for normal alkanes lengths. Longer alkyl branches causes higher laminar flame speeds, except in the case of ethylbenzene which shows a higher laminar flame speed than propylbenzene (Farrell et al., 2004).

This study shows that key differences in the chemical kinetic pathways have significant effects on the overall combustion kinetics and thus on the laminar flame speed. The calculated values for laminar flame speeds from the study of Farrell et al. (2004) should not be expected to compare well with data from other studies, since the study did not take flame stretch rate into account. However, the study gives insight into the relative flame speeds of the hydrocarbons investigated.

2.3. Experimental measurement of laminar flame speed

The experimental measurement of laminar flame speed can be done using several different experimental systems. However, it is challenging to achieve an ideal laminar flame. The aim of these experiments are to derive the speed of an infinitely flat or laminar flame from the speeds measured in an experimental system. There still is uncertainty regarding the deviations of laminar flame speeds obtained from different experimental systems (van Lipzig et al., 2011, Galmiche et al., 2012). Glassman and Yetter (2008) discussed some experimental systems used to determine the laminar flame speed of fuel and oxidiser mixtures. The flat flame burner and opposed-jet burner are discussed below, followed by a more detailed look at the constant volume combustion bomb system and its calculations.

2.3.1. Flat flame burner

The flat flame burner system for a premixed flame is considered an accurate way to determine the laminar flame speed, because it achieves a flat flame very close to an ideal situation. The premixed fuel oxidiser mixture travels through a porous metal disk or a collection of small tubes in parallel to force plug flow of the gas. By having an inert gas that flows around the burner, the edge of the flame is more accurately defined. This setup was initially only able to measure lower laminar flame speeds of the order of 15 $\mathrm{cm.s^{-1}}$ or less, because higher laminar flame speeds resulted in multi-conical flames further from the burner. Later developments included cooling of the plug, which enabled the measurement of higher laminar flame speeds. For this approach, however, extrapolation is necessary to

obtain the flame speed at zero cooling, which is then taken as the laminar flame speed (Glassman and Yetter, 2008).

A recent study by Van Lipzig et al. (2011) measured the laminar flame speeds of n-heptane, iso-octane and ethanol using a perforated plate burner. They implemented the Heat Flux method in which the perforated plate is heated at its edge by a heating jacket to the desired unburned gas temperature. The mass flow rate through the perforated plate is then adjusted until the temperature across the perforated plate is uniform and equal to the temperature of the heating jacket. The unburned gas velocity where the perforated plate is not heated by the heating jacket nor the burned gas (uniform temperature across the plate) is taken as the laminar flame speed.

The flames were reported to become cellular at equivalence ratios above 1.3, which indicated the absence of stretch and the accompanying stabilising thermo diffusive effects. Since these measurements are free of the flame stretch rate effect, it can be used to validate the derivation methods for laminar flame speed from constant volume combustion bomb and opposed-jet setups, where the flame stretch rate needs to be accounted for in the experimental calculations. The overall accuracy for the fastest flames was estimated as ± 1 $\mathrm{cm.s^{-1}}$ and compared well to previous data from constant volume combustion bomb and opposed-jet setups where linear stretch extrapolation was employed (Van Lipzig et al., 2011).

2.3.2. Opposed-jet counterflow burner

Another flat flame technique is the opposed-jet system that consists of two jets directing the flow toward each other resulting in an almost planar stagnation plane with two flat flames on both sides. In this setup the velocity of the premixed gas decreases as it approaches the flame and this enables the measurement of flame stretch. In order to determine the laminar flame speed in the absence of flame stretch, extrapolation of the experimental data to where the flame stretch is zero is required. The gas velocity profile between the two jets is required in this experimental setup, which requires complex velocity measurement techniques such as digital particle image velocimetry (Glassman and Yetter, 2008). In Figure 2.17, the two opposing jets and the two flat flames between them are shown in a photograph, while the axial and radial directions are indicated with arrows.

A study of laminar flame speeds of n-heptane and iso-octane by Davis and Law (1998) made use of the counterflow burner setup. The gas velocities between the two nozzles

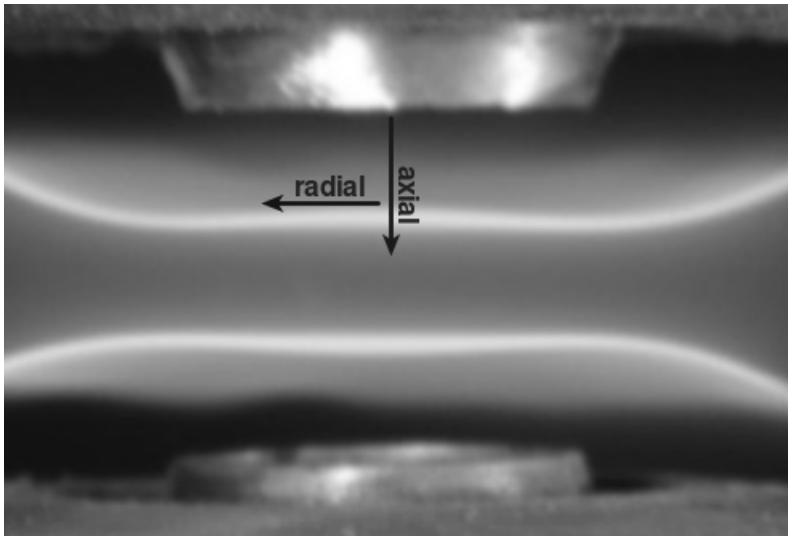

Figure 2.17.: Two flat flames of an opposed-jet counterflow burner, where the axial and radial directions are indicated. Adapted fromKumar et al. (2011).

were measured by employing an STI Argon-ion Doppler Velocimetry system from which the minimum axial velocity entering the heating zone was taken as the stretched flame speed. The flame stretch rate is calculated from the radial velocity gradient at the point of minimum axial velocity, as described above, and the dimensionless flame stretch rate, the Karlovitz number (Ka), is derived. The Karlovitz number is defined by Kumar et al. (2007) as

$$Ka = \frac{\alpha_T K}{(S_L)^2} \ . \tag{2.25}$$

In Equation 2.25, α_T is the thermal diffusivity of the unburned gas and K is twice the radial velocity gradient at the point of minimum axial velocity approaching the flame. The unstretched laminar flame speed is then obtained by extrapolation of the flame speed data to a Karlovitz number of zero. Davis and Law (1998) implemented both linear and nonlinear extrapolation. The nonlinear extrapolation is defined in Equation 2.26.

$$u_n = S_L \left[1 - (\mu_M - 1)\, Ka + Ka\, ln\left(\frac{\sigma_T - 1}{Ka}\right)\right] \tag{2.26}$$

In Equation 2.26, μ_M is the Markstein parameter and σ_T is the thermal expansion parameter, while u_n and S_L are the stretched and unstretched flames speed respectively. It

was found that the nonlinear extrapolation produced laminar flame speeds were approximately 2 $cm.s^{-1}$ slower than those produced by linear extrapolation. It was argued that the uncertainty in the velocity measurements was of the order of 1-2 $cm.s^{-1}$ and therefore motivation for the use of either the linear or nonlinear extrapolation could not be found. Model predictions of laminar flame speeds for this study showed reasonable predictions for lean mixtures, but underpredicted the laminar flame speeds for stoichiometric and fuel-rich n-heptane and air flames as well as iso-octane and air flames. It was concluded that the kinetic models used in the modelling of the laminar flame speed required further development in order to accurately predict laminar flame speeds of n-heptane and iso-octane mixtures with air (Davis and Law, 1998).

A more recent study by Kumar et al. (2007) also made use of the opposed-jet counterflow experimental setup to determine the laminar flame speeds of n-heptane and iso-octane. In this study the gas velocity was measured with digital particle image velocimetry and the laminar flame speed was derived from linear and nonlinear extrapolation to a Karlovitz number of zero, as was done by Davis and Law (1998). A variation in stretch rate effect on the flame speed, as the fuel equivalence ratio was varied, was observed in this study, and Kumar et al. (2007) pointed to the difference in Lewis numbers[2] as the cause. Fuel-lean mixtures have a Lewis number greater than one and therefore thermal conduction is more prominent, resulting in an increasing flame speed as the stretch rate or Karlovitz number decreases. The opposite was observed for stoichiometric and rich mixtures.

Since the study of Kumar et al. (2007) was done more recently, better developed chemical kinetic models were available. It was found that the model of Hasse et al. (2000) gave very good predictions for the laminar flame speeds of iso-octane. Sensitivity analyses were done by both Kumar et al. (2007) and Davis and Law (1998) to determine the sensitivity of the mass burning rate and laminar flame speed to the reaction kinetics of the individual reactions. Both studies afforded the highest sensitivity to the branching reaction: $H\bullet + O_2 \rightarrow OH\bullet + O\bullet$.

2.3.3. Constant volume combustion bomb

Laminar flame speeds of a wide variety of fuels have been determined using constant volume combustion bomb experimental systems (Rallis et al., 1965, Bradley et al., 1996,

[2]Lewis number is defined as the ratio of thermal diffusivity to mass diffusivity $\left(Le = \frac{\alpha_T}{D_{AB}}\right)$ Incropera et al. (2007).

Farrell et al., 2004, Jerzembeck et al., 2009, Far et al., 2010). The system is simpler, compared to other methods, in the sense that no flow meter is required and thereby the accompanying flow rate accuracy concerns are avoided. The result is an outwardly propagating spherical flame, unaffected by tube walls or shroud gas and therefore makes for a good experiment to give insight into the ideal case that is a perfectly flat laminar flame.

A typical constant volume combustion bomb, like the one modelled in this study, consists of a spherical cavity, the combustion chamber, in which the desired fuel oxidiser mixture is ignited in the centre of this sphere. The shape of the combustion chamber does not have to be spherical, as was shown by Far et al. (2010) where data from a spherical and cylindrical combustion bomb with similar volumes was compared. The ignition of the gas in the combustion chamber is most commonly achieved with spark plug electrodes extending to the centre where an electric spark ignites the gas as seen in Figure 2.13. The time from the spark event until the flame reaches the combustion chamber wall is generally of the order of milliseconds and therefore very fast response measurements are required to capture the flame propagation in the constant volume combustion bomb. Pressure traces from pressure transducers were initially used to determine the flame propagation, because of their fast response time. Newer constant volume combustion bombs have optical access to the combustion chamber which makes optical recordings of the flame position possible. An example of a pressure trace for a JP-8[3] flame is shown in Figure 2.18 where Far et al. (2010) compared pressure traces from a spherical and cylindrical combustion chamber, while a shadowgraph of the same fuel is shown in Figure 2.13 (Far et al., 2010).

The two combustion chambers compared in Figure 2.18 have close to equal volumes, resulting in similar pressure traces up until the flame reaches the wall in the cylindrical combustion chamber. Figure 2.18 shows that the spherical pressure trace continues uninterrupted, but the cylindrical pressure trace deviates after the flame reached its wall and is lower due to heat loss to the vessel wall. This suggests that, for combustion chambers of the same volume, the pressure rise caused by a spherical expanding flame in the combustion chambers is independent of the chamber geometry until the point where the flame reaches a chamber wall (Far et al., 2010).

The pressure trace or optical data is then used to derive a laminar flame speed for the tested fuel oxidiser mixture. To determine the laminar flame speed, the flame propagation speed is first needed, which is obtained from the experimental measurements. This is a

[3] JP-8 is a US military jet fuel.

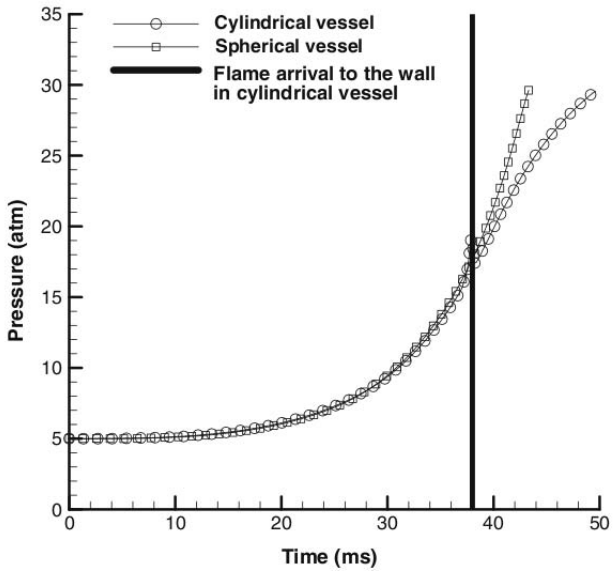

Figure 2.18.: Pressure trace for a JP-8 and air flame with initial temperature of 500 K, pressure of 5 atm and a fuel equivalence ratio of 0.8. (Far et al., 2010)

simple exercise for optical data. However, obtaining the spherical flame propagation speed from pressure trace data is not trivial. Different approaches to determining the laminar flame speed from pressure trace data are available in literature (Yates et al., 2012, Luijten et al., 2009, Rallis and Garforth, 1980).

In order to derive the laminar flame speed from constant volume combustion bomb experiments, all the intrinsic factors responsible for the difference between the outwardly propagating spherical flame speed and flat laminar flame speed, need to be identified and quantified. The outwardly propagating spherical flame is subjected to flame stretch rates, as discussed in Section 2.2.4. This is due to curvature of the flame and aerodynamic strain and therefore the flame speed will be affected by a high stretch rate at low flame radii. Since the combustion bomb is a closed system, the pressure rises as the high temperature burned gas increases, causing adiabatic heating of the unburned gas. This means the flame is propagating into continuously changing conditions in terms of temperature, pressure and flame stretch rate, making the calculation to obtain the laminar flame speed complicated.

The gas in the combustion chamber is usually ignited by a spark, which has an influence on the initial flame speed (Bradley et al., 1996). The sizes of combustion chambers do vary and give rise to different approaches for determining the laminar flame speed. In the case of

larger combustion bombs, with spherical combustion chamber diameters of approximately 40 cm, the flame propagation of the smaller radii are utilised, while the rest of the flame propagation is ignored (Bradley et al., 1998). This approach then ignores the flame speeds at higher radii where the pressure of the system increases significantly. Consequently, the flame speed data affected by the increase in the unburned gas temperature due to adiabatic heating is omitted. In other cases (Farrell et al., 2004, Far et al., 2010) only the flame speeds at the higher radii are considered and it is assumed that the stretch effects are insignificant. Several constant volume combustion bomb studies rely on the pressure trace to calculate the laminar flame speed, and therefore require pressure rise over time in the combustion chamber (Yates et al., 2012, Farrell et al., 2004). These cannot ignore the data where the pressure and the unburned gas temperature increase.

For constant volume combustion bombs with a small inner diameter[4] and no visual measurement capabilities, both the flame stretch rate and increasing pressure have a significant effect on the flame speed and should be accounted for in the laminar flame speed calculations. Different approaches for calculating the laminar flame speed from experimental constant volume combustion bomb data, are discussed in this section.

2.3.3.1. Flame speeds derived from pressure data

Since laminar flame speed is defined as the velocity at which unburned gas enters the flame, derivations of laminar flame speeds from pressure trace data focus on obtaining the rate at which unburned gas is consumed by the flame. This flame speed is the stretched normal flame speed (u_n) and is thermodynamically calculated from pressure trace data by making several assumptions (Luijten et al., 2009):

- The uniform unburned gas is initially at rest.
- The pressure remains spatially uniform during combustion.
- Total mass and volume of the vessel contents are conserved.
- External heat input, heat losses and buoyancy are negligible.
- The flame front is spherical and infinitely thin.
- The unburned gas is compressed isentropically.
- There is no heat transfer between the zones.

[4] Inner diameter of the combustion chamber less than 10 mm.

From these assumptions, Luijten et al. (2009) have derived an expression for the laminar flame speed where flame stretch is ignored. Another expression from Luijten et al. (2009) is given in Equation 2.27, where the flame stretch rate is not ignored, therefore producing the stretched normal flame speed (u_n).

$$\frac{dP}{dt} = \frac{3}{\mathcal{R}_v}\left(\frac{dx_b}{dP}\right)^{-1}\left[1-\left(\frac{P_i}{P}\right)^{1/\gamma_u}(1-x_b)\right]^{2/3}\left(\frac{P}{P_i}\right)^{1/\gamma_u}u_n \tag{2.27}$$

In Equation 2.27, P and P_i are the current and initial pressure respectively, $\mathcal{R}_v$ is the combustion chamber radius[5], x_b is the mass fraction burned and γ_u is the isentropic exponent of the unburned mixture. A complex expression for the mass fraction burned (x_b) as a function of the pressure (P) was proposed by Luijten et al. (2009). However, generally the more simple expression in Equation 2.28 is used (Lewis and von Elbe, 1961).

$$x_b = \frac{P-P_i}{P_e-P_i} \tag{2.28}$$

where P_e is the end or final pressure. Implementing Equation 2.28 in Equation 2.29 then gives Equation 2.29.

$$\frac{dP}{dt} = \frac{3\,(P_e-P_i)}{\mathcal{R}_v}\left[1-\left(\frac{P_i}{P}\right)^{1/\gamma}\frac{P_e-P}{P_e-Pi}\right]^{2/3}\left(\frac{P}{P_i}\right)^{1/\gamma}u_n \tag{2.29}$$

In Equation 2.29 it is assumed that the isentropic exponent (γ) of the burned and unburned mixtures are equal. From the derivations in the study of Luijten et al. (2009), the simpler Equation 2.30 is obtained to calculate the flame position (r_f) from the pressure trace data.

$$r_f = \mathcal{R}_v\left[1-\left(\frac{P_e-P}{P_e-P_i}\right)\left(\frac{P_i}{P}\right)^{1/\gamma}\right]^{1/3} \tag{2.30}$$

Equation 2.30 gives the radial flame position inside the constant volume combustion bomb, based on the pressure measured inside the combustion bomb. Once the flame position (r_f) is estimated from each pressure measurement, the flame propagation speed (S_n) can be calculated using Equation 2.31.

[5] $\mathcal{R}_v$ is the equivalent radius of a spherical cavity with the same volume as the combustion chamber used experimentally.

$$S_n = \frac{dr_f}{dt} \tag{2.31}$$

The flame propagation speed (S_n) or, alternatively, the stretched normal flame speed (u_n) is further used in the derivation of the laminar flame speed by considering the flame stretch rate, temperature and pressure effects on it. These derivations are discussed in the following section.

2.3.3.2. Effect of flame stretch rate

In the constant volume combustion bomb, stretch rate affects the observed burning velocity and extrapolation to zero stretch rate is required to obtain the laminar flame speed. Two effects contribute to the stretch rate imposed on flames: the curvature of the cold flame front and the flow field aerodynamic strain. The failure to accurately describe the stretch rate effect on flame speed is the most probable explanation for the variation seen for laminar flame speed data in literature. Therefore, accurate descriptions of the stretch rate and other effects are essential in order to obtain accurate values for laminar flame speed (Bradley et al., 1996).

In a study by Bradley et al. (1998), the laminar flame speed of iso-octane and a mixture of iso-octane and n-heptane was experimentally determined in a spherical constant volume combustion bomb with a radius of 380 mm. The flame propagation data was captured with high speed schlieren ciné-photography at radii below 65 mm and was used to determine the flame radius and speed. Since only a small portion of the gas is burned when the flame reaches a radius of 65 mm, a maximum pressure rise of only 70 mbar was observed in the combustion chamber, which would result in an unburned gas temperature rise of about 3 K (Bradley et al., 1998). For this reason it was safe to assume constant pressure and temperature for the measured flame speeds.

The calculations require the radius of the cold front of the flame (r_u) while the schlieren measurements give the radius of an isotherm with a temperature of about 450 K. The relation between the schlieren radius (r_{sch}) and the cold front radius (r_u) is given by Equation 2.32 (Bradley et al., 1998).

$$r_u = r_{sch} + 1.95\delta_l \left(\frac{\rho_u}{\rho_b}\right)^{0.5} \tag{2.32}$$

In Equation 2.32, ρ_u and ρ_b are the densities of the unburned and burned gas respectively, and can be assumed to remain constant in the constant temperature and pressure conditions. The flame thickness (δ_l) in Equation 2.32 is given by Equation 2.33.

$$\delta_l = \frac{\nu}{S_L} \tag{2.33}$$

where ν is the kinematic viscosity of the unburned gas and S_L is the laminar flame speed. From this, the flame propagation speed (S_n) is then determined simply by Equation 2.31, where flame position (r_f) is equal to the cold front radius (r_u). The laminar flame speed is obtained by plotting the flame propagation speed (S_n) against the overall stretch rate (α) that is obtained from Equation 2.24. An example of these plots is shown in Figure 2.19 where S_n versus α is plotted and extrapolated to zero stretch rate ($\alpha = 0$) to obtain the unstretched flame propagation speed (S_s).

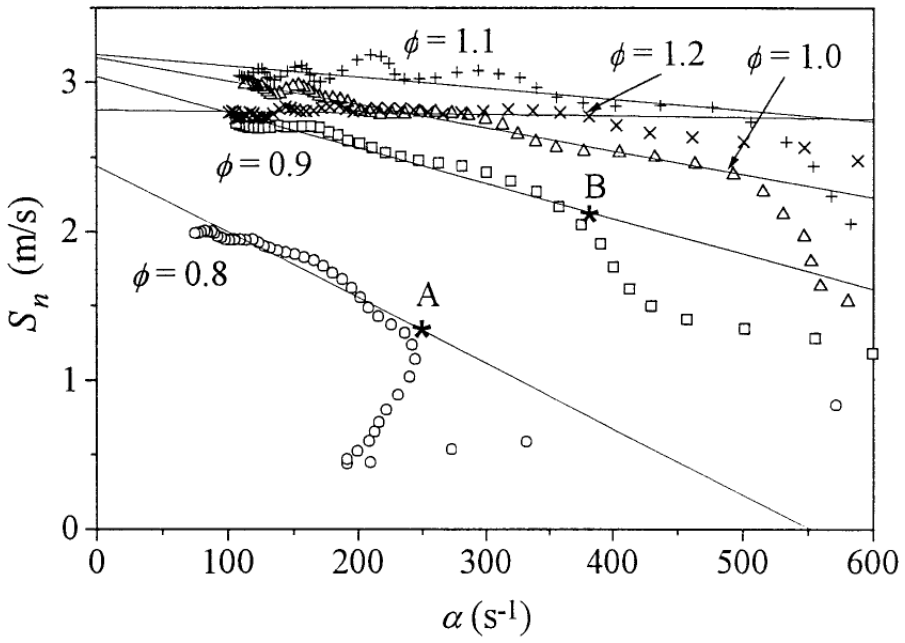

Figure 2.19.: Extrapolation to zero stretch rate of experimental data for iso-octane and air flame speeds at 358 K and 1 bar. (Bradley et al., 1998)

Figure 2.19 is equivalent to Figure 2.12 in Section 2.2.4, but here the experimental data is included to show the regression strategy. It shows that the linear regression used to determine S_s, is only applied to certain linear segments of the data. This is due to spark ignition influences at low flame radii (high stretch rates) as well as flame instabilities

and pressure increases at high flame radii (low stretch rate). The gradients of the linear regressions used in Figure 2.19, also called the burned gas Markstein lengths (L_b), describe the sensitivity of the flame speed to the flame stretch rate according to Equation 2.34.

$$S_n = S_s - L_b\alpha \tag{2.34}$$

The laminar flame speed (S_L) is then calculated from the values of S_s, obtained from extrapolations as shown in Figure 2.19 using Equation 2.35.

$$S_L = S_s\frac{\rho_b}{\rho_u} \tag{2.35}$$

Once the laminar flame speed is established, the Markstein lengths that describe the flame curvature and aerodynamic strain stretch rate effects separately, are calculated following Equation 2.36 (Bradley et al., 1998).

$$S_L - u_n = L_c\alpha_c + L_s\alpha_s \tag{2.36}$$

The stretched normal flame speed (u_n) in Equation 2.36 is obtained from the flame propagation speed (S_n) according to methods described by Bradley et al. (1996). The Markstein lengths L_c and L_s describes the laminar flame speed sensitivity to the curvature stretch rate (α_c) and the aerodynamic strain (α_s) respectively.

A nonlinear regression function is suggested by Kelley and Law (2009) to give a better approximation of the nonlinearity in the data, which is accepted to be linear in the approach followed by Bradley et al. (1996). This nonlinear regression gives a relation between the unstretched flame propagation speed (S_s), the flame propagation speed (S_n), overall flame stretch rate (α) and the sensitivity parameter or Markstein length (L_b) shown in Equation 2.37.

$$S_s\left(\frac{S_n}{S_s}\right)^2 In\left(\frac{S_n}{S_s}\right)^2 = -2L_b\alpha \tag{2.37}$$

It was shown by Kelley and Law (2009) that the nonlinear regression of Equation 2.37 can be successfully implemented to obtain the laminar flame speeds of butane and air mixtures from experimental data. This nonlinear approach was also successfully implemented by Galmiche et al. (2012) to obtain the laminar flame speeds of iso-octane and air mixtures.

To show how the nonlinear regression of Equation 2.37 compares with the linear regression of Equation 2.34, these two functions are fitted to the data from Bradley et al. (1998) for the fuel equivalence ratio of 0.8 in Figure 2.19 and the resulting regressions are shown in Figure 2.20.

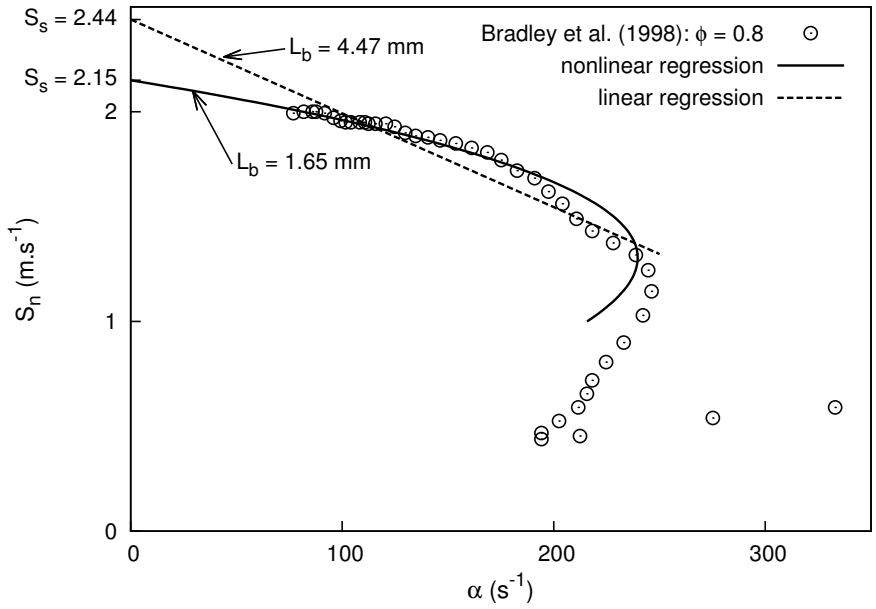

Figure 2.20.: Comparison of linear regression of Equation 2.34 and nonlinear regression of Equation 2.37 for spherical iso-octane and air flame data with initial conditions of 358 K and 1 bar and a fuel equivalence ratio of 0.8 from Bradley et al. (1998).

In Figure 2.20, the nonlinear regression produces an unstretched flame propagation speed (S_s) of 2.15 $\mathrm{m.s^{-1}}$, which is 0.29 $\mathrm{m.s^{-1}}$ lower than that produced by the linear regression. When translated to laminar flame speed (S_L) by using Equation 2.35, it results in a difference of approximately 0.05 $\mathrm{m.s^{-1}}$. This is a significant difference and therefore both these regression functions are implemented in the current work to enable more comparisons with data from literature. It should also be noted that the burned gas Markstein length (L_b) from the nonlinear regression is much lower than that from the linear regression, which is expected since Equations 2.34 and 2.37 are different. However, the Markstein length produced by the nonlinear regression of Equation 2.37 also indicates the sensitivity of the flame speed to the flame stretch rate. A flame showing a lower Markstein length from Equation 2.34 will also show a lower Markstein length from Equation 2.37.

This then describes how the laminar flame speed is obtained from optical data of a

constant volume combustion bomb, where only low values of mass fraction burned were considered to achieve constant pressure and temperature conditions. It should be noted that the flame propagation speed (S_n) and not the stretched normal flame speed (u_n) is used for the linear regression. This is due to a better linear correlation between the flame propagation speed (S_n) and overall stretch rate (α) (Bradley et al., 1996). The constant pressure and temperature simplifies the derivation of laminar flame speed. The effects of varying pressure and temperature on the laminar flame speed is discussed in the next section.

2.3.3.3. Pressure and temperature effects

The influence of pressure and temperature on the laminar flame speed is discussed in Section 2.2.2 and the fundamental effects are understood. However, in a case where the laminar flame speed is derived from pressure trace data, the flame is propagating into unburned gas with continuously changing pressure and temperature. These effects are taken into account in the laminar flame speed calculations of Far et al. (2010) where the flame stretch rate is ignored. The dependence of the laminar flame speed on the temperature is shown in Figure 2.21 (a) while the dependence of the mass burning rate on pressure is also shown in Figure 2.21 (b) as the flame propagates outwards in both cases (Far et al., 2010).

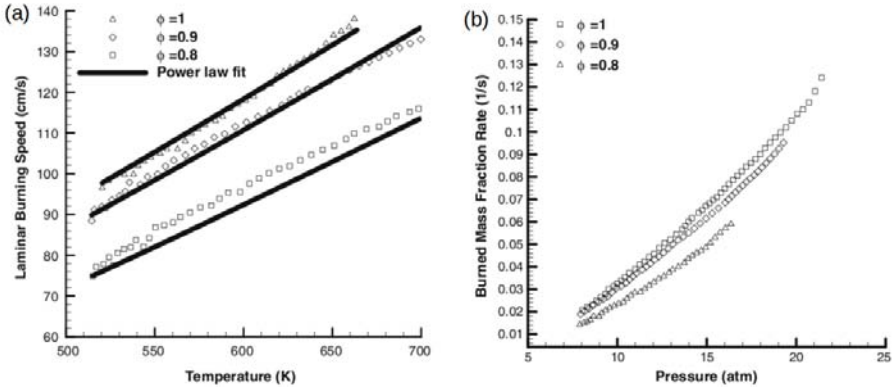

Figure 2.21.: (a) Laminar flame speed dependence on temperature. (b) Mass burn rate dependence on pressure. (Far et al., 2010)

The laminar flame speed shows a strong dependence on the temperature rise caused by adiabatic heating of the unburned gas in a constant volume combustion bomb according to Figure 2.21 (a). The laminar flame speed decreases with increasing pressure, however the

mass burn rate increases as discussed before. Figure 2.21 (b) shows the increase in mass burn rate as the pressure increases. It should be noted that this burn rate is also affected by increasing temperature. These trends are described by the single Equation 2.38, fitted to the experimental data.

$$S_L = S_{L,0}\left(1 + a_1(1-\phi) + a_2(1-\phi)^2\right)\left(\frac{T_u}{T_{u,0}}\right)^{\beta_T}\left(\frac{P}{P_0}\right)^{\beta_P} \tag{2.38}$$

In Equation 2.38, $S_{L,0}$ is the reference laminar flame speed at stoichiometric conditions ($\phi = 1$), while $T_{u,0}$ is the reference temperature and P_0 is the reference pressure. The effect of the unburned gas temperature (T_u), pressure (P) and fuel equivalence ratio (ϕ) on the laminar flame speed is given by the parameters of Equation 2.38, where $S_{L,0} = 93.6\ \mathrm{cm.s^{-1}}$, $a_1 = -0.22$, $a_2 = -4.4$, $\beta_T = 2.13$ and $\beta_P = -0.18$ for a JP-8 and air flame (Far et al., 2010). The negative value for β_P indicates that the laminar flame speed decreases with an increase in pressure. Equation 2.38 assumes the same dependence of laminar flame speed on pressure and temperature at different fuel equivalence ratios which is not always the case (Bradley et al., 1998).

Bradley et al. (1998) performed experiments at different initial temperatures and pressures and were therefore able to correlate the laminar flame speed to formulas describing the relation. This also produced the opportunity to study the effect that pressure and temperature have on the sensitivity of the flame propagation speed to the flame stretch rate. The sensitivity of the flame propagation speed to the flame stretch rate is indicated by the burned gas Markstein length (L_b) from Equation 2.34. The variation of L_b with temperature and pressure is shown in Figure 2.22.

Figure 2.22 shows that the Markstein length decreases with an increase in pressure as is expected. This is because an increase in pressure will cause a decrease in the flame thickness which results in the flame speed being less sensitive to the flame stretch rate. The Markstein length behaviour as temperature varies is more complex, as Figure 2.22 shows. An increase in temperature causes a decrease in Markstein length at low pressures, but an increase at higher pressures. In the case where the pressure and temperature of the system is increasing while the flame is experiencing significant flame stretch rates, the flame speed will be influenced by a complex combination of the effects discussed above. Decoupling these effects and determining an accurate value for laminar flame speed from the experimental data is therefore a challenging task.

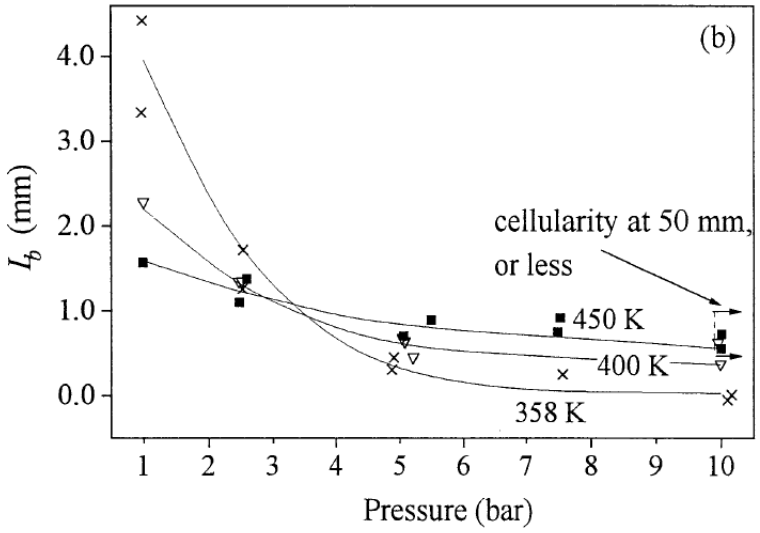

Figure 2.22.: Markstein length dependence on temperature and pressure for an iso-octane and air flame at a fuel equivalence ratio of 0.8. (Bradley et al., 1998)

2.4. Conclusion

Laminar flame speed is a fundamental combustion property of a fuel oxidiser mixture. Certain fundamental characteristics of a fuel oxidiser mixture are of importance when considering what governs the laminar flame speed, such as the adiabatic flame temperature and combustion reaction kinetics. The laminar flame speed is determined using different experimental systems, each making certain assumptions in order to derive the laminar flame speed. Of these experimental systems, the constant volume combustion bomb is the focus of this study. The intrinsic effects that accompany this experimental setup, increasing pressure and temperature as well as the decreasing flame stretch rate, and how previous work has quantified it, is shown.

It is clear from the literature that, even though the constant volume combustion bomb experimental system is a preferred experimental system, it has several limitations. The most challenging aspect of the interpretation of the experimental data is decoupling the flame stretch rate, pressure and temperature effects in order to arrive at a laminar flame speed at a specific temperature and pressure. In some experimental systems, pressure is the only measure of flame propagation, with the result that all the data collected this way is influenced by pressure. The aim of this work is to develop a model, based on fundamental mixture properties, that describes the spherical flame behaviour observed in experimental

studies. This model then shows the flame behaviour for different combustion chamber sizes and the sensitivity of the flame characteristics to fundamental mixture properties.

3. Theory and methods

The combustion system modelled in this study, an outwardly propagating spherical flame in a constant volume spherical vessel, can be described as a chemically reacting flow. In a chemically reacting flow, the system at any point in space and time is completely described if the pressure, temperature, velocity of the flow and concentration of each species are known. These properties are subject to change due to chemical reactions, fluid flow (convection), molecular transport (thermal conduction, diffusion and viscosity) and radiation in the system. In order to model this combustion system, a mathematical description of all of these processes is required (Warnatz et al., 2001).

To mathematically describe the system, the conservation of mass, species, momentum and energy is considered. The conservation laws are based on the principle that the change over time of each of the above quantities is a function of the flow into and out of a control volume as well as production or consumption. The flow into and out of the control volume is governed by the fluid flow and molecular transport, while the production or consumption is governed by the chemical reactions. The conservation of each quantity then results in a conservation equation describing the rate of change of the quantity at any point in space and time.

Each of the conservation equations, describing the rate of change, can be written as a partial differential equation (PDE) and a set of PDEs can be solved following several different approaches. A field of study where solving conservation law PDEs is the main focus of the numerical methods, is computational fluid dynamics (CFD). Here either finite difference, finite elements or spectral methods are implemented (Versteeg and Malalasekera, 1995). In CFD simulations, three-dimensional space is generally considered. However, in this study the mathematical problem is reduced to a simpler one-dimensional problem by assuming symmetry in the system. One-dimensional flame propagation is widely modelled with the PREMIX software (Kee et al., 1985) where the conservation equations for a steady state flat flame in an open system is solved. In this study a spherical propagating[1]

[1]The system modelled in this study is not a steady-state system, but rather a dynamic system where the

flame is modelled and therefore the PREMIX software can not be used.

Software for modelling propagating spherical flames has been developed by Chen (2009) as A-SURF (Simulation of Unsteady Reacting Flow using Adaptive mesh). However, this software is not available to the public. BACOL (B-spline Adaptive COLlocation) software, developed by Wang et al. (2004a) for solving one-dimensional parabolic PDEs, is implemented in this study. BACOL uses high order schemes in time and space and provides both spatial and temporal adaptivity and error control (Wang et al., 2004a).

In this chapter, the methods for all the required calculations are supplied in order to produce a mathematical system that can be solved. The derivations of the PDEs from the conservation equations for specific use in the BACOL software is discussed in Section 3.2, followed by discussions on the implementation of reaction rates (Section 3.4), molecular transport (Section 3.5) and thermochemical properties (Section 3.6). Finally, a description of the strategy followed to employ the PDE solver in the current model and the list of conditions chosen for this study are provided.

3.1. Assumptions

Several assumptions are made in order to simplify the mathematical system and to eliminate uncertainties. The assumptions made in developing the mathematical system of this study, result in a significantly simpler system, which is therefore faster to solve. Each of these assumptions are listed below.

- Angular symmetry around the centre, variation only along the radius.
- No radiative heating or cooling.
- Ideal gas law.
- The wall of the combustion chamber is perfectly insulated, i.e. an adiabatic vessel.
- The temperature range where model is valid is from 300 K to 3 000 K.
- The flame initiates at a radius of 2 mm.
- Diffusion according to Fick's law.
- Third body efficiency of all the molecules in the system is equal.
- Most of the reactions take place in the high temperature zone of the flame.

flame position changes with time.

- Constant viscosity

The most important assumptions of those listed are discussed in the immediately following sections. The assumptions of an adiabatic vessel and flame initiation at 2 mm are discussed with the boundary conditions in Section 3.3. The temperature range where the model is valid depends on the validity of the calculated heat capacities, as discussed in Section 3.6. The assumed Fickian diffusion is elaborated on in Section 3.5. The relevance of the third body efficiencies being equal is discussed in Section 3.4.2 and the assumption that most reactions take place in the high temperature zone is discussed in Section 3.4.3. The assumption of constant viscosity is explained in Section 3.2.3.

3.1.1. Symmetry

The first assumption is the greatest simplification, since it changes the mathematical system from three-dimensional to one-dimensional. This assumes that the system properties anywhere on a sphere concentric to the ignition source are the same or equivalently that the flame is perfectly spherical. Therefore, only the radius is required to indicate a specific sphere of equal properties. This approach has been taken in previous studies on spherical flames (Bradley et al., 1996, Chen, 2009) and is justified by graphical data from experimental studies, such as the shadowgraph in Figure 2.13, where the stable flame (left) is very close to a perfect sphere. This then also renders the current model incapable of modelling flame instabilities discussed in Section 2.2.5. The conservation of mass for a spherical control volume, shown in Figure 3.1, is considered as an example of the mathematical implication of the assumption.

The conservation of mass in the spherical control volume of Figure 3.1 is obtained by considering the flow of mass into and out of the volume at each of the surfaces of the volume. The co-ordinates in Figure 3.1: r, θ and ϕ , represent the radial, polar and azimuthal directions respectively. Equation 3.1, taken from Bird et al. (2002), shows the conservation of mass in a spherical control volume.

$$\frac{\partial \rho}{\partial t} + \frac{1}{r^2}\frac{\partial}{\partial r}\left(\rho r^2 u_r\right) + \frac{1}{r\sin\theta}\frac{\partial}{\partial \theta}\left(\rho u_\theta \sin\theta\right) + \frac{1}{r\sin\theta}\frac{\partial}{\partial \phi}\left(\rho u_\phi\right) = 0 \qquad (3.1)$$

In Equation 3.1, the subscripts of the velocity term (u) indicate the directional components of the velocity and ρ represents the density of the mixture. Note that here the velocity term (u) describes the diffusional and convective velocity. However, in the derivations that

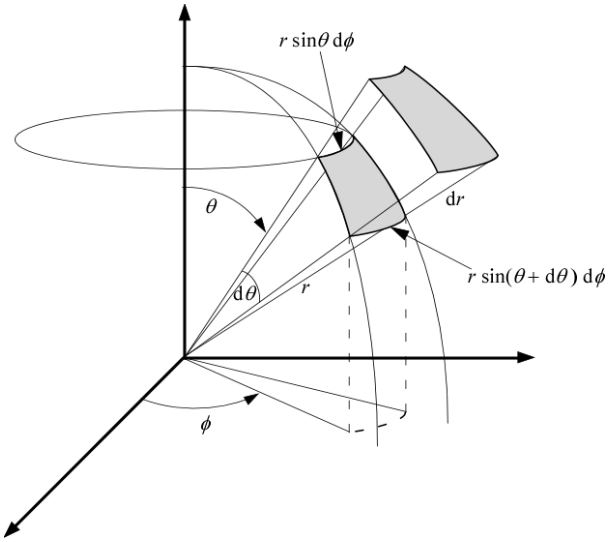

Figure 3.1.: Spherical control volume. (Saad, 2010)

follow in Section 3.2 the diffusional and convective velocities are treated separately. The assumption that the local properties, such as density (ρ) at a radius (r), are equal over the entire spherical surface with that radius, renders the partial derivatives, $\frac{\partial}{\partial\theta}$ and $\frac{\partial}{\partial\phi}$ equal to zero. Therefore Equation 3.1 is simplified significantly to produce Equation 3.2.

$$\frac{\partial\rho}{\partial t}+\frac{1}{r^2}\frac{\partial}{\partial r}\left(\rho r^2 u_r\right)=0 \tag{3.2}$$

This implies that only the flow in the radial direction is considered in the derivations that follow in this chapter. The radial component of the velocity (u_r) is from here on represented by u. This then shows the simplification obtained when assuming symmetry around the centre of the spherical flame. The model of Chen (2009) implemented the same simplification and showed good agreement with experimental results (Chen et al., 2009).

3.1.2. Radiation

The inclusion of radiative emission and absorption in a propagating flame model is a challenging task and is not attempted in the current work. The effect of radiation on laminar flame speeds were studied by Ebara et al. (2006) and Chen et al. (2007) for the specific case where the unburned gas (or initial gas mixture) contained significant

amounts of carbon dioxide. The propensity of a given species for the absorption of radiated heat is indicated by its Planck mean absorption coefficient. Carbon dioxide has a higher Planck mean absorption coefficient than n-heptane and methane (Ju et al., 1999, Wakatsuki, 2005) and therefore the presence of carbon dioxide in the unburned gas will cause a greater radiation effect on laminar flame speed than methane and n-heptane. Homonuclear diatomic molecules, such as O_2 and N_2 that make up most of the unburned gas, do not absorb infrared radiation (Wakatsuki, 2005) and therefore do not contribute to the radiative absorption.

It was concluded by Ebara et al. (2006) and Chen et al. (2007) that radiation should be included or accounted for in studies where the unburned gas contains major radiating species, such as carbon dioxide. These type of combustion studies applies to the practice of diluting the reactant mixture in the combustion chamber of an internal combustion engine with the exhaust gases (combustion products). The dilution of the unburned gas with water or carbon dioxide is outside the scope of this study and since a hydrocarbon fuel (n-heptane) has a lower Plank mean absorption coefficient, higher heat capacity and is present in small concentrations, the effect of radiation is assumed to be negligible.

3.1.3. Equation of state

The equation of state for a gas mixture relates the volume and pressure of the gas to the temperature and quantity or number of moles. The equation of state therefore dictates that for a gas mixture, if any two of the properties: pressure, temperature or concentration (moles per volume) are known, the third is also known. The equation of state used in this study is the ideal gas law, as done in many other studies (Hirschfelder et al., 1953, Margolis, 1978, Kee et al., 1985, Bradley et al., 1996, Chen et al., 2009), and is given by Equation 3.3.

$$PV = nRT \tag{3.3}$$

The ideal gas law in Equation 3.3 gives a very simple relation between the pressure (P), volume (V), temperature (T) and number of moles (n) where R is the ideal gas constant: $R = 8.314 \frac{\mathrm{J}}{\mathrm{mol.K}}$. The ideal gas law assumes that the molecules themselves occupy no volume and that they exert no intermolecular forces on each other (Koretsky, 2004). These assumptions hold for low pressures and high temperatures, where the interactions between molecules are less. The expected temperature and pressure ranges in this model

depends on the initial conditions, and for the planned work, is expected to be in the ranges of 300 K to 3 000 K and 1 bar to 15 bar. It was suggested by Hirschfelder et al. (1953) that strong deviation from ideal gas behaviour in flame models should be accounted for at pressures above 50 bar. Seeing that the critical pressure (pressure at which intermolecular forces becomes dominant) of nitrogen is 33 bar, the ideal gas law should give an accurate description of the real gas mixtures for the conditions of this study.

3.2. Conservation equations

The conservation equations developed for this study consists of the conservation of species, energy and momentum. The set of PDEs derived from the conservation equations needs to be in the correct form as BACOL inputs and therefore the results from different conservation equations are used to obtain the input PDEs. BACOL requires input PDEs where the time derivative of each element in a quantity vector (θ) at a point in space (r) and time (t) is given as explicit functions of the spatial properties, as shown in Equation 3.4.

$$\frac{\partial \theta}{\partial t} = f\left(t, r, \theta, \frac{\partial \theta}{\partial r}, \frac{\partial^2 \theta}{\partial r^2}\right), \quad r_a \leq r \leq r_b \text{ and } t \geq t_0 \tag{3.4}$$

In Equation 3.4, r_a and r_b are the spatial boundaries and t_0 is the starting time for the model. The conservation equations are developed by considering the change of a quantity, such as energy, in a control volume. Although the PDEs are used to model a spherical system, the derivations that follow are for a general one-dimensional spatial co-ordinate system. A representation of this generic control volume is shown in Figure 3.2.

In Figure 3.2, only the flow in the direction of r is considered and therefore one-dimensional conservation equations are developed. The direction of r represents the radial spatial co-ordinate for a spherical and cylindrical co-ordinate system. The area (A) of the planes at the two flow boundary surfaces at r and $r + \Delta r$, as well as the distance between the planes (Δr), as seen in Figure 3.2, are of importance in the derivations, since the volume of the control volume is approximated by $A\Delta r$ and it is used later to specify the geometric system.

The molecular transport is discussed in Section 3.5, but for now it should be mentioned that diffusive molar flux $\left(J_i^*\right)$ of species i is given by

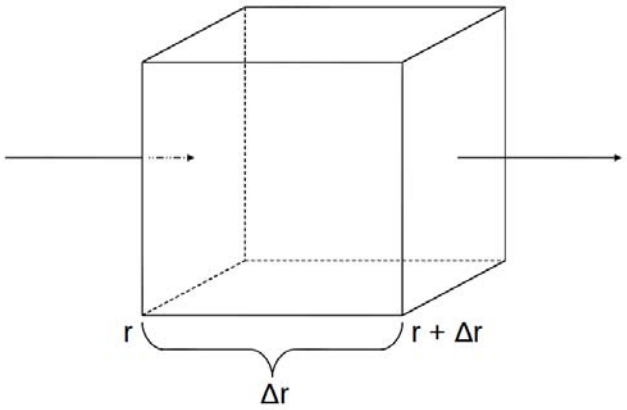

Figure 3.2.: Simplified control volume.

$$J_i^* = -D_i C_T \frac{\partial X_i}{\partial r} \tag{3.5}$$

and the thermal conduction (q) is given by

$$q = -\lambda \frac{\partial T}{\partial r} \tag{3.6}$$

where D_i is a diffusion coefficient and λ is the thermal conductivity, each a function of the concentrations (C_i) and temperature (T). In Equation 3.5, X_i is the mole fraction of species i and C_T is the total concentration, given by the sum of concentrations of all species present.

3.2.1. Conservation of species

The change in the moles of species i in the control volume is evaluated by taking into account the rate of flow into and out of the volume at the two surfaces (r *and* $r + \Delta r$) and the production or consumption of species i through reaction, for a given elapsed time Δt. The conservation of each species i is therefore given by Equation 3.7.

$$\begin{aligned} \Delta\left(C_i A \Delta r\right) &= \left(C_i u A\,|_r - C_i u A\,|_{r+\Delta r}\right)\Delta t + \left(-D_i A C_T \frac{\partial X_i}{\partial r}\,|_r + D_i A C_T \frac{\partial X_i}{\partial r}\,|_{r+\Delta r}\right)\Delta t \\ &\quad + \left(R_i A \Delta r\right)\Delta t \end{aligned} \tag{3.7}$$

In Equation 3.7, $C_i A\Delta r$ gives the amount of moles in the control volume, $C_i uA$ gives the convective molar flow, $D_i AC_T \frac{\partial X_i}{\partial r}$ gives the diffusive molar flow and $R_i A\Delta r$ gives the rate of production of species i. Equation 3.7 can be rewritten to produce Equation 3.8, which relates rate of change on the left hand side to spatial gradients on the right hand side.

$$\frac{\Delta\left(C_i A\right)}{\Delta t} = \frac{\left(C_i uA\mid_r - C_i uA\mid_{r+\Delta r}\right)}{\Delta r} + \frac{\left(-D_i AC_T \frac{\partial X_i}{\partial r}\mid_r + D_i AC_T \frac{\partial X_i}{\partial r}\mid_{r+\Delta r}\right)}{\Delta r} + R_i A \quad (3.8)$$

Equation 3.8 is converted to the differential form by taking the limit of Equation 3.8 where the length of the control volume (Δr) and the elapsed time (Δt) approaches zero to produce Equation 3.9.

$$\frac{\partial}{\partial t}\left(C_i A\right) = -\frac{\partial}{\partial r}\left(C_i Au\right) + \frac{\partial}{\partial r}\left(AD_i C_T \frac{\partial X_i}{\partial r}\right) + AR_i \quad (3.9)$$

Expanding Equation 3.9 gives Equation 3.10.

$$\begin{aligned} C_i\frac{\partial A}{\partial t} + A\frac{\partial C_i}{\partial t} &= -AC_i\frac{\partial u}{\partial r} - Au\frac{\partial C_i}{\partial r} - C_i u\frac{\partial A}{\partial r} + AD_i C_T\frac{\partial^2 X_i}{\partial r^2} + AD_i\frac{\partial X_i}{\partial r}\frac{\partial C_T}{\partial r} \\ &\quad + D_i C_T\frac{\partial X_i}{\partial r}\frac{\partial A}{\partial r} + AC_T\frac{\partial X_i}{\partial r}\frac{\partial D_i}{\partial r} + AR_i \end{aligned} \quad (3.10)$$

and since the area of the considered surfaces (A) does not change over time $\left(\frac{\partial A}{\partial t} = 0\right)$, dividing Equation 3.10 by the area gives:

$$\begin{aligned} \frac{\partial C_i}{\partial t} &= -C_i\frac{\partial u}{\partial r} - u\frac{\partial C_i}{\partial r} - C_i u\frac{1}{A}\frac{\partial A}{\partial r} + D_i C_T\frac{\partial^2 X_i}{\partial r^2} + D_i\frac{\partial X_i}{\partial r}\frac{\partial C_T}{\partial r} \\ &\quad + D_i C_T\frac{\partial X_i}{\partial r}\frac{1}{A}\frac{\partial A}{\partial r} + C_T\frac{\partial X_i}{\partial r}\frac{\partial D_i}{\partial r} + R_i \end{aligned} \quad (3.11)$$

In Equation 3.11, the derivative of the diffusion coefficient of every species i $\left(\frac{\partial D_i}{\partial r}\right)$ is given by Equation 3.12.

$$\frac{\partial D_i}{\partial r} = \sum_{k=1}^{species}\left(\frac{\partial D_i}{\partial C_k}\frac{\partial C_k}{\partial r}\right) + \frac{\partial D_i}{\partial T}\frac{\partial T}{\partial r} \quad (3.12)$$

The PDE for the concentration quantities (C_i), given by Equation 3.11, represents the final species conservation equations and is suitable as input for BACOL.

3.2.2. Conservation of energy

For the change of energy, the internal energy (U) in the control volume seen in Figure 3.2 is evaluated. The change in internal energy is described by flow of species, due to convection and diffusion, as well as heat transfer into and out of the volume at the two surfaces (r *and* $r + \Delta r$).

$$\begin{aligned}\Delta U &= \sum_{i=1}^{species} \left(C_i h_i A u \mid_r - C_i h_i A u \mid_{r+\Delta r}\right) \Delta t \\ &+ \sum_{i=1}^{species} \left(-A h_i D_i C_T \frac{\partial X_i}{\partial r} \mid_r + A h_i D_i C_T \frac{\partial X_i}{\partial r} \mid_{r+\Delta r}\right) \Delta t \\ &+ \left(-\lambda A \frac{\partial T}{\partial r} \mid_r + \lambda A \frac{\partial T}{\partial r} \mid_{r+\Delta r}\right) \Delta t \end{aligned} \tag{3.13}$$

In Equation 3.13, $C_i h_i A u$ gives the flow of enthalpy due to convection of species i, $A h_i D_i C_T \frac{\partial X_i}{\partial r}$ gives the flow of enthalpy due to diffusion of species i and $\lambda A \frac{\partial T}{\partial r}$ gives the conduction of heat. The thermodynamic relation between change in internal energy and enthalpy is defined by Koretsky (2004) as:

$$\Delta U = \Delta H - \Delta (PV) \tag{3.14}$$

Enthalpy is calculated from the molar enthalpies of each of the species present in the system as shown in Equation 3.15.

$$\Delta H = \Delta \left(\sum_{i=1}^{species} \left(C_i h_i A \Delta r\right) \right) \tag{3.15}$$

This molar enthalpy is defined as:

$$h_i(T) = h_{f,i(298\text{K})} + \int_{298}^{T} c_{p,i}\,dT \tag{3.16}$$

$$\text{and } \frac{\partial h_i}{\partial T} = c_{p,i} \tag{3.17}$$

In Equation 3.16, $h_{f,i(298\text{K})}$ represents the heat of formation of species i at 298 K and $c_{p,i}$ is the molar constant pressure heat capacity of species i. From now on the summation over all the present species as seen in Equation 3.15 will be indicated with a summation sign only. The pressure (P) in Equation 3.14 is obtained from the equation of state (ideal gas law) as a function of the total molar concentration and temperature as shown in Equation 3.18.

$$\begin{aligned} PV &= nRT \\ P &= \frac{n}{V}RT \\ P &= CRT \\ P &= \sum C_i RT \end{aligned} \tag{3.18}$$

The conservation of energy from Equation 3.13 can then be rewritten as indicated in Equation 3.19.

$$\begin{aligned} \Delta\left(\sum C_i h_i A \Delta r\right) &= \sum \left(C_i h_i A u\,|_r - C_i h_i A u\,|_{r+\Delta r}\right)\Delta t \\ -\Delta\left(\sum C_i R T A \Delta r\right) &\quad + \sum \left(-A h_i D_i C_T \frac{\partial X_i}{\partial r}\,|_r + A h_i D_i C_T \frac{\partial X_i}{\partial r}\,|_{r+\Delta r}\right)\Delta t \\ &\quad + \left(-\lambda A \frac{\partial T}{\partial r}\,|_r + \lambda A \frac{\partial T}{\partial r}\,|_{r+\Delta r}\right)\Delta t \end{aligned} \tag{3.19}$$

Equation 3.19 is converted to the differential form by rewriting it to the form of Equation 3.8 and taking the length of the control volume (Δr) and the elapsed time (Δt) as infinitely small to produce Equation 3.20.

$$\sum \frac{\partial}{\partial t}(C_i h_i A) - \sum \frac{\partial}{\partial t}(C_i RTA) = -\sum \frac{\partial}{\partial r}(uAC_i h_i) + \sum \frac{\partial}{\partial r}\left(Ah_i D_i C_T \frac{\partial X_i}{\partial r}\right) + \frac{\partial}{\partial r}\left(\lambda A \frac{\partial T}{\partial r}\right) \quad (3.20)$$

Equation 3.20 is expanded in order to simplify it. This is done separately for the left hand side (LHS), Equation 3.21, and right hand side (RHS), Equation 3.22, for easier presentation.

The left hand side;

$$\sum Ah_i \frac{\partial C_i}{\partial t} + \sum AC_i \frac{\partial h_i}{\partial t} + \sum C_i h_i \frac{\partial A}{\partial t} = LHS$$
$$-\sum ARC_i \frac{\partial T}{\partial t} - \sum ART \frac{\partial C_i}{\partial t} - \sum RC_i T \frac{\partial A}{\partial t} \quad (3.21)$$

and right hand side;

$$\begin{aligned} RHS = & -\sum uAC_i \frac{\partial h_i}{\partial r} - \sum uAh_i \frac{\partial C_i}{\partial r} - \sum AC_i h_i \frac{\partial u}{\partial r} - \sum uC_i h_i \frac{\partial A}{\partial r} \\ & + \sum AD_i h_i C_T \frac{\partial^2 X_i}{\partial r^2} + \sum AD_i h_i \frac{\partial X_i}{\partial r}\frac{\partial C_T}{\partial r} + \sum AD_i C_T \frac{\partial X_i}{\partial r}\frac{\partial h_i}{\partial r} \\ & + \sum Ah_i C_T \frac{\partial X_i}{\partial r}\frac{\partial D_i}{\partial r} + \sum D_i h_i C_T \frac{\partial X_i}{\partial r}\frac{\partial A}{\partial r} \\ & + A\lambda \frac{\partial^2 T}{\partial r^2} + A\frac{\partial T}{\partial r}\frac{\partial \lambda}{\partial r} + \lambda \frac{\partial T}{\partial r}\frac{\partial A}{\partial r} \end{aligned} \quad (3.22)$$

From Equation 3.17 it can be shown that

$$\begin{aligned} \frac{\partial h_i}{\partial r} &= \frac{\partial h_i}{\partial T}\frac{\partial T}{\partial r} \\ &= c_{p,i}\frac{\partial T}{\partial r} \\ \text{and } \frac{\partial h}{\partial t} &= c_{p,i}\frac{\partial T}{\partial t} \end{aligned} \quad (3.23)$$

Again the area (A) does not change with time and so, by dividing the left hand side (Equation 3.21) and right hand side (Equation 3.22) by the area (A) and implementing the result of Equation 3.23, the following equation is obtained.

The left hand side;

$$\sum h_i \frac{\partial C_i}{\partial t} + \sum C_i c_{p,i} \frac{\partial T}{\partial t} - \sum RC_i \frac{\partial T}{\partial t} - \sum RT \frac{\partial C_i}{\partial t} = LHS \tag{3.24}$$

and right hand side:

$$\begin{aligned} RHS \;=\; & -\sum uC_i c_{p,i} \frac{\partial T}{\partial r} - \sum uh_i \frac{\partial C_i}{\partial r} - \sum C_i h_i \frac{\partial u}{\partial r} - \sum uC_i h_i \frac{1}{A}\frac{\partial A}{\partial r} \\ & + \sum D_i h_i C_T \frac{\partial^2 X_i}{\partial r^2} + \sum D_i h_i \frac{\partial X_i}{\partial r}\frac{\partial C_T}{\partial r} + \sum D_i c_{p,i} C_T \frac{\partial X_i}{\partial r}\frac{\partial T}{\partial r} \\ & + \sum h_i C_T \frac{\partial X_i}{\partial r}\frac{\partial D_i}{\partial r} + \sum D_i h_i C_T \frac{\partial X_i}{\partial r}\frac{1}{A}\frac{\partial A}{\partial r} \\ & + \lambda \frac{\partial^2 T}{\partial r^2} + \frac{\partial T}{\partial r}\frac{\partial \lambda}{\partial r} + \lambda \frac{\partial T}{\partial r}\frac{1}{A}\frac{\partial A}{\partial r} \end{aligned} \tag{3.25}$$

From the conservation of species in Section 3.2.1, Equation 3.11 is multiplied by the molar enthalpy (h_i) and summed for each species to give Equation 3.26.

$$\begin{aligned} \sum h_i \frac{\partial C_i}{\partial t} \;=\; & -\sum C_i h_i \frac{\partial u}{\partial r} - \sum uh_i \frac{\partial C_i}{\partial r} - \sum uC_i h_i \frac{1}{A}\frac{\partial A}{\partial r} \\ & + \sum D_i h_i C_T \frac{\partial X_i}{\partial r}\frac{1}{A}\frac{\partial A}{\partial r} + \sum D_i h_i C_T \frac{\partial^2 X_i}{\partial r^2} \\ & + \sum D_i h_i \frac{\partial X_i}{\partial r}\frac{\partial C_T}{\partial r} + \sum h_i C_T \frac{\partial X_i}{\partial r}\frac{\partial D_i}{\partial r} + \sum R_i h_i \end{aligned} \tag{3.26}$$

Now the left hand side of Equation 3.26 is subtracted from the energy conservation equation LHS (Equation 3.24) to give the new LHS for the energy conservation equation shown in Equation 3.27.

$$\sum C_i c_{p,i} \frac{\partial T}{\partial t} - \sum RC_i \frac{\partial T}{\partial t} - \sum RT \frac{\partial C_i}{\partial t} = LHS \tag{3.27}$$

This should be done for the RHS as well and therefore the right hand side of Equation 3.26 is subtracted from the energy conservation equation RHS (Equation 3.25) to give the new

energy conservation equation RHS shown in Equation 3.28.

$$\begin{aligned} RHS &= -\sum uC_i c_{p,i}\frac{\partial T}{\partial r} + \sum D_i c_{p,i} C_T \frac{\partial X_i}{\partial r}\frac{\partial T}{\partial r} \\ &\quad +\lambda\frac{\partial^2 T}{\partial r^2} + \frac{\partial T}{\partial r}\frac{\partial \lambda}{\partial r} \\ &\quad +\lambda\frac{\partial T}{\partial r}\frac{1}{A}\frac{\partial A}{\partial r} - \sum R_i h_i \end{aligned} \tag{3.28}$$

The LHS (Equation 3.27) and RHS (Equation 3.28) of the energy conservation equation remains equal and therefore the energy conservation equation is simplified in Equation 3.29.

$$\begin{aligned} \sum C_i \left(c_{p,i} - R\right)\frac{\partial T}{\partial t} - \sum RT\frac{\partial C_i}{\partial t} &= -\sum uC_i c_{p,i}\frac{\partial T}{\partial r} + \sum D_i c_{p,i}\frac{\partial C_i}{\partial r}\frac{\partial T}{\partial r} \\ &\quad +\lambda\frac{\partial^2 T}{\partial r^2} + \frac{\partial T}{\partial r}\frac{\partial \lambda}{\partial r} \\ &\quad +\lambda\frac{\partial T}{\partial r}\frac{1}{A}\frac{\partial A}{\partial r} - \sum R_i h_i \end{aligned} \tag{3.29}$$

From Equation 3.29, the derivative of temperature to time is then given by Equation 3.30.

$$\begin{aligned} \frac{\partial T}{\partial t} &= -u\frac{\sum C_i c_{p,i}}{\sum C_i \left(c_{p,i} - R\right)}\frac{\partial T}{\partial r} + \frac{\sum D_i c_{p,i} C_T \frac{\partial X_i}{\partial r}}{\sum C_i \left(c_{p,i} - R\right)}\frac{\partial T}{\partial r} + \frac{\lambda}{\sum C_i \left(c_{p,i} - R\right)}\frac{\partial^2 T}{\partial r^2} \\ &\quad +\frac{1}{\sum C_i \left(c_{p,i} - R\right)}\frac{\partial T}{\partial r}\frac{\partial \lambda}{\partial r} + \frac{\lambda}{\sum C_i \left(c_{p,i} - R\right)}\frac{\partial T}{\partial r}\frac{1}{A}\frac{\partial A}{\partial r} \\ &\quad -\frac{\sum R_i h_i}{\sum C_i \left(c_{p,i} - R\right)} + \frac{RT}{\sum C_i \left(c_{p,i} - R\right)}\sum \frac{\partial C_i}{\partial t} \end{aligned} \tag{3.30}$$

In Equation 3.30, the derivative of thermal conductivity $\left(\frac{\partial \lambda}{\partial r}\right)$ is given by Equation 3.31.

$$\frac{\partial \lambda}{\partial r} = \sum_{k=1}^{species}\left(\frac{\partial \lambda}{\partial C_k}\frac{\partial C_k}{\partial r}\right) + \frac{\partial \lambda}{\partial T}\frac{\partial T}{\partial r} \tag{3.31}$$

The time derivative term in Equation 3.30 $\left(\sum \frac{\partial C_i}{\partial t}\right)$ is simply the sum of Equation 3.11

for each species i. The PDE for the temperature quantity (T) given in Equation 3.30 represents the final energy conservation equation and is suitable as input for BACOL.

3.2.3. Conservation of momentum

The change in momentum in the control volume seen in Figure 3.2 will be evaluated taking into account the forces on the volume at the surfaces, the flow of momentum into and out of the volume as well as the molecular transport of momentum at the surfaces (r *and* $r + \Delta r$):

$$\begin{aligned} \Delta\left(\rho u A \Delta r\right) &= \sum F \Delta t + \left(\rho u^2 A \mid_r - \rho u^2 A \mid_{r+\Delta r}\right) \Delta t \\ &\quad + \sum \left(-A D_i C_T \frac{\partial X_i}{\partial r} M_i u \mid_r + A D_i C_T \frac{\partial X_i}{\partial r} M_i u \mid_{r+\Delta r}\right) \Delta t \\ &\quad \left(-\frac{4}{3} A \mu \frac{\partial u}{\partial r} \mid_r + \frac{4}{3} A \mu \frac{\partial u}{\partial r} \mid_{r+\Delta r}\right) \Delta t \end{aligned} \tag{3.32}$$

In Equation 3.32, $\rho u A \Delta r$ gives the momentum in the control volume, F is the forces that the pressure (P) exerts on the control volume, $\rho u^2 A$ gives the flow of momentum due to convection, $A D_i C_T \frac{\partial X_i}{\partial r} M_i u$ gives the transfer of momentum due to diffusion and $\frac{4}{3} A \mu \frac{\partial u}{\partial r}$ gives the stress tensor. When considering the momentum of a fluid, the mass is of importance and this shows in Equation 3.32 where the density of the fluid (ρ) and the molar mass of each species (M_i) are required. The dynamic viscosity (μ) is assumed to be constant, since the only implication it has on the momentum balance is the smoothing of the spatial velocity profiles.

The resultant force term in Equation 3.32 should take all the forces in the direction of r into account, which includes forces on the surfaces other than the two perpendicular to the radial direction at r and $r + \Delta r$. Forces acting on the control volume are caused by the pressure, which exerts a force on every surface of the control volume. A different variation of the general control volume of Figure 3.2 is given in Figure 3.3, where the surfaces that are not perpendicular to the radial direction are at an angle to it.

The visible surfaces in Figure 3.3 are indicated by A_1, B_1 and C_1 and the surfaces opposite them are referred to as A_2, B_2 and C_2. Further, the projected area of the control volume in the direction of r is indicated by A_p. Figure 3.3 therefore shows a control volume where the surfaces A_1 and A_2 are perpendicular to the direction r, and the surfaces B_1, B_2, C_1

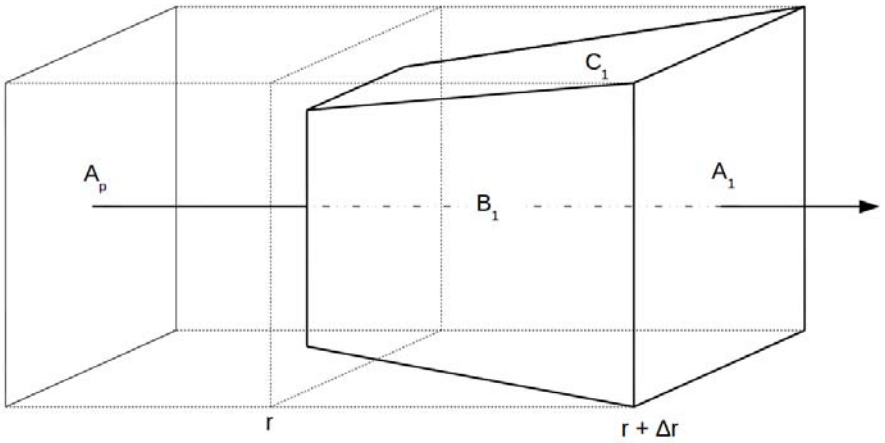

Figure 3.3.: General control volume with side surface at an angle to the radial direction.

and C_2 are not parallel to the direction r, but at an angle to it. This causes the forces resulting from the pressure on surfaces B_1, B_2, C_1 and C_2 to have a component in the direction of r. To account for the all these forces on the control volume, the total force in the positive direction of r is approximated as the pressure (P) at the point r multiplied by the projected surface area (A_p) of the control volume. By multiplying the pressure (P) with the projected area rather than the area of A_1, the resulting forces from the pressure on the surfaces B_1, B_2, C_1 and C_2 are also taken into account along with the force on the surface A_1. Similarly the total force in the negative direction of r is taken as the pressure at the point $r + \Delta r$ multiplied by the projected area of the control volume (A_p).

This approach does not apply to other terms in Equation 3.32, since the assumption of symmetry renders the convective velocity and diffusion through the surfaces B_1, B_2, C_1 and C_2 equal to zero and therefore no components in the r direction are present. The pressure is, however, applying forces on all the surfaces of the control volume and should be accounted for completely. Equation 3.32 is then written as Equation 3.33.

$$\begin{aligned}\Delta\left(\rho u A \Delta r\right) &= A_p\left(P\mid_r - P\mid_{r+\Delta r}\right)\Delta t + \left(\rho u^2 A\mid_r - \rho u^2 A\mid_{r+\Delta r}\right)\Delta t \\ &\quad + \sum\left(-AD_iC_T\frac{\partial X_i}{\partial r}M_i u\mid_r + AD_iC_T\frac{\partial X_i}{\partial r}M_i u\mid_{r+\Delta r}\right)\Delta t \\ &\quad + \left(-\frac{4}{3}A\mu\frac{\partial u}{\partial r}\mid_r + \frac{4}{3}A\mu\frac{\partial u}{\partial r}\mid_{r+\Delta r}\right)\Delta t \end{aligned} \tag{3.33}$$

The projected area (A_p) is written outside the brackets in Equation 3.33 since it is equal

for both the cases where the forces in the positive and negative direction of r are considered. Equation 3.33 is converted to the differential form by rewriting it to the form of Equation 3.8 and taking the length of the control volume (Δr) and the elapsed time (Δt) as infinitely small. For the limit where Δr approaches zero in Figure 3.3, the projected area (A_p) will approach the situation where $A_1 = A_p = A_2$ and is therefore equal to the general area term (A). This then produces Equation 3.34.

$$\frac{\partial}{\partial t}(\rho u A) = -A\frac{\partial}{\partial r}(P) - \frac{\partial}{\partial r}\left(\rho u^2 A\right) + \frac{\partial}{\partial r}\left(AD_i C_T \frac{\partial X_i}{\partial r} M_i u\right) + \frac{\partial}{\partial r}\left(\frac{4}{3}A\mu\frac{\partial u}{\partial r}\right) \quad (3.34)$$

The density of the gas is given as a function of the concentrations of each species (C_i) and its molar mass (M_i) shown in Equation 3.35.

$$\rho = \sum C_i M_i \quad (3.35)$$

The pressure is given by Equation 3.18 and therefore Equation 3.34 is rewritten as:

$$\begin{aligned}\sum \frac{\partial}{\partial t}(C_i M_i u A) &= -A\sum \frac{\partial}{\partial r}(C_i R T) - \sum \frac{\partial}{\partial r}\left(C_i M_i u^2 A\right) + \frac{\partial}{\partial r}\left(AD_i C_T \frac{\partial X_i}{\partial r} M_i u\right) \\ &\quad + \frac{\partial}{\partial r}\left(\frac{4}{3}A\mu\frac{\partial u}{\partial r}\right) \end{aligned} \quad (3.36)$$

Equation 3.36 is expanded to give Equation 3.37.

$$\begin{aligned}\sum C_i M_i u\frac{\partial A}{\partial t} &= -\sum ART\frac{\partial C_i}{\partial r} - \sum ARC_i\frac{\partial T}{\partial r} \\ +\sum AuM_i\frac{\partial C_i}{\partial t} &\quad -\sum Au^2 M_i\frac{\partial C_i}{\partial r} - \sum C_i M_i u^2\frac{\partial A}{\partial r} - \sum 2AC_i M_i u\frac{\partial u}{\partial r} \\ +\sum AC_i M_i\frac{\partial u}{\partial t} &\quad +\sum AM_i D_i C_T\frac{\partial X_i}{\partial r}\frac{\partial u}{\partial r} + \sum AM_i u D_i C_T\frac{\partial^2 X_i}{\partial r^2} \\ &\quad +\sum AM_i u D_i\frac{\partial X_i}{\partial r}\frac{\partial C_T}{\partial r} + \sum M_i u D_i C_T\frac{\partial X_i}{\partial r}\frac{\partial A}{\partial r} \\ &\quad +\sum AM_i u C_T\frac{\partial X_i}{\partial r}\frac{\partial D_i}{\partial r} + \frac{4}{3}A\mu\frac{\partial^2 u}{\partial r^2} \\ &\quad +\frac{4}{3}\mu\frac{\partial u}{\partial r}\frac{\partial A}{\partial r} + \frac{4}{3}A\frac{\partial u}{\partial r}\frac{\partial \mu}{\partial r}\end{aligned} \quad (3.37)$$

The area (A) does not change with time and by dividing Equation 3.37 by the area (A), Equation 3.38 is obtained.

$$\begin{aligned}\sum uM_i\frac{\partial C_i}{\partial t} &= -\sum RT\frac{\partial C_i}{\partial r}-\sum RC_i\frac{\partial T}{\partial r}\\ +\sum C_iM_i\frac{\partial u}{\partial t} &\quad -\sum u^2M_i\frac{\partial C_i}{\partial r}-\sum C_iM_iu^2\frac{1}{A}\frac{\partial A}{\partial r}-\sum 2C_iM_iu\frac{\partial u}{\partial r}\\ &\quad +\sum M_iD_iC_T\frac{\partial X_i}{\partial r}\frac{\partial u}{\partial r}+\sum M_iuD_iC_T\frac{\partial^2X_i}{\partial r^2}+\sum M_iuD_i\frac{\partial X_i}{\partial r}\frac{\partial C_T}{\partial r}\\ &\quad +\sum M_iuD_iC_T\frac{\partial X_i}{\partial r}\frac{1}{A}\frac{\partial A}{\partial r}+\sum M_iuC_T\frac{\partial X_i}{\partial r}\frac{\partial D_i}{\partial r}\\ &\quad +\frac{4}{3}\mu\frac{\partial^2u}{\partial r^2}+\frac{4}{3}\mu\frac{\partial u}{\partial r}\frac{1}{A}\frac{\partial A}{\partial r}+\frac{4}{3}\frac{\partial u}{\partial r}\frac{\partial \mu}{\partial r}\end{aligned} \tag{3.38}$$

From the conservation of species in Section 3.2.1, Equation 3.11 is multiplied by the molar mass (M_i) and velocity (u), and then summed for each species to give Equation 3.39.

$$\begin{aligned}\sum uM_i\frac{\partial C_i}{\partial t} &= -\sum C_iM_iu\frac{\partial u}{\partial r}-\sum u^2M_i\frac{\partial C_i}{\partial r}-\sum C_iM_iu^2\frac{1}{A}\frac{\partial A}{\partial r}\\ &\quad +\sum uD_iM_iC_T\frac{\partial X_i}{\partial r}\frac{1}{A}\frac{\partial A}{\partial r}+\sum uD_iM_iC_T\frac{\partial^2X_i}{\partial r^2}\\ &\quad +\sum uD_iM_i\frac{\partial X_i}{\partial r}\frac{\partial C_T}{\partial r}+\sum uM_iC_T\frac{\partial X_i}{\partial r}\frac{\partial D_i}{\partial r}+\sum uR_iM_i\end{aligned} \tag{3.39}$$

Subtracting Equation 3.39 from Equation 3.38 then gives Equation 3.40.

$$\begin{aligned}\sum C_iM_i\frac{\partial u}{\partial t} &= -\sum RT\frac{\partial C_i}{\partial r}-\sum RC_i\frac{\partial T}{\partial r}-\sum C_iM_iu\frac{\partial u}{\partial r}-\sum M_iD_iC_T\frac{\partial X_i}{\partial r}\frac{\partial u}{\partial r}\\ &\quad -u\sum R_iM_i+\frac{4}{3}\mu\frac{\partial^2u}{\partial r^2}+\frac{4}{3}\mu\frac{\partial u}{\partial r}\frac{1}{A}\frac{\partial A}{\partial r}+\frac{4}{3}\frac{\partial u}{\partial r}\frac{\partial \mu}{\partial r}\end{aligned} \tag{3.40}$$

The reaction mass balance term ($\sum R_iM_i$) is equal to zero and so Equation 3.40 can be written as:

$$\frac{\partial u}{\partial t} = -\frac{RT}{\sum C_i M_i}\sum \frac{\partial C_i}{\partial r} - \frac{R\sum C_i}{\sum C_i M_i}\frac{\partial T}{\partial r} - u\frac{\partial u}{\partial r} - \frac{u\sum D_i M_i C_T \frac{\partial X_i}{\partial r}}{\sum C_i M_i}\frac{\partial u}{\partial r} + \frac{4}{3}\frac{\mu}{\sum C_i M_i}\frac{\partial^2 u}{\partial r^2} + \frac{4}{3}\frac{\mu}{\sum C_i M_i}\frac{\partial u}{\partial r}\frac{1}{A}\frac{\partial A}{\partial r} + \frac{4}{3\sum C_i M_i}\frac{\partial u}{\partial r}\frac{\partial \mu}{\partial r} \tag{3.41}$$

In Equation 3.41, the derivative of viscosity $\left(\frac{\partial \mu}{\partial r}\right)$ is given by Equation 3.42.

$$\frac{\partial \mu}{\partial r} = \sum_{k=1}^{species}\left(\frac{\partial \mu}{\partial C_k}\frac{\partial C_k}{\partial r}\right) + \frac{\partial \mu}{\partial T}\frac{\partial T}{\partial r} \tag{3.42}$$

Equation 3.41 is a PDE for convectional velocity (u) and represents the conservation of momentum equation. Equations 3.11, 3.30 and 3.41 are all in a suitable form to be used as input in BACOL and represent all the conservation equations. The derived PDEs describe the change in concentration of each species (C_i), temperature (T) and convective velocity (u) at each point in the solution domain. These quantities are represented by the quantity vector (θ) in Equation 3.4.

3.2.4. Geometry of the system

These derivations then supply the formulas required as input in the one-dimensional PDE solver. However, certain terms in these equations are not yet fully defined. The area term (A) in the PDE equations is not defined yet and is a result of the simplification made to the control volume in Figure 3.2. This area term introduces the effect of the geometric system on the mathematical model. For a laminar flat flame, the area of the surfaces on the control volume remains constant; therefore the area (A) is not a function of the spatial co-ordinate (r) which then gives Equation 3.43.

$$\frac{\partial A}{\partial r} = 0 \tag{3.43}$$

For a spherical geometry, the area (A) is a function of the spatial co-ordinate (r) as shown in Equation 3.44.

$$A = 4\pi r^2 \tag{3.44}$$

This dependence of the area term (A) on the spatial co-ordinate (r) defines the geometric system mathematically and influences all the terms in Equation 3.11, 3.30 and 3.41 that include $\frac{1}{A}\frac{\partial A}{\partial r}$. Table 3.1 gives A and $\frac{1}{A}\frac{\partial A}{\partial r}$ as functions of r for different geometric systems.

Table 3.1.: The area terms for different geometries.

Geometry	A	$\frac{1}{A}\frac{\partial A}{\partial r}$
Flat	-	0
Cylindrical	$2\pi r$	$\frac{1}{r}$
Spherical	$4\pi r^2$	$\frac{2}{r}$

By implementing the different functions of $\frac{1}{A}\frac{\partial A}{\partial r}$ in Table 3.1 into the derived PDEs, the geometry of the mathematical system is defined. This simple and effective way to change the geometric system makes the model versatile. The final equations used to model the spherical flame are given by Equations 3.45, 3.46 and 3.47, where $\frac{1}{A}\frac{\partial A}{\partial r} = \frac{2}{r}$ is implemented.

$$\begin{aligned}\frac{\partial C_i}{\partial t} &= -C_i\frac{\partial u}{\partial r} - u\frac{\partial C_i}{\partial r} - C_i u\frac{2}{r} + D_i C_T\frac{\partial^2 X_i}{\partial r^2} + D_i\frac{\partial X_i}{\partial r}\frac{\partial C_T}{\partial r} \\ &\quad + D_i C_T\frac{2}{r}\frac{\partial X_i}{\partial r} + C_T\frac{\partial X_i}{\partial r}\frac{\partial D_i}{\partial r} + R_i \end{aligned} \tag{3.45}$$

$$\begin{aligned}\frac{\partial T}{\partial t} &= -u\frac{\sum C_i c_{p,i}}{\sum C_i\left(c_{p,i}-R\right)}\frac{\partial T}{\partial r} + \frac{\sum D_i c_{p,i} C_T\frac{\partial X_i}{\partial r}}{\sum C_i\left(c_{p,i}-R\right)}\frac{\partial T}{\partial r} + \frac{\lambda}{\sum C_i\left(c_{p,i}-R\right)}\frac{\partial^2 T}{\partial r^2} \\ &\quad + \frac{1}{\sum C_i\left(c_{p,i}-R\right)}\frac{\partial T}{\partial r}\frac{\partial \lambda}{\partial r} + \frac{\lambda}{\sum C_i\left(c_{p,i}-R\right)}\frac{2}{r}\frac{\partial T}{\partial r} \\ &\quad - \frac{\sum R_i h_i}{\sum C_i\left(c_{p,i}-R\right)} + \frac{RT}{\sum C_i\left(c_{p,i}-R\right)}\sum\frac{\partial C_i}{\partial t} \end{aligned} \tag{3.46}$$

$$\begin{aligned}\frac{\partial u}{\partial t} &= -\frac{RT}{\sum C_i M_i}\sum\frac{\partial C_i}{\partial r} - \frac{R\sum C_i}{\sum C_i M_i}\frac{\partial T}{\partial r} - u\frac{\partial u}{\partial r} - \frac{u\sum D_i M_i C_T\frac{\partial X_i}{\partial r}}{\sum C_i M_i}\frac{\partial u}{\partial r} \\ &\quad + \frac{4}{3}\frac{\mu}{\sum C_i M_i}\frac{\partial^2 u}{\partial r^2} + \frac{4}{3}\frac{\mu}{\sum C_i M_i}\frac{2}{r}\frac{\partial u}{\partial r} + \frac{4}{3\sum C_i M_i}\frac{\partial u}{\partial r}\frac{\partial \mu}{\partial r} \end{aligned} \tag{3.47}$$

The calculations to determine the reaction rate term (R_i) are discussed in Section 3.4, while the calculations for the diffusion coefficients (D_i) and thermal conductivity (λ) are provided in Section 3.5. The constant pressure heat capacities (c_p) are obtained from polynomial fits as discussed in Section 3.6.

3.3. Boundary conditions

The PDEs derived from the conservation equations in Section 3.2 are all parabolic and therefore two boundary conditions and initial conditions are required to be able to solve them. For parabolic PDEs, the initial spatial conditions needs to be defined at t_0 as well as the conditions at the spatial boundaries (r_a and r_b) over time. BACOL requires the initial conditions of the parabolic PDE solver as Dirichlet conditions where the quantity vector (θ) at the initial time t_0 for each spatial point r (where $r_a \leq r \leq r_b$) should be provided. The conditions at the spatial boundaries, r_a and r_b, over time ($t \geq t_0$) should be supplied to BACOL as Dirichlet or Neumann conditions. Therefore either the spatial derivative or value for each element in the quantity vector (θ) should be supplied as shown in Equation 3.48.

$$b\left(t, \theta, \frac{\partial \theta}{\partial r}\right) = 0 \tag{3.48}$$

In Equation 3.48, the function b defines the boundary condition where it equals zero and is a function of time (t), the quantity vector (θ) and the spatial derivative of the quantity vector $\left(\frac{\partial \theta}{\partial r}\right)$. A boundary condition in the form of Equation 3.48 should be supplied for both spatial boundaries, r_a and r_b.

Different approaches for the initial conditions can be followed. However, the composition, temperature and pressure of the initial unburned gas are the most important information provided by the initial conditions. One approach to the initial conditions is to include a small section of hot combustion product to provide the energy required for the initiation of the propagating flame, while the rest of the initial spatial domain consists of unburned gases, as was done by Bradley et al. (1996). The approach followed in this study is to define the entire initial spatial domain as unburned gas at the specified initial conditions, while the spatial boundary conditions are employed to initiate combustion. Therefore, the initial temperature is set to the desired value and the convective velocity is set to zero, while the initial concentration of each species is set to represent the unburned gas with

the required fuel equivalence ratio and pressure. This then will define the quantity vector (θ), which is equal for each spatial point at the initial time (t_0).

For this study, one of the spatial boundaries (r_a) represents the centre of the spherical combustion chamber where the flame is initiated, while the other spatial boundary (r_b) represents the combustion chamber wall. The centre boundary (r_a) is not located at a radius of zero, but rather at a radius of 2 mm to avoid mathematical difficulties from the term $\frac{1}{A}\frac{\partial A}{\partial r}$ where the radius (r) approaches zero. At the centre of the combustion chamber (r_a) it is assumed that the conditions are such that no diffusion of species take place, the temperature is affected by some external energy source (electric spark) and that the convective velocity is zero. This translate to zero spatial gradients for each species, a predefined temperature profile and of course a convective velocity of zero. The same assumptions are made for the combustion chamber wall, except here perfect insulation is assumed, therefore no thermal conduction, which translates into a temperature gradient of zero. Unless stated otherwise, the combustion chamber wall boundary (r_b) is located at a radius of 50 mm to represent a constant volume combustion bomb with an inner diameter of 100 mm. The spatial boundary conditions are defined by the equations supplied in Table 3.2.

Table 3.2.: Boundary conditions.

	Chamber centre (r_a)	Chamber wall (r_b)
Species concentrations (C_i)	$\frac{\partial C_i}{\partial r} = 0$	$\frac{\partial C_i}{\partial r} = 0$
Temperature (T)	Equation 3.49	$\frac{\partial T}{\partial r} = 0$
Convective velocity (u)	$u = 0$	$u = 0$

The assumption for the boundary condition of temperature at the chamber wall is not entirely accurate. However, it simplifies the mathematical system by ignoring specialised calculations for heat transfer between the fluid and solid wall. Another alternative to this assumption is to assume the temperature of the gas at the wall remains constant ($T = T_i$), which will result in heat transfer to the wall and thus heat loss out of the system. Since the time required for the flame to consume all the unburned gas is of the order of milliseconds, the heat loss at the chamber wall is minimal. Therefore the assumption that no heat transfer takes place at the chamber wall is acceptable and simplifies the mathematical system.

All of the equations supplied in Table 3.2 are readily implemented in the form of Equa-

tion 3.48 into BACOL. The boundary condition for temperature at the centre of the combustion chamber (r_a) is given by Equation 3.49.

$$T - \frac{T_i + T_{ad}}{2} - \left(\frac{T_i - T_{ad}}{2}\right) \tanh\left[SR\left(t - t_{spark}\right)\right] = 0 \tag{3.49}$$

Equation 3.49 provides the boundary condition for the temperature at the centre of the combustion chamber as a function of the temperature (T) and time (t). The rest of the symbols in Equation 3.49 represent constants, where T_i and T_{ad} are the initial and adiabatic flame temperatures respectively, SR is the spark rate and t_{spark} gives the time at which the spark event will take place. Figure 3.4 gives the temperature profile, produced by Equation 3.49, that serves as the boundary condition at the point of ignition.

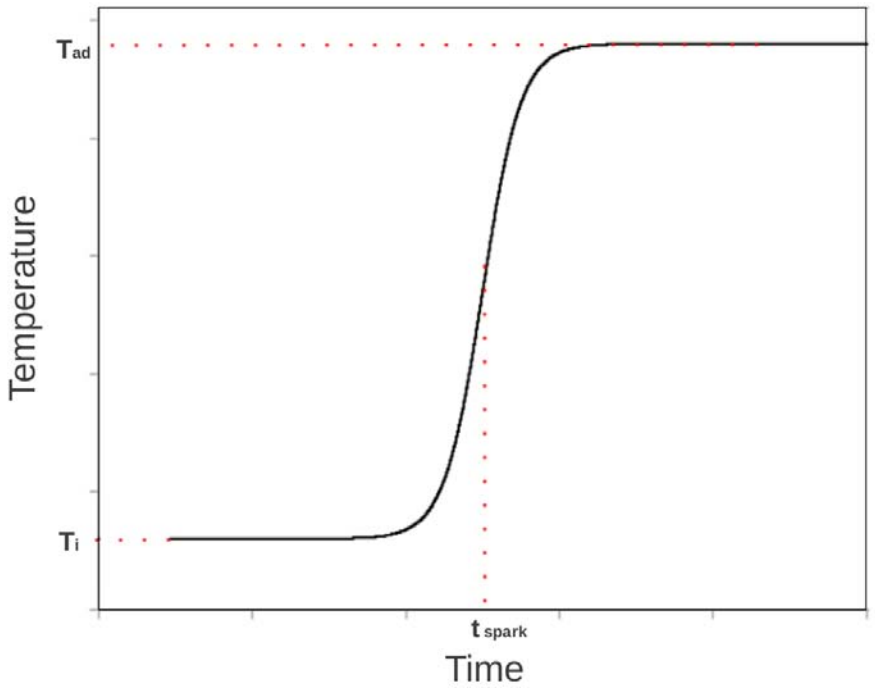

Figure 3.4.: Flame initiating boundary temperature from Equation 3.49.

Figure 3.4 shows how Equation 3.49 causes an increase in the boundary temperature from the initial temperature (T_i) to the adiabatic flame temperature (T_{ad}) at the specified time (t_{spark}). The spark rate (SR) determines the gradient of the temperature increase seen in Figure 3.4 and therefore the time duration of the spark event, where a greater value for SR in Equation 3.49 will result in a faster temperature increase. It is not essential in the model for the value of T_{ad} to be accurate, as it only serves to "ignite" or initiate

reaction. However, it will cause inaccuracies in the burned gas temperature profile.

Another possibility to describe the combustion initiating temperature boundary condition at the centre of the combustion chamber is to specify a zero temperature gradient with a certain period of a negative temperature gradient. This will cause "conductive heating" to increase the temperature at r_a during the spark event, while ensuring insulation or no thermal conduction the rest of the time. The only drawback of this approach is that the amount of heat transfered into the system is not easily controlled and therefore the boundary temperature may increase to outside the temperature limits (Section 3.6).

3.4. Reaction rates

The flame is described in Section 2.1 as a wave of reactions, where reaction rates govern the rate of production or consumption of species as well as the rate of heat release. The reaction rate term (R_i) in the PDEs, derived in Section 3.2, represents the rate at which the concentration of species i (C_i) is increasing due to chemical reaction. Therefore the unit for R_i is moles per unit volume per unit time. The reaction rate (RR_k) of each of the reactions, as seen in Section 2.1.2.2, represents the rate of those reactions and therefore the rate at which each of the species, involved in that specific reaction k, change according to its stoichiometric coefficient ($\nu_{k,i}$). The stoichiometric coefficient ($\nu_{k,i}$) for a species i in each reaction k is taken from the reaction formulas provided, such as those seen in Table 2.3. As an example, take Reaction 2 ($k = 2$) in Table 2.3 where the product (P) represents carbon dioxide (CO_2) and water (H_2O):

$$X + 12.5O_2 \rightarrow 8CO_2 + 9H_2O \tag{3.50}$$

From this reaction the stoichiometric coefficients are:

$$\begin{aligned} \nu_{2,X} &= -1 \\ \nu_{2,O_2} &= -12.5 \\ \nu_{2,CO_2} &= 8 \\ \nu_{2,H_2O} &= 9 \end{aligned}$$

The stoichiometric coefficient ($\nu_{2,i}$) for the rest of the species in the system, not involved in Reaction 2 from Table 2.3, is zero. The rate of change of species i in the system (R_i) is therefore the summation given in Equation 3.51.

$$R_i = \sum_k (\nu_{k,i} RR_k) \tag{3.51}$$

The reaction rate (RR_k) of the reaction k is given by Equation 2.19 in Section 2.1.2.2 and is therefore dependent on the composition, temperature and pressure at that point in space and time.

3.4.1. Heat release rate

The rate of heat release due to chemical reaction is represented by the $\sum R_i h_i$ term in Equation 3.30 and is the only place in the PDEs where the molar enthalpy of species occurs in the calculations. It should be noted that this then incorporates the heat of reaction of all the reactions, where the heat of reaction ($\Delta h_{rxn,k,T}$) of a single reaction k at any temperature (T) is given by Equation 3.52 (Koretsky, 2004).

$$\Delta h_{rxn,k,T} = \sum_i \left(\nu_{k,i} h_{f,i(298\text{K})}\right) + \sum_i \left(\nu_{k,i} \int_{298}^{T} c_{p,i} dT\right) \tag{3.52}$$

The rate at which heat is released by all the reactions is given by Equation 3.53.

$$\begin{aligned} \textit{heat release rate} &= \sum_k (RR_k \Delta h_{rxn,k,T}) \\ &= \sum_k \left(RR_k \sum_i \left[\nu_{k,i} \left(h_{f,i(298\text{K})} + \int_{298}^{T} c_{p,i} dT\right)\right]\right) \end{aligned} \tag{3.53}$$

From the definition of molar enthalpy in Equation 3.16, the total heat release rate is written as Equation 3.54.

$$\begin{aligned} heat\ release\ rate &= \sum_k \left(RR_k \sum_i (\nu_{k,i} h_i) \right) \\ &= \sum_k \sum_i (RR_k \nu_{k,i} h_i) \\ &= \sum_i \left(h_i \sum_k (\nu_{k,i} RR_k) \right) \end{aligned} \tag{3.54}$$

Equation 3.51 defines R_i and is substituted into Equation 3.54 to give Equation 3.55.

$$heat\ release\ rate = \sum_i R_i h_i \tag{3.55}$$

Equation 3.55 therefore shows that the heat release rate term ($\sum R_i h_i$) in Equation 3.30 is equivalent to the total heat release rate calculated from the heats of reaction ($\Delta h_{rxn,k,T}$) of each reaction k and therefore holds.

3.4.2. Unimolecular reactions

The reaction rates specified by Equation 2.19 in Section 2.1.2.2, show that some reaction rates depend on the concentration [M], which in the case of the Schreiber model (Schreiber et al., 1994) represents the total concentration of species. This dependence is caused by unimolecular reactions where a molecule undergoes decomposition or isomerisation as shown by the unimolecular reactant-to-product representation in Reaction 3.56 (Law, 2006).

$$\mathrm{R} \rightarrow \mathrm{P} \tag{3.56}$$

However, in these reactions the reactant molecule requires sufficient energy, which is transfered to it in a collision with a third molecule, M. Therefore, Reaction 3.56 rather represents a series of reactions where the reactant (R) is activated to R* which then reacts to form the products as shown by Reaction 3.57.

$$\begin{aligned} R + M &\rightleftarrows R^* + M \\ R^* &\rightarrow P \end{aligned} \tag{3.57}$$

This then shows how the rate of the overall reaction (Reaction 3.56) is dependent on the concentration of a third molecule (M). The concentration of the third molecule might be represented by the total molar concentration or as a weighted linear combination of the concentrations of certain molecules. The weights in the linear combination of concentrations indicate the third body efficiency of each molecule, since different third molecules may have different effects on the reaction rate due to differences in the ability to activate the reactant molecule (Ashman and Haynes, 1998). Therefore, even though the third molecule is not seen in the overall reactions, it is included in the mechanism and therefore affects the reaction rate. In this study the different third body efficiencies are assumed to be equal and therefore the total concentration is taken as the concentration of the third molecule.

3.4.3. Implementation and validation of reaction kinetics

As discussed in Section 2.1.2.2, the reaction mechanism for combustion chemistry can be highly complex and requires thousands of species and reactions to give a detailed description of the combustion process. However, a very simple global reaction mechanism is employed in the current model in order to decrease computational expense and stiffness of the system. The Schreiber global model (Schreiber et al., 1994), discussed in Section 2.1.2.2, is a well established and simple model, which is able to predict the ignition delay times of different gasoline PRF mixtures with acceptable accuracy.

To validate the reaction kinetic scheme used in the current model, the ignition delay times of iso-octane are considered. This gives a good representation of the overall combustion kinetics at certain conditions and is easily compared with results from detailed chemical kinetic mechanisms. The ignition delay times were calculated using the current model with modifications to have no molecular transport or convective velocity. The initial conditions were given as constant across the spatial domain and represented the condition at which the ignition delay time is calculated.

A modification is made to the Schreiber global model (Schreiber et al., 1994), since the

run time required to solve one spherically propagating flame in the combustion bomb using the Schreiber global model, as it is, is unacceptably long. For this reason only two reactions, representing the high temperature combustion kinetics, are included. A two-step combustion mechanism to model the laminar flame speed of kerosene was developed by Franzelli et al. (2010) and it was reported that the model accurately produced the laminar flame speed of kerosene at different pressures, temperatures and equivalence ratios. This simplification greatly reduces the run time of the model, since it neglects the more complicated low temperature combustion chemistry of the Schreiber model, which includes a reversible reaction.

Reactions 1 and 2 from Table 2.3 of Section 2.1.2.2, as reported by Schreiber et al. (1994), are given here as Reactions 3.58 and 3.59 where the fuel (F) is replaced with iso-octane (C_8H_{18}) and the product (P) is replaced with carbon dioxide (CO_2) and water (H_2O).

$$C_8H_{18} \rightarrow X \tag{3.58}$$

$$X + 12.5O_2 \rightarrow 8CO_2 + 9H_2O \tag{3.59}$$

These reactions are then used to calculate the ignition delay times of a stoichiometric iso-octane and air mixture at different pressures and temperatures. Figure 3.5 shows a comparison between the ignition delay times calculated with the simplified Schreiber model and calculated with CHEMKIN (Kee et al., 2000) using the detailed chemical mechanism developed by Mehl et al. (2009) for iso-octane.

Figure 3.5 shows that merely omitting the low temperature combustion chemistry results in inaccurate ignition delay time sensitivity to pressure. The high temperature ignition delay times calculated at the reference pressure of 10 bar correlate well with the detailed kinetic model prediction. However, at 1 bar and 20 bar they are underpredicted and overpredicted respectively. To account for this, the pressure dependence parameter of the first reaction rate (RR_1) in Equation 2.19 was adjusted. Figure 3.6 shows the comparison of the ignition delay times calculated with the adjusted simplified combustion model and the detailed kinetic mechanism (Mehl et al., 2009).

The adjusted simplified Schreiber global model succeeds in producing accurate ignition delay times at high temperatures for a stoichiometric iso-octane and air mixture at different pressures, as shown in Figure 3.6. The pressure dependence parameter of the first

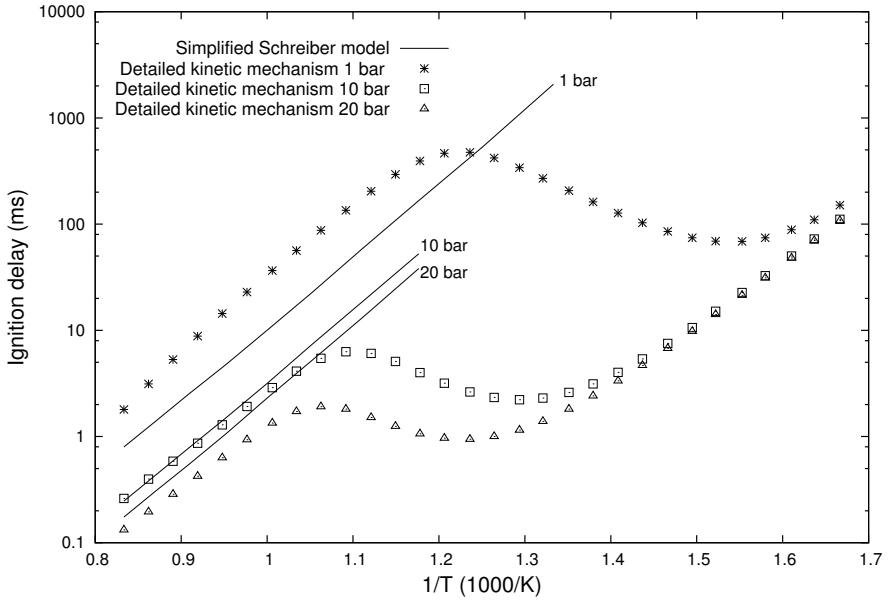

Figure 3.5.: Comparison of ignition delay times of stoichiometric iso-octane and air mixtures calculated from the simplified Schreiber global model and the detailed chemical kinetic mechanism of Mehl et al. (2009).

reaction rate in Equation 2.19 was adjusted from 0.5 to 1.0, which resulted in much better dependence of the ignition delay times on pressure. This correlation shows that the very simple kinetic mechanism employed in this model describes the overall reaction rate and energy release timing accurately at high temperatures. Therefore, assuming that most of the reaction takes place in the high temperature zone of the flame, the adjusted simplified Schreiber global model is sufficient for implementation in the flame speed model.

3.5. Molecular transport

When considering combustion modelling in terms of a propagating flame, it should be realised that this process is essentially dependent on the molecular transport of energy, species and momentum in the system. Therefore the inclusion of mathematical descriptions of the molecular transport properties of a mixture is required to model a propagating flame. The molecular transport of species, energy and momentum in a system are described by transport coefficients in the PDEs derived in Section 3.2. The species, energy and momentum fluxes are described by the diffusion coefficient, thermal conductivity and viscosity respectively.

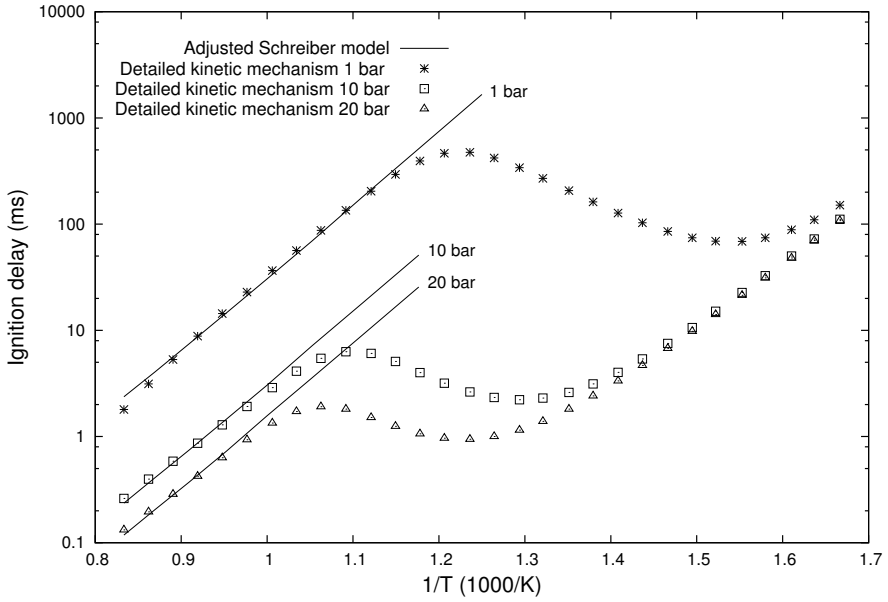

Figure 3.6.: Comparison of ignition delay times of stoichiometric iso-octane and air mixtures calculated from the adjusted simplified Schreiber global model and the detailed chemical kinetic mechanism of Mehl et al. (2009).

The diffusion of species in a mixture can resemble a rather complex mathematical problem, since the overall species flux must still adhere to the conservation of mass (Kee et al., 2003). However, in a simplified system, where the total concentration is constant and the diffusion of a dilute component i is regarded, the molar flux is given by Fick's law:

$$J_i^* = -D_i \frac{dC_i}{dr} \tag{3.60}$$

Here the diffusion coefficient (D_i) describes the linear relation between the molar flux $\left(J_i^*\right)$ and the spatial concentration gradient ($\frac{dC_i}{dr}$) of the solute species i. Note that a slightly different formulation for the molar diffusive flux $\left(J_i^*\right)$ is used in the model, where the total concentration does not remain constant. The thermal conductivity of a mixture represents a similar relation where the energy flux is given by:

$$q = -\lambda \frac{dT}{dr} \tag{3.61}$$

Here the thermal conductivity (λ) describes the linear relation between energy flux (q) and the spatial temperature gradient ($\frac{dT}{dr}$) of the mixture, which is also known as Fourier's

law of thermal conduction (Warnatz et al., 2001).

These relations show that the inclusion of molecular transport in the PDEs, derived from the conservation equations, is not a complex matter, provided the transport coefficients are known. However, the evaluation of the transport coefficients for mixtures can be computationally expensive, depending on the desired accuracy. Approximations for the transport coefficients of a mixture can be based on mixture averaging rules of the pure components, but this approach lacks accuracy. More rigorous multicomponent formulations exist to give accurate evaluations of the transport coefficients for a mixture. The methods followed to obtain molecular transport coefficients in this study are derived from specialised theory in statistical mechanics as well as molecular interactions and collisions (Kee et al., 2003).

The theory for determining the transport coefficients is based on the fundamental processes responsible for the observed phenomena. In the gas phase, these fundamental processes are collisions between molecules and therefore a theoretical description is required to produce a quantitative characterisation. The methods followed in this section to obtain a quantitative characterisation are taken from the textbook of Kee et al. (2003), where a more detailed discussion can be found. The methods for obtaining the collision integrals are supplied in Appendix B.1.

3.5.1. Thermal conductivity

The methods in this section for calculating the respective transport coefficients are based on the Chapman-Enskog theory. There are several options available for the evaluation of the coefficients. Calculating the thermal conductivity for the case of pure species can be used to estimate the thermal conductivity of a mixture by implementing mixture-averaged transport formulas. Although this option is computationally less expensive, it may lack required accuracy to model a specific system, in which case the more complex and computationally more expensive multicomponent evaluations or Maxwell-Stefan approach may be implemented.

3.5.1.1. Pure species and mixture-averaged thermal conductivity

The transport parameters for the species used in this work are given in Table B.2. The pure species thermal conductivity for single atoms is given by:

$$\lambda_k = \frac{5}{2} c_{v,trans} \left(\frac{5}{16} \frac{\sqrt{\pi m_k k_B T}}{\pi m_k \mathcal{A} \sigma_k^2 \Omega_{kk}^{(2,2)\bigstar}} \right) \tag{3.62}$$

In Equation 3.62, k_B is Boltzmann's constant, T is the temperature, m_k is the mass of the molecule, $\mathcal{A}$ is Avogadro's number, σ_k is the net collision diameter of species k and $\Omega_{kk}^{(2,2)\bigstar}$ is the collision integral obtained from Equation B.2 in Appendix B.1. The translational contribution to the heat capacity ($c_{v,trans}$) is sufficient for a single atom species, such as hydrogen atoms. However, for more complex molecules the formulation of Equation 3.63 is used (Kee et al., 2003).

$$\lambda_k = \left(\frac{5}{16} \frac{\sqrt{\pi m_k k_B T}}{\pi m_k \mathcal{A} \sigma_k^2 \Omega_{kk}^{(2,2)\bigstar}} \right) (f_{trans} c_{v,trans} + f_{rot} c_{v,rot} + f_{vib} c_{v,vib}) \tag{3.63}$$

where

$$f_{trans} = \frac{5}{2} \left(1 - \frac{2}{\pi} \frac{c_{v,rot}}{c_{v,trans}} \frac{A}{B} \right) \tag{3.64}$$

$$f_{rot} = \frac{\rho D_{kk}}{\omega_k} \left(1 + \frac{2}{\pi} \frac{A}{B} \right) \tag{3.65}$$

$$f_{vib} = \frac{\rho D_{kk}}{\omega_k} \tag{3.66}$$

$$A = \frac{5}{2} - \frac{\rho D_{kk}}{\omega_k} \tag{3.67}$$

$$B = Z_{rot} + \frac{2}{\pi} \left(\frac{5}{3} \frac{c_{v,rot}}{R} + \frac{\rho D_{kk}}{\omega_k} \right) \tag{3.68}$$

The values for the different contributions to the heat capacity ($c_{v,trans}$, $c_{v,rot}$, $c_{v,vib}$) are calculated using;

$$c_{v,trans} = \frac{3}{2} R \tag{3.69}$$

$$c_{v,rot} = R \quad (\textit{linear molecule}) \tag{3.70}$$

$$c_{v,rot} = \frac{3}{2} R \quad (\textit{nonlinear, polyatomic molecule}) \tag{3.71}$$

$$c_{v,vib} = c_v - c_{v,trans} - c_{v,rot} \tag{3.72}$$

where c_v is the molar constant volume heat capacity as calculated from the polynomial fits to temperature from Section 3.6. The density of the gas (ρ), consisting only of species k, is calculated from the ideal gas law as a function of the pressure (P), molar mass of species k (M_k) and temperature (T).

$$\rho = \frac{PM_k}{RT} \tag{3.73}$$

In the above equations ω_k represents the pure species viscosities and is given by Equation 3.74.

$$\omega_k = \frac{5}{16}\frac{\sqrt{\pi m_k k_B T}}{\pi \sigma_k^2 \Omega_{kk}^{(2,2)\star}} \tag{3.74}$$

The self-diffusion coefficient (D_{kk}) is given by Equation 3.75.

$$D_{kk} = \frac{3}{8}\frac{\sqrt{\pi k_B^3 T^3/m_k}}{P\pi \sigma_k^2 \Omega_{kk}^{(1,1)\star}} \tag{3.75}$$

The rotational relaxation collision number (Z_{rot}) is related to the number of collisions required to deactivate a rotationally excited molecule. This number is reported in literature for different species at 298 K. The temperature dependence of the rotational relaxation collision number is given by Equation 3.76.

$$Z_{rot}(T) = Z_{rot}(298\text{K})\frac{F(298\text{K})}{F(T)} \tag{3.76}$$

The temperature dependent function in Equation 3.76 is calculated using Equation 3.77, which includes the characteristic attractive well-depth (ε).

$$F(T) = 1 + \frac{\pi^{3/2}}{2}\left(\frac{\varepsilon/k_B}{T}\right)^{1/2} + \left(\frac{\pi^2}{4} + 2\right)\left(\frac{\varepsilon/k_B}{T}\right) + \pi^{3/2}\left(\frac{\varepsilon/k_B}{T}\right)^{3/2} \tag{3.77}$$

By following the method above, the pure species thermal conductivity coefficients are calculated. These coefficients are independent of pressure and can therefore be approximated by a polynomial fit of the logarithm of the temperature as shown in Equation 3.78. This ensures simpler formulations, especially in the case where derivatives of the thermal

conductivity coefficient are formulated.

$$In\,\lambda_k = \sum_{n=1}^{N} a_{n,k}\,(In\,T)^{n-1} \tag{3.78}$$

Using polynomials up to the third order should be sufficient to accurately fit the values calculated by the formulation in Equation 3.78 (Kee et al., 2003). This will reduce the computational expense by using the more complex method only once and fitting Equation 3.78 to the obtained values as an approximation used in the main model.

The pure species thermal conductivities are used in the mixture averaged approach to calculate the thermal conductivity of the mixture. The thermal conductivity (λ) is calculated as a function of the mole fractions (X_k) and pure species thermal conductivity (λ_k) using Equation 3.79 (Kee et al., 2003).

$$\lambda = \frac{1}{2}\left(\sum_{k=1}^{K} X_k\lambda_k + \left(\sum_{k=1}^{K}\frac{X_k}{\lambda_k}\right)^{-1}\right) \tag{3.79}$$

These formulations then present a much simpler, but less accurate method to obtain the thermal conductivity of a mixture, compared to the computationally expensive multicomponent evaluations. The accuracy of the mixture average approach for the specific application thereof should be evaluated to determine whether it is sufficiently rigorous, as is done in Section 3.5.1.2.

3.5.1.2. Validation of thermal conductivity

The thermal conductivity for pure species present in the system is calculated following the procedure proposed in Section 3.5.1.1 and therefore includes the polynomial fit of Equation 3.78 and excludes the mixture averaged approach of Equation 3.79. Figure 3.7 shows the comparison of the calculated thermal conductivity to values from literature for pure species over a range of temperatures at atmospheric pressure.

The calculation used in this model to obtain the thermal conductivity of pure species shows reasonable accuracy for oxygen, carbon dioxide and nitrogen, as seen in Figure 3.7. However, the thermal conductivity of water vapour is overpredicted by the model calculation. The cause of this overprediction is not known. However, it should be noted that water is the only molecule of the four that has a dipole moment. Although the methods

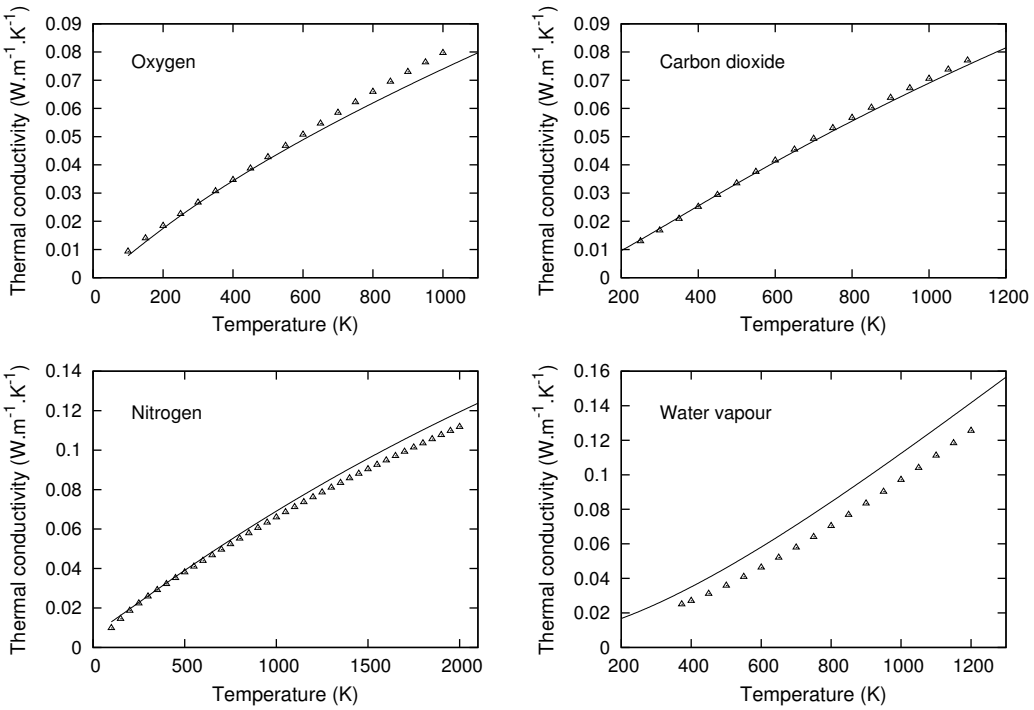

Figure 3.7.: Comparison of calculated values (lines) and literature values from NIST Chemistry WebBook (2011) (triangles) for the thermal conductivity of pure species at atmospheric pressure.

followed does take the polarity of the molecules into account, it is possible that an over adjustment is made. The accuracy of the mixture averaged approach for calculating the thermal conductivity of a mixture of gases (Equation 3.79) is evaluated by calculating the thermal conductivity of air as a mixture of oxygen and nitrogen and then comparing it to literature data as seen in Figure 3.8.

The comparison in Figure 3.8 shows that the mixture averaged approach gives accurate data for air thermal conductivity below 2 000 K. Above this temperature the model underpredicts the thermal conductivity. The lack of accuracy at higher temperatures is acceptable, since high temperature gradients are expected in a temperature range mostly below 2 000 K, which is where accurate thermal conductivity values are important.

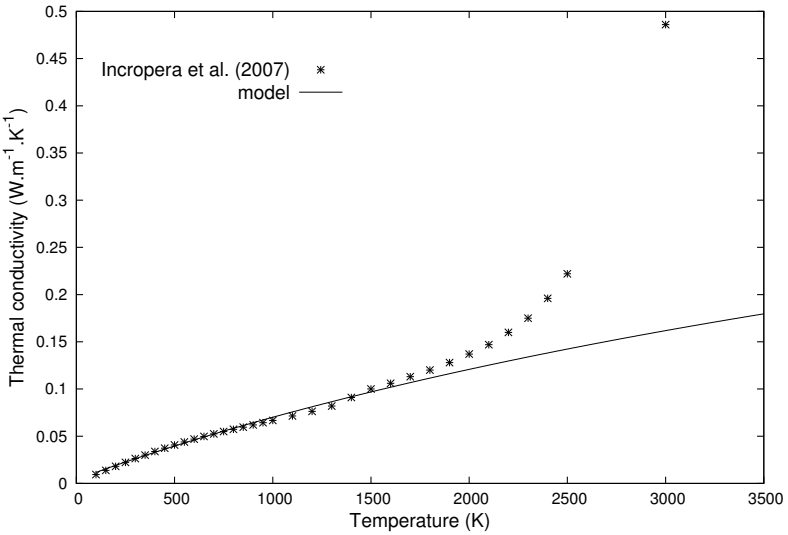

Figure 3.8.: Comparison of thermal conductivity of air for calculated values (lines) and literature data from Incropera et al. (2007) (stars).

3.5.2. Diffusion coefficients

The diffusion of the species close to the flame front of a propagating flame is of significant magnitude, since high concentration gradients are caused by consumption and production of species. The diffusion coefficients that govern the diffusion rates in this model are based on the collision principles discussed in Appendix B.1 and are calculated following the method of Section 3.5.2.1. The method is validated in Section 3.5.2.2 by comparison with diffusion coefficients from literature.

3.5.2.1. Binary diffusion coefficients and the mixture-averaged evaluation

In order to describe the diffusion of a species k in a mixture, the effect of every other species in the mixture on the diffusion velocity of species k should be taken into account. For this reason binary diffusion coefficients are used to describe the diffusion interaction of each possible pair of species in the mixture. The more complex multicomponent evaluation of the transport properties also produces binary diffusion coefficients referred to as the multicomponent diffusion coefficients. However, a first approximation of the binary diffusion coefficient of species j and k $\left(\mathcal{D}_{jk}\right)$ is given by Equation 3.80 (Kee et al., 2003).

$$\mathcal{D}_{jk} = \frac{3}{16} \frac{\sqrt{2\pi k_B^3 T^3 / m_{jk}}}{P\pi\sigma_{jk}^2 \Omega_{jk}^{(1,1)\bigstar}} \tag{3.80}$$

In Equation 3.80, P is the pressure of the mixture, $\Omega_{kk}^{(1,1)\bigstar}$ is the collision integral given by Equation B.1, σ_{jk} is the reduced net collision diameter given by Equation B.5 and m_{jk} is the reduced mass of the two molecules given by Equation 3.81.

$$m_{jk} = \frac{m_j m_k}{m_j + m_k} \tag{3.81}$$

The binary diffusion coefficients may also be approximated by a polynomial fit of the logarithm of the temperature, as suggested for the pure species thermal conductivities. Equation 3.82 is used for this approximation, which is similar to Equation 3.78, and ensures simpler formulations for calculating the diffusion coefficients.

$$ln\,\mathcal{D}_{jk} = \sum_{n=1}^{N} a_{n,jk} \left(ln\,T\right)^{n-1} \tag{3.82}$$

Since the binary diffusion coefficients are dependent on pressure, the polynomial in Equation 3.82 will produce the binary diffusion coefficient at a certain reference pressure, where the pressure used in Equation 3.80 when obtaining the fit is the reference pressure. Therefore, any binary diffusion coefficient calculated from the fit in Equation 3.82 should be adjusted for the pressure by simply multiplying with the reference pressure and dividing by the desired pressure (Kee et al., 2003).

These binary diffusion coefficients are implemented in the Stefan-Maxwell formulation to give an accurate approximation of the diffusion velocities or in the mixture-averaged evaluation, which gives a less accurate approximation of the diffusion velocities. The mixture-averaged evaluation results in a single diffusion coefficient $\left(D_{jm}\right)$ that describes the diffusion of the species j through the mixture (m). Assuming the isobaric and isothermal conditions for the Stefan-Maxwell formulation and that the diffusion velocities of all other species are equal, the diffusion coefficient of species j is approximated by Equation 3.83 (Kee et al., 2003).

$$D_{jm} = \frac{1 - X_j}{\sum_{j \neq k}^{K} X_k / \mathcal{D}_{jk}} \tag{3.83}$$

The molar species flux of species k $\left(J_k^*\right)$ is then given by Equation 3.84.

$$J_k^* = -D_{km} C_T \frac{dX_k}{dz} \tag{3.84}$$

This formulation is different from the one supplied in Equation 3.60, where the diffusion of species k in Equation 3.84 is driven by the mole fraction gradient of species k $\left(\frac{\partial X_k}{\partial z}\right)$. This ensures that the driving force for diffusion is independent of a total concentration gradient $\left(\sum \frac{\partial C_k}{\partial z}\right)$, as would be the case in the presence of a temperature gradient. Therefore, even if a total concentration gradient exists, the diffusion of any species k will only take place if there is a mole fraction gradient of species k.

Although several assumptions are made to calculate the diffusive species fluxes using the mixture-averaged evaluation, it is computationally much less expensive than the multi-component evaluation. For more accurate approximations of the diffusive fluxes the multicomponent evaluation or Maxwell-Stefan formulation can be implemented. The basic Maxwell-Stefan formulation is briefly discussed in Appendix B.2.

3.5.2.2. Validation of binary diffusion coefficients

The diffusion coefficients of species in the mixture are important transport parameters implemented in the model to describe the molecular transport of species. Although literature data for binary diffusion coefficients is limited, data for simple and well known mixtures, such as air, is available. In Table 3.3, comparisons between the computed values and literature data for certain binary diffusion coefficients are given.

Table 3.3.: Binary diffusion coefficient comparison

Species A	Species B	Temperature (K)	Source	Binary diffusion coefficient $\mathcal{D}_{AB}$ $\left(\frac{m^2}{s}\right)$	
				Literature	Calculated
carbon dioxide	nitrogen	293	Incropera et al. (2007)	0.16×10^{-4}	0.15×10^{-4}
carbon dioxide	oxygen	273	Incropera et al. (2007)	0.14×10^{-4}	0.13×10^{-4}
oxygen	nitrogen	273	Incropera et al. (2007)	0.18×10^{-4}	0.18×10^{-4}
oxygen	nitrogen	1 000	Yos et al. (1963)	1.64×10^{-4}	1.65×10^{-4}
oxygen	nitrogen	2 000	Yos et al. (1963)	5.14×10^{-4}	5.22×10^{-4}
octane	nitrogen	303	Galloway and Sage (1967)	7.10×10^{-6}	6.81×10^{-6}

Table 3.3 shows that the calculated values for binary diffusion coefficients compare well with the data available from literature. The inaccuracy seen in Table 3.3 is small and therefore insignificant, showing the reliability of the calculations used. The diffusion coef-

ficients for the mixture are calculated from Equation 3.83. However, since nitrogen makes up the larger fraction of the gases in the combustion system, these coefficients will relate closely to the binary diffusion coefficients with nitrogen.

This then shows that the calculated transport coefficients compare well with data from literature and therefore the methods followed in Section 3.5.2.1 are accurate at the conditions of the comparisons. Limited data for transport coefficients at a wider range of pressures and temperatures makes the validation of the methods used challenging. The mixture averaged approach, followed in the calculations of this study, is a significant compromise on computational expense, at the cost of accuracy, compared to a multicomponent evaluation. Yet it is considered as a good approximation in some cases (Kee et al., 2003, Holley et al., 2009) and some form of it has been implemented in several studies (Kumar et al., 2011, Holley et al., 2009, Kumar et al., 2007, Bradley et al., 1996).

3.6. Thermochemical properties

The equations for the conservation of energy require certain thermodynamic properties of the species in the system, such as the molar enthalpy (h_i) and constant pressure heat capacity ($c_{p,i}$). The molar enthalpy for species i is defined in Equation 3.16 in Section 3.2.2, which shows it as a function of the heat of formation of species i ($h_{f,i(298\mathrm{K})}$) and the integral of the constant pressure heat capacity ($c_{p,i}$) over a temperature (T) range. Therefore, if the constant pressure heat capacity as a function of temperature is known, the molar enthalpy can be calculated.

3.6.1. Heat capacity

The constant pressure heat capacity for many different components can be found in many sources, such as thermodynamic textbooks (Koretsky, 2004), where it is supplied in the form of a polynomial fit. CHEMKIN thermodynamic input requires five coefficients of a polynomial fit to describe the constant pressure heat capacity over a defined range of temperatures as shown in Equation 3.85 (Kee et al., 2000).

$$\frac{c_{p,i}}{R} = a_{1,i} + a_{2,i}T + a_{3,i}T^2 + a_{4,i}T^3 + a_{5,i}T^4 \tag{3.85}$$

In Equation 3.85, $a_{k,i}$ represents the polynomial coefficients that describe the molar con-

stant pressure heat capacity $(c_{p,i})$ as a function of the temperature (T), while R is the ideal gas constant. To increase the accuracy of these polynomial fits, the temperature range is divided into two parts, a lower and upper temperature range. These ranges can be specified according to the available data and in general the lower range is from 300 K to 1 000 K while the upper range is from 1 000 K to 3 000 K. Data below 300 K and above 3 000 K is not easily obtainable and therefore it is assumed that the model developed in this study is only valid in the temperature range of 300 K to 3 000 K. The data used in this study is refitted to the polynomial fits from the CHEMKIN input file for thermodynamic data supplied by Curran et al. (2002) with their mechanism for gasoline PRFs. The refitted polynomial coefficients are shown in Table 3.4.

Table 3.4.: Polynomial coefficients for Equation 3.85.

	a_1	a_2	a_3	a_4	a_5
300 K $\leq T \leq$ 1 000 K					
iso-octane	-3.91	1.06×10^{-1}	-6.15×10^{-5}	1.25×10^{-8}	1.67×10^{-12}
oxygen	3.08	1.66×10^{-3}	-6.63×10^{-7}	1.57×10^{-10}	-4.29×10^{-14}
carbon dioxide	2.26	9.51×10^{-3}	-7.32×10^{-6}	2.06×10^{-9}	1.03×10^{-14}
water	3.96	-2.69×10^{-4}	1.94×10^{-6}	-6.13×10^{-10}	-4.49×10^{-14}
nitrogen	3.51	-3.83×10^{-4}	1.25×10^{-6}	-4.37×10^{-10}	-1.37×10^{-14}
1 000 K $\leq T \leq$ 5 000 K					
iso-octane	23.30	3.64×10^{-2}	-2.95×10^{-6}	-2.35×10^{-9}	4.00×10^{-13}
oxygen	3.18	1.60×10^{-3}	-7.09×10^{-7}	1.37×10^{-10}	-9.60×10^{-15}
carbon dioxide	4.20	3.49×10^{-3}	-1.41×10^{-6}	2.55×10^{-10}	-1.71×10^{-14}
water	2.71	3.06×10^{-3}	-9.27×10^{-7}	1.36×10^{-10}	-7.96×10^{-15}
nitrogen	2.80	1.65×10^{-3}	-6.29×10^{-7}	1.09×10^{-10}	-7.07×10^{-15}

Table 3.4 gives the coefficients for polynomial fits of Equation 3.85 to produce the molar constant pressure heat capacity (c_p) of different species as a function of the temperature. Table 3.4 shows that the data is only available for certain temperature ranges; therefore the model is not applicable at temperatures outside the specified range. However, since this model employs a numerical solver, it is important to provide the model with values for c_p outside the temperature range to ensure the solver converges even when unrealistic temperatures are tried as possible solutions. Therefore the c_p at temperatures above the defined range is given the value of c_p at the upper limit of the range, and the c_p at temperatures below the defined range is given the value of c_p at the lower limit of the range. There is no data available for the constant pressure heat capacities of the intermediate representative species (X) and therefore it is assumed that it is equal to that of the fuel species in the system. This assumption is valid, since the intermediate is only

present in the system as very small molar fractions and therefore will not have a significant influence on the thermodynamic system.

3.6.2. Heat of formation

Another thermochemical property, required to calculate the molar enthalpies as defined by Equation 3.16, is the heat of formation $\left(h_{f,i(298\mathrm{K})}\right)$ of each species in the system at a reference temperature (298 K). The heats of formation are also available in many sources, such as textbooks, and can be derived from CHEMKIN thermodynamic input files. Table 3.5 shows the heat of formation and molar mass (M_i) for each species implemented in this study as taken from NIST WebBook (Afeefy et al., 2011), while those of the species representing the intermediates are derived according to the chemical reactions.

Table 3.5.: Heat of formation $\left(h_{f,i(298\mathrm{K})}\right)$ and molar mass (M_i) of all used species. (Afeefy et al., 2011)

	$M_i \left(\frac{\mathrm{kg}}{\mathrm{mol}}\right)$	$h_{f,i(298\mathrm{K})} \left(\frac{\mathrm{kJ}}{\mathrm{mol}}\right)$
iso-octane	114	-224.1
high temperature intermediate (X)	114	485.8
oxygen	32	0.0
carbon dioxide	44	-393.5
water	18	-241.8
nitrogen	28	0.0

The data supplied in Table 3.5, together with the constant pressure heat capacities (c_p) as functions of temperature then supplies all the required thermodynamic data. The molar masses from Table 3.5 are required in the PDE derived for the conservation of momentum (Equation 3.41). The molar mass of the intermediate representative species (X) is derived to ensure conservation of mass in the reactions from Table 2.3 in Section 2.1.2.2. The heat of formation for the intermediate representative species (X) is derived from the data for heat of reaction specified by Schreiber et al. (1994).

3.7. PDE solver

The solution of the mathematical system, derived in Section 3.2, requires a robust PDE solver capable of efficiently and accurately solving a system that contains steep gradients

in the flame zone, while the flame zone is progressing through the spatial domain. By including more nodes or mesh points for the numerical solver to solve, a more accurate solution of steep gradients is obtained. However, an increase in mesh points will increase the computational expense of the solver and render it slow and thus inefficient. Here, BACOL has an advantage in that it implements continuous spatial mesh adaptation techniques that automatically concentrate the mesh points in the areas of steep gradients (the flame zone in this case), while the rest of the spatial domain is sparsely populated with mesh points. Therefore, BACOL has both the advantage of accuracy and efficiency in that it can accurately solve steep gradients, but requires less mesh points.

3.7.1. Background on BACOL

Developed by Wang, Keast and Muir in 2004, BACOL is a PDE solver and is written in Fortran 77 (Wang et al., 2004a). The BACOL package is based on the method of lines and employs the collocation method with a B-spline basis for the spatial discretisation. In this case, the collocation method approximates the spatial solution in the subspace between any two consecutive mesh points at a certain time with a piecewise polynomial. This approximate solution is used to calculate a residual from the adapted PDEs and the solver then attempts to minimise the total residual by optimising the piecewise polynomials (Wang et al., 2004a).

The piecewise polynomial in each subspace is determined by B-spline curves, which are a general form of Bezier curves. These curves have the advantage of staying within the polygon determined by the approximated points and therefore no major deviation from the apparent trend is observed, as is sometimes the case for pure polynomial approximations. Another advantage is that, when one of the points that the B-splines are approximating changes, it has only a "local" effect on the curve and does not influence the complete approximation (Gerald and Wheatley, 2004). The degree of the piecewise B-spline curves is represented by a parameter ($kcol$) chosen by the user and determines the number of subintervals between two consecutive mesh points over which the B-splines are calculated.

The time integration in BACOL is achieved by employing a modification of the widely used initial value differential algebraic equation (DAE) solver, DASSL. The DASSL code is based on backward differentiation formula methods, which utilise an interpolation of a number of previous time steps to approximate the time derivative at the next time step. This well developed code also has step size and order selection strategies to minimise

the errors associated with the time integration (Brenan et al., 1989). The modifications made to DASSL, in order to solve a PDE system in BACOL, are discussed by Wang et al. (2004a).

As mentioned before, BACOL has the ability to continuously adapt the spatial mesh according to the solution behaviour in order to increase accuracy and efficiency. To achieve this, a second piecewise polynomial approximation of one order higher than the original is calculated and compared with the original approximation after each time step. The two solutions are compared by means of calculating a spatial error estimate given in Equation 3.86 (Wang et al., 2004a).

$$E_s = \sqrt{\int_0^1 \left(\frac{U_s(x,t) - \bar{U}_s(x,t)}{ATOL_s + RTOL_s |U_s(x,t)|} \right)^2 dx}, \quad s = 1, ..., NPDE \tag{3.86}$$

In Equation 3.86, E_s is the spatial error estimate for s-th component and $U_s(x,t)$ is the approximated solution of the s-th component, while $\bar{U}_s(x,t)$ is the second approximate solution of one order higher than that of $U_s(x,t)$. Further, $ATOL_s$ is the absolute tolerance and $RTOL_s$ is the relative tolerance, allowed for the s-th component of the PDEs, and are supplied by the user. $NPDE$ is the number of PDEs to be solved and is also supplied by the user. These spatial error estimates are calculated for each component in the set of PDEs and, if any of them is greater than or equal to one, re-meshing will be carried out (Wang et al., 2004a). Thus BACOL is capable of adapting both the spatial mesh and temporal step size to control and balance both the spatial and temporal error estimates.

3.7.2. Structure of BACOL

The BACOL package is downloaded as a set of Fortran 77 subroutines and functions of which the most important ones are the BACOL-subroutine and the VALUES-subroutine. These two subroutines call all other subroutines and functions in the package. BACOL makes use of the Basic Linear Algebra Subprograms (BLAS) library of which the required logarithms are either supplied with the BACOL package or can be called from the system libraries. The structure of the BACOL subroutines and functions are shown in Figure 3.9, showing that the BACOL- and VALUES-subroutines are called from the MAIN program which is generated by the user.

The MAIN program seen in Figure 3.9 is the driver program for BACOL and first calls the

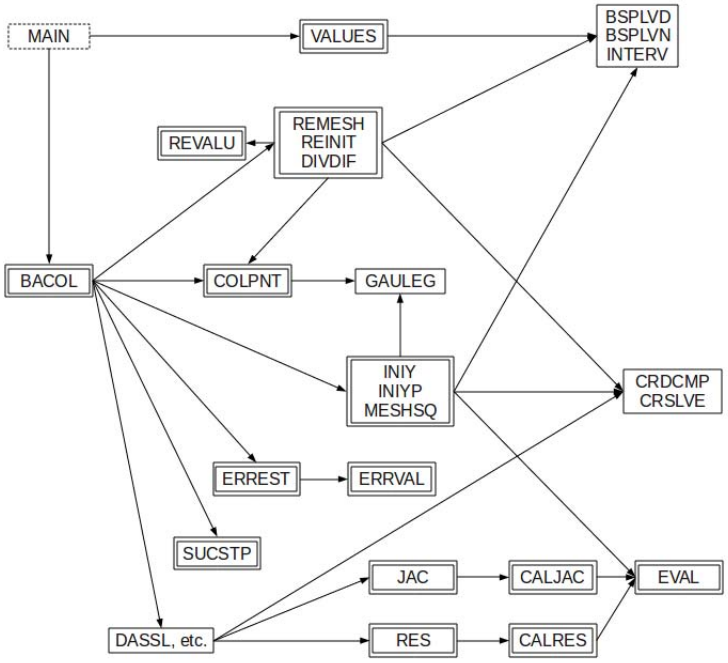

Figure 3.9.: Structural layout of the BACOL software package. (Wang et al., 2004a)

BACOL-subroutine, which carries out the numerical calculations to obtain a solution, after which the VALUES-subroutine is called to extract the solution at defined spatial points. The structure of the BACOL package is not of particular importance for the purpose of use. However, the driver program is of importance, since it supplies all the switches and parameters which specify the solution strategy to BACOL and extracts the calculated solution. BACOL requires certain subroutines that communicate the mathematical system to it, containing the PDEs derived in Section 3.2 and other required input. These subroutines are called by BACOL and should therefore adhere to a specified format. The user supplied subroutines called by BACOL are discussed in Section 3.8.3, while the driver program is discussed in detail in Section 3.8.1.

3.7.3. Example problem

One of the example problems used in a study by Wang et al. (2004c) to compare the performance of adaptive one dimensional parabolic PDE solvers, is considered in this section. The driver program for the problem is downloaded from (Wang et al., 2004b) and is compiled on a Linux system using GFortran. This section is included to show that

the compilation of the software is executed correctly and to demonstrate the basic usage of BACOL.

The mathematical system describes a reaction-diffusion-convection system for modelling a catalytic surface reaction. It consists of four PDEs to describe the time-space behaviour of four components ($NPDE = 4$). The four PDEs are given in input ready form in Equation 3.87.

$$\begin{aligned}
\frac{\partial\theta_1}{\partial t} &= -\frac{\partial\theta_1}{\partial x} + n\left(D_1\theta_3 - W_1\theta_1\left(1-\theta_3-\theta_4\right)\right) + \frac{1}{Pe_1}\frac{\partial^2\theta_1}{\partial r^2} \\
\frac{\partial\theta_2}{\partial t} &= -\frac{\partial\theta_2}{\partial x} + n\left(D_2\theta_4 - W_2\theta_2\left(1-\theta_3-\theta_4\right)\right) + \frac{1}{Pe_1}\frac{\partial^2\theta_2}{\partial r^2} \\
\frac{\partial\theta_3}{\partial t} &= W_1\theta_1\left(1-\theta_3-\theta_4\right) - D_1\theta_3 - G\theta_3\theta_4\left(1-\theta_3-\theta_4\right)^2 + \frac{1}{Pe_2}\frac{\partial^2\theta_3}{\partial r^2} \\
\frac{\partial\theta_4}{\partial t} &= W_2\theta_2\left(1-\theta_3-\theta_4\right) - D_2\theta_4 - G\theta_3\theta_4\left(1-\theta_3-\theta_4\right)^2 + \frac{1}{Pe_2}\frac{\partial^2\theta_4}{\partial r^2} \quad (3.87)
\end{aligned}$$

In Equation 3.87, θ_1 and θ_2 represent non-dimensionalised concentrations, while θ_3 and θ_4 represent coverage of adsorbed reactants on the catalytic wall. The time domain is represented by t, while the spatial domain is represented by x. Pe_1 and Pe_2 are Péclet numbers and D_1, D_2, G, W_1 and W_2 are Damkohler numbers. The PDEs supplied in Equation 3.87 are defined for $0 < x < 1$ and $t > 0$ and the initial conditions are given at $t = 0$ as:

$$\theta_1 = 2 - r,\ \ \theta_2 = r,\ \ \theta_3 = 0\ \ and\ \ \theta_4 = 0\ \ for\ \ 0 < x < 1.$$

The boundary conditions for this problem are given in Table 3.6.

Table 3.6.: Boundary conditions for the example problem at $t > 0$.

Component	$x = 0$	$x = 1$
θ_1	$\frac{\partial\theta_1}{\partial x} = -Pe_1\left(2 - r - \theta_1\right)$	$\frac{\partial\theta_1}{\partial x} = 0$
θ_2	$\frac{\partial\theta_2}{\partial x} = -Pe_1\left(r - \theta_2\right)$	$\frac{\partial\theta_2}{\partial x} = 0$
θ_3	$\frac{\partial\theta_3}{\partial x} = 0$	$\frac{\partial\theta_3}{\partial x} = 0$
θ_4	$\frac{\partial\theta_4}{\partial x} = 0$	$\frac{\partial\theta_4}{\partial x} = 0$

The values chosen for the parameters are: $W_1 = W_2 = 30$, $D_1 = 1.5$, $D_2 = 1.2$,

$G = 1000$, $r = 0.96$, $n = 1$ and $Pe_1 = Pe_2 = 100$. From this the mathematical system described above is solved with BACOL for $0 < t < 18$, extracting the solution every 0.05 time units. The results are shown in Figure 3.10.

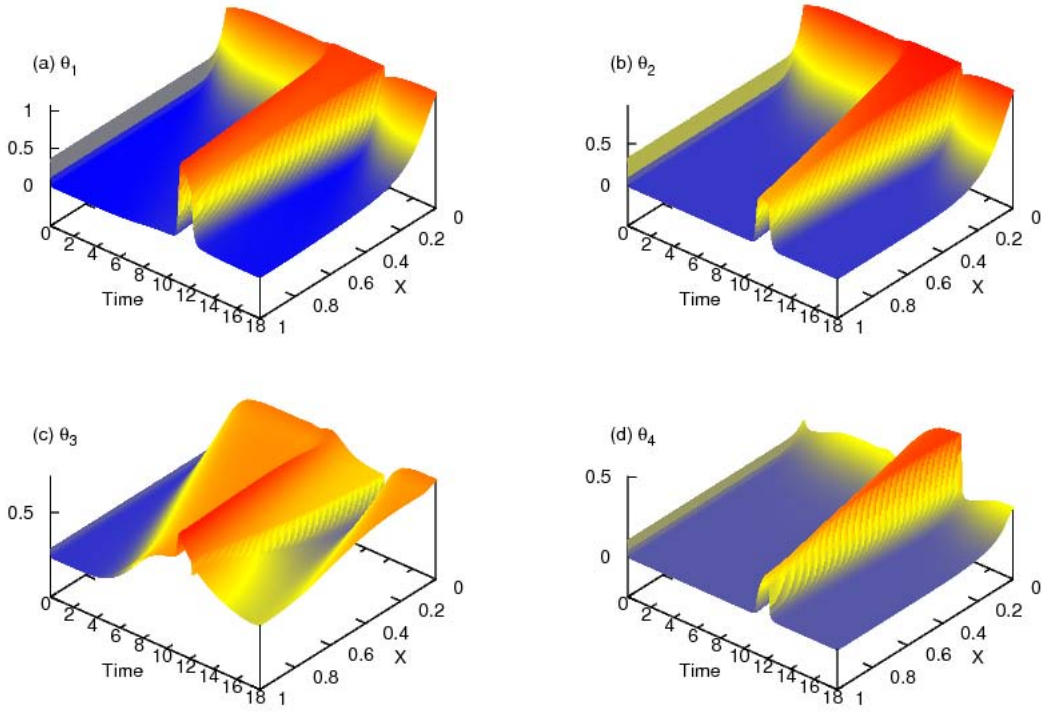

Figure 3.10.: Space time solution for each component in the example problem as calculated by BACOL.

Figure 3.10 shows that the solutions for all components are smooth over most of the temporal domain, with a wavefront with a steep gradient moving from $x = 0$ to $x = 1$ when $9 < t < 10$. This shows that BACOL treats a solution with wave-like behaviour efficiently due to its spatial adaptive techniques. The results shown in Figure 3.10 compare well with the high precision solution calculated by Wang et al. (2004c). This shows that the compilation of the downloaded BACOL software is carried out correctly and produces results consistent with those in literature.

3.8. Model description

The PDE solver, discussed in Section 3.7, requires certain mathematical instructions and several other inputs for switches and parameters. These instructions and inputs are provided in the form of coded functions and subroutines for this particular application. Since the mathematical system is complex, as seen in Section 3.2, numerous functions and routines are created to simplify the code of the subroutines that provide the mathematical instructions to BACOL. As mentioned in Section 3.7.2, the MAIN program is used to call the BACOL-subroutine and the VALUES-subroutine. The BACOL related subroutines make use of several user supplied subroutines as mathematical instructions, as is shown in Figure 3.11.

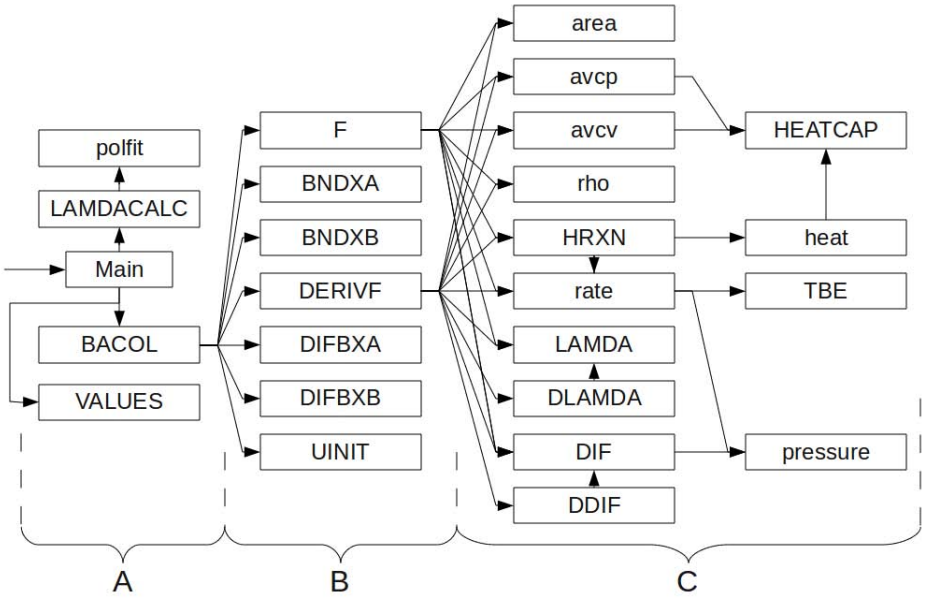

Figure 3.11.: Software layout showing user defined subroutines and functions.

The structure in Figure 3.11 shows how the subroutines and functions interact with each other, where every block represents either a subroutine or function. The main program fulfills an organising purpose to provide user options and to call and recall the necessary code. Figure 3.11 shows a section A which indicates the MAIN program and the subroutines called directly form it, LAMDACALC, BACOL and VALUES. The BACOL-subroutine is complex and make use of the interaction structure shown in Figure 3.9. From the BACOL and BACOL-related routines, the subroutines of section B in Figure 3.11 are called. These subroutines provide the mathematical system of Sections 3.2 and 3.3 to BACOL

and are therefore written in a format accessible to BACOL, but coded for this specific mathematical system. The functions of section C in Figure 3.11 are written to simplify the code of the subroutines in section B, by providing values and derivatives for properties required directly in the mathematical system of Section 3.2.

In this section, each of the functions and subroutines represented by a block in section A and B of Figure 3.11, will be briefly discussed with the MAIN program discussed in more detail. The property functions in section C of Figure 3.11 are discussed in Appendix C. Since BACOL is written in Fortran 77, all the instructions coded for this study are also written in Fortran for convenient interaction.

3.8.1. MAIN program

A commented code for the MAIN program is provided in Appendix D.1 and is divided into five different parts. In Part A, the MAIN program declares BACOL required variables and other variables to be used for initial input to BACOL, similar to the driver program for the example problem in Section 3.7.3. Then, in Part B, the MAIN program gives values for all the chemical property parameters of the species and reaction system parameters. These variables are declared in a module, chemphys.f (compiled as a module), to make these properties and parameters accessible by all functions and subroutines. Most of the parameters in the chemphys-module are set in Part B of the code at the start of the run and do not change. Certain constants, such as the ideal gas constant (R), are also declared in the chemphys module for convenient access.

Next the required information and options for BACOL are set in Part C of the code by giving the appropriate input values for several BACOL parameters. The initial conditions for the unburned gas are also set in Part C of the code, where the correct molar concentrations are calculated from the chosen temperature, pressure and fuel equivalence ratio. Once the initial unburned gas conditions are set, MAIN program calls the LAMDACALC-subroutine, coded for this study, as seen in Figure 3.11. The LAMDACALC-subroutine is discussed in Section 3.8.2. Important parameters that are given values in Part C are the tolerance specifiers: $ATOL$ and $RTOL$. The absolute tolerance allowed for each element in the solution is specified by $ATOL$ and, according to guidelines by Brenan et al. (1989), should be chosen to reflect the lowest number where the solution is still significant. The relative tolerance for each element is specified by $RTOL$ and, according to guidelines by Brenan et al. (1989), should be chosen to reflect the number of significant digits required

in each solution element. Since different elements in the solution requires different levels of accuracy, the tolerances for each element is specified individually for BACOL.

When all the required parameters are set, a loop is initiated in Part D of the MAIN program, which calls each step of BACOL. The iterations are set up to call BACOL, which calculates five steps in each loop, after which the solution at the last time step is obtained by calling the VALUES-subroutine. Once a solution is obtained, certain calculations are executed to obtain important values, including the flame front position and flame speed. The flame front position is estimated by linear interpolation to find the position of a certain temperature isotherm which lies in or near the flame. In this study, the 1 000 K isotherm was used to calculate the flame position. However, the position of any isotherm is easily calculated from the produced data.

The last part of the MAIN program, Part E, is still included in the main loop and is utilised to capture the calculated data into text files. The solution as produced by BACOL includes the species concentrations, convective velocity and temperature at each radial point at the current time step and is read into a text file to ensure data retrieval even if the MAIN program fails at some point. To reduce the size of data files, the solution data is only captured at set time intervals and not for each loop, since the time steps might become very small in which case a large amount of unimportant data is captured. Other important information, such as the number of spatial intervals used by BACOL, is also captured.

Once all the data from the current step is captured, the MAIN program tests for certain conditions, after which the next iteration of the main loop is called. The first test determines whether the spark or ignition event has been reached, in which case the tolerances are decreased to obtain more accurate solutions. Further, if the time step is too small the loop is broken and MAIN program ends, since solving the entire flame progression will take too long to complete. The last time segment, when the flame is very close to the combustion chamber wall, solves very slowly. Since little important data is generated in the last segment of the flame propagation, the main loop is broken when the flame front reaches a point 0.7 mm away from the chamber wall and the flame propagation model is considered to be complete.

This then describes the MAIN program and its control over the strategy used to model flame propagation. Section 3.8.3 will give a brief description of each of the subroutines included in section B of Figure 3.11.

3.8.2. Subroutine LAMDACALC

The LAMDACALC-subroutine is called before BACOL in the MAIN program, since its purpose is to simplify the calculations required to obtain the thermal conductivity and diffusion coefficients for each BACOL iteration. This is achieved by calculating the pure species thermal conductivities and binary diffusion coefficients over a range of temperatures following the procedures of Section 3.5. As suggested in Sections 3.5.1.1 and 3.5.2.1, the polynomials of Equations 3.78 and 3.82 are fitted to the calculated values with the POLFIT-subroutine, which is obtained from the SLATEC Common Mathematical Library (Shampine et al., 1974). Therefore the result of the LAMDACALC-subroutine is a set of parameters for Equations 3.78 and 3.82 describing the behaviour of the pure species thermal conductivities and binary diffusion coefficients over a set temperature range. The parameters for the polynomial fit are declared in the chemphys-module and are therefore accessible from any subroutine or function.

3.8.3. BACOL required subroutines

The mathematical system is supplied to the BACOL solver by means of the subroutines of section B in Figure 3.11, which are written in a format accessible to BACOL. The PDEs are supplied to BACOL in the form of Equations 3.11, 3.30 and 3.41, while the boundary conditions for the system are defined in the form of the equations in Table 3.2. Another important requirement of the BACOL solver is the Jacobian matrix, which is given to BACOL as the derivatives of the equations used to calculate PDEs and boundary conditions. Some of these subroutines make extensive use of functions from section C in Figure 3.11, while others are simpler and require fewer calculations. Each subroutine from section B in Figure 3.11 is discussed in this section.

3.8.3.1. Subroutine F

The PDEs resulting from the conservation of species, energy and momentum, Equations 3.11, 3.30 and 3.41[2], are calculated in the F-subroutine. The commented code for this subroutine is given in Appendix D.2. BACOL passes an array containing the solution or possible solution (U), which contains the concentration of each species, convective velocity and temperature, at a certain point in time (T) and space (X) to the F-subroutine.

[2]For a spherical system these are Equations 3.45, 3.46 and 3.47.

Therefore the array (U) has a dimension of the number of PDEs which is solved, indicated by the variable *NPDE* in the code. From this, the result of Equation 3.11 for each species and also Equations 3.30 and 3.41 are calculated. The structure shown in Figure 3.11 is utilised in order to simplify the calculation of these equations by calculating different parts of it in different functions. The layout showing which function calculates which part of the equations is given in Figure 3.12.

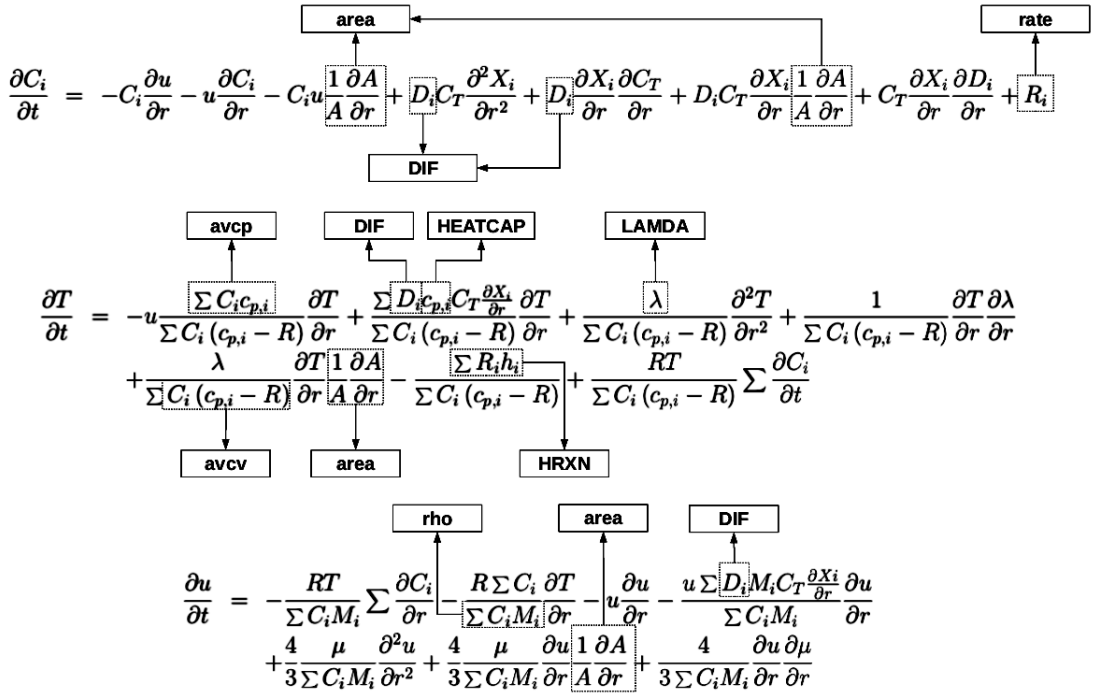

Figure 3.12.: Functions used in the F-subroutine

Figure 3.12 shows that certain properties in Equations 3.11, 3.30 and 3.41 are calculated by functions, which are called from the F-subroutine. Since each of these properties are obtained through extended calculations, the code is simplified significantly by utilising functions to calculate them. Note that Figure 3.12 does not show every property in the equations that is calculated by calling a function, but rather which properties are calculated with functions. For example the density property ($\sum C_i M_i$) recurs several times in Equation 3.41, but it is only indicated once in Figure 3.12 that the rho-function is used to calculate it.

Some summation calculations are also performed in the F-subroutine, such as the summation required to calculate the $\frac{\partial \lambda}{\partial r}$ term from Equation 3.31, in order to simplify the code. The output of the F-subroutine is the FVAL array that contains *NPDE* elements

calculated from Equation 3.11 for each species and also Equations 3.30 and 3.41. For convenience, the Equations 3.11, 3.30 and 3.41 will be referred to as the F-equations for the rest of this chapter. The functions called in the F-subroutine, included in section C in Figure 3.11, are discussed briefly in Appendix C.

3.8.3.2. Subroutines BNDXA and BNDXB

BACOL also requires boundary conditions for the mathematical system, which in this case represent the conditions at the centre of the spherical combustion chamber (BNDXA) and at the chamber wall (BNDXB). The boundary condition for each species, the temperature and convective velocity are mathematically described by the equations in Table 3.2. This mathematical description is used to calculate the values for the BVAL array with $NPDE$ elements in both the BNDXA- and BNDXB-subroutines. As noted in Section 3.3, the boundary conditions are solved when each of the values in the BVAL array is zero.

The time of the spark event is determined by t_{spark} in Equation 3.49 and is set to 10 ms. The spark rate (SR) in Equation 3.49 is taken as 3 000, which gives a relatively fast spark event of approximately 2 ms. The spark rate has a distinguishable effect on the flame propagation in the first 5 mm of the flame motion, but this effect is not investigated in this study. For this reason, a high spark rate is chosen to minimise the influence of the spark energy on the initial flame propagation.

3.8.3.3. Subroutine DERIVF

Once the F-equations and the boundary conditions are supplied to BACOL, the mathematical system is completely described. However, further mathematical input is required to solve the system. The Jacobian matrix is calculated by BACOL from user supplied subroutines where the derivatives of all the equations used in the F-, BNDXA- and BNDXB-subroutines are calculated. The commented code for this subroutine is given in Appendix D.3. In this study, the DERIVF-subroutine supplies the analytical derivatives of the F-equations (Equations 3.11, 3.30 and 3.41), making it the most complicated piece of code written for this study. Each of these equations is differentiated with respect to each of the solution variables, which are the species concentrations, convective velocity and temperature, to populate the DFDU array. The DERIVF-subroutine also requires the derivative of each F-equation with respect to the first and second order spatial derivative of each solution variable, for instance $\frac{\partial T}{\partial r}$ and $\frac{\partial^2 T}{\partial r^2}$. The results of the differentiations

with respect to the first order spatial derivatives are captured in the DFDUX array, while the results of the differentiations with respect to the second order spatial derivatives are captured in the DFDUXX array.

These analytical differentiations also make use of the functions shown in section C of Figure 3.11 and it also requires the derivatives of these functions. For this reason, each of these functions is written so as to also calculate the analytical differentiation of the function to any of the solution variables, if requested. Sections 3.2, 3.4, 3.5 and 3.6 show that all the functions used in the F-equations, as shown in Figure 3.12, are functions of the solution variables only and not their spatial derivatives. However, the summations of Equations 3.12 and 3.31 becomes very complex if an analytical differentiation is attempted. Therefore the second order derivatives of the thermal conductivity (λ) and diffusion coefficients (D_i) are estimated numerically in the DLAMDA-subroutine and DDIF-subroutine respectively. Several other summations are carried out in the DERIVF-subroutine to calculate the many summations in the F-equations.

The approach of making use of analytical differentiation, and therefore an analytical Jacobian matrix, results in very complex code for the DERIVF-subroutine with numerous opportunities for error. This subroutine is therefore validated graphically to ensure that the derived gradients followed the slope of the functions over changing solution variables. Given the amount of time spent on developing and debugging this subroutine, it is used with confidence in this model.

3.8.3.4. Subroutine DIFBXA and DIFBXB

The same differentiations required for the F-equations in the DERIVF-subroutine are also required for the boundary conditions in the DIFBXA- and DIFBXB-subroutines. The equations of Table 3.2 are differentiated with respect to the solution variables as well as the first and second order spatial derivatives of the solution variables. Similar to the DERIVF-subroutine, here the DBDU, DBDUX and DBDUXX arrays are used to capture these derivatives. These subroutines also require the differentiation of the equations in Table 3.2 with respect to time, which is captured in the DBDT array. The differentiations of the boundary conditions at the centre of the chamber are calculated in the DIFBXA-subroutine, while those at the chamber wall are calculated in the DIFBXB-subroutine. Due to the simplicity of the boundary conditions for this system, the DIFBXA- and DIFBXB-subroutines are less complicated.

3.8.3.5. Subroutine UINIT

The initial conditions over the entire spatial domain are set in the UINIT-subroutine, where any initial species concentrations, velocity or temperature profiles can be supplied. Since the ignition event is introduced by the boundary condition at the centre of the combustion chamber in this study, the initial conditions over the entire spatial domain is the same, a homogeneous mixture. Section 3.3 describes the initial conditions specified in this study. The initial conditions are specified in the MAIN program in the *start* array, which is declared in the chemphys.f module and is therefore accessible by the UINIT-subroutine. The initial conditions supplied to BACOL then set the conditions at which the flame propagation is modelled, such as the fuel equivalence ratio, initial pressure and initial temperature.

3.8.4. Property functions

In Section 3.8.3.3, it is mentioned that some subroutines become very complicated when input for the BACOL solver is calculated. The functions in section C of Figure 3.11 each calculate a certain property of the mixture from the solution variables, in order to simplify and organise the code better. The solution variables are passed to these functions in the solution array, or U array. Each of these functions does not only calculate the specific property, but also calculates the derivative of the property with respect to any of the solution variables. This in itself can render some of the functions to be more complex and therefore validation of the results of the functions is important. Each function in section C of Figure 3.11 is discussed in Appendix C.

All these subroutines and functions then supply all required mathematical descriptions to the BACOL related subroutines in order to solve the system for each consecutive time step. This then concludes the discussion of the code implemented in this study. The results provided in Chapter 4 for a spherical propagating flame is generated by numerical integration of the PDEs from Section 3.2 using the code described in this section.

3.9. Conditions investigated

The aim of this work is to provide a model capable of describing the outward propagation of a spherical flame with reasonable accuracy and to gather some insights into the sensitivity

of the flame characteristics to certain fuel properties. The conditions investigated in this study are chosen for the purpose of comparison with experimental data from previous studies and are used as base case for sensitivity analyses. Experimental data for iso-octane and air flames in a constant volume combustion bomb was generated in the study of Yates et al. (2012). This particular combustion bomb has a spherical combustion chamber with an inside diameter of 100 mm and is equipped with only a pressure transducer to capture the flame propagation data. In another study by Bradley et al. (1998), experimental data for flame speed of iso-octane and air was obtained from a constant volume combustion bomb with an inside diameter of 380 mm with optical access.

The model developed in this study is used to simulate these runs and compare the results to that of the experimental runs. This study will focus on the experimental runs of iso-octane and air at 370 K and 1 bar, with all the conditions listed in Table 3.7.

Table 3.7.: Conditions modelled in this study

fuel	iso-octane
oxidiser	air
initial temperature	370 K
initial pressure	1 bar
fuel equivalence ratios	0.8, 0.9, 1.0, 1.1 and 1.2
combustion chamber radius	50 mm and 190 mm

The conditions in Table 3.7 then serve as the base case for the sensitivity analyses, where the sensitivities of the laminar flame speed and Markstein length to oxygen, intermediate and fuel diffusion as well as the thermal conductivity and reaction kinetics are investigated. Therefore, to meet the research objectives, the model is used for the following:

1. Validation against the raw flame speed data of experimental studies.
2. Derivation of the laminar flame speed and Markstein length from the model results.
3. Description of the sensitivity of the laminar flame speed and Markstein length to different combustion mixture properties.

By following the solution strategy of Section 3.8 to solve the mathematical system of Section 3.2, the spherical flame propagation of iso-octane and air mixtures is modelled to produce the results given in Chapter 4.

4. Results and Discussion

The model developed in this study is based on conservation equations, which incorporate many fundamental properties of the gas mixture, such as the reaction rates and thermal conductivity. The conservation equations are derived into a set of partial differential equations, which captures the change in species concentrations, convective velocity and temperature. By assuming symmetry of the space around the centre of the spherical flame, the set of partial differential equations is reduced to one-dimensional space. To numerically solve this set of partial differential equations, the BACOL solver is employed, which is capable of producing meaningful results, but requires long periods of time to solve one flame condition[1]. It is found that the simple two-step high temperature part of the reaction mechanism from Schreiber et al. (1994) greatly reduced the time required to solve and is sufficient to describe all the studied flame behaviours in this work.

The model was implemented to simulate the experiments carried out for iso-octane and air mixtures in a constant volume combustion bomb in the studies of Yates et al. (2012) and Bradley et al. (1998). The results from the model are analysed to produce meaningful quantities, the laminar flame speed (S_L) and the burned gas Markstein length (L_b), at the simulated conditions. By comparing the simulated results and derived combustion characteristics with that from experimental work, the capability of the model to describe the propagation of a spherical flame in a closed combustion chamber will be shown.

The conditions simulated were for iso-octane and air with initial temperature of 370 K and initial pressure of 1 bar as specified in Table 3.7. These conditions are chosen since they were easily comparable to experimental results from the studies of Yates et al. (2012) and Bradley et al. (1998) and therefore it is possible to determine a level of accuracy for these cases. The conditions for the study of Yates et al. (2012) are modelled first to show the pressure increase for the smaller combustion chamber (10 mm diameter). It is found that further improvement of the model is required to achieve an acceptable accuracy.

[1] To model a flame that progresses through a closed spherical space with a 50 mm radius takes approximately 44 hours per CPU on a 3.3 GHz Core i7 machine.

The comparison between the simulated results and the experimental results is shown and discussed in Sections 4.2 and 4.3. The difference between a smaller and larger combustion chamber is modelled and discussed in Section 4.4. Once confidence in the ability of the model to predict flame characteristics is established in Section 4.5, the sensitivities of laminar flame speed and burned gas Markstein length to fundamental properties of the system are tested. The results for the sensitivity analyses are shown in Section 4.6. The resulting sensitivities are discussed and the concentration profiles of the species as well as the temperature profile over the flame front at different conditions are used as explanations for some of the observed trends.

4.1. Basic model results

The model developed for this study produces a pressure trace as a function of time since it allows for the compression of the entire combustion chamber through the inclusion of a momentum balance. The ability of the model to describe the pressure increase makes it a valuable tool, since many propagating flame models assume constant pressure (Bradley et al., 1996, Margolis, 1978). If it can be shown that the model gives a representative description of flame behaviour in the constant volume combustion bomb, then useful studies on the mechanisms that govern the observed phenomena can be done.

The raw model results are text files containing a matrix of values for each time step, while each matrix contains the profiles of the solution variables across the spacial domain or the radius of the combustion chamber in this case. From the solution variable profiles[2] many other properties, such as pressure, at any time step and radial position can be calculated. Since the combustion chamber is filled with gas, the pressure will equalise very fast. Therefore one of the objectives listed for the model in Section 1.3 is to describe the pressure increase in the combustion chamber while the pressure remains spatially uniform. This is not a trivial task, since the total concentration of the gas will vary along the radius of the combustion chamber due to temperature differences. For this reason the momentum balance is included to generate a convective velocity (u) which moves the gas from high pressure to lower pressure, while maintaining the conservation species.

The radial pressure profiles are calculated from the modelled raw data for a combustion chamber with an inside diameter of 100 mm containing an iso-octane and air mixture with initial temperature of 370 K and an initial pressure of 1 bar. For the interpretation

[2]Species concentrations, convective velocity and temperature profiles

of the model results, the flame position is taken as the position of the 1 000 K isotherm on the temperature profile across the radius of the combustion chamber. The pressure profiles are shown in Figure 4.1, for the specific times where the flame positions are 2 mm, 30 mm, 40 mm, 46 mm, 48 mm and 49 mm (as indicated by the circles).

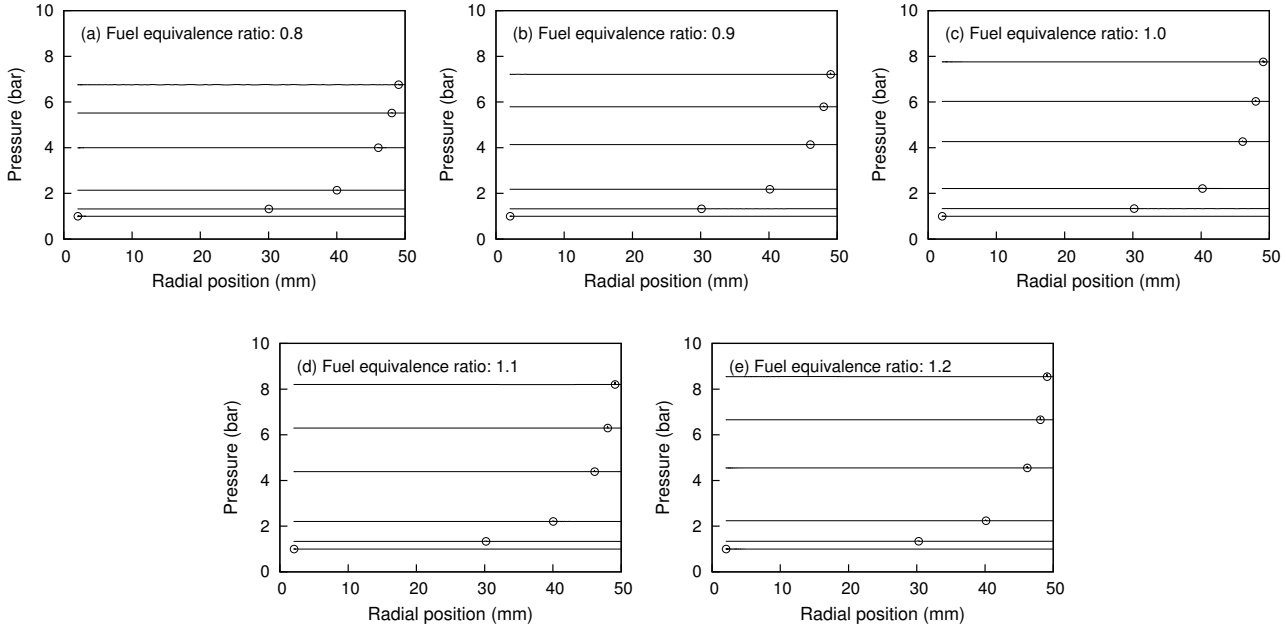

Figure 4.1.: Model-predicted radial pressure profiles across a 100 mm inside diameter combustion chamber at different flame positions (indicated by circles) for iso-octane and air mixtures at initial temperature of 370 K and initial pressure of 1 bar.

Figure 4.1 shows that the calculated pressures are uniform across the radius or spatial domain, even though the pressure increases over time. The scale used in Figure 4.1 is too large to show the small disturbances in the seemingly uniform pressure profiles. The standard deviation of the radial pressures from the spatial average at each flame position and fuel equivalence ratio in Figure 4.1 is given in Table 4.1.

The standard deviations given in Table 4.1 are much smaller than the corresponding average pressures. The small deviations occur around the model boundaries (centre and wall of combustion chamber) as well as at the flame front position. However, a largest difference of 2% is calculated between the radial pressure and the average spatial pressure for all the time steps and the fuel equivalence ratios. This supports the notion that the pressure across the radius of the combustion chamber remains uniform. This also shows

Table 4.1.: Average spatial pressures and the standard deviation from the averages for the different fuel equivalence ratios and flame positions in Figure 4.1.

	Average spatial pressure bar					Standard deviation $\times 10^{-4}$ bar				
Fuel equivalence ratio	0.8	0.9	1.0	1.1	1.2	0.8	0.9	1.0	1.1	1.2
Radial flame position										
2 mm	1.0	1.0	1.0	1.0	1.0	5.1	2.0	2.2	1.8	6.5
30 mm	1.3	1.3	1.3	1.3	1.3	2.3	6.9	7.0	8.5	11.0
40 mm	2.1	2.2	2.2	2.2	2.2	3.4	6.4	9.0	13.4	17.0
46 mm	4.0	4.1	4.3	4.4	4.5	5.0	8.8	14.2	18.8	25.7
48 mm	5.5	5.8	6.0	6.3	6.7	6.3	10.8	19.1	23.5	31.2
49 mm	6.8	7.2	7.8	8.2	8.5	50.9	13.1	18.2	32.2	34.7

the functionality of including the momentum balance, which provides the mechanism to increase the pressure over time while maintaining a uniform pressure over the spatial domain.

Once the position of the flame front for every time step is determined, the propagation speed or flame speed is calculated as the numerical derivative to time. Although BACOL determines the size of the time steps, the data at every 0.1 ms interval are used to ensure more representative numerical derivatives by providing an average flame speed for any specific time step. The flame positions calculated from the model data, together with the pressure, for a spherical combustion chamber with an inside diameter of 100 mm containing an iso-octane and air mixture with initial temperature of 370 K and an initial pressure of 1 bar, are given in Figure 4.2.

Figure 4.2 (a-e) shows the flame position, derived from the model data, versus time as the flame propagates through the combustion chamber. The flame position for this model starts at 2 mm, as seen in Figure 4.2, since that is the boundary condition specified to the model as discussed in Section 3.3. The time scale on the x-axis in Figure 4.2 (a-e) shows that the modelled flame for the fuel rich mixtures propagates faster than the fuel lean mixtures. Although the flame position as a function of time generally follows a similar trend, subtle differences in the flame propagation over time for the different fuel equivalence ratios are visible in Figure 4.2 (a-e), especially in the initial stages of flame propagation. Figure 4.2 (f) shows the pressure versus flame position for the studied fuel equivalence ratios, where the trends follow each other very closely. The small deviations of the pressures from each other in Figure 4.2 (f) are contributed to the different maximum

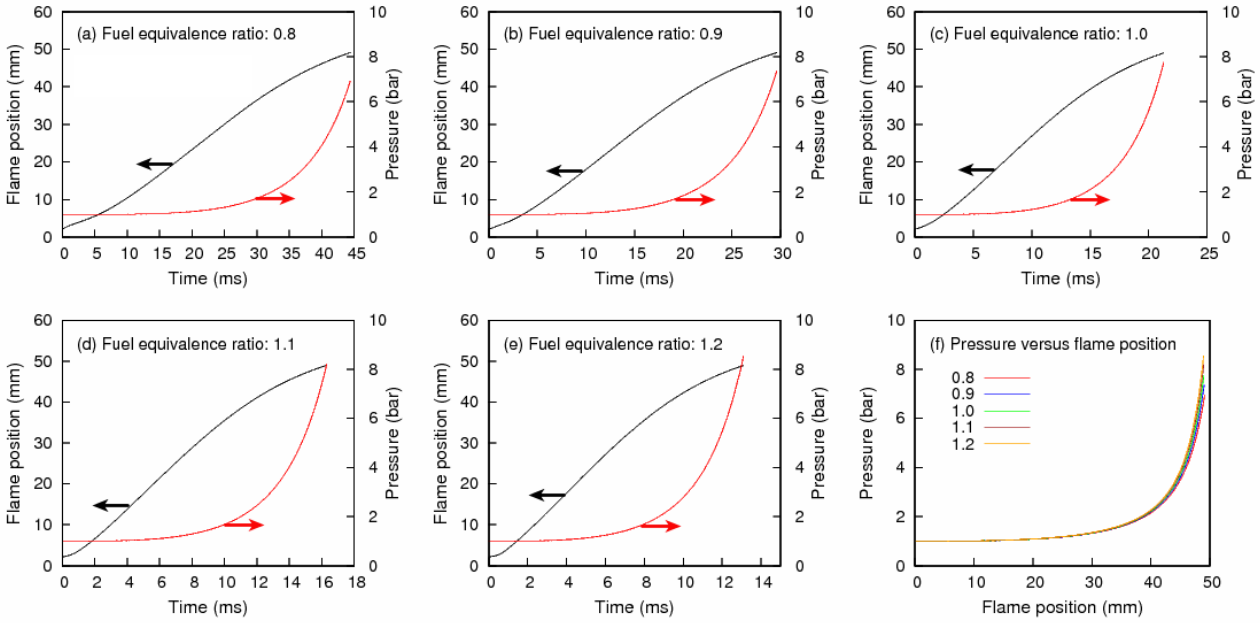

Figure 4.2.: Model-predicted flame position and pressure trace for a combustion bomb with iso-octane and air at an initial temperature of 370 K and initial pressure of 1 bar.

pressures reached for different fuel equivalence ratios as shown in Figure 4.2 (a-e). At the point in time where the flame has reached a radial position of 25 mm and is halfway through the radius, the pressure has only increased by approximately 18%.

From the trends shown in Figure 4.2, the flame speeds and flame stretch rates are readily obtained and used to derive flame characteristics such as the laminar flame speed and Markstein lengths. Therefore the model succeeded in producing data for a propagating spherical flame through a constant volume combustion chamber, including the pressure increase as a result of the combustion. The flame behaviour and characteristics are compared to experimental data in the following section to investigate the accuracy of the model.

4.2. Comparison with experimental results

The experiments from the study of Yates et al. (2012) were done in a combustion bomb with an inner diameter of 100 mm and the pressure inside the chamber was measured with a pressure transducer. Therefore only the pressure rise over time is available for these experiments and further analysis of the experimental data is required in order to obtain

meaningful flame speed data. As a first approach, the pressure trace produced by the model is compared to the pressure trace measured directly from the experiments in the work of Yates et al. (2012). Figure 4.3 shows the individual comparisons of the pressure trace for the experiments and the simulated data for the base case, which is iso-octane and air combustion with an initial temperature of 370 K and initial pressure of 1 bar.

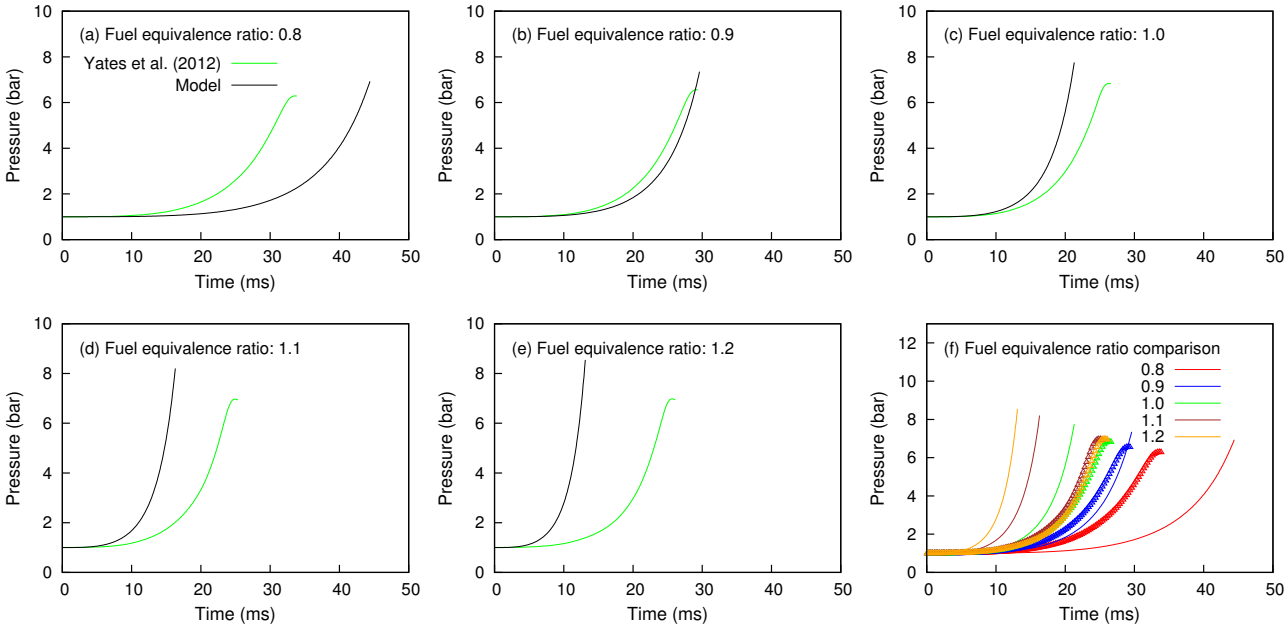

Figure 4.3.: Comparison between experimental pressure trace data from Yates et al. (2012) and the model-predicted pressure trace data for combustion bomb experiments with iso-octane and air at an initial temperature of 370 K and initial pressure of 1 bar.

The pressure traces in Figure 4.3 show the expected increase in pressure in the combustion chamber as the spherical flame front propagates through the chamber after the gas mixture is ignited. The experimental data in Figure 4.3 shows that the pressure rises from 1 bar to approximately 7 bar in the chamber over a period of approximately 30 milliseconds. The pressure rises predicted by the model show slightly higher final pressures and the pressure rise does not compare well with the experimental data. For the fuel lean mixtures, Figure 4.3 (a) shows that the pressure rise calculated by the model is too slow, while for the fuel rich mixtures, Figure 4.3 (c), (d) and (e) shows that the calculated pressure rise is too fast. Figure 4.3 (b) show a good comparison between the calculated pressure rise and the experimental pressure rise. However, Figure 4.3 (f) shows that the

trend of pressure rise calculated by the model for different fuel equivalence ratios, does not agree with that from the experimental data. Here the experimental pressure rise for the fuel equivalence ratios of 1.0, 1.1 and 1.2 are similar, while the modelled flame shows faster pressure rise for higher fuel equivalence ratios. This indicates that the flame speeds predicted by the model will not compare well with the flame speeds calculated from the experimental pressure trace data.

To calculate the flame position in the combustion chamber from the experimental data, Equation 2.30 in Section 2.3.3.1 of Chapter 2 is employed. Once the flame position is calculated for the experimental data of Yates et al. (2012), the flame speed at any point can be calculated either numerically from the calculated flame positions or by calculating the derivative of Equation 2.30 with respect to time. From the model-produced flame position data in Figure 4.2, the flame speeds are calculated and presented versus the flame position in Figure 4.4. The experimental flame speed data from Yates et al. (2012) and Bradley et al. (1998) is also plotted in Figure 4.4, in order to compare how the flame speed behaves at different stages of the propagation.

The flame speed data given in Figure 4.4 shows several of the expected behaviours of an outwardly propagating flame in a closed combustion chamber. The increasing flame speed after ignition is well presented by the experimental data from Bradley et al. (1998), while the decreasing flame speed at larger flame radii shown by the data of Yates et al. (2012) is typical where an increase in pressure occurs. The model-produced flame speeds in Figure 4.4 show most of the behaviours of the experimental data, but lack accuracy. A discussion of each of the identified behaviours in Figure 4.4 as well as the ability of the model to describe them will follow.

The experimental data from Bradley et al. (1998) for the flame speeds shown in Figure 4.4 is obtained from a larger combustion bomb (380 mm diameter), but only the flame speeds for the first 50 mm of the flame propagation is shown. This data is not obtained from pressure traces, but from optical access to the combustion chamber. This makes accurate flame position measurements possible at the initial stages of flame propagation, where pressure rises are undetectable. In Figure 4.4 (a), (c), (d) and (e), a small decrease in the experimental flame speeds from Bradley et al. (1998) is shown at the initial stage of the flame, which is said to be caused by the ignition energy. When the ignition energy is just above the minimum required, the ignition causes a higher flame speed, after which the flame speed decreases rapidly. In the work of Bradley et al. (1996) it was shown for a methane and air flame that the flame speed is unaffected by the ignition energy at a

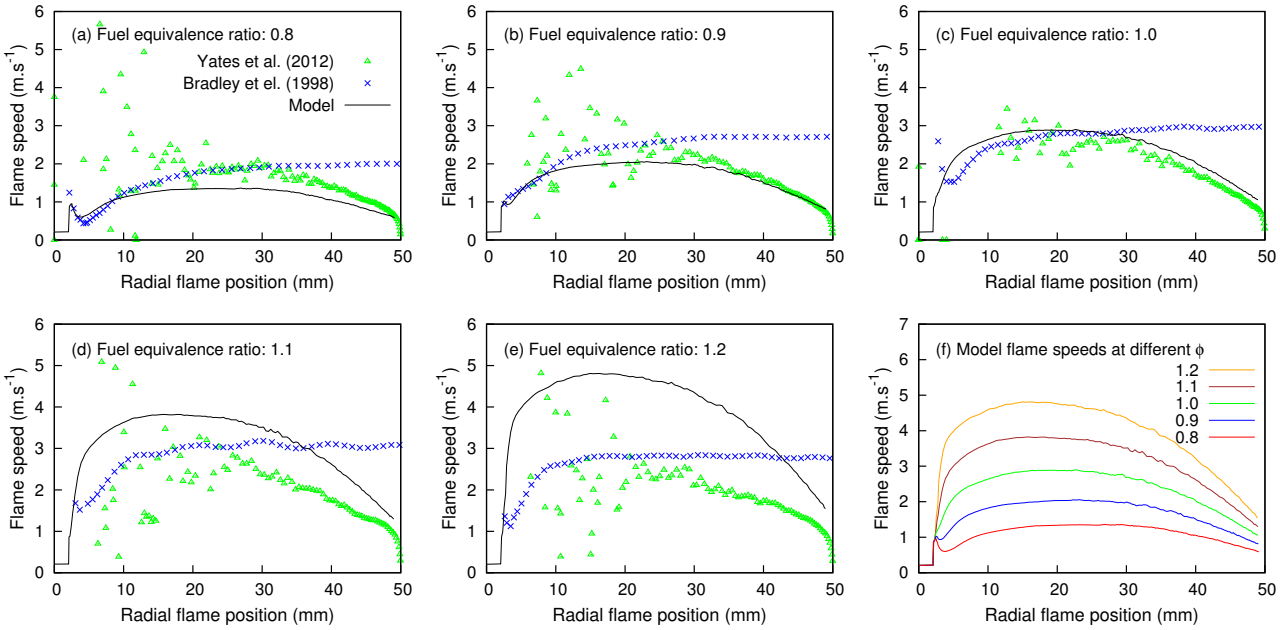

Figure 4.4.: Model-predicted flame speeds and experimentally obtained flame speeds from the study of Yates et al. (2012) for combustion bomb experiments with iso-octane and air at an initial temperature of 370 K and initial pressure of 1 bar together with experimental flame speed data from Bradley et al. (1998) for iso-octane air mixtures in a larger combustion bomb with initial conditions of 358 K and 1 bar.

radius greater than 6 mm.

When only the flame speeds at flame radii greater than 6 mm for the experimental data from Bradley et al. (1998) in Figure 4.4 are considered, it can be shown how the flame speed increases during the first stage of flame propagation and then flattens out to an almost constant flame speed. The increase in flame speed is explained by the decrease in flame stretch rate as the flame radius increases, as is discussed in Section 2.2.4. The flame speeds from Bradley et al. (1998) do not decrease after the flame position surpassed a radius of 20 mm as is observed for the experimental data from Yates et al. (2012). This is because the pressure for the experiments of Bradley et al. (1998) do not increase significantly over the flame propagation range shown in Figure 4.4, due to the larger combustion bomb used.

The experimental flame speed data from Yates et al. (2012) in Figure 4.4, is derived from the pressure trace data shown in Figure 4.3 by implementing Equation 2.31. Fig-

ure 4.4 shows that the flame speed data calculated from the pressure trace does not yield representative flame speeds during the first part of the flame propagation until a radial flame position of approximately 25 mm is reached, since that is where the first significant pressure increase is detectable. During the stage of "constant" pressure in Figure 4.2, the flame speeds that are calculated show great variation since the differentiation of the data is influenced by instrumental noise (Yates et al., 2012). However, during the pressure rise stage of the experiment the flame speed can be calculated more accurately and forms a trend, as shown in Figure 4.4. The decrease in flame speed at higher flame radii is caused by the pressure increase, as is discussed in Section 2.2.2.

The experimental data from Bradley et al. (1998) and from the study of Yates et al. (2012) is obtained for similar initial conditions and therefore it can be seen in Figure 4.4 that the data sets from the two different experiments seems to complement one another. The only difference in the conditions that influence the flame speed on the two data sets is the pressure increase in the experiments from Yates et al. (2012) and therefore it is expected that the flame speed behaviour for the two experiments should be the same until the flame reaches a radius in the Yates et al. (2012) data where the pressure differs from the initial pressure. This is confirmed in Section 4.4, where the base case conditions are modelled for a 100 mm and 380 mm diameter spherical constant volume combustion bomb. Therefore the experimental data from Bradley et al. (1998) may be considered as an estimate for the unavailable initial flame speed data from the experimental work of Yates et al. (2012).

The model-predicted flame speeds for an iso-octane and air mixture in a 100 mm diameter combustion bomb with initial conditions of 370 K and 1 bar, shown in Figure 4.4, show good correlation with the experimental results for a stoichiometric mixture (c). The model-predicted flame speed for the first part of the flame propagation correlates well with the experimental data from Bradley et al. (1998), while the second part correlates well with the experimental data from Yates et al. (2012). This further supports the notion that the two sets of experimental data in Figure 4.4 complement each other. The model therefore shows that the flame speed increases initially, due to a decrease in the flame stretch rate as the flame radius increases and then decreases again as the pressure in the combustion chamber increases during the last part of the flame propagation. This confirms the ability of the model to produce both these effects of flame behaviour.

The model-predicted flame speeds for fuel lean mixtures, Figure 4.4 (a) and (b), are lower than that from the experiments, while the model-predicted flame speeds are much higher

than the experimental flame speeds for fuel rich mixtures shown in Figure 4.4 (d) and (e). Figure 4.4 (f) shows that the model-predicted flame speeds increase as the fuel equivalence ratio increases from 0.8 to 1.2, which is not what is seen for the experimental results where the fuel equivalence ratio of 1.1 shows the highest flame speeds. An attempt is made to identify the cause of this inaccuracy and to make justified adjustments to the model in order to produce more accurate flame speeds while maintaining the proven ability of the model to describe several flame behaviours.

4.3. Adjustment to improve model results

Further investigation into the reason why the model predictions do not show the correct trend for flame speeds as a function of the fuel equivalence ratio shows that there are significant amounts of oxygen left in the burned gas fractions (combustion product) for the stoichiometric and fuel rich mixtures (fuel equivalence ratios of 1.0, 1.1 and 1.2). This implies that the modelled flames are all effectively fuel lean, since oxygen remains while fuel is consumed completely. This is shown in Figure 4.5, where the fuel plus intermediate mole fraction and normalised oxygen mole fraction profiles across the flame front at a flame position of 25 mm is shown for the five fuel equivalence ratios modelled. Note that Figure 4.5 shows five different flame fronts at the same radius of 25 mm, but they are separated on the spatial co-ordinate in this figure for better comparison. A flame front is here identified by the steep mole fraction gradients across it.

In Figure 4.5, each of the flame front mole fraction profiles is labeled according to the fuel equivalence ratio it represents, where the dashed line represents the fuel mole fraction and the solid line represents the oxygen mole fraction divided by 12.5 [3]. The fuel equivalence ratio of the unburned gas (to the right of Figure 4.5) is accurate. However, the fuel mole fraction becomes insignificantly small across the flame front, while that of oxygen does not, for both the fuel rich and fuel lean mixtures. In the model, Reactions 3.58 and 3.59 are separate steps. However, for complete reaction the fuel and air react with each other according to the combined stoichiometry of these two reactions. The mole fraction of the intermediate species (X) reaches a very low maximum of approximately 0.001 in the flame front and then reacts away and therefore makes a small contribution to the fuel plus intermediate profile in Figure 4.5. No error in the way the reaction stoichiometry is represented in the code could be found and therefore the reaction stoichiometry is

[3] The stoichiometric factor from Reaction 2 in Table 2.3

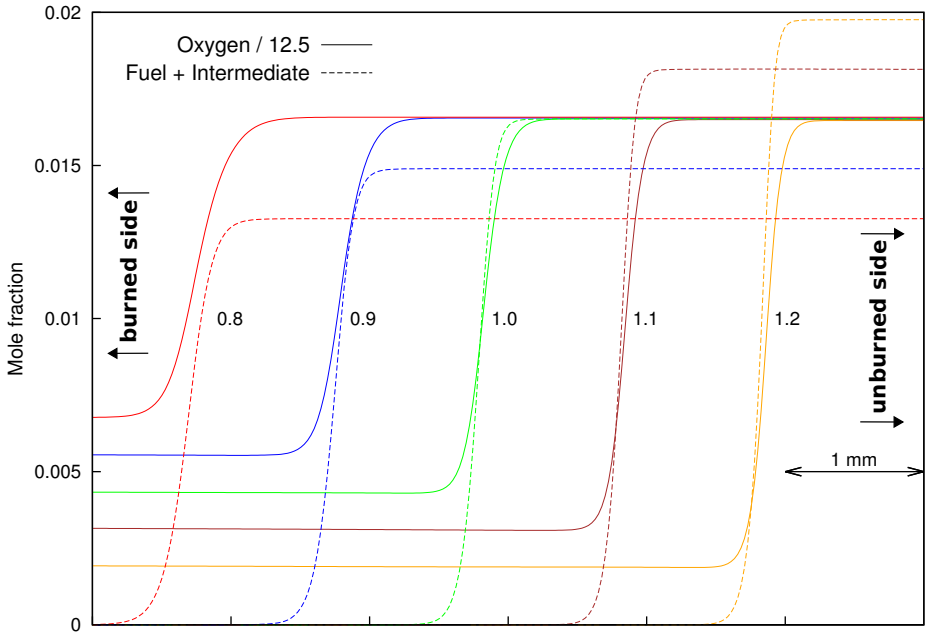

Figure 4.5.: Fuel and normalised oxygen mole fraction across the flame front at a flame position of 25 mm for the five modelled fuel equivalence ratios.

considered to be correct. Despite this, there is still oxygen left after all the fuel reacted for the fuel rich mixtures ($\phi > 1.0$).

This indicates that the difference in the diffusional velocities of the fuel and oxygen is not adequately described in the current modelling approach, since only diffusion can change the local fuel to oxygen concentration ratio. In this non-steady state system, the oxygen diffusion is significantly faster than that of the fuel and therefore the flame becomes locally fuel lean while creating a fuel rich region just ahead of the flame. This is seen clearly for the stoichiometric ($\phi = 1.0$) fuel and oxygen mole fraction profiles in Figure 4.5. For this reason the modelled flame approaches local stoichiometry in the reaction zone when the unburned gas is initiated as more fuel rich. This is seen in Figure 4.5 where the oxygen mole fraction in the burned gas (to the left) decreases with an increase in fuel equivalence ratio to reach zero at a fuel equivalence ratio higher than 1.2. This then translates to higher flame speeds at higher fuel equivalence ratios in the range considered here. This phenomenon is described in the work of Bechtold and Matalon (1999), where it is shown that, if the deficient reagent has a relatively high rate of diffusion, it is possible to have amounts of the deficient reagent left on the burned gas side while the excess reagent is completely consumed.

The diffusional fluxes of the individual species in this model are based on Equation 3.5, while the diffusion coefficients are calculated from the mixture-averaged approach, as discussed in Section 3.5.2.1. It is shown in Section 3.5.2.2 that the binary diffusion coefficients calculated by the model are accurate when compared to results from literature and can therefore be eliminated as a possible reason for the inaccuracy observed in Figure 4.4. The mixture-averaged approach is known to have lower accuracy compared to more complex approaches such as the Stefan-Maxwell approach discussed in Appendix B.2. The complexity of the Stefan-Maxwell approach makes it challenging and computationally expensive to implement into the current model. However, to investigate whether the Stefan-Maxwell approach will produce different results in the model, it is employed to predict the diffusional fluxes of each species across the flame front. This is based on the species concentration and temperature profiles calculated by the model using the mixture-averaged approach. The diffusional fluxes of fuel and oxygen are calculated across the flame front profiles of Figure 4.5, where the flame front of different fuel air ratios at a position of 25 mm is considered and is shown in Figure 4.6.[4]

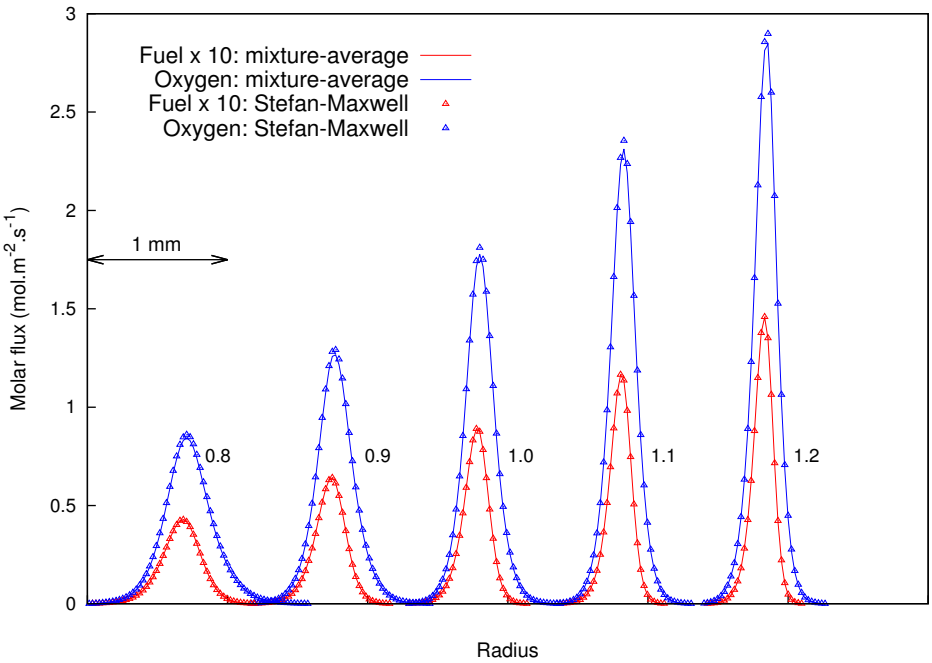

Figure 4.6.: Fuel and oxygen diffusional fluxes across the flame front for the five different fuel air ratios and at a radial flame position of 25 mm.

[4]Note that the molar fluxes in Figure 4.6 is given as positive, while it is towards the centre of the combustion chamber and should be indicated as negative according to the notation used in this study.

The Stefan-Maxwell approach gives very similar results to those of the mixture-averaged approach in this specific application, as seen in Figure 4.6. Thus, both these approaches produce a much higher diffusional flux for oxygen than that of the fuel. Figure 4.6 also shows that the region of significant diffusion of oxygen is wider than that of the fuel, which is not apparent from Figure 4.5. It is this higher oxygen diffusion that causes the effect shown in Figure 4.5 where an oxygen rich region local to the flame front results in unreacted oxygen on the burned gas side. The good comparison between the results from the two approaches in Figure 4.6 indicates that it is not due to the use of the simplified mixture-average approach that the resulting diffusional flux of oxygen appears to be high.

Although the root cause for the inaccuracy seen in the modelled flame speeds of Figure 4.4 is not identified in this study, it is known that only the relative diffusional velocities of the species could alter the local fuel air ratio. It is further shown in Section 3.5.2.2 that the binary diffusion coefficients are calculated accurately and Figure 4.6 shows that the mixture-average approach used in this model is sufficient to describe the diffusion of this system. Another aspect of the model that might be the cause of the inaccuracy is the very simple chemical kinetic model implemented. This two-reaction chemical kinetic mechanism is capable of describing the ignition delay time of a homogeneous mixture of fuel and air at high temperatures. However, for describing the chemical reactions in a flame, where the diffusion of combustion intermediate species is taking place, the current chemical mechanism is limited to describing the molecular transport of only one intermediate species. The investigation into incorporating a more representative chemical kinetic model into the current flame model is not pursued in this study and it is suggested that this should be considered for possible further improvement of the model.

In an attempt to produce more accurate results for flame speeds shown in Figure 4.4, the oxygen diffusional flux is forced to be lower in the model by decreasing the calculated diffusion coefficient by 75%. This number is found by the incremental decrease of the oxygen diffusion coefficient until better correlation between the model and experimental results is seen and less or very little oxygen is seen in the burned gas of the fuel rich mixtures. The effect that this adjustment has on the species profiles across the flame front and the diffusional fluxes of oxygen and fuel is shown in Figure 4.7.

The adjustment to the oxygen diffusion coefficient resulted in the depletion of oxygen in the burned gas side of the flame front for initially fuel rich mixtures, as shown in Figure 4.7 (a). The effect of the above mentioned adjustment on the diffusional fluxes of the fuel and oxygen seen in Figure 4.7 (b) is unexpected, in that the peak diffusional flux of oxygen

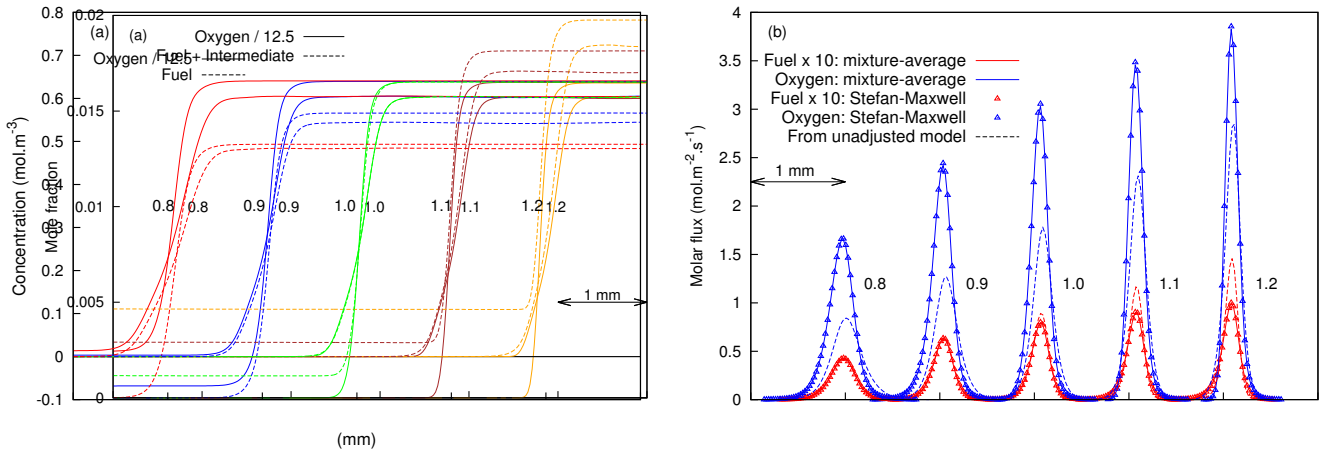

Figure 4.7.: The effect of the adjustment to the oxygen diffusion coefficient on the species profiles (a) and diffusional fluxes (b) of the fuel and oxygen in the system, at a flame position of 25 mm.

increased while the peak diffusional flux of the fuel decreased. This could be attributed to the higher concentration gradients across the flame front for oxygen, and lower gradients for the fuel. Figure 4.7 (b) also shows that the oxygen diffusional flux peaks shifted closer to the flame front (to the left) when comparing the results from the adjusted model to that of the unadjusted model. Note that the diffusional flux of oxygen remains much higher than that of fuel for the model with the adjusted oxygen diffusion coefficient.

The adjustment to the oxygen diffusion coefficient resulted in a model that produces results for the outward flame speed of a spherical flame that are more comparable to the available experimental results. Figure 4.8 shows the individual comparisons of the pressure trace for both experimental results and results from the adjusted model for the base case, which is iso-octane and air combustion with an initial temperature of 370 K and initial pressure of 1 bar.

The experimental pressure data (Yates et al., 2012) for iso-octane and air mixtures with a fuel equivalence ratio of 0.9 and higher is predicted well by the model with the adjusted oxygen diffusion coefficient in Figure 4.8 (b),(c),(d) and (e). However, for the fuel lean case in Figure 4.8 (a), the model still produces a pressure rise that is significantly slower than that observed in the experiments. Figure 4.8 (f) shows that the experimental trend of the pressure rise rates with respect to different fuel equivalence ratios is better matched by the adjusted model. When comparing Figure 4.3 and Figure 4.8, it is seen that the adjustment of the oxygen diffusion coefficient significantly improved the model's ability

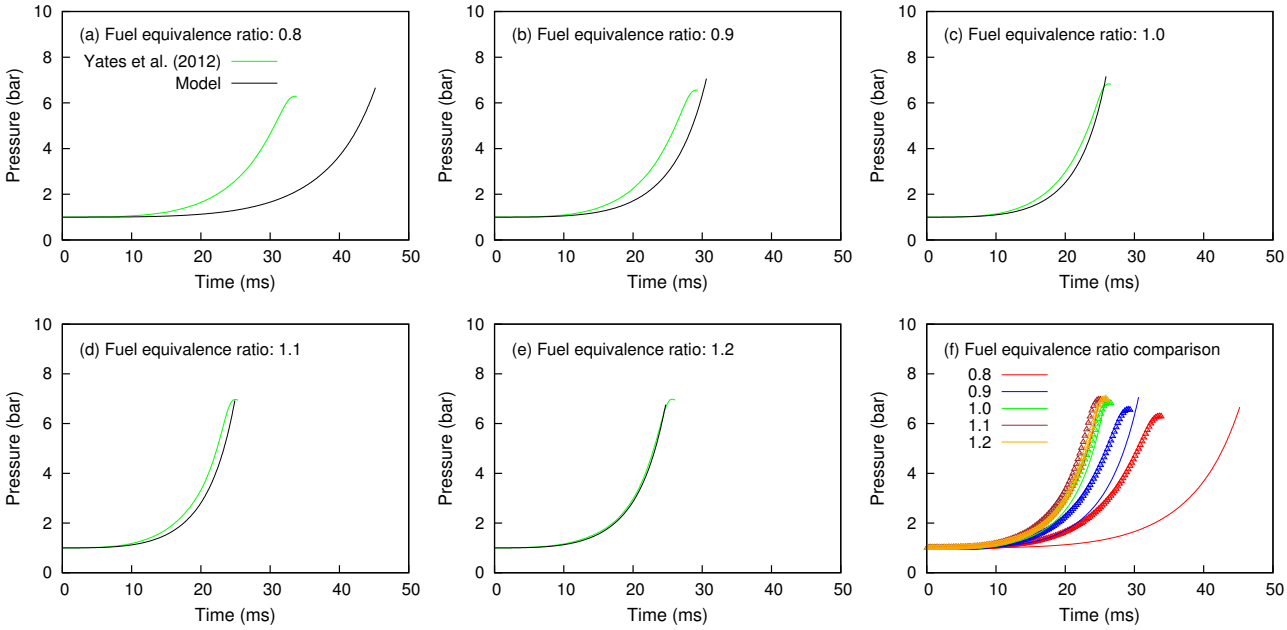

Figure 4.8.: Comparison between experimental pressure trace data (Yates et al., 2012) and the predicted pressure trace from the adjusted model for combustion bomb experiments with iso-octane and air at an initial temperature of 370 K and initial pressure of 1 bar.

to accurately describe the propagation of a spherical flame. As was done for Figure 4.4, the flame position and flame speed is derived from the model data and compared to data derived from the experimental pressure traces of the study of Yates et al. (2012) and experimental optical data from the study of Bradley et al. (1998) in Figure 4.9.

In Figure 4.9, both the predictions of the unadjusted model and adjusted model are shown. The adjusted model is referred to as merely the "model" from here on. The predictions for the flame speed from the model do not differ significantly from those of the unadjusted model for the cases of Figure 4.9 (a) and (b) with fuel equivalence ratios of 0.8 and 0.9 respectively. However, a significant improvement is seen in Figure 4.9 (d) and (e) where the model produces flame speeds that correlate well with the experimental data. The reason for this is explained in Section 4.6, where the sensitivity of the model results to oxygen diffusion is investigated.

The trend of flame speed with respect to the fuel equivalence ratio is now described better by the model, as shown in Figure 4.9 (f). Here the flame speeds from the model seem to reach a maximum for a fuel equivalence ratio close to 1.1 as compared to Figure 4.4 (f)

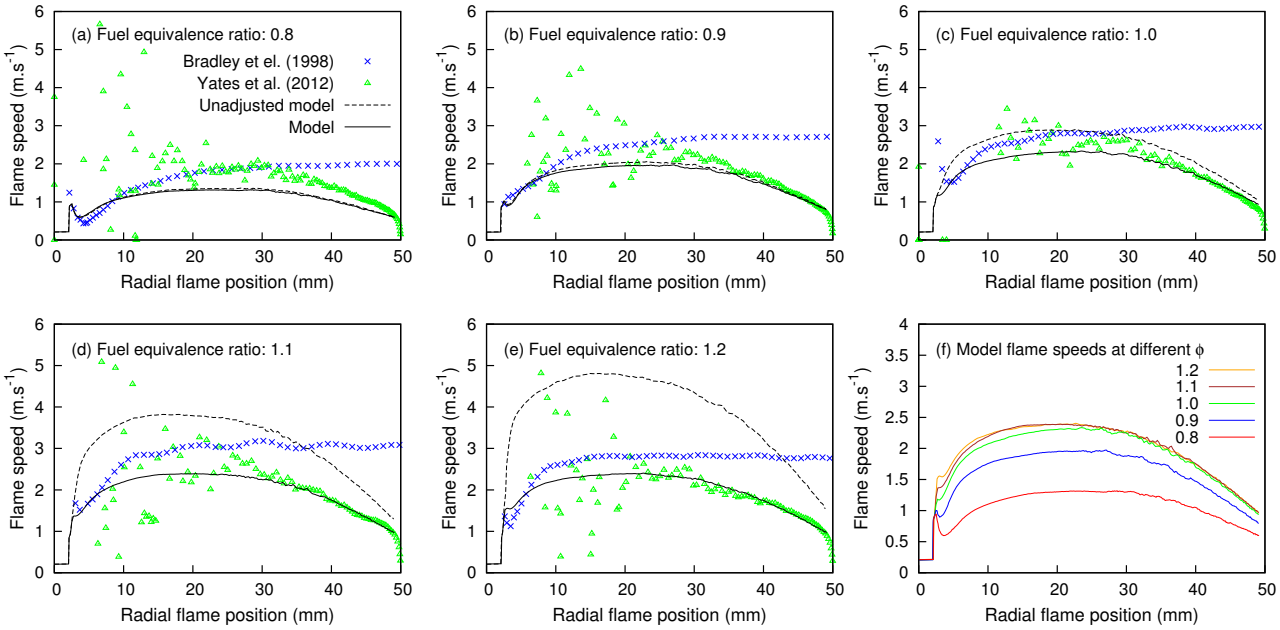

Figure 4.9.: Model-predicted flame speeds and experimentally obtained flame speeds from the study of Yates et al. (2012) for combustion bomb experiments with iso-octane and air at an initial temperature of 370 K and initial pressure of 1 bar together with experimental flame speed data from Bradley et al. (1998) for iso-octane air mixtures in a larger combustion bomb with initial conditions of 358 K and 1 bar.

where the flame speeds from the unadjusted model are significantly higher for the mixture with a fuel equivalence ratio of 1.2. Again a correlation of the model is seen with both sets of experimental data, where the model describes the initial increase in flame speed similar to the data from Bradley et al. (1998) and also describes the later decrease in flame speed similar to the data from Yates et al. (2012).

4.4. Results for different combustion chamber volumes

The previous model results are generated for a constant volume combustion bomb with a spherical cavity with an inner diameter of 100 mm. However, many other experimental studies make used of constant volume combustion bombs with a larger combustion chamber (Galmiche et al., 2012, Far et al., 2010, Kelley and Law, 2009, Farrell et al., 2004, Bradley et al., 1998). In this section the model conditions from Table 3.7 are repeated

for a combustion chamber with an inner diameter of 380 mm. This then resembles the experimental work of Bradley et al. (1998). The flame speed results for the first 50 mm is shown in Figure 4.10 along with the model results from Figure 4.9 and the experimental results from Bradley et al. (1998) and Yates et al. (2012).

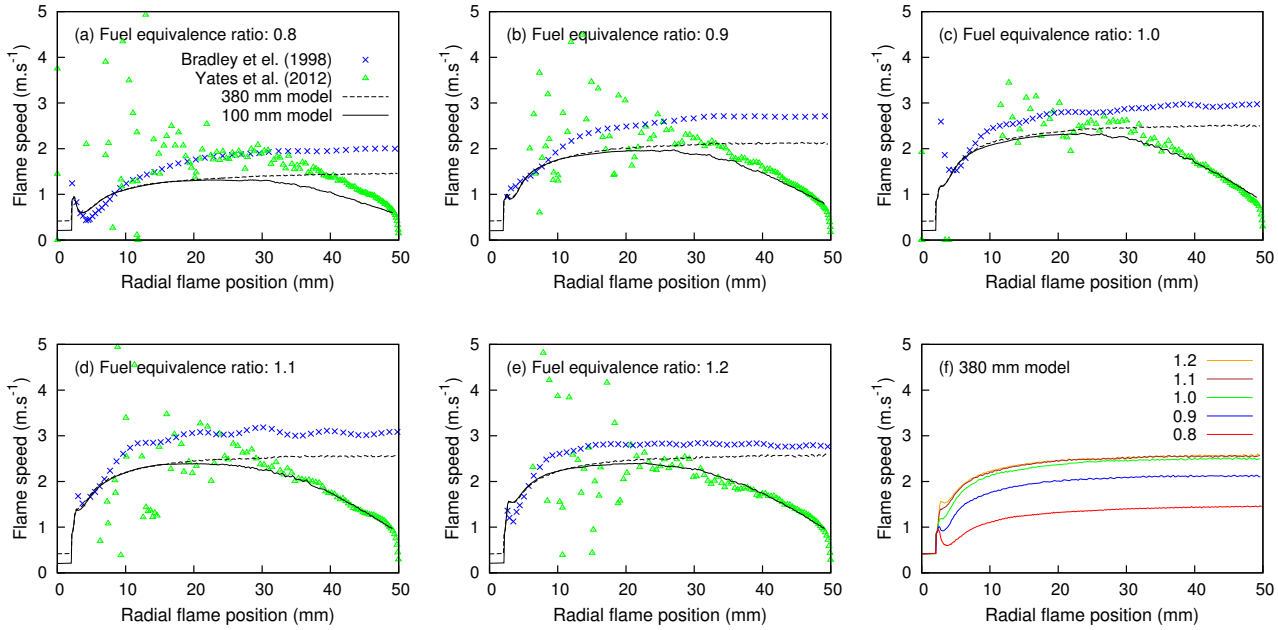

Figure 4.10.: Model-predicted flame speeds for a 100 mm and 380 mm inner diameter combustion chamber with an iso-octane and air mixture at initial conditions of 370 K and 1 bar as well as the experimental results of Yates et al. (2012) (100 mm) and Bradley et al. (1998) (380 mm).

Figure 4.10 shows that the initial flame speeds produced by the model for a 100 mm and 380 mm combustion chamber inner diameter are the same. This then implies that the initial flame speed data from the study of Yates et al. (2012) should be very similar to the initial flame speed data from Bradley et al. (1998) in Figure 4.10. It also supports the statement that the flame is subject to very similar effects during the first portion of the flame propagation and that the two sets of experimental data shown in Figure 4.9 complete each other.

It is only when the pressure starts increasing significantly, approximately 0.05 bar at a flame radius of 17 mm in Figure 4.10 (c), that the modelled flame speed for the 100 mm and 380 mm combustion chambers start to deviate from each other. Therefore it can be concluded that the initial flame behaviour in a combustion bomb, before a significant

pressure increase takes place, is independent of the combustion chamber volume. This is also concluded from experimental data from the study of Kelley and Law (2009).

4.5. Derived flame characteristics

The model succeeds in better describing the initial flame speed increase due to decrease in flame stretch rate, the later flame speed decrease due to increase in pressure and the flame speed behaviour with respect to fuel equivalence ratio. Therefore the data from the model is used to produce estimations of the laminar flame speed and Markstein lengths for the case of a mixture of iso-octane and air at an initial temperature of 370 K and initial pressure of 1 bar at different fuel equivalence ratios. The laminar flame speed is a widely quoted fuel combustion property, while the Markstein length is also reported in many studies (Bradley et al., 1998, Chen, 2011, Jerzembeck et al., 2009, Liao et al., 2004, Yates et al., 2012, Galmiche et al., 2012) and is an accepted indication of the sensitivity of the flame speed to the flame stretch rate. This then gives the opportunity to compare the combustion properties produced by the model developed in this study with that from literature. To obtain the estimations for the laminar flame speed and Markstein length, the spherical burned gas flame speed data is plotted against the flame stretch rate as is done in Figure 4.11.

In Figure 4.11, different regimes of flame propagation can be identified. Since the flame stretch rate decreases significantly as the flame radius increases, it approaches a minimum at the largest flame radius. Therefore the data at the lowest flame stretch rate (left side of Figure 4.11) represent the end of the flame propagation and the flame originates at the other ends of the trend lines formed by the data points. The direction of the data in Figure 4.11 with regards to time is indicated by the arrow. In Figure 4.11, this shows that the flame stretch rate and flame speed at flame initiation are very similar for different fuel equivalence ratios. This common region of origin for the trends, indicated in Figure 4.11, is due to the common initial behaviour of the flame speed at the same initial flame radius seen in Figure 4.9. This can be ascribed to the strategy used in the model to describe the ignition event, as discussed in Section 3.3, where the boundary temperature rise is forced at a defined rate.

The ignition regime shown in Figure 4.11 shows the data where the flame position is below 10 mm and, based on Figure 4.9, it is assumed that the flame speed is influenced by the ignition energy in this regime. In this regime the flame speed for the fuel equivalence

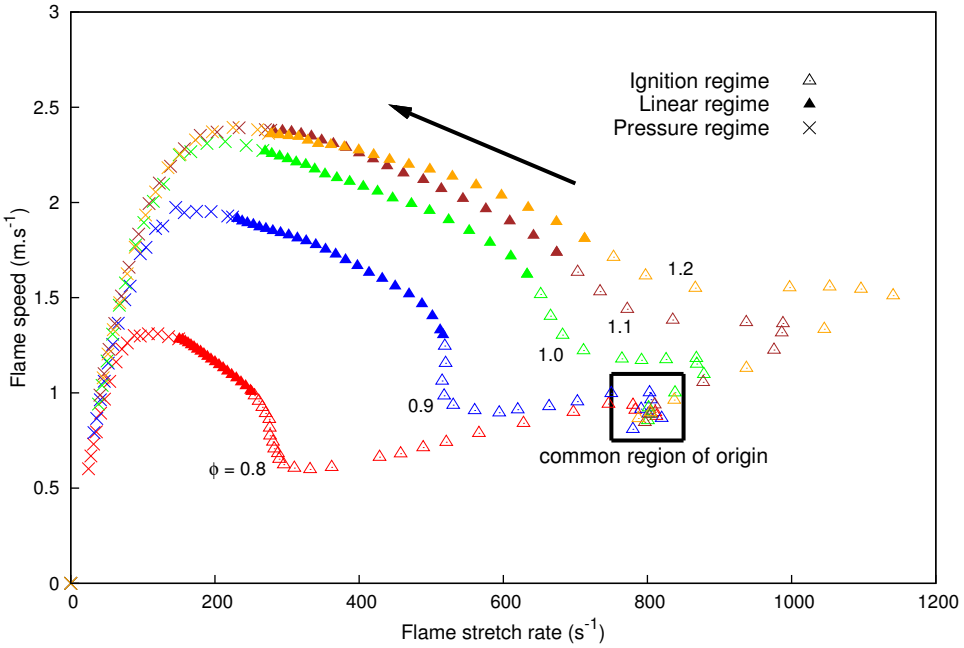

Figure 4.11.: Model-produced flame speed of iso-octane versus the flame stretch rate for outwardly propagating spherical flame with different initial fuel to air ratios in a 100 mm diameter combustion chamber.

ratios of 0.8 and 0.9 decrease immediately from the common region of origin, whereas the flame speed for the fuel equivalence ratios of 1.0, 1.1 and 1.2 increases. However less apparent, this is also seen in Figure 4.9 and can be ascribed to the different minimum ignition energies required for the different fuel equivalence ratio mixtures (Yano and Ito, 1979). The ignition energy effects are not the focus of this study and therefore the part of the trends that is influenced by the ignition energy is not further discussed.

Two other regimes are identified and indicated in Figure 4.11: the linear regime where the flame speeds are predominantly influenced by the flame stretch rate and the pressure regime where the flame speeds decrease due to an increase in pressure. The pressure regime during the last portion of flame propagation is the part of the trends at the lowest flame stretch rate in Figure 4.11, where a significant decrease in flame speed is seen as the flame stretch rate decreases. The pressure regime is defined here as the data where the pressure in the combustion chamber is 5% higher than the initial pressure[5]. The regime of specific interest to this study, is where the flame speed increases due to a decrease in flame stretch rate, where the pressure increase is small and where the flame

[5]For the initial pressure of 1 bar, this increase is 5 kPa.

is no longer influenced by the ignition energy. The data in this regime is influenced by the flame stretch rate only and therefore it is simpler to account for this one effect in order to derive the unstretched flame speed or burned gas laminar flame speed (S_s). In Figure 4.11 this regime is indicated as the linear regime, where there is an almost linear correlation between the flame speed and the flame stretch rate, especially for the fuel lean mixtures ($\phi < 1.0$). The linear regimes in Figure 4.11 are therefore defined as data where the radial flame position is greater than 10 mm and the pressure increase is less than 5% of the initial pressure.

When Figure 4.11 is compared to Figure 2.19 in Section 2.3.3.2, which shows the experimental trends for the flame speed versus flame stretch rate from the study of Bradley et al. (1998), similarities in the trends are seen. Although the trends in Figure 2.19 only show the flame speed behaviour below a flame stretch rate of 600 s^{-1}, for the fuel equivalence ratio of 0.8, the flame shows similar behaviour at the high flame stretch rates or the ignition regime. Both the model and the experimental results show a fast decrease in flame speed after the ignition event, followed by an increase before the linear regime is reached. In both Figure 2.19 and Figure 4.11 the gradient of the part of the trend that is in the linear regime, increases (becomes less negative) as the fuel equivalence ratio increases. The experimental trends from the study of Bradley et al. (1998) does not show a decrease in flame speed at the lower flame stretch rates in Figure 2.19, since the experiments are done in a larger combustion bomb where only the initial flame speed data, where the pressure remains constant, is considered. This shows that the model succeeds in producing the same trends as is observed experimentally for a spherical flame.

To obtain the estimations for laminar flame speed and Markstein length, both the widely used linear regression (Equation 2.34) and the nonlinear regression (Equation 2.37), suggested by Kelley and Law (2009), are fitted to the data in the linear regimes in Figure 4.11. The regressions of this data are shown in Figure 4.12.

The linear and nonlinear regression approaches are shown in Figure 4.12 (a) and (b) respectively. In Figure 4.12 (a) the linear regression is implemented and the Markstein length is defined as the negative of the gradient of the linear lines that approximate the respective data. The nonlinear regression function, discussed in Section 2.3.3.2 and suggested by Kelley and Law (2009), is implemented in Figure 4.12 (b) and produces a curved approximation to the flame speed versus flame stretch rate.

Different Markstein lengths can be defined, as is discussed in the work of Bradley et al. (1996). However, in this study only the sensitivity of the burned gas flame speed to flame

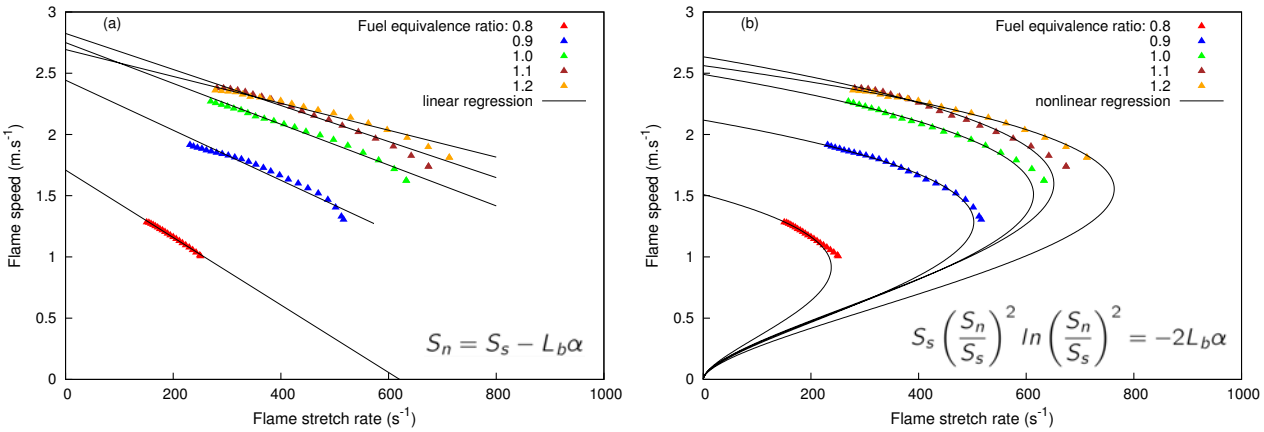

Figure 4.12.: (a) Linear regression and (b) nonlinear regression of the model-produced flame speed data for iso-octane and air at 370 K and 1 bar in a 100 mm diameter combustion chamber.

stretch rate is considered. The burned gas laminar flame speed (S_s) is then obtained from the regression of the flame speed (S_n) data in the linear regime to a zero flame stretch rate (α), as described by Equations 2.34 and 2.37. The linear regression method is also used by Bradley et al. (1996), where the laminar flame speed (S_L) is calculated from the burned gas laminar flame speed (S_s) using Equation 2.35. By following this method, the laminar flame speeds and Markstein lengths for the different fuel equivalence ratios in Figure 4.12 are estimated with both the linear and nonlinear regression functions and given in Table 4.2.

It should be noted that the Markstein lengths, given in Table 4.2, give the sensitivity of the flame propagation speed to the flame stretch rate and are also referred to as the burned gas Markstein length in the work of Bradley et al. (1996). The burned gas laminar flame speeds and the Markstein lengths in Table 4.2 are derived from the regression functions represented by the approximating solid lines in Figure 4.11 (a) and (b). The density fraction is obtained from the raw model data, where the density of the burned gas (ρ_b) and the unburned gas (ρ_u) are calculated. The laminar flame speed (S_L) in Table 4.2 is then calculated from Equation 2.35 and represent the unstretched laminar flame speed as defined in Section 2. The laminar flame speeds and Markstein lengths from Table 4.2 are compared with experimental values from the study of Bradley et al. (1998) for iso-octane and air mixtures at 358 K and 1 bar and from the study of Galmiche et al. (2012) for iso-octane and air mixtures at 373 K and 1 bar, in Figure 4.13 (a) and (b).

The laminar flame speeds produced by implementing both the linear and nonlinear regres-

Table 4.2.: Flame speed characteristics derived from Figure 4.12 for an iso-octane and air mixture at 370 K and 1 bar.

Fuel equivalence ratio	Density fraction $\left(\frac{\rho_b}{\rho_u}\right)$	Burned gas laminar flame speed (S_s) $m.s^{-1}$	Markstein length (L_b) mm	Laminar flame speed (S_L) $m.s^{-1}$
		Linear regression		
0.8	0.147	1.71	2.76	0.251
0.9	0.134	2.44	2.04	0.328
1.0	0.134	2.75	1.67	0.369
1.1	0.137	2.82	1.47	0.388
1.2	0.140	2.69	1.10	0.377
		Nonlinear regression		
0.8	0.148	1.51	1.11	0.219
0.9	0.134	2.12	0.78	0.284
1.0	0.133	2.49	0.75	0.334
1.1	0.137	2.63	0.74	0.362
1.2	0.138	2.56	0.62	0.359

sion to the model data in Figure 4.13 (a), are significantly lower than those reported by Bradley et al. (1998) and Galmiche et al. (2012). However, the trend of the laminar flame speed for different fuel equivalence ratios shows some agreement. The laminar flame speed reaches a maximum value near a fuel equivalence ratio of 1.1, which is commonly ascribed to the adiabatic flame temperature that reaches a maximum value in the same vicinity. However, the simple chemical model implemented into this flame propagation model does not account for dissociation reactions, discussed in Section 2.1.1, and therefore does not predict a maximum adiabatic flame temperature near a fuel equivalence ratio of 1.1, but rather at 1.0. This suggests that the maximum laminar flame speed predicted by the model occurs on the slightly fuel rich side due to the preferential diffusion of oxygen, as seen in Figure 4.7 (a). The laminar flame speeds derived from the model data might be lower than the experimental data from Bradley et al. (1998) and from Galmiche et al. (2012) due to the forced reduction of the oxygen diffusion. However, this adjustment is still justified since it produces the correct laminar flame speed trend for different fuel equivalence ratios. Further, it is also seen in Figure 4.13 (a) that the laminar flame speed derived from the nonlinear regression is lower than that derived from the linear regression, which is expected and discussed by Kelley and Law (2009).

The Markstein lengths derived from the linear regression of the model data compares well with the experimental data from Bradley et al. (1998) and follows the same trend, where it decreases as the fuel equivalence ratio increases, as discussed in Section 2.2.4.

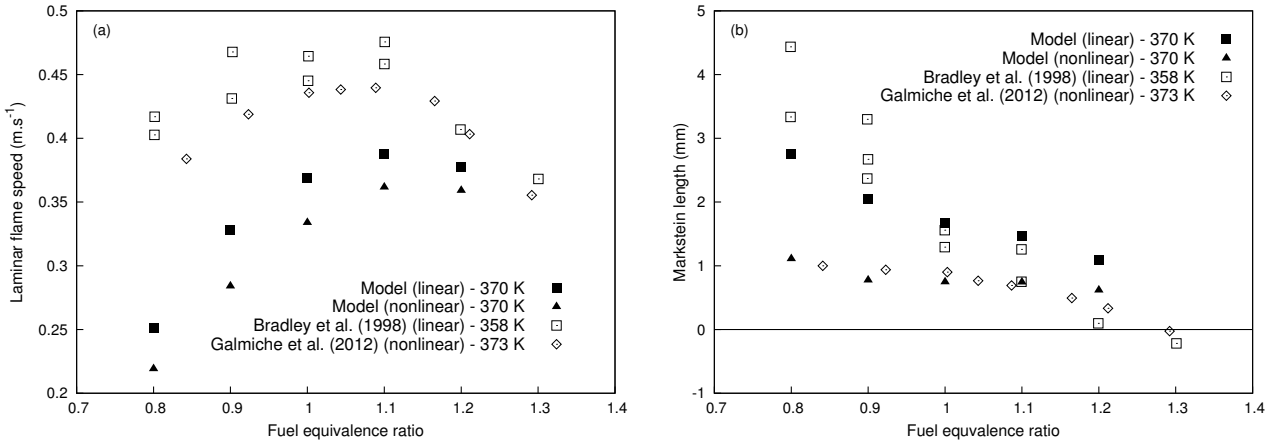

Figure 4.13.: Laminar flame speed (a) and Markstein lengths (b) for an iso-octane, air mixture at 1 bar estimated from the model for 370 K and reported by Bradley et al. (1998) for 358 K and by Galmiche et al. (2012) for 373 K.

Although the linear derived Markstein lengths compare very well with the experimental data from Bradley et al. (1998) for the stoichiometric mixture (fuel equivalence ratio of 1.0), Figure 4.13 shows that the experimental Markstein lengths are higher for the lower fuel equivalence ratios and lower for the higher fuel equivalence ratios than those calculated from the model data. The sensitivity study in Section 4.6.1 will show that the linear derived Markstein length is less sensitive to the fuel equivalence ratio due to the adjustment to the oxygen diffusion rate, which is a key influence in this trend as mentioned in Section 2.2.4.

The Markstein lengths derived from the nonlinear regression, shown in Figure 4.13 (b), are significantly lower than the linear derived Markstein lengths, but show the same trend as the linear derived Markstein lengths for different fuel equivalence ratios. In Equation 2.37, used for the nonlinear regression, the Markstein length (L_b) still represents the sensitivity of the flame speed to the flame stretch rate. However, the magnitude of the nonlinear measure for Markstein length does not agree with that from the linear regression (Equation 2.34). The nonlinear Markstein lengths derived from the model-produced data in Figure 4.13 (b), compare very well with the experimental data for nonlinear derived Markstein lengths from Galmiche et al. (2012). Both the linear and nonlinear regression is therefore implemented successfully on the model-produced data and give meaningful estimates for the Markstein lengths which compare well with experimental data. In Figure 4.11, it can be seen that the linear regime for the mixture with a fuel equivalence ratio

of 1.2 is curved and therefore linear regression is less accurate here.

It is clear from this comparison with experimental data that the model does not succeed in predicting the exact laminar flame speeds for the conditions studied, but does predict the flame behaviour for different fuel equivalence ratios as the flame propagates through the spherical, constant volume combustion chamber. The flame behaviours that are described by the model developed in this study are listed below.

- The pressure increase in the combustion chamber as the flame propagates outwards is captured by the model, which shows a uniform pressure across the spatial domain that increases over time.
- The increase in flame speed due to decreasing flame stretch rate as well as the decreasing flame speed due to the increasing pressure are both captured by the model, as seen in Figure 4.9.
- The correct flame speed trends for different fuel equivalence ratios are shown in Figure 4.9.
- The model-produced flame speed versus flame stretch rate, shown in Figure 4.11, demonstrate very similar trends as the experimentally obtained trends from Bradley et al. (1998) shown in Figure 2.19.
- The laminar flame speeds from the model, shown in Figure 4.13 (a), shows the correct trend for different fuel equivalence ratios as is seen from the experimental data of Galmiche et al. (2012) and Bradley et al. (1998).
- Both the linear and nonlinear Markstein lengths derived from the model data, compare very well with the respective experimental data of Bradley et al. (1998) and Galmiche et al. (2012).

The adjustment made to the model, where the oxygen diffusion rate is decreased, improves the model in terms of producing better trends for the flame propagation for different fuel equivalence ratios. Since the model succeeds in describing the flame behaviour for changing parameters such as pressure and flame stretch rate, it will now be implemented to do a sensitivity study of the laminar flame speeds and Markstein lengths on various fuel properties for the conditions in Table 3.7.

4.6. Sensitivity analysis

In the above section, the model is shown to be capable of producing flame speed data for a spherical iso-octane and air flame in a constant volume combustion bomb that correlates with experimentally produced data. This is now used as the base case for sensitivity analyses of the physical and chemical properties of the combustion mixture on the laminar flame speed and Markstein length. The first property to be varied is the diffusion coefficient of oxygen in the mixture to show how adjustment to this parameter effects the results. The sensitivity to the fuel molecule diffusion coefficient, the intermediate molecule diffusion coefficient, the thermal conductivity of the unburned mixture and the reaction kinetics will be determined as well. The responses are labelled as "high" for an increase in the varying property and as "low" for a decrease. The sensitivity of the laminar flame speed and the Markstein length derived from the nonlinear regression, is tested in this section. Since more consistent fits are achieved from the nonlinear regression, the sensitivities of the linear regression results are not reported as there is less confidence in their validity.

4.6.1. Sensitivity to oxygen diffusion

To demonstrate the effect of the diffusion of oxygen on the model results, the adjusted oxygen diffusion coefficient is varied by 20%. This variation is implemented on the 75% reduced mixture diffusion coefficient. Since the oxidising agent in combustion experiments is oxygen in most cases and oxygen diffusion is well defined for these experiments, the 20% is chosen as an arbitrary variation. This is to show both the sensitivity of the system to oxygen diffusion and the effect of the adjustment made to the model. The resulting influence on the flame speed is shown in Figure 4.14 where the flame speed is plotted versus the flame position.

Figure 4.14 shows that a higher oxygen diffusion coefficient results in higher flame speeds and this effect is stronger for the stoichiometric and fuel rich mixtures ($\phi \geq 1.0$) in (c), (d) and (e). For the fuel lean case, with a fuel equivalence ratio of 0.8 in Figure 4.14 (a), no effect on the flame speed is shown. This is due to oxygen being the limiting factor for the fuel rich mixtures and therefore faster oxygen diffusion results in higher rates of energy release. This also explains the effect seen in Figure 4.14 (b) for a fuel equivalence ratio of 0.9, where the increase in oxygen diffusion does not have a significant effect, but the decrease in oxygen diffusion resulted in slower flame speeds with a 2.5% lower flame

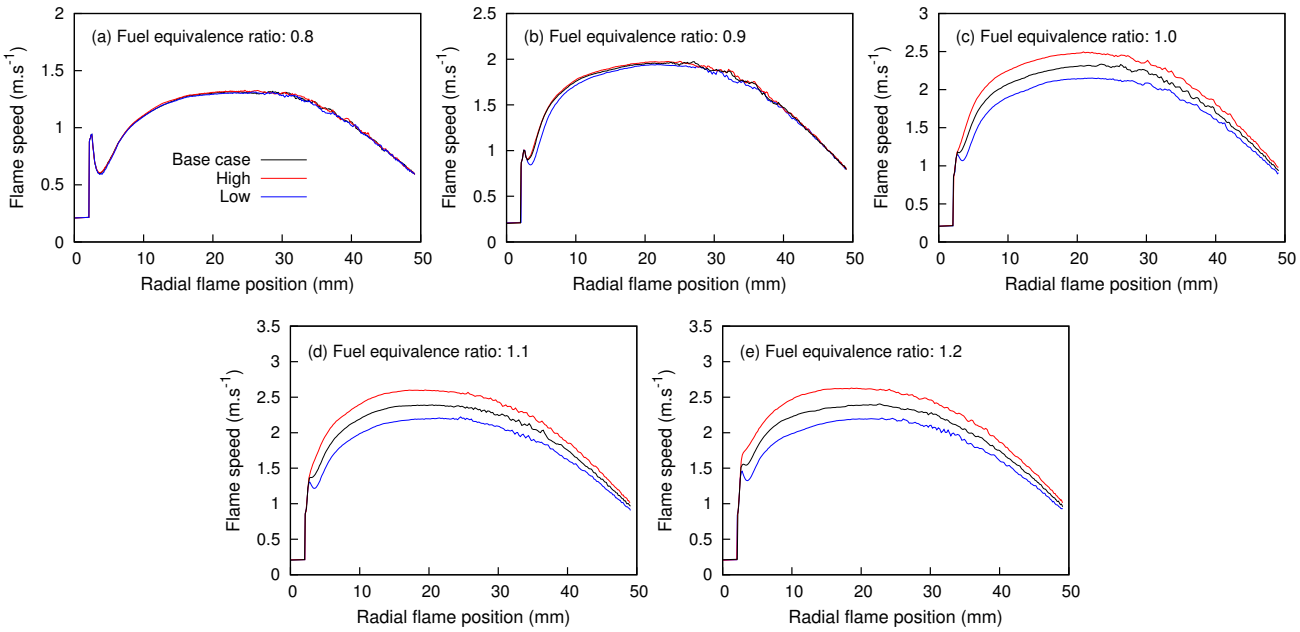

Figure 4.14.: Sensitivity of the flame speed to a 20% variation in oxygen diffusion coefficient for an iso-octane and air mixture at initial temperature and pressure of 370 K and 1 bar.

speed at a flame radius of 10 mm. Figure 4.14 shows that the sensitivity of the flame speeds to the oxygen diffusion is most pronounced for fuel rich mixtures, which made it a good choice for the 75% adjustment[6] to achieve more accurate flame speed profiles.

For a fuel equivalence ratio of 0.9 in Figure 4.14 (b), the oxygen concentration local to the reaction zone of the flame is in excess and therefore an increase in oxygen diffusion into the reaction zone does not influence the heat release rate significantly. However, when the oxygen diffusion into the flame is decreased, the mixture local to the reaction zone becomes fuel rich, resulting in lower flame speeds due to lower heat release rates. It is therefore notable that the flame speeds in Figure 4.14 show a stronger sensitivity to the diffusion of oxygen when the oxygen is the limiting reagent. In a study of Holley et al. (2009) it is also reported that the laminar flame speeds of n-dodecane and air flames are more sensitive to oxygen diffusion for fuel rich mixtures as compared to fuel lean mixtures.

The initial decrease in flame speed, right after the ignition event, is seen to be more severe when the oxygen diffusion is decreased in Figure 4.14 (b), (c), (d) and (e). This effect

[6]The 75% adjustment to oxygen diffusion is already included here as it forms part of the base case.

indicates that oxygen diffusion influences the minimum ignition energy required to initiate a spherical flame, in that the required ignition energy increase when the oxygen diffusion is decreased for mixtures where oxygen is the limiting reagent.

To quantify the effect of oxygen diffusion on the flame characteristics, the laminar flame speeds and Markstein lengths are calculated by implementing nonlinear regression of the data. The sensitivity of the flame characteristics to oxygen diffusion is shown in Figure 4.15.

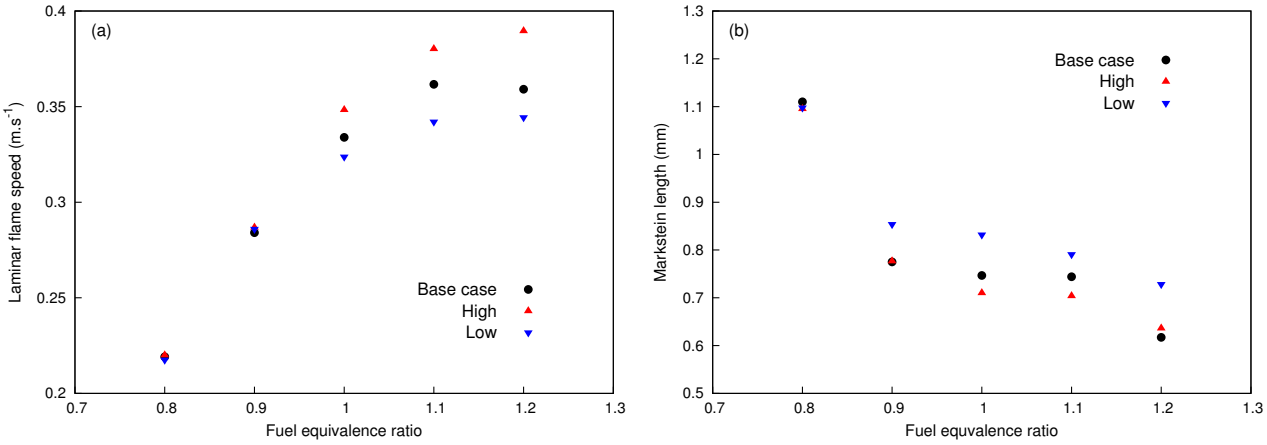

Figure 4.15.: Sensitivity of the laminar flame speed (a) and Markstein length (b) to a 20% variation in oxygen diffusion coefficient for an iso-octane and air mixture at initial temperature and pressure of 370 K and 1 bar.

Figure 4.15 (a) shows that an increase in oxygen diffusion increases the laminar flame speeds for the fuel equivalence ratios of 1.0, 1.1 and 1.2, which is expected from the trends in Figure 4.14. This again shows that the sensitivity of the flame speed to oxygen diffusion is more pronounced when the oxygen is the limiting reagent. The sensitivities of the Markstein lengths to oxygen diffusion, shown in Figure 4.15 (b), shows that the Markstein lengths increase when the oxygen diffusion decreases. Interestingly, the lower flame speed seen for a fuel equivalence ratio of 0.9 in Figure 4.14 (b) for a decreased oxygen diffusion does not translate into a significantly lower laminar flame speed in Figure 4.15 (a). However, the Markstein length for a fuel equivalence ratio of 0.9 in Figure 4.15 (b) shows a significant increase of 10% for lower oxygen diffusion. Markstein lengths for the flames with lower oxygen diffusion deviate further from the base case than that with higher oxygen diffusion. Therefore it may be concluded that the model shows that the Markstein length is more sensitive to a decrease in oxygen diffusion than an increase,

suggesting a nonlinear sensitivity.

Oxygen diffusion has an influence on the sensitivity of the flame speed to the flame stretch rate (Markstein length), due to the curvature of the flame. A highly curved flame or a flame with a smaller radius is in contact with more unburned gas containing high concentrations of oxygen. In a situation where oxygen is a limiting reagent ($\phi \geq 1.0$), the diffusion of oxygen into the curved flame front will decrease the fuel equivalence ratio local to the reaction zone to a value closer to 1.0 (stoichiometric mixture) and result in a higher heat release rate and consequently higher flame speed. Therefore this effect is dependent on the curvature or radius of the flame and is accounted for by the Markstein length. The observation that the laminar flame speed for a fuel equivalence ratio of 0.9 is affected very little by a decrease in oxygen diffusion while the Markstein length increases significantly, shows that the Markstein length is more sensitive to oxygen diffusion than the laminar flame speed. This statement implies that the flame speed of a curved flame is more sensitive to oxygen diffusion than that of a flat flame.

4.6.2. Sensitivity to fuel molecule diffusion

The diffusion coefficient of the fuel is varied to show how this effects the flame characteristics in the model results. For different fuel molecules, the diffusion coefficient will vary significantly. To show this, the diffusion coefficients for different fuel molecules in a stoichiometric mixture with air at 1 bar and 400 K are calculated and given in Table 4.3. The diffusion coefficients are calculated by following the approach described in Section 3.5.2.1 and using the transport data provided in the mechanism of Mehl et al. (2011).

Table 4.3.: Diffusion coefficients of different fuel molecules in a stoichiometric air mixture at 400 K and 1 bar.

Molecule	Diffusion coefficient $\frac{m^2}{s}$	Fractioned to iso-octane
iso-octane	1.15×10^{-4}	1.00
n-heptane	1.20×10^{-4}	1.04
toluene	1.35×10^{-4}	1.17
methane	3.76×10^{-4}	3.27

Table 4.3 shows that the diffusion coefficient with respect to the stoichiometric air mixture varies significantly for different fuel molecules. The calculated diffusion coefficient for methane is three times higher than that of iso-octane. The sensitivity of the flame

characteristics to fuel molecule diffusion is determined with a variation of 20% in the calculated fuel diffusion coefficient. From Table 4.3 it is seen that this variation will result in a higher diffusion coefficient that is approximate to that of toluene. The influence of varying the fuel diffusion coefficient is shown in Figure 4.16 where the flame speeds are plotted against flame position.

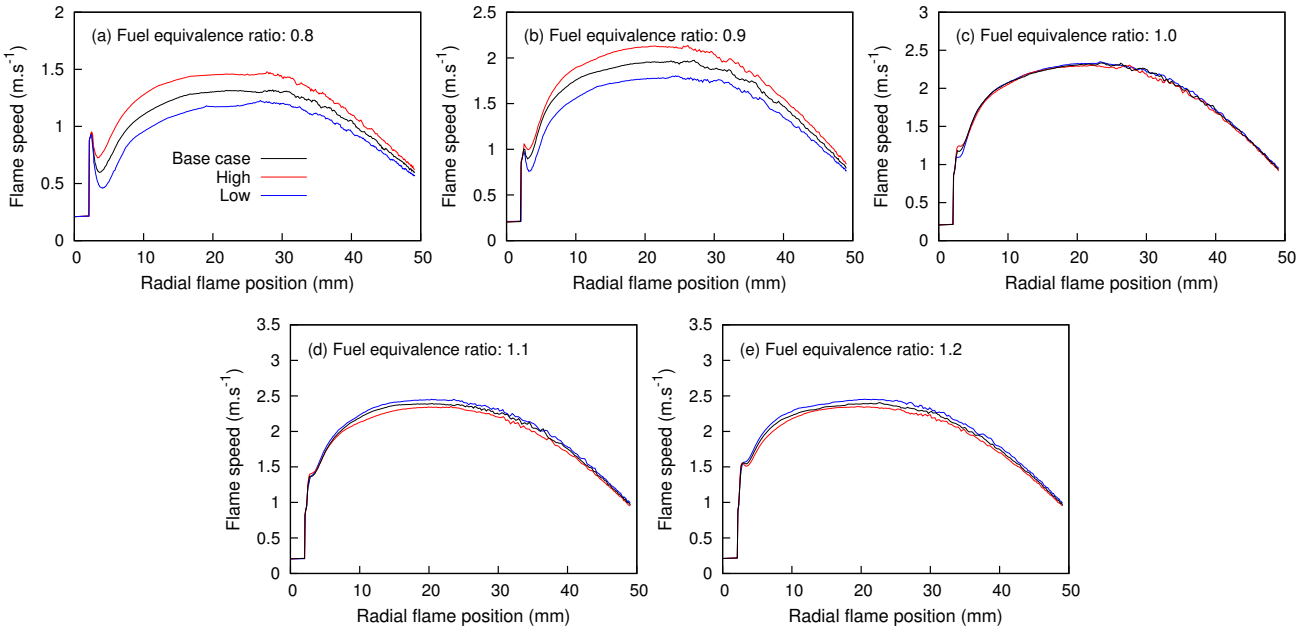

Figure 4.16.: Sensitivity in the flame speed to a 20% variation in the fuel molecule (F) diffusion coefficient for an iso-octane and air mixture at initial temperature and pressure of 370 K and 1 bar.

In Figure 4.16 (a) and (b) it is seen that a higher fuel diffusion increases the flame speed for the fuel lean mixtures, while Figure 4.16 (d) and (e) show that a higher fuel diffusion decrease the flame speed for fuel rich mixtures. Again the effect of fuel diffusion is stronger in mixtures where the fuel is the limiting reagent ($\phi < 1.0$). The decrease in flame speed when, fuel diffusion is increased for the fuel rich mixtures, indicates the effect that the fuel molecule has on the heat capacity of the mixture. Although it is here the case that the fuel is in excess and that an increase in fuel diffusion will not increase the heat release rate, an increase in fuel diffusion into the flame will influence the flame temperature. This effect is not visible for the oxygen rich mixtures in Figure 4.14, where the oxygen diffusion sensitivity is shown, since oxygen has a weaker effect on the heat capacity of the burned gas mixture.

Further, Figure 4.16 shows that the decrease in fuel diffusion causes a more severe decrease in flame speed after flame initiation and that this effect is greatest for a fuel equivalence ratio of 0.8 and becomes smaller as the fuel equivalence ratio increase. Therefore the fuel diffusion has a similar effect as that of oxygen diffusion on the minimum ignition energy required, as discussed in Section 4.6.1, except for the opposite trend with respect to the fuel equivalence ratio is shown. For a fuel equivalence ratio of 1.2 in Figure 4.16 (e), it is seen that the flame speed decrease after flame initiation is more severe for an increase in fuel diffusion, which is related to the increased heat capacity of the burned gas and the effect it has on the minimum ignition energy required. The laminar flame speeds and Markstein lengths are calculated from the nonlinear regression and compared in Figure 4.17.

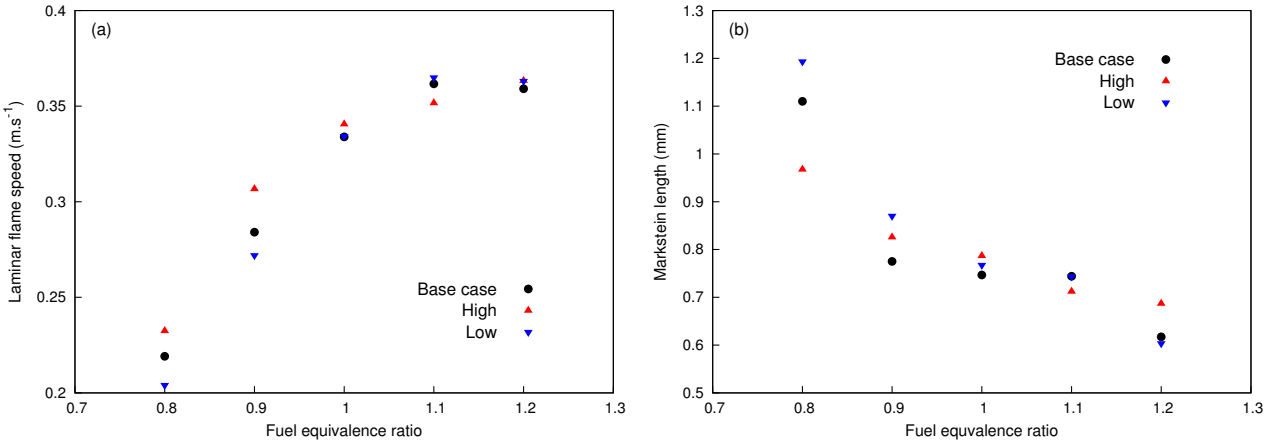

Figure 4.17.: Sensitivity of the laminar flame speed (a) and Markstein length (b) to a 20% variation in fuel (F) diffusion coefficient for an iso-octane and air mixture at initial temperature and pressure of 370 K and 1 bar.

Figure 4.17 (a) shows that, for fuel lean mixtures ($\phi < 1.0$), an increase in fuel diffusion increases the laminar flame speed, while the opposite effect is seen for fuel equivalence ratios higher than 1.0. The sensitivity of the laminar flame speed to the fuel diffusion in Figure 4.17 (a) is stronger for the fuel lean mixtures where the fuel is the limiting reagent. The effect, where the laminar flame speed increases with an increase in fuel diffusion for fuel lean mixtures, is caused by an increase in heat release rate due to an increase in the limiting reagent. For the fuel rich mixtures ($\phi > 1.0$), fuel is not the limiting reagent and an increase in fuel diffusion will not cause in increase in heat release rate. However, since the fuel is in excess for the fuel rich mixtures, a higher fuel diffusion into the flame will increase the heat capacity of the burned gas, resulting in a lower local flame temperature

and decreasing flame speed.

The sensitivity of the Markstein lengths to fuel diffusion, shown in Figure 4.17 (b), is similar to that seen for oxygen diffusion in Figure 4.15 (b), but here the sensitivity is stronger for fuel lean mixtures. In Figure 4.17 (b), the sensitivity of the Markstein length to the fuel diffusion is very weak for fuel equivalence ratios of 1.0 and 1.1, with an opposite effect visible for a fuel equivalence ratio of 1.2. The same mechanisms identified as causing the effect on the laminar flame speed in Figure 4.17 (a), are causing the observed sensitivity of the Markstein lengths to fuel diffusion. Since a more curved flame or a flame with a small radius has a higher ratio of contact area with unburned gas to flame volume, a variation in fuel diffusion into the flame will be more severe. This then results in the Markstein length being sensitive to the fuel diffusion coefficient for fuel lean mixtures where fuel is the limiting reagent, as seen in Figure 4.17 (b).

4.6.3. Sensitivity to intermediate molecule diffusion

In the current model the intermediate species is given the same properties as the fuel. However, it represents a whole spectrum of possible species that form as the fuel molecules break down. These intermediate species can therefore vary in size and complexity and include free radicals. The assumption made that this is a single species and that it has the same properties as the fuel is based on the fact that these species only exist in small amounts in the reaction zone. However, it is very likely that these intermediate species are mostly made up of relatively small molecules such as methyl and hydrogen radicals. These smaller species have different molecular transport properties and will diffuse much faster than an intermediate species with the same properties as the fuel. Therefore, the properties of intermediate species are varied to show how an intermediate representing smaller and larger molecules will influence the flame characteristics. To represent a smaller intermediate species, the properties of the methyl radical from the mechanism of Mehl et al. (2011) are used.

If the intermediates are to diffuse much faster, the reaction mechanism will be influenced severely in that the intermediate concentration profile will be more flat. This will result in slower overall reaction rates, since more time will be required to reach the critical intermediate concentration where rapid heat release is triggered. Therefore, the reaction stoichiometry is also adjusted to form eight moles of intermediate for every mole of fuel that reacts. Since the reaction stoichiometry is adjusted, the reaction rate function is

also adjusted to counteract the stoichiometry adjustment. This ensures that the reaction mechanism is only affected by the increased diffusion of intermediate species and not by the adjusted stoichiometry. For a slower intermediate diffusion, the same approach as discussed above is used, but here the intermediate is given the properties of n-decane from the mechanism of Mehl et al. (2011). The effects of the these variations on the flame speed of an iso-octane and air mixture at initial conditions of 370 K and 1 bar is shown in Figure 4.18, where low refers to the low diffusion expected from the n-decane properties and high refers to the high diffusion expected from the methyl radical properties.

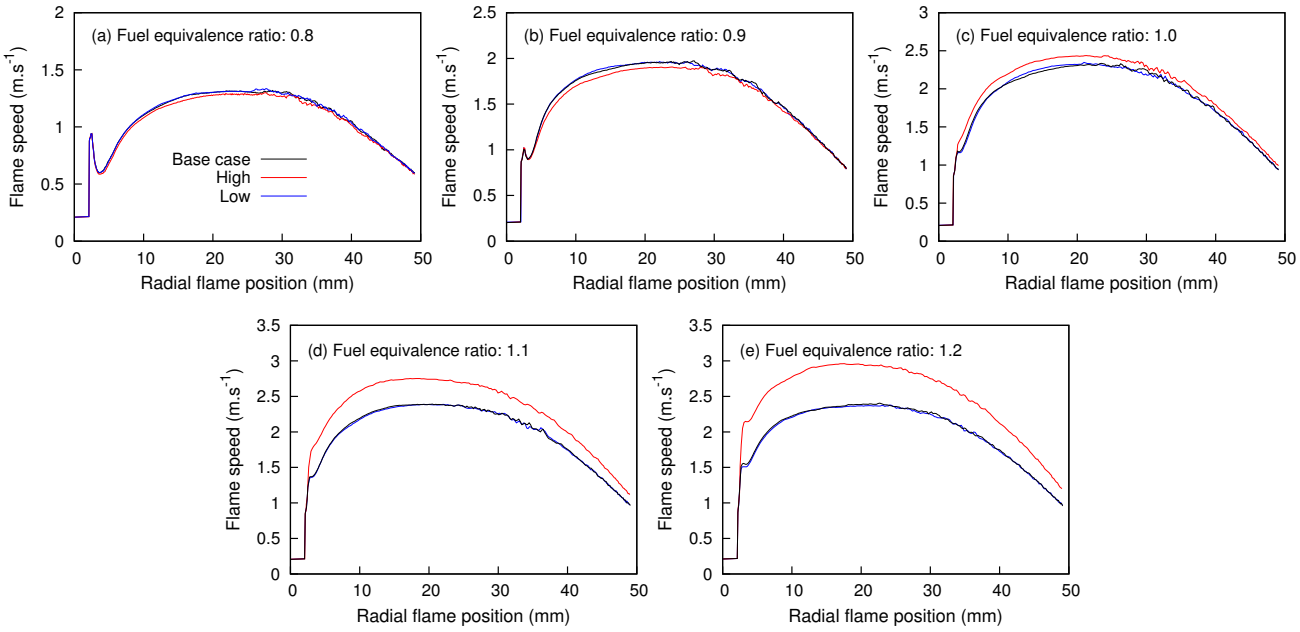

Figure 4.18.: Sensitivity of the flame speed to variation in the intermediate species (X) diffusion properties for an iso-octane and air mixture at initial temperature and pressure of 370 K and 1 bar.

Figure 4.18 (a) and (b) shows that for fuel lean mixtures ($\phi < 1.0$), a smaller intermediate species, having a higher diffusivity, causes a slight decrease in flame speed. This effect is observed since the fuel is the limiting reagent for fuel lean mixtures and a faster diffusion of intermediates will result in more fuel having to react in order to reach the critical intermediate concentration to trigger rapid heat release. The higher continuous diffusion of intermediates out of the reaction zone results in lower rates of heat release and hence the flame speeds are lower. The opposite effect is seen in Figure 4.18 (c), (d) and (e), where a smaller molecule that represents the intermediate species causes the flame

speeds to increase for the stoichiometric and fuel rich mixtures ($\phi \geq 1.0$). For the fuel rich mixtures, the fuel is in excess and, at the high temperatures in the burned gas, the fuel will react to form high concentrations of the unreacted intermediate, due to the unavailability of oxygen. When the intermediate species are represented by a smaller molecule, the intermediates will diffuse faster from the burned gas into the reaction zone, causing a higher rate of heat release.

Therefore two opposite effects are seen in Figure 4.18 for a higher intermediate diffusion caused by the smaller intermediate species. In Figure 4.18 (a) and (b) the fuel is the limiting reagent and when the intermediates diffuse out of the reaction zone faster, the rate limiting step is slowed down and the rate of heat release is decreased, causing lower flame speeds. In Figure 4.18 (c), (d) and (e), the fuel is in excess causing a reservoir of intermediates in the burned gas, where a higher diffusion into the reaction zone will cause an increase in the rate of heat release and therefore higher flame speeds. The increase in size of the molecule that represents the intermediate species, resulting in slower diffusion, does not significantly influence the flame speeds in Figure 4.18. The effects observed in Figure 4.18 is quantified by obtaining the laminar flame speed and Markstein length for each case and comparing it in Figure 4.19.

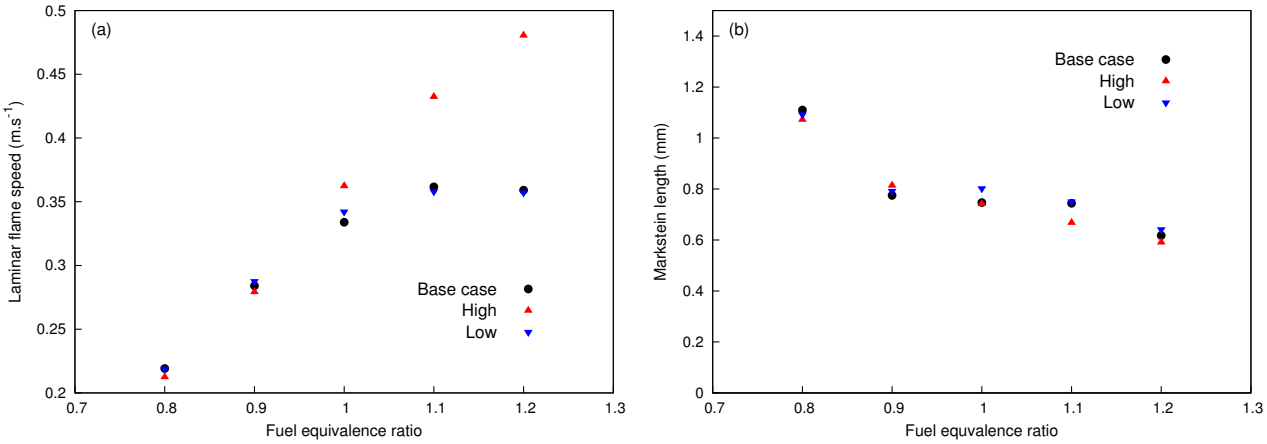

Figure 4.19.: Sensitivity of the laminar flame speed (a) and Markstein length (b) to a variation in the intermediate species (X) diffusion properties for an iso-octane and air mixture at initial temperature and pressure of 370 K and 1 bar.

Figure 4.19 (a) shows that a smaller intermediate species causes a higher intermediate diffusion that significantly increases the laminar flame speed for mixtures with a fuel equivalence ratio of 1.0, 1.1 and 1.2. For fuel lean mixtures in Figure 4.19 (a), the

smaller intermediate species caused the laminar flame speed to decrease. The slightly lower laminar flame speeds of the fuel lean mixtures is ascribed to the flattening of the intermediate concentration peak, due to the higher diffusion of the smaller molecules. This is shown in Figure 4.20, where the mole fractions of the intermediate species (X) and temperature profile across the flame front at a position of 10 mm is shown.

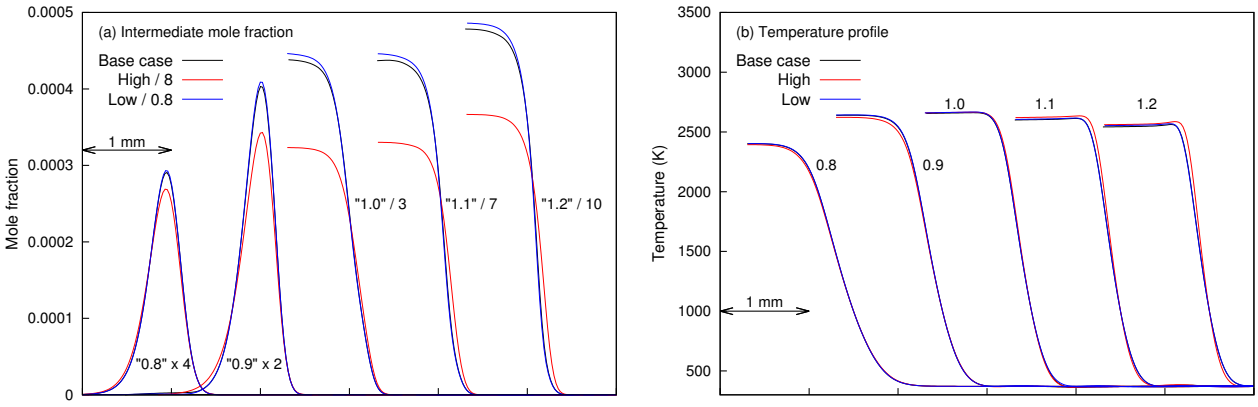

Figure 4.20.: Sensitivity of the intermediate (X) mole fraction (a) and temperature (b) across the flame front at a flame position of 10 mm to a variation in the intermediate species diffusion properties.

In Figure 4.20 (a), the mole fractions for the smaller intermediate with higher diffusion (high) is divided by 8 and that of the bigger molecules (low) is divided by 0.8 to yield profiles that can be compared. Further, the intermediate mole fractions for different fuel equivalence ratios in Figure 4.20 (a) are also scaled as indicated for better resolution of the profiles. Figure 4.20 (a) then shows that, for the fuel equivalence ratios of 0.8 and 0.9, the smaller intermediate (high) resulted in a wider or flatter peak in the intermediate mole fractions. This causes a lower heat release rate and therefore lower flame speeds. The higher laminar flame speeds obtained for the stoichiometric and fuel rich mixtures in Figure 4.19 (a), are caused by the faster diffusion of the smaller molecules from the high intermediate concentrations in the burned gas into the reaction zone. This causes the critical intermediate concentration to be reached faster, resulting in higher flame speeds. Figure 4.20 (a) shows the high intermediate mole fractions in the burned gas for fuel equivalence ratios of 1.0, 1.1 and 1.2. The larger molecule representing the intermediate species and therefore resulting in slower intermediate diffusion, does not have a significant effect on the laminar flame speeds, as shown in Figure 4.19 (a).

For the fuel lean mixtures in Figure 4.19 (b), the variation of the intermediate molecule size has very small effects on the Markstein lengths. However, for the stoichiometric and fuel rich mixtures, the smaller molecule representing the intermediate species causes the Markstein lengths to decrease slightly, as shown in Figure 4.19 (b). Further investigation shows that smaller intermediate molecules cause the flame thickness to decrease. This is seen in Figure 4.20 (b), where the temperature gradient for the fuel rich mixtures are steeper for the smaller intermediate molecules (high). This is because the critical intermediate concentration is reached faster when the smaller molecule diffuses faster from the high intermediate concentrations in the burned gas. For a thinner curved flame, the difference between the inner and outer flame surface areas is less compared to a thicker flame, which suggests that the flame speed of a flame with a lower flame thickness is less sensitive to the flame stretch rate. Again, the influence of a larger molecule representing the intermediate species on the Markstein lengths in Figure 4.19 (b) is very small.

The use of a smaller intermediate molecule, such as the methyl radical, in the model, will represent a flame more realistically. However, Figure 4.19 (a) shows that the way a smaller intermediate species is implemented here is not producing sensible results. Further improvement of this model should include the implementation of a chemical kinetic model that provides more representative intermediate species.

4.6.4. Sensitivity to thermal conductivity

Another property of the mixture that may vary for different fuel molecules is the thermal conductivity of the mixture. The thermal conductivity for a mixture of species is calculated from Equation 3.79 in this model. Although the thermal conductivity of pure fuel components varies significantly, the reaction stoichiometry causes the fuel and air mixture to be made up of mostly nitrogen. For this reason, a fuel with a relatively high pure thermal conductivity will result in only a fractionally higher thermal conductivity for a stoichiometric fuel and air mixture. Hydrogen is an exception to this because of its high thermal conductivity and stoichiometry, resulting in combustion mixtures with very high thermal conductivities. The variation of the unburned gas thermal conductivity for different fuels is considered to establish the required variation. Although the variation suggested here is aimed at the thermal conductivity of the unburned gas, the thermal conductivity of the all stages of the flame, including the burned gas, is varied by the same percentage.

To obtain a sensible amount to vary the mixture thermal conductivity by, the thermal conductivity of a stoichiometric mixture of methane and air is considered. Although pure methane has a thermal conductivity that is more than twice that of pure iso-octane, it results in a stoichiometric mixture with air with a thermal conductivity that is approximately 5% higher than that of a stoichiometric iso-octane and air mixture at 400 K. Therefore the thermal conductivity of the mixture at any point is varied by 5% to see the effect on the flame characteristics and the resulting flame speeds are shown in Figure 4.21.

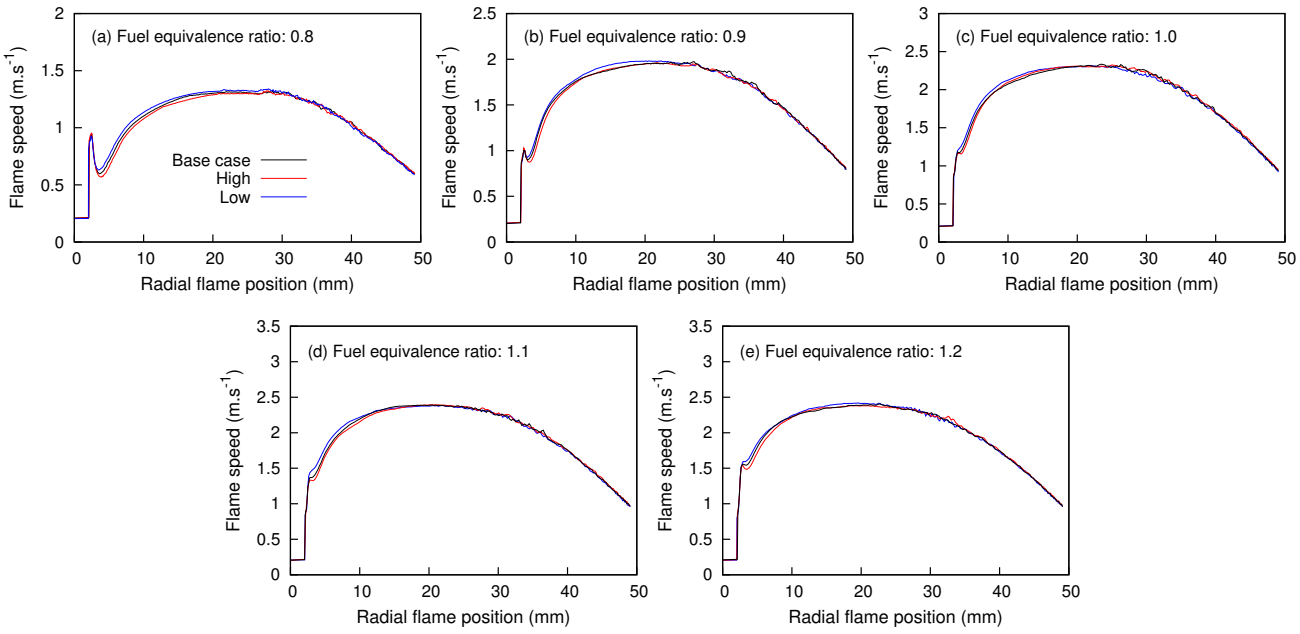

Figure 4.21.: Sensitivity of the flame speed to a 5% variation in the thermal conductivity (λ) of an iso-octane and air mixture at initial temperature and pressure of 370 K and 1 bar.

The effect of the variation in thermal conductivity of the mixture on the flame speeds is very small in Figure 4.21. Although, for smaller flame radii (< 10 **mm**), Figure 4.21 shows that a higher thermal conductivity of the mixture results in a slower flame speed. This effect is not intuitive and is explained by the combined effect of flame curvature and thermal conductivity. For a highly curved flame or a flame with a small radius (< 10 **mm**), the flame is in contact with more cold, unburned gas. In this case, a higher thermal conductivity will transfer heat away from the reaction zone into the cold unburned gas faster. This results in lower temperatures in the reaction zone, causing slower reactions and therefore a slower rate of heat release. This effect disappears for flames with a larger

radius, where the flame is in contact with less cold, unburned gas, requiring less energy to heat up and therefore having a smaller effect on the rate of heat release. This effect is better shown in the laminar flame speeds and Markstein lengths calculated for this sensitivity study. The laminar flame speed and Markstein lengths are calculated from the nonlinear regression of the data and the results are shown in Figure 4.22.

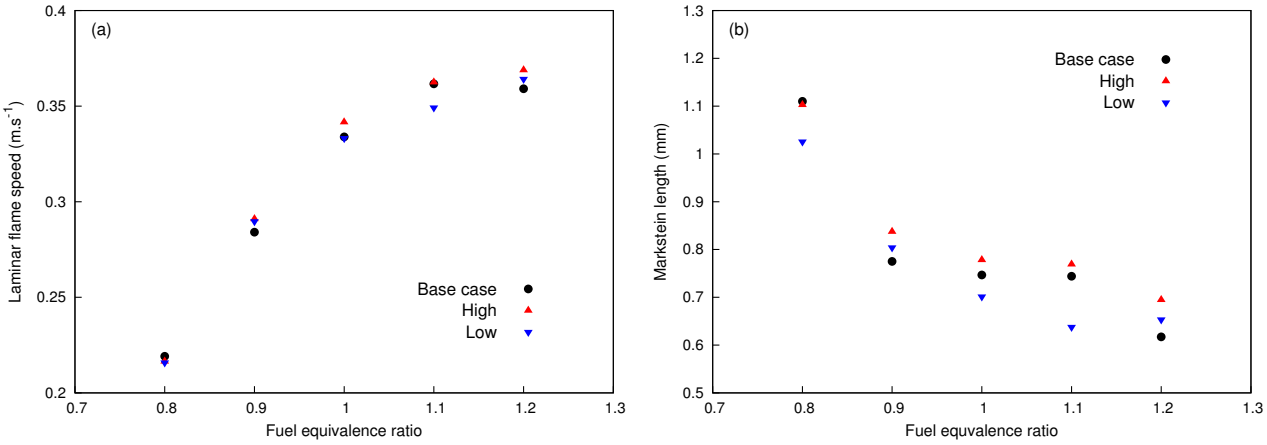

Figure 4.22.: Sensitivity of the laminar flame speed (a) and Markstein length (b) to a 5% variation in the thermal conductivity for an iso-octane and air mixture at initial temperature and pressure of 370 K and 1 bar.

The laminar flame speeds of the fuel lean mixtures ($\phi < 1.0$) in Figure 4.22 (a) are not affected significantly by the variation in thermal conductivity. However, for the stoichiometric and fuel rich mixtures ($\phi \geq 1.0$) in Figure 4.22 (a), the higher thermal conductivities produced a slightly higher laminar flame speed. Figure 4.22 (b) shows that an increase in the thermal conductivity of the mixtures produces higher Markstein lengths for the flames. Thus, a higher thermal conductivity renders the flame speed more sensitive to the flame stretch rate. This is expected from Figure 4.21, where the flames with higher thermal conductivities have lower flame speeds at small flame radii and this difference decreases as the flame radius increases.

Thus, for the fuel lean mixtures in Figure 4.22 (a), the laminar flame speeds stay virtually unchanged for a variation in the mixture thermal conductivity, while the Markstein lengths in Figure 4.22 (b) show a significant sensitivity. This suggest that this effect is caused by the same combined effect of the flame curvature and thermal conductivity discussed above. The stoichiometric and fuel rich mixtures in Figure 4.22 show that the laminar flame speeds increase slightly and the Markstein lengths increase significantly for an increase in thermal

conductivity of the mixture. It is clear from Figure 4.22, that the laminar flame speeds show a relatively weak sensitivity to the thermal conductivity, while the Markstein lengths show a stronger sensitivity.

4.6.5. Sensitivity to the reaction kinetics

The reaction kinetics is regarded as the most prominent fuel property that influences the flame speed (Farrell et al., 2004) and it is therefore important to show the sensitivity of the model-predicted flame characteristics to this fuel property. Again, the aim is to adjust the reaction kinetics to compare with that of another fuel and to then show how this effects the model-produced results. Toluene has higher ignition delay times than iso-octane, even in the higher temperatures (above 1 000 K) and also falls in the gasoline range with iso-octane. The reaction kinetics in this model are simply adjusted to be slower by changing the pre-exponential parameter of Reaction 1 in Table 2.3 until the ignition delay times calculated by the model agree with experimental data. Experimental ignition delay data for toluene at the conditions of interest to this study is not widely available, but experimental data used in Figure 4.23 is sufficient. The ignition delay time data for a stoichiometric toluene and air mixture at 20 bar is obtained from a detailed kinetic mechanism (Mehl et al., 2009) and is also shown in Figure 4.23.

The pre-exponential parameter of Reaction 1 in Table 2.3 is reduced from 5×10^8 to 1×10^8 to give the results in Figure 4.23. It is shown in Figure 4.23 that, above a temperature of 1 000 K, the 10 bar ignition delay times calculated by the model, closely resembles the experimental ignition delay data for toluene at 13 bar. However, the adjustment to the kinetic model employed in this work does not produce ignition delay data for toluene, that agree with that obtained from the detailed kinetic mechanism in Figure 4.23. At temperatures higher than 1 200 K, there is agreement between the ignition delay data obtained from the adjusted kinetic model of this work and that obtained from the detailed kinetic mechanism Mehl et al. (2009). However, in Figure 4.23 a sharper increase in ignition delay as the temperature decreases, is seen for the data from the detailed kinetic mechanism, as compared to that of the kinetic model of this work.

Figure 4.23 confirms that at a temperature of 1 200 K, the ignition delay data for toluene from the adjusted model used in the current study compares well with the experimental data for toluene at 13 bar (Pasternak et al., 2008) and the modelled data at 20 bar from the detailed kinetic mechanism (Mehl et al., 2009). It is therefore sufficient to conclude

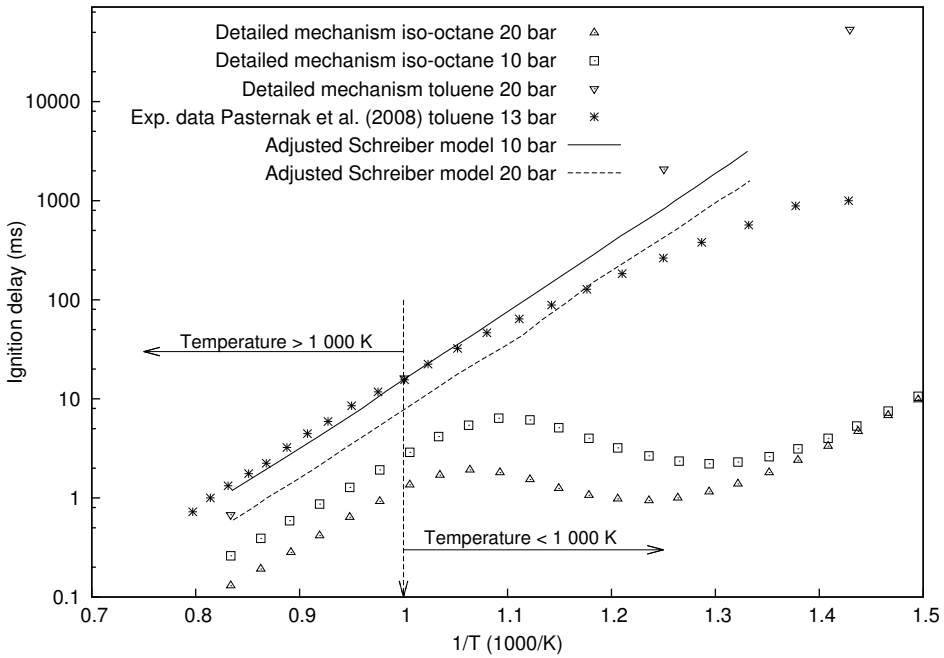

Figure 4.23.: Ignition delay times for iso-octane and toluene, with the results from adjusted model that resembles the toluene data. The detailed mechanism is from Mehl et al. (2009) and the experimental data is from Pasternak et al. (2008).

that the adjustment to the reaction kinetics for the current study, produces ignition delay times that are similar to that of toluene at higher temperatures. The reaction kinetics are therefore decreased to approximate that of toluene and the effects on the flame speeds from this is shown in Figure 4.24.

The flame speeds for all the fuel and air mixtures investigated in Figure 4.24 are much lower for the decreased kinetics than for the base case. The initial decrease in flame speed after the ignition event is also more severe when the reaction kinetics are slower, indicating that the minimum ignition energy required for flame initiation increases when the reaction kinetics decreases. The slower reaction kinetics decreases the heat release rate in the reaction zone, resulting in slower flame propagation speeds. The slower reaction kinetics also causes a thicker flame, or a decreased temperature gradient, since there is more time available for the heat to transfer deeper into the unburned gas.

After the ignition energy effects, the flame speeds for the reduced reaction kinetics show the same behaviour as that of the base case flame speeds in Figure 4.24. The increase in flame speed due to the decrease in flame stretch rate and the following decrease in

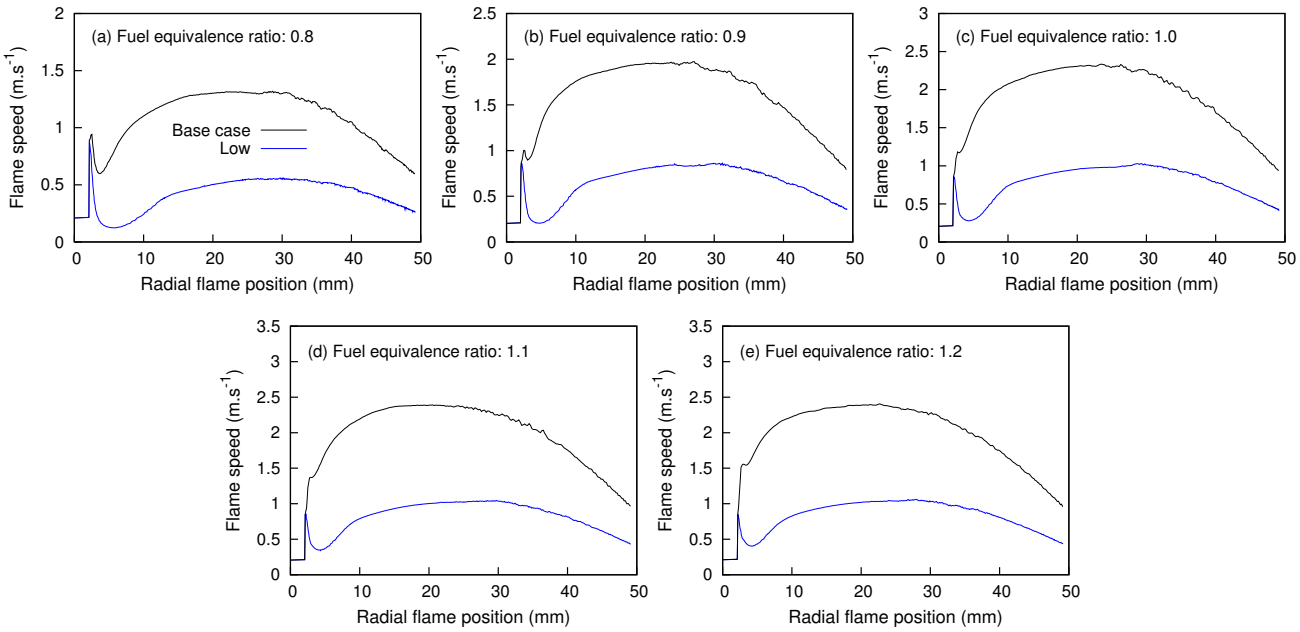

Figure 4.24.: Sensitivity of the flame speed to variation in the combustion reaction kinetics for an iso-octane and air mixture at initial temperature and pressure of 370 K and 1 bar.

flame speed due to the pressure increase inside the combustion chamber are seen for the flames with reduced reaction kinetics. However, the maximum flame speed for the reduced reaction kinetics is reached at greater flame radii than that of the base case in Figure 4.24. Therefore the model-produced data for the reduced reaction kinetics shows that the flame speeds are less sensitive to a pressure increase. This is caused by the decreased temperature gradient across the flame front, heating more unburned gas ahead of the flame while the density or pressure of the gas has a smaller effect. This large variation in the flame speeds of Figure 4.24 is also seen for both the laminar flame speeds and Markstein lengths as shown in Figure 4.25.

The laminar flame speeds for the reduced reaction kinetics in Figure 4.25 (a) show more than a 10 $\mathbf{cm.s^{-1}}$ decrease compared to the base case for the complete range of fuel and air mixtures modelled. This drastic decrease in laminar flame speeds is expected from the flame speed data in Figure 4.24 and is again explained by the lower rate of heat release that translates into lower flame speeds. The reduced reaction kinetics cause significantly higher Markstein lengths in Figure 4.25 (b), implying that the reduced reaction kinetics

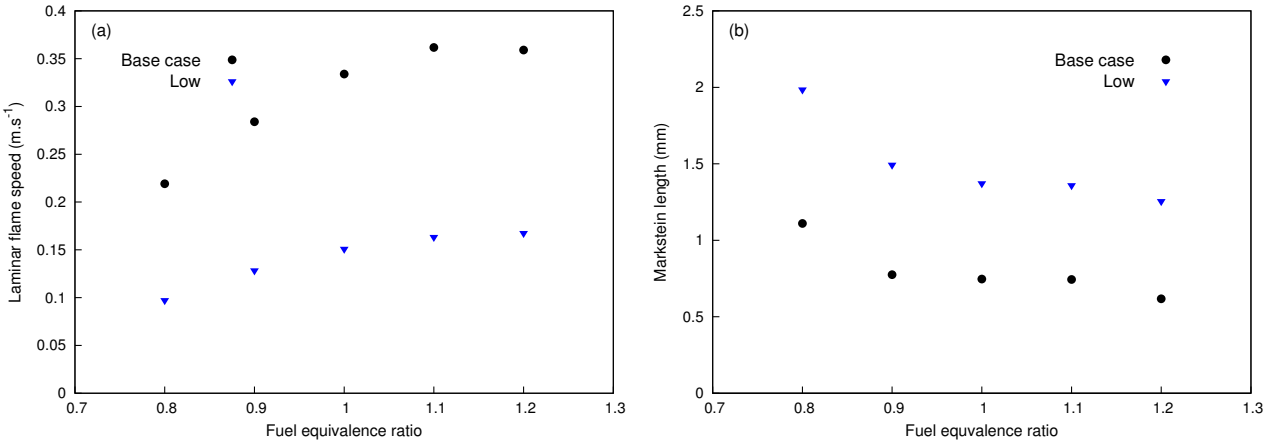

Figure 4.25.: Sensitivity of the laminar flame speed (a) and Markstein length (b) to a variation in the combustion reaction kinetics for an iso-octane and air mixture at initial temperature and pressure of 370 K and 1 bar.

causes the flame speeds to be more sensitive to the flame stretch rate. The slower flames of the reduced kinetics have much greater flame thicknesses or lower temperature gradients across the flame front, causing the flame speeds to be more sensitive to the curvature of the flame and therefore have higher Markstein lengths. Interestingly, the flame speed reported by Farrell et al. (2004) for toluene is greater than that reported for iso-octane (base case). However, only the reactions kinetics in this sensitivity study represents that of toluene, while the rest of the fuel properties still represents iso-octane. This indicates that the higher adiabatic flame temperature of toluene has a strong effect and causes a higher flame speed.

4.7. Summary of results

The model is improved by reducing the diffusion coefficient of oxygen by 75% in order to produce more accurate flame profiles, as shown in Figure 4.13 (a). Figure 4.8 in Section 4.3 shows the ability of the model to describe the pressure increase, where a spherical flame in a spherical combustion chamber from the experimental work of Yates et al. (2012) is simulated. The model-produced flame speeds are compared to the experimental flame speeds measured by Bradley et al. (1998) and Yates et al. (2012) in Figure 4.9.

Although the accuracy is improved by the adjustment to the oxygen diffusion, there is still a notable difference between the model-produced flame speeds and the experimental data.

Nevertheless, the model produces a flame speed that decreases as the flame approaches the combustion chamber wall, very similar to what is shown in the experimental work of Yates et al. (2012). Further, the modelled flames show both the ignition behaviour and initial flame speed increase due to a decreasing flame stretch rate that is also observed in the experimental flames of Bradley et al. (1998) when comparing Figure 4.11 and Figure 2.19. Therefore the model succeeds in describing the complex behaviour of a spherical flame propagating through a closed volume and can be used to gain a better understanding of the fundamental mechanisms that cause this behaviour.

The laminar flame speeds are calculated for the mixtures modelled and this also yields the Markstein lengths of the mixtures. The laminar flame speeds and Markstein lengths derived from the model data, are compared to experimental data from literature in Figure 4.13. Here the model produces laminar flame speed trends similar to those of literature and Markstein lengths that resemble both the values and trends from literature.

Although the model lacks accuracy, it is employed to show the qualitative effects of certain fuel properties on the flame behaviour in order to compare model-predicted responses to that in literature and give insight into the fundamental mechanisms that govern these behaviours. This is achieved through the sensitivity analyses where the laminar flame speed and Markstein length are the measure responses when varying fuel properties. The sensitivity of the laminar flame speeds to the respective parameters is given in Table 4.4, where it is taken as the percentage calculated from the difference between the high and low responses divided by the response for the base case.

Table 4.4.: Laminar flame speed sensitivities at 370 K and 1 bar.

Fuel equivalence ratio		0.8	0.9	1.0	1.1	1.2
Base case laminar flame speed $(m.s^{-1})$		0.219	0.284	0.334	0.362	0.359
	% varied	Sensitivities				
Oxygen diffusion	40%	1%	0%	8%	11%	13%
Fuel molecule diffusion	40%	14%	13%	2%	-4%	0%
Intermediate diffusion		-3%	-3%	6%	21%	35%
Thermal conductivity	10%	0%	0%	3%	4%	1%
Reaction kinetics		56%	55%	55%	55%	53%

Similarly, the sensitivities of the Markstein lengths calculated from the model data to the varied parameters are given in Table 4.5.

The sensitivities in Tables 4.4 and 4.5 give the model-predicted laminar flame speed and Markstein length responses to changes of the fuel properties. Some of the responses or

Table 4.5.: Markstein length sensitivities at 370 K and 1 bar.

Fuel equivalence ratio		0.8	0.9	1.0	1.1	1.2
Base case Markstein length (mm)		1.11	0.78	0.75	0.74	0.62
	% varied	Sensitivities				
Oxygen diffusion	40%	0%	-9%	-15%	-11%	-13%
Fuel molecule diffusion	40%	-19%	-5%	2%	-4%	14%
Intermediate diffusion		-2%	3%	-8%	-11%	-8%
Thermal conductivity	10%	8%	4%	11%	21%	6%
Reaction kinetics		-79%	-93%	-84%	-83%	-103%

sensitivities from Tables 4.4 and 4.5 have been reported in literature.

4.8. Sensitivities from literature

There are very few similar sensitivity studies found in literature and therefore comparisons are limited. Several sensitivity studies have been done on the reaction kinetics (Holley et al., 2009, Kumar et al., 2007, Davis and Law, 1998). However, these studies were usually for flat flames with detailed chemical kinetic mechanisms to show which reactions are the rate determining steps. In the work of Chen (2009), the flame speeds and burned gas Markstein lengths of different mixtures of methane and dimethyl-ether (DME) were simulated. By adding more DME to the mixture, the effective fuel diffusion was decreased, which caused an increase in the Markstein length for the fuel lean mixtures. This confirms the negative sensitivity of the Markstein length to the fuel diffusion for the fuel lean mixtures in Table 4.5.

The possibility of these kind of comparisons are rare, since the fuel properties are not varied independently from each other, as for the above case where the thermal conductivity of the mixture will change as well when the DME content is increased. Another such a comparison is possible from the work of Clingman and Pease (1956), where different inert gases were used in a methane and oxygen flame, shown in Figure 2.10 in Section 2.2.3. Here, the use of helium, with a higher thermal conductivity, instead of argon resulted in higher flame speeds for fuel lean and fuel rich mixtures. This then confirms the positive sensitivities of the laminar flame speeds to thermal conductivity in Table 4.4.

The diffusion of propane and octane molecules differs, where propane has a 1.7 times higher diffusion coefficient than octane (Bechtold and Matalon, 2001). The work of Bechtold and Matalon (2001) shows that the Markstein lengths of octane and propane

differ more for fuel lean mixtures than for fuel rich mixtures, showing that the smaller fuel molecule will have a lower Markstein length. This then confirms the sensitivities of the Markstein lengths to the fuel diffusion reported in Table 4.5, where a higher fuel diffusion causes a lower Markstein length and this effect decreases for more fuel rich mixtures.

The experimental laminar flame speeds reported for toluene and iso-octane in the work of Johnston and Farrell (2005) at 450 K and 304 kPa, are reported as very similar. The Markstein lengths reported by Johnston and Farrell (2005) for toluene are also lower than that of iso-octane. However, Table 4.4 shows that for a fuel with similar ignition delay times as that of toluene, the current model produce laminar flame speeds that are of the order of 50% lower than that of iso-octane. Table 4.5 shows that the Markstein lengths of a fuel with similar ignition delay times as toluene have much higher Markstein lengths than that of iso-octane. This comparison therefore does not show agreement, due to the sensitivities of Table 4.4 and Table 4.5 being obtained by changing only the reaction kinetics. Other fuel properties of toluene, such as higher fuel diffusion and a higher adiabatic flame temperature, also play a role to produce the experimental results reported by Johnston and Farrell (2005). This then shows that comparisons from literature with the results in Table 4.4 and Table 4.5 are challenging, since no similar studies have been done.

The model therefore succeeds in describing the complex behaviour of an outwardly propagating, spherical flame and can be used to make qualitative predictions on the effects of different fuel properties, as well as how the experimental setup will influence the experimental results.

5. Conclusion

The laminar flame speed of a fuel is a fundamental combustion property that impacts engine efficiencies and has been extensively studied both experimentally and theoretically. In this study, a very common experimental setup for laminar flame speed measurements, the constant volume combustion bomb, is modelled. It is the aim of this model to describe the behaviour of an outwardly propagating spherical flame in a closed volume, as is the case for a constant volume combustion bomb. This behaviour includes the laminar flame speed, the Markstein length and the response of the flame speed to an increasing pressure in the closed volume. For this study, a mixture of iso-octane and air is considered at initial conditions of 370 K and 1 bar at different fuel equivalence ratios.

The model results show a flame front that propagates through the spatial domain. The uniform pressure across the spatial domain increases as the flame front approaches the combustion chamber wall at a radius of 50 mm, as shown in Figure 4.1. The oxygen diffusion coefficient is adjusted to 25% of the originally calculated value to produce a more accurate flame speed trend over different fuel equivalence ratios. A list of key results from the modelling of the flame behaviour is given:

- The flame speed versus flame radius trends in Figure 4.9 show how the model succeeds in describing the flame speed increase as the flame stretch rate decreases during the initial stages of flame propagation.
- Figure 4.9 also show how the model succeeds in describing the flame speed decrease as the pressure of the system increases in the final stages of flame propagation.
- It is seen in Figure 4.11 that the trends produced by the model show agreement with the experimental trends in Figure 2.19 from Bradley et al. (1998).
- Table 4.2 shows that the laminar flame speeds derived from the nonlinear regression are on average 3 $\mathbf{cm.s^{-1}}$ lower than the laminar flame speeds derived from the linear regression[1].

[1] See Equations 2.34 and 2.37.

- Figure 4.13 (a) shows that the laminar flame speed from the model goes through a maximum around a fuel equivalence ratio of 1.1.
- The laminar flame speeds produced by the model in Figure 4.13 (a) are lower than the experimentally obtained laminar flame speeds.
- The Markstein lengths produced by the model in Figure 4.13 (b) show good agreement with the experimental data, which shows a decreasing trend as the fuel equivalence ratio increases.

The model is used to produce a sensitivity analysis of the laminar flame speeds and the Markstein lengths with respect to oxygen, fuel and intermediate molecule diffusion as well as thermal conductivity and reaction kinetics. The aim of the sensitivity analysis is to provide insight into the effect that the fundamental mixture properties have on the flame behaviour for a constant volume combustion bomb. The results for the sensitivity of the laminar flame speeds are given in Table 4.4 and that for the Markstein lengths are given in Table 4.5. A list of the conclusions from the sensitivity analysis follows:

- The sensitivity of the laminar flame speed to oxygen diffusion shows an opposite trend to that of the sensitivity to fuel diffusion with regards to fuel equivalence ratio in Table 4.4. This is also seen for the Markstein length sensitivities in Table 4.5.
- The sensitivity of the flame behaviour to different intermediate molecule properties shows that a smaller intermediate molecule will decrease the laminar flame speed of a fuel lean mixture, but increase that of a fuel rich mixture.
- Table 4.4 shows that the laminar flame speed displays a low sensitivity to a typical variation in the thermal conductivity of the system. However, the Markstein length sensitivities in Table 4.5 show that an increase in the thermal conductivity results in a flame speed that is more sensitive to the flame stretch rate.
- The effect of varying the thermal conductivity on the Markstein length is the opposite effect as what is seen for varying the oxygen and fuel diffusion, where an increase in diffusion causes a decrease in the Markstein length for the mixture where the species is the limiting reagent.
- The slower reaction kinetics result in lower laminar flame speeds and higher Markstein lengths.

In Section 4.7, the results of the sensitivity analyses are compared to similar effects found in literature. However, the same type of sensitivity analysis cannot be found in literature.

For most cases the sensitivity analysis produces results that agrees with effects found in literature. The sensitivity analysis provides some insights as to what might be expected for the results from fuels with different properties in a constant volume combustion bomb.

Some recommendations for further study and development of this work are listed below:

- The incorporation of more complex reaction mechanisms where more realistic intermediate species are defined may result in better predictions for the laminar flame speeds in Figure 4.13. However, it is suggested that reaction mechanisms that include reversible reactions be avoided, since this significantly increases the time required by the solver to solve the system.
- As mentioned before, the high temperature part of the reaction mechanism of Schreiber et al. (1994) used in this study proves to be sufficient. It is therefore suggested not to include low temperature reaction mechanisms unnecessarily, since they are more complex and include reversible reactions.
- The ignition event approach employed in this study results in ignition effects that are unexpectedly similar to those in experimental data. It is suggested that the ignition effects on initial flame behaviour are studied, which can be done by employing more realistic ignition event approaches together with sensitivity analyses.
- The set of conditions modelled in this work can easily be expanded to different fuels, reaction mechanisms and geometric systems, such as larger combustion bombs or cylindrical flames. Even though the model as it stands now lacks some accuracy, it is capable of producing qualitative results for complicated flame characteristics.

It is therefore concluded that the model succeeds in delivering on the research objectives listed in Section 1.3. However, the accuracy of the results can be improved. When considering the complex interaction of fundamental properties that take place in a flame, the value of a model like the one developed in this work is appreciated. Since it models these interactions and produces results that predicts the flame behaviour of experimental setups, the model enables one to gain insight into the fundamental mechanisms of the flame propagation process.

Bibliography

Afeefy, H. Y., Liebman, J. F. and Stein, S. E. *NIST Chemistry WebBook, Nist Standard Reference Database*, chapter Neutral Thermochemical Data, page 20899. Number 69. National Institute of Standards and Technology, Gaithersburg MD, 2011. retrieved July 12, 2012.

Ashman, P. J. and Haynes, B. S. Rate coefficient of H+O2+M->HO2+M (M=H2O, N2, Ar, CO2). *Symposium (International) on Combustion*, 27(1):185–191, 1998. ISSN 0082-0784. Twenty-Seventh Sysposium (International) on Combustion Volume One.

Bechtold, J. K. and Matalon, M. Effects of stoichiometry on stretched premixed flames. *Combustion and Flame*, 119(3):217–232, 1999. ISSN 0010-2180.

Bechtold, J. K. and Matalon, M. The dependence of the markstein length on stoichiometry. *Combustion and Flame*, 127(1-2):1906–1913, 2001. ISSN 0010-2180.

Bird, R. B., Stewart, W. E. and Lightfoot, E. N. *Transport phenomena*. Wiley International edition. J. Wiley, 2002. ISBN 9780471410775.

Bourdon, A., Rymer, G. and Wanker, R. Optimization of a 5-step kinetic scheme for HCCI applications. *S.A.E. transactions.*, 113:357–366, 2004. ISSN 0096-736X. 2004-01-0559.

Bradley, D., Hicks, R. A., Lawes, M., Sheppard, C. G. W. and Woolley, R. The measurement of laminar burning velocities and markstein numbers for iso-octane-air and iso-octane-n-heptane-air mixtures at elevated temperatures and pressures in an explosion bomb. *Combustion and Flame*, 115(1-2):126–144, 1998. ISSN 0010-2180.

Bradley, D., Gaskell, P. H. and Gu, X. J. Burning velocities, markstein lengths, and flame quenching for spherical methane-air flames: A computational study. *Combustion and Flame*, 104(1-2):176–198, 1996. ISSN 0010-2180.

Brenan, K. E., Campbell, S. L., Campbell, S. L. V. and Petzold, L. R. *Numerical Solution of Initial-Value Problems in Differential-Algebraic Equations*. Classics in Applied Math-

ematics. Society for Industrial and Applied Mathematics, 1989. ISBN 9780898713534.

Chen, Z., Burke, M. P. and Ju, Y. Effects of compression and stretch on the determination of laminar flame speeds using propagating spherical flames. *Combustion Theory and Modelling*, 13(2):343–364, 2009.

Chen, Z. *Studies on the initiation, propagation, and extinction of premixed flames*. PhD thesis, Princeton University, 2009.

Chen, Z. On the extraction of laminar flame speed and markstein length from outwardly propagating spherical flames. *Combustion and Flame*, 158(2):291–300, 2011. ISSN 0010-2180.

Chen, Z., Qin, X., Xu, B., Ju, Y. and Liu, F. Studies of radiation absorption on flame speed and flammability limit of CO2 diluted methane flames at elevated pressures. *Proceedings of the Combustion Institute*, 31(2):2693–2700, 2007. ISSN 1540-7489.

Clingman, W. H. and Pease, R. N. Critical considerations in the measurement of burning velocities of bunsen burner flames and interpretation of the pressure effect. measurements and calculations for methane1. *Journal of the American Chemical Society*, 78 (9):1775–1780, 1956.

Curran, H. J., Gaffuri, P., Pitz, W. J. and Westbrook, C. K. A comprehensive modeling study of iso-octane oxidation. *Combustion and Flame*, 129(3):253–280, 2002. ISSN 0010-2180.

Dagaut, P. On the kinetics of hydrocarbons oxidation from natural gas to kerosene and diesel fuel. *Phys. Chem. Chem. Phys.*, 4:2079–2094, 2002.

Daintith, J. *A Dictionary of Chemistry*. Oxford Dictionary of Chemistry. Oxford University Press, Oxford, UK, 5th edition, 2004. ISBN 9780198609186.

Davis, S. G. and Law, C. K. Laminar flame speeds and oxidation kinetics of iso-octane-air and n-heptane-air flames. *Symposium (International) on Combustion*, 27(1):521–527, 1998. ISSN 0082-0784. Twenty-Seventh Sysposium (International) on Combustion Volume One.

Duncan, J. B. and Toor, H. L. An experimental study of three component gas diffusion. *AIChE Journal*, 8(1):38–41, 1962. ISSN 1547-5905.

Ebara, T., Iki, N., Takahashi, S. and Park, W.-H. Effect of radiation reabsorption on laminar burning velocity of methane premixed flame containing with steam and carbon

dioxide. *JSME International Journal Series B Fluids and Thermal Engineering*, 49(2): 260–264, 2006.

Far, K. E., Parsinejad, F. and Metghalchi, H. Flame structure and laminar burning speeds of JP-8/air premixed mixtures at high temperatures and pressures. *Fuel*, 89(5):1041–1049, 2010. ISSN 0016-2361.

Farrell, J. T., Johnston, R. J. and Androulakis, I. P. Molecular structure effects on laminar burning velocities at elevated temperature and pressure. *Society of Automotive Engineers Inc*, 2004-01-29:36, 2004.

Floweday, G. A new functional global auto-ignition model for hydrocarbon fuels - part 2 of 2: Model formulation, development and performance assessment. *SAE Int. J. Fuels Lubr. SAE International Journal of Fuels and Lubricants*, 3(2):757–772, 2010. ISSN 1946-3952.

Franzelli, B., Riber, E., Sanjose, M. and Poinsot, T. A two-step chemical scheme for kerosene-air premixed flames. *Combustion and Flame*, 157(7):1364–1373, 2010. ISSN 0010-2180.

Galloway, T. R. and Sage, B. H. Prediction of the transport properties of paraffin hydrocarbons. *Chemical Engineering Science*, 22(7):979–995, 1967. ISSN 0009-2509.

Galmiche, B., Halter, F. and Foucher, F. Effects of high pressure, high temperature and dilution on laminar burning velocities and markstein lengths of iso-octane/air mixtures. *Combustion and Flame*, 159(11):3286–3299, 2012. ISSN 0010-2180.

Gerald, C. F. and Wheatley, P. O. *Applied numerical analysis*. Pearson/Addison-Wesley, Boston, 2004.

Glassman, I. and Yetter, R. A. *Combustion*. Academic Press, 2008.

Griffiths, J. F. Reduced kinetic models and their application to practical combustion systems. *Progress in Energy and Combustion Science*, 21(1):25–107, 1995. ISSN 0360-1285.

Griffiths, J. F., Hughes, K. J., Schreiber, M. and Poppe, C. A unified approach to the reduced kinetic modeling of alkane combustion. *Combustion and Flame*, 99(3-4):533–540, 1994. ISSN 0010-2180. 25th Symposium (International) on Combustion Papers.

Hasse, C., Bollig, M., Peters, N. and Dwyer, H. A. Quenching of laminar iso-octane flames at cold walls. *Combustion and Flame*, 122(1-2):117–129, 2000. ISSN 0010-2180.

Hirschfelder, J. O., Curtiss, C. F. and Campbell, D. E. The theory of flame propagation. IV. *The Journal of Physical Chemistry*, 57(4):403–414, 1953.

Holley, A. T., You, X. Q., Dames, E., Wang, H. and Egolfopoulos, F. N. Sensitivity of propagation and extinction of large hydrocarbon flames to fuel diffusion. *Proceedings of the Combustion Institute*, 32(1):1157–1163, 2009. ISSN 1540-7489.

Höök, M., Li, J., Johansson, K. and Snowden, S. Growth rates of global energy systems and future outlooks. *Natural Resources Research*, 21(1):23–41, 2012. ISSN 1520-7439.

Huang, Y., Sung, C. J. and Eng, J. A. Laminar flame speeds of primary reference fuels and reformer gas mixtures. *Combustion and Flame*, 139(3):239–251, 2004. ISSN 0010-2180.

Hui, X. and Sung, C.-J. Laminar flame speeds of transportation-relevant hydrocarbons and jet fuels at elevated temperatures and pressures. *Fuel*, 109(0):191–200, 2013. ISSN 0016-2361.

IEA. Key world energy statistics 2012, 2012. URL `http://www.iea.org/publications/freepublications/publication/kwes.pdf`. (International Energy Agency).

Incropera, F. P., DeWitt, D. P., Bergman, T. L. and Lavine, A. S. *Fundamentals of heat and mass transfer*. John Wiley & Sons, 6th edition, 2007. ISBN 9780471457282.

Jerzembeck, S., Peters, N., Pepiot-Desjardins, P. and Pitsch, H. Laminar burning velocities at high pressure for primary reference fuels and gasoline: Experimental and numerical investigation. *Combustion and Flame*, 156(2):292–301, 2009. ISSN 0010-2180.

Johnston, R. J. and Farrell, J. T. Laminar burning velocities and markstein lengths of aromatics at elevated temperature and pressure. *Proceedings of the Combustion Institute*, 30(1):217–224, 2005. ISSN 1540-7489.

Ju, Y., Guo, H., Liu, F. and Maruta, K. Effects of the lewis number and radiative heat loss on the bifurcation and extinction of CH4/O2-N2-He flames. *Journal of Fluid Mechanics*, 379(1):165–190, 1999. ISSN 0022-1120.

Kee, R. J., Grcar, J. F., Smooke, M. D., Miller, J. A. and Meeks, E. Premix: A fortran program for modeling steady laminar one-dimensional premixed flames. *Sandia National Laboratories*, SAND85-8240, 1985.

Kee, R. J., Rupley, F. M., Miller, J. A., Coltrin, M. E., Grcar, J. F., Meeks, E., Moffat,

H. K., Lutz, A. E., Dixon-Lewis, G., Smooke, M. D., Warnatz, J., Evans, G. H., Larson, R. S., Mitchell, R. E., Petzold, L. R., Reynolds, W. C., Caracotsios, M., Stewart, W. E., Glarborg, P., Wang, C. and Adigun, O. *CHEMKIN: A software package for the analysis of gas-phase chemical and plasma kinetics*. Reaction Design, Inc., San Diego, CA, release 3.6 edition.

Kee, R. J., Coltrin, M. E. and Glarborg, P. *Chemically reacting flow: theory and practice*. Wiley-Interscience, 2003. ISBN 9780471261797.

Kelley, A. P. and Law, C. K. Nonlinear effects in the extraction of laminar flame speeds from expanding spherical flames. *Combustion and Flame*, 156(9):1844–1851, 2009. ISSN 0010-2180.

Kelley, A. P., Liu, W., Xin, Y. X., Smallbone, A. J. and Law, C. K. Laminar flame speeds, non-premixed stagnation ignition, and reduced mechanisms in the oxidation of iso-octane. *Proceedings of the Combustion Institute*, 33(1):501–508, 2011. ISSN 1540-7489.

Koretsky, M. D. *Engineering and chemical thermodynamics*. Wiley, 2004. ISBN 9780471385868.

Krishna, R. and Wesselingh, J. A. The maxwell-stefan approach to mass transfer. *Chemical Engineering Science*, 52(6):861–911, 1997. ISSN 0009-2509.

Kumar, K., Freeh, J. E., Sung, C. J. and Huang, Y. Laminar flame speeds of preheated iso-octane / O2 / N2 and n-heptane / O2 / N2 mixtures. *J. Propulsion Journal of Propulsion and Power*, 23(2):428–436, 2007. ISSN 0748-4658.

Kumar, K., Sung, C.-J. and Hui, X. Laminar flame speeds and extinction limits of conventional and alternative jet fuels. *Fuel*, 90(3):1004–1011, 2011. ISSN 0016-2361.

Law, C. K. *Combustion physics*. Cambridge University Press, 2006. ISBN 9780521870528.

Law, C. K. Dryden lecture: Fuel options for next generation chemical propulsion. In *Aerospace Sciences Meetings*, pages 1–30. American Institute of Aeronautics and Astronautics, January 2011.

Law, C., Makino, A. and Lu, T. On the off-stoichiometric peaking of adiabatic flame temperature. *Combustion and Flame*, 145(4):808–819, 2006. ISSN 0010-2180.

Le Chatelier, H. L. and Mallard, E. Combustion des melanges gazeux explosifs. *Annales*

des Mines, 4:379–568, 1883.

Lefebvre, A. H. *Gas turbine combustion*. Combustion: An International Series. Taylor & Francis, 1999. ISBN 9781560326731.

Lemmon, E. W., McLinden, M. O. and Friend, D. G. Nist chemistry webbook, 2011. URL `http://webbook.nist.gov/chemistry/`.

Lewis, B. and von Elbe, G. V. *Combustion, flames and explosions of gases*. Cambridge series of physical chemistry. Academic Press, 1961.

Liao, S. Y., Jiang, D. M., Gao, J., Huang, Z. H. and Cheng, Q. Measurements of markstein numbers and laminar burning velocities for liquefied petroleum gas-air mixtures. *Fuel*, 83(10):1281–1288, 2004. ISSN 0016-2361.

Luijten, C. C. M., Doosje, E. and de Goey, L. P. H. Accurate analytical models for fractional pressure rise in constant volume combustion. *International Journal of Thermal Sciences*, 48(6):1213–1222, 2009. ISSN 1290-0729.

Margolis, S. B. Time-dependent solution of a premixed laminar flame. *Journal of Computational Physics*, 27(3):410–427, 1978. ISSN 0021-9991.

Marshall, S. P., Taylor, S., Stone, C. R., Davies, T. J. and Cracknell, R. F. Laminar burning velocity measurements of liquid fuels at elevated pressures and temperatures with combustion residuals. *Combustion and Flame*, 158(10):1920–1932, 2011. ISSN 0010-2180.

Mehl, M., Curran, H. J., Pitz, W. J. and Westbrook, C. K. Chemical kinetic modeling of component mixtures relevant to gasoline. In *European Combustion Meeting*, Vienna, Austria, 2009.

Mehl, M., Pitz, W. J., Westbrook, C. K. and Curran, H. J. Kinetic modeling of gasoline surrogate components and mixtures under engine conditions. *Proceedings of the Combustion Institute*, 33(1):193–200, 2011. ISSN 1540-7489.

Pasternak, M., Mauss, F., Meyer, P., Ingle, A. and Seidel, L. Characteristic fuel value for homogeneous combustion. Technical Report 2, Brandenburg University of Technology, Cottbus, Germany, 2008. URL `http://www.tu-cottbus.de/fakultaet4/de/thermodynamik/forschung/projekte/characteristic-fuel-value-for-homogeneous-combustion.html`.

Rallis, C. J. and Garforth, A. M. The determination of laminar burning velocity. *Progress*

in Energy and Combustion Science, 6(4):303–329, 1980. ISSN 0360-1285.

Rallis, C. J., Garforth, A. M. and Steinz, J. A. Laminar burning velocity of acetylene-air mixtures by the constant volume method: Dependence on mixture composition, pressure and temperature. *Combustion and Flame*, 9(4):345–356, 1965. ISSN 0010-2180.

Saad, T. 9. derivation of the continuity equation in spherical coordinates. http://pleasemakeanote.blogspot.com/2010/02/9-derivation-of-continuity-equation-in.html, July 2010. URL `http://pleasemakeanote.blogspot.com/2010/02/9-derivation-of-continuity-equation-in.html`.

Schreiber, M., Sakak, A. S., Lingens, A. and Griffiths, J. F. A reduced thermokinetic model for the autoignition of fuels with variable octane ratings. *Symposium (International) on Combustion*, 25(1):933–940, 1994. ISSN 0082-0784. Twenty-Fifth Symposium (International) on Combustion.

Shampine, L. F., Davenport, S. M. and Huddleston, R. E. Polfit, 1974. URL `http://www.netlib.org/slatec/src/polfit.f`.

van Lipzig, J. P. J., Nilsson, E. J. K., de Goey, L. P. H. and Konnov, A. A. Laminar burning velocities of n-heptane, iso-octane, ethanol and their binary and tertiary mixtures. *Fuel*, 90(8):2773–2781, 2011. ISSN 0016-2361.

Versteeg, H. K. and Malalasekera, W. *An introduction to computational fluid dynamics: the finite volume method*. Longman Scientific & Technical, 1995. ISBN 9780582218840.

Wakatsuki, K. *High temperature radiation absorption of fuel molecules and an evaluation of its influence on pool fire modeling*. PhD thesis, University of Maryland, College Park, Md., 2005. URL `http://hdl.handle.net/1903/2366`.

Wang, R., Keast, P. and Muir, P. Bacol: B-spline adaptive collocation software for 1-D parabolic PDEs. *ACM Trans. Math. Softw.*, 30:454–470, December 2004a. ISSN 0098-3500.

Wang, R., Keast, P. and Muir, P. Bacol, 2004b. URL `http://www.cs.usask.ca/home/rong/`. retrieved June 15, 2010.

Wang, R., Keast, P. and Muir, P. A comparison of adaptive software for 1D parabolic PDEs. *Journal of Computational and Applied Mathematics*, 169(1):127–150, 2004c. ISSN 0377-0427.

Warnatz, J., Maas, U. and Dibble, R. W. *Combustion: physical and chemical fundamentals, modeling and simulation, experiments, pollutant formation*. Springer, 2001. ISBN 9783540677512.

Westbrook, C. K., Pitz, W. J., Mehl, M. and Curran, H. J. Detailed chemical kinetic reaction mechanisms for primary reference fuels for diesel cetane number and spark-ignition octane number. *Proceedings of the Combustion Institute*, 33(1):185–192, 2011. ISSN 1540-7489.

Yano, T. and Ito, K. Minimum ignition energies and quenching distances of methanol blends. *Hokkaido University - Bulletin of the Faculty of Engineering*, (94):31–37, 1979.

Yates, A., Burger, V. and Viljoen, C. A method for determining the laminar flame speed of jet fuels using combustion bomb pressure. *Proceedings of the ASME Turbo Expo*, 2 (68117):41–51, June 2012.

Yos, J. M., MA, R. A. C. W. and DIV., A. D. Transport properties of nitrogen, hydrogen, oxygen, and air to 30,000 K., 1963. URL `http://oai.dtic.mil/oai/oai?&verb=getRecord&metadataPrefix=html&identifier=AD0435053`.

Zheng, J., Miller, D. L. and Cernansky, N. P. A global reaction model for the HCCI combustion process. Technical report, October 2004. URL `http://dx.doi.org/10.4271/2004-01-2950`.

A. Nomenclature

Symbol		Description		Units
$\mathcal{A}$	-	Avogadro's number $\left(6.022 \times 10^{23}\ molecule.mol^{-1}\right)$	-	molecule.mol^{-1}
A	-	area of planes of control volume normal to the radial direction	-	m^2
A_p	-	projected area of control volume on a plane	-	m^2
A_{RR}	-	pre-exponential constant for reaction rate	-	(mol m s)
A_1 , A_2	-	surfaces of the control volume in Figure 3.3	-	-
A , B	-	expanding functions for Equations 3.67 and 3.68	-	-
$ATOL$	-	model parameter that specifies absolute tolerance	-	-
$ATOL_s$	-	absolute tolerance for s-th component	-	-
a_1 , a_2	-	fuel equivalence ratio parameters for Equation 2.38	-	-
$a_{n,k}$	-	coefficient for the logarithmic fit of Equations 3.78 and 3.82	-	-
$a_{1,i}$ ..., $a_{5,i}$	-	coefficient for the polynomial fit for of the heat capacity of species i in Equation 3.85	-	-
B_1 , B_2	-	surfaces of the control volume in Figure 3.3	-	-
BVAL	-	model variable for the results array from the boundary subroutines		
$b(\,)$	-	boundary condition function as input to BACOL	-	-
C_i	-	concentration of species i	-	mol.m^{-3}

Symbol		Description		Units
C_T	-	total concentration	-	$mol.m^{-3}$
C_1 , C_2	-	surfaces of the control volume in Figure 3.3	-	-
C_{3+} , C_4	-	Octane Number adjustment parameters	-	-
C_p	-	volumetric constant pressure heat capacity	-	$J.K^{-1}.m^{-3}$
C_v	-	volumetric constant volume heat capacity	-	$J.K^{-1}.m^{-3}$
c_p	-	molar constant pressure heat capacity	-	$J.mol^{-1}.K^{-1}$
$c_{p,i}$	-	molar constant pressure heat capacity of species i	-	$J.mol^{-1}.K^{-1}$
c_v	-	molar constant volume heat capacity	-	$J.mol^{-1}.K^{-1}$
$c_{v,trans}$, $c_{v,rot}$, $c_{v,vib}$	-	translational, rotational and vibrational components of c_v	-	$J.mol^{-1}.K^{-1}$
$\mathcal{D}_{ij}$	-	binary diffusion coefficient of species i and j	-	$m^2.s^{-1}$
D	-	diffusion coefficient	-	$m^2.s^{-1}$
D_i	-	diffusion coefficient of species i in the mixture	-	$m^2.s^{-1}$
$D_{j,m}$	-	diffusion coefficient of species j with regards to the mixture (m)	-	$m^2.s^{-1}$
D_{kk}	-	self-diffusion coefficient of species k	-	$m^2.s^{-1}$
D_1 , D_2	-	Damkohler numbers in Equation 3.87	-	-
DFDU	-	model variable for the array that contains the derivatives of each F-functions to each of the solution variables		
DFDUX	-	model variable for the array that contains the derivatives of each F-functions to the first order spatial derivative of each of the solution variables		

Symbol		Description		Units
DFDUXX	-	model variable for the array that contains the derivatives of each F-functions to the second order spatial derivative of each of the solution variables		
$\frac{\partial T}{\partial r}$	-	first order spatial derivative of temperature (T)	-	$K.m^{-1}$
$\frac{\partial^2 T}{\partial r^2}$	-	second order spatial derivative of temperature (T)	-	$K.m^{-2}$
$\frac{\partial \lambda}{\partial r}$	-	spatial derivative of the thermal conductivity (λ)	-	$J.K^{-1}.m^{-2}.s^{-1}$
E	-	activation energy	-	$J.mol^{-1}$
E_s	-	spatial error estimate for the s-th component from Equation 3.86		
F	-	force	-	N
$F(T)$	-	temperature dependent adjustment function for Z_{rot}	-	-
FVAL	-	model variable for the array that contains the result of the F-subroutine		
$f()$	-	differential equation function as input to BACOL	-	-
f_{trans} , f_{rot} , f_{vib}	-	scalars for the linear combination of $c_{v,trans}$, $c_{v,rot}$ and $c_{v,vib}$	-	-
G	-	Damkohler number in Equation 3.87	-	-
g	-	order of reaction rate	-	-
H	-	enthalpy	-	J
h_0	-	molar enthalpy at absolute zero temperature ($T = 0\ K$)	-	$J.mol^{-1}$
h_i	-	molar enthalpy of species i	-	$J.mol^{-1}$
h_{T_1}	-	molar enthalpy at temperature $= T_1$	-	$J.mol^{-1}$
$h_{f(T_0)}$	-	molar heat of formation at temperature $= T_0$	-	$J.mol^{-1}$

Symbol		Description		Units
$h_{f,i(298K)}$	-	molar heat of formation of species i at 298 K	-	J.mol^{-1}
$\Delta h_{rxn,k,T_1}$	-	heat of reaction for reaction k at temperature $= T_1$	-	J.mol^{-1}
J^*	-	diffusive molar flux	-	mol.m^{-2}.s^{-1}
J_i^*	-	diffusive molar flux of species i	-	mol.m^{-2}.s^{-1}
K	-	2 $\times$ radial velocity gradient at minimum axial velocity point (Equation 2.25)	-	s^{-1}
Ka	-	Karlovitz number	-	-
k_B	-	Boltzmann's constant $\left(1.381 \times 10^{-23}\ J.molecule^{-1}.K^{-1}\right)$	-	J.molecule^{-1}.K^{-1}
$kcol$	-	model parameter that specifies degree of piecewise B-spline approximations	-	-
k_i	-	reaction rate constant for reaction i	-	(mol m s)
L_b	-	burned gas Markstein length	-	m
L_c	-	Markstein length for curvature stretch rate	-	m
L_s	-	Markstein length for aerodynamic strain	-	m
Le	-	Lewis number, defined as the ratio of thermal diffusivity to mass diffusivity	-	-
M_i	-	molar mass of species i	-	kg.mol^{-1}
$\dot{m}$	-	mass burning rate or mass flow rate	-	kg.m^{-2}.s^{-1}
$m_{j,k}$	-	reduced mass of the two molecules of species j and k	-	kg
m_k	-	mass of molecule for species k	-	kg
$NPDE$	-	number of partial differential equations	-	-
n	-	number of moles	-	mol

Symbol		Description		Units
n_i	-	number of moles of species i (See Equation 2.9)	-	mol
ON	-	Octane Number or Research Octane Number (RON)	-	-
$optn$	-	model variable that specifies to which solution variable a certain property is differentiated to	-	-
P	-	pressure	-	Pa
P_0	-	reference pressure	-	Pa
P_i , P_e	-	initial and end pressure respectively in a combustion chamber	-	Pa
Pe_1 , Pe_2	-	Péclet numbers in Equation 3.87	-	-
q	-	thermal conduction or heat transfer rate	-	$\mathrm{J.m^{-2}.s^{-1}}$
$\mathcal{R}_v$	-	radius of spherical combustion chamber of equivalent volume	-	m
R	-	ideal gas constant $\left(8.314\ \mathrm{J.mol^{-1}.K^{-1}}\right)$	-	$\mathrm{J.mol^{-1}.K^{-1}}$
R_i	-	rate of production of species i	-	$\mathrm{mol.m^{-3}.s^{-1}}$
RR_k	-	reaction rate for reaction k	-	$\mathrm{mol.m^{-3}.s^{-1}}$
$RTOL$	-	model parameter that specifies relative tolerance	-	-
$RTOL_s$	-	relative tolerance for s-th component	-	-
r	-	radial co-ordinate or position	-	m
Δr	-	change in radial position or step distance	-	m
r_a , r_b	-	spatial boundaries for the model at point a and b	-	m
r_f	-	radius of flame front	-	m
r_{sch}	-	schlieren radius (equivalent to the radius of the 450 K isotherm)	-	m

Symbol		Description		Units
r_u	-	radius of cold flame front or unburned gas	-	m
req	-	model variable that specifies the species for which a certain property is calculated	-	-
S_L	-	laminar flame speed	-	as defined
$S_{L,0}$	-	reference laminar flame speed	-	$m.s^{-1}$
S_n	-	flame propagation speed	-	$m.s^{-1}$
S_s	-	unstretched flame propagation speed	-	$m.s^{-1}$
SR	-	spark rate, controlling the rate of temperature increase	-	-
T	-	temperature	-	K
T_0	-	reference temperature	-	K
T_{ad}	-	adiabatic flame temperature	-	K
T_i	-	initial temperature of unburned gas	-	K
T_u	-	temperature of unburned gas	-	K
$T_{u,0}$	-	reference unburned gas temperature	-	K
T	-	model variable for time	-	s
t	-	time	-	s
t_0	-	initial time or time at start of model	-	-
t_{spark}	-	time of ignition event	-	s
U	-	internal energy	-	J
U	-	model variable for the solution array containing the concentrations, convective velocity and temperature		
$U_s(x,t)$	-	approximated solution for s-th component	-	-

Symbol		Description		Units
$\bar{U}_s(x,t)$	-	second approximated solution for s-th component of one order higher	-	-
u	-	radial fluid velocity instead of u_r or just convective velocity	-	$m.s^{-1}$
u_n	-	stretched normal flame speed	-	$m.s^{-1}$
u_r	-	fluid velocity in radial direction	-	$m.s^{-1}$
u_θ	-	fluid velocity in polar direction	-	$m.s^{-1}$
u_ϕ	-	fluid velocity in azimuthal direction	-	$m.s^{-1}$
V	-	volume of control volume $= A\Delta r$ or just volume	-	m^3
v_k	-	diffusion velocity of species k	-	$m.s^{-1}$
W_1 , W_2	-	Damkohler numbers in Equation 3.87	-	-
X	-	model variable for spatial position	-	m
X_i	-	mole fraction of species i	-	-
x	-	spatial co-ordinate in Equation 3.87	-	-
x_b	-	mass fraction burned	-	-
y	-	represents any of the solution variables	-	-
Δy	-	incremental change in any of the solution variables	-	-
Z_{rot}	-	rotational relaxation collision number	-	-
z	-	represent any of the solution variables	-	-
Greek letters				
α	-	flame stretch rate	-	s^{-1}
α_c	-	flame stretch rate due to curvature of cold flame front	-	s^{-1}

Symbol		Description		Units
α_s	-	aerodynamic flow field strain	-	s^{-1}
α_T	-	thermal diffusivity of unburned gas	-	$m^2.s^{-1}$
$\alpha_{t,i}$	-	polarisability of species i	-	$angstrom^3$
β	-	reciprocal of temperature term (See Equation 2.2)	-	-
β_T , β_P	-	exponential coefficients for Equations 2.21 and 2.38	-	-
γ	-	isentropic exponent for both burned and unburned gas	-	-
γ_u	-	isentropic exponent of unburned gas	-	-
δ_l	-	flame thickness	-	m
ε	-	characteristic attractive well-depth	-	$J.molecule^{-1}$
θ	-	quantity or solution vector	-	-
θ	-	polar co-ordinate	-	rad
$\theta_{1,\ldots,4}$	-	components of the solution vector in Equation 3.87	-	-
λ	-	thermal conductivity	-	$J.K^{-1}.m^{-1}.s^{-1}$
λ_i	-	pure thermal conductivity of species i	-	$J.K^{-1}.m^{-1}.s^{-1}$
μ	-	dynamic viscosity	-	Pa.s
μ_M	-	Markstein parameter	-	-
$\mu_{t,i}$	-	dipole moment of species i	-	Debye
ν	-	kinematic viscosity of unburned gas	-	$m^2.s^{-1}$
$\nu_{k,i}$	-	stoichiometric coefficient of species i in reaction k	-	-
π	-	ratio between the circumference and diameter of circle (3.1416)	-	-
ρ	-	density	-	$kg.m^{-3}$

Symbol		Description		Units
ρ_u , ρ_b	-	density of the unburned and burned gas respectively	-	$kg.m^{-3}$
σ_j	-	Lennard-Jones collision diameter of species j	-	m
$\sigma_{j,k}$	-	reduced net collision diameter of the interaction between species j and k	-	m
σ_T	-	thermal expansion parameter	-	-
τ_{ign}	-	ignition delay time	-	ms
ϕ	-	fuel equivalence ratio	-	-
ϕ	-	azimuthal co-ordinate	-	rad
$\Omega_{kk}^{(1,1)\bigstar}$, $\Omega_{kk}^{(2,2)\bigstar}$	-	collision integrals	-	-
$\dot{\omega}$	-	reaction rate	-	$kg.m^{-3}.s^{-1}$
ω_k	-	pure species viscosity of species k	-	Pa.s

B. Supplementary methods

B.1. Collision principles

Molecules in the gas phase interact via long-ranged attractions and short-range repulsive forces. This interaction is described by an interaction potential energy as a function of the intermolecular distance and orientation. Figure B.1 shows the Lennard-Jones interaction depicting the intermolecular potential function.

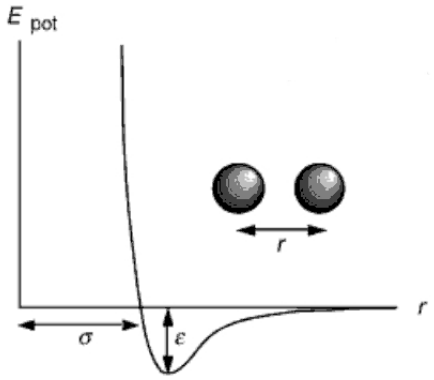

Figure B.1.: Lennard-Jones potential. (Warnatz et al., 2001)

In Figure B.1 the negative interaction potential (E_{pot}) values represents the long-ranged attractions and the positive values represents the short-range repulsive forces. At the minimum value for the interaction potential, the characteristic attractive well-depth (ε) is defined as seen in Figure B.1. Also, the distance where the interaction potential is zero, is defined as the net collision diameter (σ) as seen in Figure B.1. The characteristic interaction potential between unlike molecules are described by the parameters ε_{ij} and σ_{ij} which are obtained by making use of *combining rules*. (Kee et al., 2003)

The collision integrals $\Omega_{ij}^{(1,1)\star}$ and $\Omega_{ij}^{(2,2)\star}$ are commonly used values to obtain transport coefficients and can be estimated with convenient empirical fits derived from the interac-

tion potential (E_{pot}) as a function of the distance between the centres of mass (r_{ij}) of molecules i and j. These empirical fits are shown in Equations B.1 and B.2 (Kee et al., 2003).

$$\Omega_{ij}^{(1,1)\bigstar} \approx \left[a_1 T^{*-a_2} + (T^* + a_3)^{-a_4}\right] \left[1 + \frac{\left(e^{a_5/T^*} - e^{-a_6/T^*}\right)\left(\tilde{\delta}_{ij}^*\right)^2}{2 + 2.5\tilde{\delta}_{ij}^*}\right] \quad \text{(B.1)}$$

$$\Omega_{ij}^{(2,2)\bigstar} \approx \left[b_1 T^{*-b_2} + (T^* + b_3)^{-b_4}\right] \left[1 + \frac{\left(e^{b_5/T^*} - e^{-b_6/T^*}\right)\left(\tilde{\delta}_{ij}^*\right)^2}{2 + 2.5\tilde{\delta}_{ij}^*}\right] \quad \text{(B.2)}$$

The dimensionless parameter δ_{ij}^* is a function of ε_{ij}, σ_{ij}, the dipole moments of the molecules ($\mu_{t,i}$ and $\mu_{t,j}$) and the spatial orientation of the collision, while $\tilde{\delta}_{ij}^*$ in Equations B.1 and B.2 is the maximum value of δ_{ij}^* based on the spatial orientation of the collision. Further, in Equations B.1 and B.2, T^* is the reduced temperature as a function of the absolute temperature (T), Boltzmann's constant (k_B) and the interaction well depth (ε_{ij}):

$$T^* = \frac{k_B T}{\varepsilon_{ij}} \quad \text{(B.3)}$$

The values for the parameters of the empirical fit in Equations B.1 and B.2 are given in Table B.1.

Table B.1.: Values for empirical fit for collision integrals in Equations B.1 and B.2. (Kee et al., 2003)

j	a_j	b_j
1	1.0548	1.0413
2	0.15504	0.11930
3	0.55909	0.43628
4	2.1705	1.6041
5	0.093193	0.095661
6	1.5	2.0

The $i-j$ interaction parameters are calculated from the pure species parameters using the Lorentz-Berthelot combining rules and include an induction energy term to account

for induced dipole where a polar and non polar molecule collide.

$$\varepsilon_{ij} = \xi^2 \sqrt{\varepsilon_i \varepsilon_j} \tag{B.4}$$

$$\sigma_{ij} = \left(\frac{\sigma_i + \sigma_j}{2}\right) \xi^{-1/6} \tag{B.5}$$

$$\tilde{\delta}^*_{ij} = \frac{1}{2} \frac{\mu_{t,i} \mu_{t,j}}{\varepsilon_{ij} \sigma^3_{ij}} \tag{B.6}$$

The induction energy term (ξ) is a function of the reduced polarisability $\left(\alpha^*_{t,i}\right)$ for the non polar molecule (i) and the reduced dipole moment $\left(\mu^*_{t,j}\right)$ for the polar molecule (j) as shown in Equation B.7.

$$\xi = 1 + \frac{1}{4} \alpha^*_{t,i} \mu^*_{t,j} \sqrt{\frac{\varepsilon_j}{\varepsilon_i}} \tag{B.7}$$

$$\alpha^*_{t,i} = \frac{\alpha_{t,i}}{\sigma^3_i} \tag{B.8}$$

$$\mu^*_{t,j} = \frac{\mu_{t,j}}{\sqrt{\varepsilon_j \sigma^3_j}} \tag{B.9}$$

The potential well depth $\left(\frac{\varepsilon_i}{k_B}\right)$, collision diameter ($\sigma_i$), dipole moment ($\mu_{t,i}$), polarisability ($\alpha_{t,i}$) and rotational relaxation collision number (Z_{rot}) for each species i used in this work are given in Table B.2. From this the collision integrals ($\Omega^{(1,1)\bigstar}_{ij}$ and $\Omega^{(2,2)\bigstar}_{ij}$) can be calculated, which describe the collision interactions between the molecules (Kee et al., 2003). The collision integrals are directly implemented into the evaluation of the transport coefficients, discussed in Section 3.5. The transport parameters, such as the net collision diameter, are obtained from transport parameter databases used for combustion modelling with the CHEMKIN package (Kee et al., 2000). The parameters used in this model are obtained from the transport database file of Mehl et al. (2011) and are given in Table B.2.

Table B.2.: Transport parameters for species used in this model. (Mehl et al., 2011)

symbol units	potential well depth $\left(\frac{\varepsilon}{k_B}\right)$ K	collision diameter (σ) $Angstrom$	dipole moment (μ_t) $Debye^a$	polarisability (α_t) $Angstrom^3$	rotational relaxation collision number (Z_{rot}) at 298 K
iso-octane	458.5	6.414	0.0	0.00	1.0
intermediate	458.5	6.414	0.0	0.00	1.0
oxygen	107.4	3.458	0.0	1.60	3.8
carbon dioxide	244.0	3.763	0.0	2.65	2.1
water	572.4	2.605	1.844	0.0	4.0
nitrogen	97.53	3.621	0.0	1.76	4.0

[a] $1\ Debye = 10^{-18}\ cm^{3/2}.erg^{1/2}$

B.2. The Maxwell-Stefan formulation

The Maxwell-Stefan approach to multicomponent diffusion is computationally much more expensive than the mixture average approach discussed in Section 3.5.2.1. However, the Maxwell-Stefan approach is briefly discussed in this section for comparison and to show its complexity. In certain cases, multi component diffusion may differ appreciably from Fick's law for diffusion. This is shown in the well known two-bulb diffusion experiment of Duncan and Toor (1962) where certain species in a gas mixture display diffusional behaviour that defies Fick's law (Equation 3.60).

The Maxwell-Stefan approach takes the effect of relative motion of the gas molecules on each species into account and thereby derives a correlation between the diffusional driving forces for all the species in the mixture and their relative velocities or fluxes. By assuming ideal thermodynamic interactions and that the diffusional driving forces are the mole fraction gradients, the Maxwell-Stefan approach is written in the simpler matrix equation of Equation B.10 (Krishna and Wesselingh, 1997).

$$-C_T\left(\nabla \mathrm{X}\right) = [B]\,\mathrm{J} \tag{B.10}$$

In Equation B.10, C_T is the total concentration of the gas mixture, while $(\nabla \mathrm{X})$ and J are vectors containing the derivatives of the mole fractions and the diffusional fluxes of all but one of the species in the mixture. Further $[B]$ is a $(species - 1) \times (species - 1)$ matrix of which the elements are functions of the mole fractions of each species and the binary diffusion coefficients calculated in Section 3.5.2.1. The elements of the matrix $[B]$ in Equation B.10 is given by Equation B.11 (Krishna and Wesselingh, 1997).

$$B_{ij} = \begin{cases} \frac{X_i}{\mathcal{D}_{in}} + \sum_{\substack{k=1 \\ k \neq i}}^{n} \frac{X_k}{\mathcal{D}_{ik}} & for\ i = j \\ X_i \left(\frac{1}{\mathcal{D}_{in}} - \frac{1}{\mathcal{D}_{ij}} \right) & for\ i \neq j \end{cases} \tag{B.11}$$

In Equation B.11, $1 \leq i \leq n-1$ and $1 \leq j \leq n-1$ where n represents the number of species in the mixture and also the specific species to be excluded from Equation B.10. Further, X_i is the mole fraction of species i and $\mathcal{D}_{ij}$ is the binary diffusion coefficient of species i and j. Once Equation B.10 is solved, the diffusional flux of the remaining species (n) is calculated by making some assumption about the total molar flux of all the species. However, Equation B.10 gives the diffusional driving force $(\nabla \mathrm{X})$ as a function of the diffusional fluxes (J) which is the inverse of what one requires in the mathematical system derived in Section 3.2. Therefore, to obtain the diffusional fluxes (J) from the diffusional driving forces $(\nabla \mathrm{X})$, the inverse of matrix B will be required as shown in Equation B.12 (Krishna and Wesselingh, 1997).

$$\mathrm{J} = -C_T \left[B^{-1} \right] (\nabla \mathrm{X}) \tag{B.12}$$

Equation B.12 will therefore give the diffusional fluxes of the species in the system based on the Maxwell-Stefan approach to multicomponent diffusion. As is clear, this approach is computationally more expensive, especially since it requires the inverse of a matrix, which will impact greatly on a numerical system where this calculation is required at several points in the domain at each time step. The implementation of this multicomponent approach to diffusion is not pursued, but might be considered for future developments.

C. Description of property functions

The property functions are indicated in Section C of Figure 3.11, where it is shown that the subroutines required by BACOL (Section B of Figure 3.11) call the property functions. These property functions calculate mixture properties such as thermal conductivity (λ) and species properties such as reaction rate (R_i). This is required in the calculation of the partial differential equations (Equations 3.11, 3.30 and 3.41) derived from the conservation equations. The terms in these equations, calculated by property functions discussed in this appendix, are shown in Figure 3.12.

C.1. Function HEATCAP

This function calculates the constant pressure molar heat capacity $\left(c_{p,i}\right)$ of any species i requested[1], using Equation 3.85 and the parameters provided in Part B of the MAIN program. From the solution variables, passed to this function in the solution array (U), the function calculates the molar heat capacity of the requested species, specified by the *req* integer. The function also calculates the derivative of the molar heat capacity of the requested species to the solution variable specified by the *optn* integer. Therefore this function operates as follows: if the value of *optn* is zero, the molar heat capacity of the *req*-th species is returned, or else the derivative of the *req*-th heat capacity to the *optn*-th solution variable is returned. This function limits the temperature range, since Equation 3.85 is limited to a certain temperature range. The heat capacity at any temperature above the maximum limit is taken as the heat capacity at the maximum temperature and similarly at temperatures below the minimum temperature limit, the heat capacity at the minimum temperature is returned.

[1] See Figure 3.12.

C.2. Function heat

The heat-function calculates molar enthalpy (h_i) of any species i using Equation 3.16, which implies the integration of Equation 3.85 over a temperature range. Since the differentiation of the molar enthalpy is also required, this function calls the HEATCAP function of Appendix C.1. This function is limited to the same temperature range as that of the HEATCAP function. Although the heat function is not directly called by any of the subroutines in section B of Figure 3.11, it is required to calculate the heat of reaction.

C.3. Function TBE

The third body efficiency or TBE-function calculates the pseudo concentration of the third molecule in the unimolecular reactions, as discussed in Section 3.4.2. The chemical kinetic model of Schreiber et al. (1994) used in this work, takes this concentration to be equal to the total concentration of the mixture at that point in time and space. Therefore the TBE function is a very simple function in this case. However, other chemical kinetic models might be used in future, requiring more complex calculations for the pseudo concentration of the third molecule in the unimolecular reactions.

C.4. Function pressure

This function is very simple and calculates the pressure of the system from the ideal gas law, as shown in Equation 3.18. It further has the capability to calculate the derivative of the pressure to any of the solution variables. As shown in Figure 3.11, the pressure-function is called by several other functions as is expected for such a fundamental property.

C.5. Function area

The area-function is used to specify the geometry of the system by calculating the value of $\frac{1}{A}\frac{\partial A}{\partial r}$ according to the equations in Table 3.1. This geometric term is a function of the spatial position only and therefore only the X value from BACOL is passed to the area-function. This also implies that the derivative of this function to any of the solution variables is zero. All three equations from Table 3.1 is included in this function, with a

option of which to use. This makes the change to different geometry systems convenient, however for this study, only the spherical geometry system is considered.

C.6. Functions avcp and avcv

The avcp- and avcv-functions are used to calculate the volumetric heat capacity for constant pressure and constant volume respectively, abbreviated from average C_p and average C_v. As indicated in Figure 3.12, these functions calculate values for $\sum C_i c_{p,i}$ and $\sum C_i \left(c_{p,i} - R\right)$ respectively. Therefore the HEATCAP-function is called to calculate the molar constant pressure heat capacity of each species. Since these functions are dependent on the solution variables, the derivative of these functions to any of the solution variables is calculated at request.

C.7. Function rho

The rho-function calculates the density of the gas mixture (ρ) from the concentrations of all the individual species using Equation 3.35. The density is presented by $\sum C_i M_i$ in Figure 3.12 and Equation 3.41, the PDE derived from the conservation of momentum. This density calculation requires the molar mass of each species (M_i) which is supplied along with other parameters in Part B of the MAIN program. Again, this function has the capability to calculate the derivative of the density with respect to any of the solution variables at request.

C.8. Function rate

This function calculates the rate at which any species is produced or consumed by chemical reaction, which is represented by R_i in Figure 3.12. This calculation is done by calculating the reaction rate of each reaction using Equation 2.19 and adding the reaction rates according to the summation of Equation 3.51. Since this rate-function is a complicated calculation which is dependent on the species concentrations, temperature, pressure and third molecule concentration, the differentiation of this function to any of the solution variables is quite complex. This also implies that this function will call the TBE- and pressure-functions, as is indicated by Figure 3.11. The accuracy and reliability of this

function is of particular importance for the model and is validated in the ignition delay time calculations of Section 3.4.3.

C.9. Function HRXN

The HRXN-function calculates the rate of heat release from chemical reactions and is abbreviated from heat of reaction. This function produces a value for Equation 3.55, which is the summation of the product between the rate of reaction and enthalpy of each species. This function is a good example of the simplification of the code with the use of functions, since this function merely calls the rate- and heat-functions for the summation. The differentiation of this function is also simpler, in which case the product rule is implemented conveniently.

C.10. Function LAMDA

This LAMDA-function calculates the thermal conductivity of the gas mixture from the species concentrations and temperature to produce a value for λ in Equation 3.30. The polynomial fit of Equation 3.78 in the LAMDACALC-subroutine simplifies the calculations required in the LAMDA-function to obtain the pure species thermal conductivities. The mixture average rule of Equation 3.79 is then applied to obtain an approximation of the thermal conductivity of the gas mixture. The temperature range of the polynomial fit of Equation 3.78 in the LAMDACALC-subroutine needs to be accounted for in the LAMDA-function, and therefore temperature limits similar to that in the HEATCAP-function are implemented. This function also requires differentiation with respect to the solution variables, which are much simpler analytical calculations in this case where the polynomial fit and mixture averaged approaches are followed.

C.11. Function DIF

This function calculates the diffusion coefficient of any of the species in the mixture to produce a value for D_i in Equations 3.11, 3.30 and 3.41, as indicated in Figure 3.12. Again, polynomial fits generated in the LAMDACALC-subroutine, similar to those for the thermal conductivities, are used to obtain the binary diffusion coefficients. The binary

diffusion coefficients are used in the mixture averaged approach of Equation 3.83, to give the diffusion coefficient of a certain species in the gas mixture. Temperature limits are required to resemble the temperature range of the polynomial fits. It should be noted that the binary diffusion coefficients are dependent on the pressure of the system and therefore the pressure-function is called. This function also calculates the differentiation with respect to the solution variables, if requested.

C.12. Functions DLAMDA and DDIF

The DLAMDA- and DDIF-functions calculate the numerical second order derivatives of the thermal conductivity (λ) and diffusion coefficients (D_i) respectively, as mentioned in Section 3.8.3.3. This is necessary to avoid the rather complex further analytical differentiation of the first order derivatives with respect to any of the solution variables, as is required for the differentiation of Equations 3.12 and 3.31. The second order numerical differentiation of the thermal conductivity is calculated in the DLAMDA-function by using Equation C.1.

$$\frac{\partial}{\partial y}\left(\frac{\partial \lambda}{\partial z}\right)|_{y_p} = \frac{\frac{\partial \lambda}{\partial z}|_{y_p+\Delta y} - \frac{\partial \lambda}{\partial z}|_{y_p-\Delta y}}{2\Delta y} \tag{C.1}$$

Equation C.1 gives a numerical approximation of the derivative of $\frac{\partial \lambda}{\partial z}$ with respect to y where $y = y_p$, while the increment Δy is chosen to be very small so as to give a more accurate approximation. It should be noted that z and y in Equation C.1 do not necessarily represent the same solution variable and therefore offers a simpler approach to calculate these second order derivatives. The second order derivatives of the diffusion coefficients are calculated in a similar manner. The use of the analytical first order derivatives from the LAMDA- and DIF-functions to calculate the numerator of the fraction on the right-hand-side of Equation C.1 further simplifies the calculations of the DLAMDA- and DDIF-functions.

D. Codes

Listing D.1: Commented code for Main program

```
C-----------------------------------------------------------------------
C DRIVING PROGRAM FOR THE SYSTEM OF PDE's DESCRIBING A
C SPHERICAL PROPAGATING FLAME.
C-----------------------------------------------------------------------
C CONSTANTS:
      USE chemphys
      implicit none
C
CCCCCCCCCCCCCCCCCCCCCCCCCCCCCCCCCCCCCCCCCCCCCCCCCCCCCCCCCCCCCCCCCCCCCCCCC
CCCCCCCCCCCCCCCCCCCCCCCCCCCCC PART A CCCCCCCCCCCCCCCCCCCCCCCCCCCCCCCCCC
CCCCCCCCCCCCCCCCCCCCCCCCCCCCCCCCCCCCCCCCCCCCCCCCCCCCCCCCCCCCCCCCCCCCCCCC
C
C                          DEFINING VARIABLES
C
        INTEGER                  KCOL
C                                KCOL IS THE NUMBER OF COLLOCATION POINTS
C                                TO BE USED IN EACH SUBINTERVAL, WHICH IS
C                                EQUAL TO THE DEGREE OF THE PIECEWISE
C                                POLYNOMIALS MINUS ONE.
C                                1 < KCOL < 11.
        PARAMETER               (KCOL = 5)
C
C                                NUMBER OF PDES
        INTEGER                  NPDE
        PARAMETER               (NPDE = species+2)
C
        INTEGER                  NINTMX
C                                MAXIMAL NUMBER OF INTEVALS ALLOWED
        PARAMETER               (NINTMX = 2000)
        INTEGER                  MAXVEC
```

```
C                                THE DIMENSION OF THE VECTOR OF
C                                BSPLINE COEFFICIENTS
      PARAMETER                 (MAXVEC = NPDE*(NINTMX*KCOL+2))
      INTEGER                    LRP
C                                SEE THE COMMENT FOR RPAR
      PARAMETER                 (LRP =134+NINTMX*(35+35*KCOL+31*NPDE
     +                                 +38*NPDE*KCOL+8*KCOL*KCOL)+14*KCOL
     +                                 +79*NPDE+NPDE*NPDE*(21
     +                                 +4*NINTMX*KCOL*KCOL+12*NINTMX*KCOL
     +                                 +6*NINTMX))
C
      INTEGER                    LIP
C                                SEE THE COMMENT FOR IPAR
      PARAMETER                 (LIP = 115+NPDE*((2*KCOL+1)*NINTMX+4))
      INTEGER                    LENWRK
C                                THE DIMENSION OF ARRAY WORK WHEN WE
C                                CALL VALUES
      PARAMETER                 (LENWRK =(KCOL+2)+KCOL*(NINTMX+1)+4)
C
C                               THE NUMBER OF POINTS OF THE SOLUTION ARRAY
      INTEGER                    pointsout
      PARAMETER                  (pointsout=2001)
C
      INTEGER                    NDER
C                                THE DIMENSION OF UOUT
      PARAMETER                 (NDER = 2)
      DOUBLE PRECISION           XA
C                                THE LEFT BOUNDARY POINT
      PARAMETER                 (XA = 0.002D0)
      DOUBLE PRECISION           XB
C                                THE RIGHT BOUNDARY POINT
      PARAMETER                 (XB = 0.05D0)
C-----------------------------------------------------------------------

      DOUBLE PRECISION           T0
C                                T0 < TOUT IS THE INITIAL TIME.
C
      DOUBLE PRECISION           TOUT
C                                TOUT IS THE DESIRED FINAL OUTPUT TIME.
```

```
C
      DOUBLE PRECISION        ATOL(NPDE)
C                             ATOL IS THE ABSOLUTE ERROR TOLERANCE
C                             REQUEST AND IS A SCALAR QUANTITY IF
C                             MFLAG(2) = 0.
C
      DOUBLE PRECISION        RTOL(NPDE)
C                             RTOL IS THE RELATIVE ERROR TOLERANCE
C                             REQUEST AND IS A SCALAR QUANTITY IF
C                             MFLAG(2) = 0.
C
      INTEGER                 NINT
C                             NINT IS THE NUMBER OF SUBINTERVALS
C                             DEFINED BY THE SPATIAL MESH X.
C
      DOUBLE PRECISION        X(NINTMX+1)
C                             X IS THE SPATIAL MESH WHICH DIVIDES THE
C                             INTERVAL [X_A,X_B] AS: X_A = X(1) <
C                             X(2) < X(3) < ... < X(NINT+1) = X_B.
C
      INTEGER                 MFLAG(7)
C                             THIS VECTOR OF USER INPUT DETERMINES
C                             THE INTERACTION OF BACOL WITH DASSL.
C
C     WORK STORAGE:
      DOUBLE PRECISION        RPAR(LRP)
C                             RPAR IS A FLOATING POINT WORK ARRAY
C                             OF SIZE LRP.
C
      INTEGER                 IPAR(LIP)
C                             IPAR IS AN INTEGER WORK ARRAY
C                             OF SIZE LIP.
C
C-----------------------------------------------------------------------
      DOUBLE PRECISION        Y(MAXVEC)
C                             ON SUCCESSFUL RETURN FROM BACOL, Y IS
C                             THE VECTOR OF BSPLINE
C                             COEFFICIENTS AT THE CURRENT TIME T0.
C
```

```
      INTEGER                 IDID
C                             IDID IS THE BACOL EXIT STATUS FLAG
C                             WHICH IS BASED ON THE EXIT STATUS FROM
C                             DASSL ON ERROR CHECKING PERFORMED BY
C                             BACOL ON INITIALIZATION.
C-----------------------------------------------------------------------
      DOUBLE PRECISION        UOUT(NPDE,pointsout,NDER+1)
C                             THE APPROXIMATION SOLUTIONS AT A SET
C                             OF POINTS
      DOUBLE PRECISION        VALWRK(LENWRK)
C                             VALWRK IS A WORK ARRAY IN VALUES
      DOUBLE PRECISION        XOUT(pointsout)
C                             XOUT IS A SET OF SPATIAL POINTS FOR
C                             OUTPUT
C
C-----------------------------------------------------------------------
C                       New variables
C
C
      DOUBLE PRECISION        TIME
C                             TIME holds the current time step of the
C                             solution and is obtained from the RPAR
C                             work array of BACOL.

      DOUBLE PRECISION        frontA,frontB,speed,dt
C                             frontA and frontB hold the flame
C                             position of the previous and current
C                             time steps repsectively and dt is the
C                             prevous time step. From them speed is
C                             calculated which is the flamespeed.

      DOUBLE PRECISION        steps,laststep,TT
C                             steps is the amount of time steps taken,
C                             laststep is the amount of steps at the
C                             last data capture time and TT is the
C                             time interval between data capture times

      DOUBLE PRECISION        Ntotal(species),Atotal(4)
C                             Ntotal is an array used to calculate the
```

```
C                       total amount of moles of each species
C                       thoughout the entire spatial domain.
C                       From the total amounts of species, the
C                       total amount of each atom is calculated
C                       and stored in Atotal for each time step.

      DOUBLE PRECISION  calc(NPDE),calcx(NPDE),calcxx(NPDE)
C                       calc(NPDE) is used as a working array
C                       which holds the solution array at any
C                       point in space and time to calculate
C                       certain properties at that point.
C                       calcx(NPDE) and calcxx(NPDE) holds the
C                       first and second spatial derivatives of
C                       each element in calc respectively.

      DOUBLE PRECISION  spark
C                       spark is the timing of the spark event

      DOUBLE PRECISION  OctaneNumber,OctCorA,OctCorB
C                       The research octane number (RON) of the
C                       unburned gas mixture is given and stored
C                       in OctaneNumber and OctCorA and OctCorB
C                       is the parameters used in the Schreiber
C                       model to adjust of RON.

      DOUBLE PRECISION  EqR
C                       EqR is given as user input and specifies
C                       the fuel equivalence ration of the
C                       unburned gas mixture.

      DOUBLE PRECISION  timer
C                       timer is the amount of real time seconds
C                       that elapsed during the current run.

      INTEGER           now(3),timerA,timerB,hour
C                       now holds the current hour, minutes and
C                       seconds of the computer time as integers
C                       timerA holds the real time difference
C                       between the last to time steps or
```

```
C                               solutions. timerB is used to calculate
C                               timerA and holds the amount of seconds
C                               in the last hour, while hour holds the
C                               integer for the last hour.

        INTEGER                 I,II,j,k,ender,nog,flag,flagB
C                               These integers are counters in loops
C                               or flags certain conditions.

        INTEGER                 result
C                               result is used to call system commands.
C
C-----------------------------------------------------------------------
C                               FUNCTIONS
C
C                               Functions called in model.f
        DOUBLE PRECISION        KEQ
        DOUBLE PRECISION        TBE,pressure,HRXN,LAMDA
C
C
C-----------------------------------------------------------------------
C SUBROUTINES CALLED:
C                               BACOL
C                               VALUES
C                               LAMDACALC
C-----------------------------------------------------------------------
C
C
CCCCCCCCCCCCCCCCCCCCCCCCCCCCCCCCCCCCCCCCCCCCCCCCCCCCCCCCCCCCCCCCCCCCCCCCCCCCCCCCCC
CCCCCCCCCCCCCCCCCCCCCCCCCCCCCC PART B CCCCCCCCCCCCCCCCCCCCCCCCCCCCCCCCCCCCCCCCCC
CCCCCCCCCCCCCCCCCCCCCCCCCCCCCCCCCCCCCCCCCCCCCCCCCCCCCCCCCCCCCCCCCCCCCCCCCCCCCCCC
C
C                          INPUT VALUES FOR PARAMETERS
C
C     Calculating the octane correction parameter
      OctaneNumber = 100.0D0
      OctCorA = (110.0D0-OctaneNumber)/10.0D0
      OctCorB = ((110.0D0-OctaneNumber)/10.0D0)**0.5D0
C
```

```
C-----------------------------------------------------------------------
C                          REACTION DATA INPUT
      stoich(1,1) = -1.0D0
      stoich(1,2) = 1.0D0
      stoich(1,3) = 0.0D0
      stoich(1,4) = 0.0D0
      stoich(1,5) = 0.0D0
      stoich(1,6) = 0.0D0

      stoich(2,1) = 0.0D0
      stoich(2,2) = -1.0D0
      stoich(2,3) = -12.5D0
      stoich(2,4) = 8.0D0
      stoich(2,5) = 9.0D0
      stoich(2,6) = 0.0D0
C
      ratecoef(1,1) = 1.0D0
      ratecoef(1,2) = 0.0D0
      ratecoef(1,3) = 0.0D0
      ratecoef(1,4) = 0.0D0
      ratecoef(1,5) = 0.0D0
      ratecoef(1,6) = 0.0D0
      ratecoef(1,7) = 0.0D0
      ratecoef(1,8) = 5.0D8
      ratecoef(1,9) = -18.050D3
      ratecoef(1,10) = 1.0D0

      ratecoef(2,1) = 0.0D0
      ratecoef(2,2) = 1.0D0
      ratecoef(2,3) = 1.0D0
      ratecoef(2,4) = 0.0D0
      ratecoef(2,5) = 0.0D0
      ratecoef(2,6) = 0.0D0
      ratecoef(2,7) = 1.0D0
      ratecoef(2,8) = 7.0D6
      ratecoef(2,9) = -7.2D3
      ratecoef(2,10) = 0.0D0
C
C-----------------------------------------------------------------------
```

```
C                        PHYSICAL PROPERTIES INPUT

C     CP = Heat capacity parameters
C
C     Fitted
      CP(1,1,1) = -3.91D0*R
      CP(1,2,1) = 1.06D-1*R
      CP(1,3,1) = -6.15D-5*R
      CP(1,4,1) = 1.25D-8*R
      CP(1,5,1) = 1.67D-12*R

      CP(2,1,1) = -3.91D0*R
      CP(2,2,1) = 1.06D-1*R
      CP(2,3,1) = -6.15D-5*R
      CP(2,4,1) = 1.25D-8*R
      CP(2,5,1) = 1.67D-12*R
C     Fitted

      CP(3,1,1) = 3.08D0*R
      CP(3,2,1) = 1.66D-3*R
      CP(3,3,1) = -6.63D-7*R
      CP(3,4,1) = 1.57D-10*R
      CP(3,5,1) = -4.29D-14*R

      CP(4,1,1) = 2.26D0*R
      CP(4,2,1) = 9.51D-3*R
      CP(4,3,1) = -7.32D-6*R
      CP(4,4,1) = 2.06D-9*R
      CP(4,5,1) = 1.03D-14*R

      CP(5,1,1) = 3.96D0*R
      CP(5,2,1) = -2.69D-4*R
      CP(5,3,1) = 1.94D-6*R
      CP(5,4,1) = -6.13D-10*R
      CP(5,5,1) = -4.49D-14*R

      CP(6,1,1) = 3.51D0*R
      CP(6,2,1) = -3.83D-4*R
      CP(6,3,1) = 1.25D-6*R
```

```
      CP(6,4,1) = -4.37D-10*R
      CP(6,5,1) = -1.37D-14*R
C
C     Fitted data
      CP(1,1,2) = 2.33D1*R
      CP(1,2,2) = 3.64D-2*R
      CP(1,3,2) = -2.950D-6*R
      CP(1,4,2) = -2.35D-9*R
      CP(1,5,2) = 4.0D-13*R

      CP(2,1,2) = 2.33D1*R
      CP(2,2,2) = 3.64D-2*R
      CP(2,3,2) = -2.950D-6*R
      CP(2,4,2) = -2.35D-9*R
      CP(2,5,2) = 4.0D-13*R
C     Fitted data

      CP(3,1,2) = 3.18D0*R
      CP(3,2,2) = 1.60D-3*R
      CP(3,3,2) = -7.09D-7*R
      CP(3,4,2) = 1.37D-10*R
      CP(3,5,2) = -9.60D-15*R

      CP(4,1,2) = 4.20D0*R
      CP(4,2,2) = 3.49D-3*R
      CP(4,3,2) = -1.41D-6*R
      CP(4,4,2) = 2.55D-10*R
      CP(4,5,2) = -1.71D-14*R

      CP(5,1,2) = 2.71D0*R
      CP(5,2,2) = 3.06D-3*R
      CP(5,3,2) = -9.27D-7*R
      CP(5,4,2) = 1.36D-10*R
      CP(5,5,2) = -7.96D-15*R

      CP(6,1,2) = 2.80D0*R
      CP(6,2,2) = 1.65D-3*R
      CP(6,3,2) = -6.29D-7*R
      CP(6,4,2) = 1.09D-10*R
```

```
      CP(6,5,2) = -7.07D-15*R
C
C     MW = molecular weight
C
      MW(1) = (8.0D0*12.0D0+18.0D0)*1.0D-3
      MW(2) = (8.0D0*12.0D0+18.0D0)*1.0D-3
      MW(3) = (32.0D0)*1.0D-3
      MW(4) = (12.0D0+32.0D0)*1.0D-3
      MW(5) = (18.0D0)*1.0D-3
      MW(6) = (28.0D0)*1.0D-3
C
C     HF = heat of formations
C
      HF(1) = -224.1D3
      HF(2) = HF(1) + 709.9D3
      HF(3) = 0.0D0
      HF(4) = -393.5D3
      HF(5) = -241.8D3
      HF(6) = 0.0D0

C
C     TRANS  = transport parameters
C
      TRANS(1,1) = 2.0D0
      TRANS(1,2) = 458.5D0
      TRANS(1,3) = 6.414D0
      TRANS(1,4) = 0.0D0
      TRANS(1,5) = 0.0D0
      TRANS(1,6) = 1.0D0
C
      TRANS(2,1) = 2.0D0
      TRANS(2,2) = 458.5D0
      TRANS(2,3) = 6.414D0
      TRANS(2,4) = 0.0D0
      TRANS(2,5) = 0.0D0
      TRANS(2,6) = 1.0D0
C
      TRANS(3,1) = 1.0D0
      TRANS(3,2) = 107.4D0
```

```
      TRANS(3,3) = 3.458D0
      TRANS(3,4) = 0.0D0
      TRANS(3,5) = 1.6D0
      TRANS(3,6) = 3.8D0
C
      TRANS(4,1) = 1.0D0
      TRANS(4,2) = 244.0D0
      TRANS(4,3) = 3.763D0
      TRANS(4,4) = 0.0D0
      TRANS(4,5) = 2.65D0
      TRANS(4,6) = 2.1D0
C
      TRANS(5,1) = 2.0D0
      TRANS(5,2) = 572.4D0
      TRANS(5,3) = 2.605D0
      TRANS(5,4) = 1.844D0
      TRANS(5,5) = 0.0D0
      TRANS(5,6) = 4.0D0
C
      TRANS(6,1) = 1.0D0
      TRANS(6,2) = 97.53D0
      TRANS(6,3) = 3.621D0
      TRANS(6,4) = 0.0D0
      TRANS(6,5) = 1.76D0
      TRANS(6,6) = 4.0D0
C
C
CCCCCCCCCCCCCCCCCCCCCCCCCCCCCCCCCCCCCCCCCCCCCCCCCCCCCCCCCCCCCCCCCCCCCCCCCCCC
CCCCCCCCCCCCCCCCCCCCCCCCCCCCC PART C CCCCCCCCCCCCCCCCCCCCCCCCCCCCCCCCCCCCCCC
CCCCCCCCCCCCCCCCCCCCCCCCCCCCCCCCCCCCCCCCCCCCCCCCCCCCCCCCCCCCCCCCCCCCCCCCCCC
C
C                       SET INITIAL CONDITIONS
C

      T0 = 0.0D0
      TOUT = 0.5D0
      TIME = 0.0D0
      dt = 0.01D0
      spark = 0.01D0
```

```
      frontB = 0.0D0
      frontA = 0.0D0
      TT = 0.0D0
      flag = 0
      flagB = 0
      timer = 0.0D0
      timerA = 0
      timerB = 0
      hour = 0
      CALL itime(now)
      hour = now(1)
      timerB = now(3) + 60*now(2)

      NINT = 10


C     Fuel composition
      EqR = 1.0D0
      steps = 0.0D0

C     Set initial properties
      start(NPDE) = 3.68D2
      start(1) = 1.0D5/(R*start(NPDE)
     &           *(1.0D0+(1.25D1/EqR)*(1.0D0+7.9D1/2.1D1)))
      start(2) = 1.0D-40
      start(3) = start(1)*1.25D1/EqR
      start(4) = 1.0D-10
      start(5) = 1.0D-10
      start(6) = start(3)*7.9D1/2.1D1
      start(NPDE-1) = 0.0D0
      pressref = 10.0D0*1.0D5
      initpress = pressure(start,NPDE,0)

      CALL LAMDACALC(start,NPDE)


C     DEFINE THE MESH BASED ON A UNIFORM STEP SIZE.
      X(1) = XA
      DO 10 I = 2, NINT
```

```
            X(I) = XA + ((I-1) * (XB - XA)) / NINT
   10 CONTINUE
         X(NINT+1) = XB

C        INITIALIZE THE MFLAG VECTOR.
         DO 20 I = 1, 7
            MFLAG(I) = 0
   20 CONTINUE
         MFLAG(2) = 1
         MFLAG(4) = 1
C         MFLAG(5) = 1
C         IDID = 0

         DO I = 1, LIP
            IPAR(I) = 0
         END DO
         IPAR(8) = 5

         DO I = 1, LRP
            RPAR(I) = 0.0D0
         END DO

         DO I = 1,species
           ATOL(I) = 1.0D-5
           RTOL(I) = 1.0D-1
         END DO
         ATOL(NPDE-1) = 1.0D-5
         RTOL(NPDE-1) = 1.0D-2
         ATOL(NPDE) = 1.0D-1
         RTOL(NPDE) = 1.0D-4


         WRITE(6,'(/A)') 'THE INPUT IS   '
         WRITE(6,'(/A, I3, A, I4, 2(A, E8.2))') 'KCOL =', KCOL, ', NINT =',
        &  NINT, ', ATOL(1) =', ATOL(1), ', RTOL(1) =', RTOL(1)


C
CCCCCCCCCCCCCCCCCCCCCCCCCCCCCCCCCCCCCCCCCCCCCCCCCCCCCCCCCCCCCCCCCCCCCCCCCC
```

```
CCCCCCCCCCCCCCCCCCCCCCCCCCCCCC PART D CCCCCCCCCCCCCCCCCCCCCCCCCCCCCCCCCC
CCCCCCCCCCCCCCCCCCCCCCCCCCCCCCCCCCCCCCCCCCCCCCCCCCCCCCCCCCCCCCCCCCCCCCCC
C

      DO WHILE (IDID .NE. 2 .AND. IDID .NE. 3)

      WRITE(6,'(/A, E14.6)') 'TOUT = ', TOUT
      WRITE(6,'(/A, 1p,E14.6, A,$)') 'Initial pressure is',
     &                            pressure(start,NPDE,0)/1.0D5, ' bar.'
      WRITE(6,'(A, 3p,E14.6, A)') ' Initial temperature is',
     &                             start(NPDE),' K. '

      WRITE(6,'(/A,5E14.6)') 'Current time: ' , TIME ,TIME - dt, timer,
     &                       timer/3.6D3

CCCCCCCCCCCCCCCCCCCCCCCCCCCCCCCCCCCCCCCCCCCCCCCCCCCCCCCCCCCCCCCCCCCCCCCCC

      CALL BACOL(T0, TOUT, ATOL, RTOL, NPDE, KCOL, NINTMX, NINT, X,
     &           MFLAG, RPAR, LRP, IPAR, LIP, Y, IDID)

C     CHECK FOR AN ERROR FROM BACOL.
      WRITE(6,'(/A, I5)') 'IDID =', IDID
      IF (IDID .LT. 1) GOTO 100

      steps = steps + 1.0D0
      dt = TIME
      TIME = RPAR(ipar(52)-1+4)

      WRITE(6,'(/A, E14.6)') 'Current time = ', TIME

      XOUT(1) = XA
      DO 30 I = 2, pointsout-1
         XOUT(I) = XA + DBLE(I - 1) * (XB - XA)/(DBLE(pointsout-1))
   30 CONTINUE
      XOUT(pointsout) = XB

      CALL VALUES(KCOL, XOUT, NINT, X, NPDE, pointsout, NDER, UOUT,
     &            Y, VALWRK)
```

```
CCCCCCCCCCCCCCCCCCCCCCCCCCCCCCCCCCCCCCCCCCCCCCCCCCCCCCCCCCCCCCCCCCCCCCCCCCCCCCC

      WRITE(6,'(/A)') 'THE OUTPUT IS  '
      WRITE(6,'(/A, I3, A, I4)') 'KCOL =', KCOL, ', NINT =', NINT
      WRITE(6,'(/A,$)') '  XOUT       '
      DO I=1,NPDE
      WRITE(6,'(A,I3,A,$)') '   UOUT(',I,')  '
      END DO

      WRITE (6,'(/A)')''
      DO 40 I = 1, pointsout,200
         WRITE(6, '(1p,15E14.6)') XOUT(I), (UOUT(k,I,1), k=1,NPDE)
   40 CONTINUE
      WRITE (6,'(/A)')''
C

C       CALCULATE COMPONENT BALANCE

      DO K = 1,species
      Ntotal(K) = 0.0D0
      END DO

      DO K = 1,species
        DO I = 1,pointsout
         Ntotal(k) = Ntotal(k) + UOUT(k,I,1)*4.0D0*pi*XOUT(I)**2.0D0
        END DO
      Ntotal(k) = (Ntotal(k)/dble(pointsout))*(XB-XA)
      END DO

      Atotal(1)= 7.0D0*(Ntotal(1)+Ntotal(2))+Ntotal(4)
      Atotal(2)= 16.0D0*(Ntotal(1)+Ntotal(2))+ 2.0D0*Ntotal(5)
      Atotal(3)= 2.0D0*(Ntotal(3)+Ntotal(4))+ Ntotal(5)
      Atotal(4)= 2.0D0*Ntotal(6)

C       CALCULATE FLAMEFRONT POSITION

      k = 1
      IF (UOUT(NPDE,1,1) .GT. 10.0D2) THEN
      DO I = 1,pointsout-1
```

```
      IF (UOUT(NPDE,I,1) .LT. 10.0D2 .AND. k .EQ. 1) THEN
      k = 2
      frontA = frontB
      frontB = XOUT(I)+((XOUT(I-1)-XOUT(I))/(UOUT(NPDE,(I-1),1)
     &          -UOUT(NPDE,I,1)))*(10.0D2-UOUT(NPDE,I,1))
      END IF
      END DO
      END IF

      speed = (frontB-frontA)/(TIME - dt)

CCC   TIMER         CCC

      CALL itime(now)
      IF (hour .EQ. now(1)) THEN
      timerA = (now(3) + 60*now(2)) - timerB
      ELSE
      timerA = (now(3) + 60*now(2) + 60*60*1) - timerB
      END IF

      timerB = now(3) + 60*now(2)
      timer = timer + dble(timerA)
      hour = now(1)

C
CCCCCCCCCCCCCCCCCCCCCCCCCCCCCCCCCCCCCCCCCCCCCCCCCCCCCCCCCCCCCCCCCCCCCCCC
CCCCCCCCCCCCCCCCCCCCCCCCCCCCCC PART E CCCCCCCCCCCCCCCCCCCCCCCCCCCCCCCCCC
CCCCCCCCCCCCCCCCCCCCCCCCCCCCCCCCCCCCCCCCCCCCCCCCCCCCCCCCCCCCCCCCCCCCCCCC
C
CCCCCC              DATA CAPTURE
C     MAIN
      IF (TIME .GT. TT + 0.00001D0) THEN
      DO 50 I = 1, pointsout
         DO k = 1,NPDE
         calc(k) = UOUT(k,I,1)
         END DO
         WRITE(20,'(18E14.6)') XOUT(I),(UOUT(k,I,1), k=1,NPDE),
     &                         pressure(calc,NPDE,0),HRXN(calc,NPDE,0),
     &                         TIME,steps
```

```
   50 CONTINUE
      TT = TIME - dble(MOD(TIME,0.00001D0))
      flag = 0
      flagB = 0
      laststep = steps

C     MESH
      DO I = 1,NINT
      WRITE(19,'(5E14.6)') TIME,X(I)
      END DO

      WRITE(19,'(/A)') ' '
      WRITE(20,'(/A)') ' '


      END IF


C     FLAME
      DO I = 1,NPDE
      calc(I) = UOUT(1,I,1)
      END DO

      WRITE(10,'(8E14.6)') TIME, frontB, speed, start(1)*1.1D1/start(4),
     &                     LAMDA(calc,NPDE,0),UOUT(1,NPDE,2),
     &                     LAMDA(calc,NPDE,0)*UOUT(1,NPDE,2)


C     RUN DATA
      WRITE(16,'(2I5,17E14.6)') NINT,flag,TIME,timer,steps,frontB,speed,
     &                          steps-laststep,(ATOL(I) , I=1,NPDE)
C     Mass balance
      WRITE(17,'(17E14.6)') TIME, (Atotal(I) , I = 1,4)


      WRITE(6,'(/A, E14.6)') 'Flamefront position is ', frontB
      WRITE(6,'(/A, E14.6)') 'Flame speed is ', speed
      WRITE(6,'(/A, 5I5)') 'NINT = ', NINT , flag, timerA
```

```
      WRITE(6,'(/A, 3I5)') 'TIME = ', (now(I) , I=1,3)

      IF (dt .GT. spark) THEN
        DO I = 1,species
          ATOL(I) = 1.0D-5
          RTOL(I) = 1.0D-2
        END DO
        ATOL(NPDE-1) = 1.0D-4
        RTOL(NPDE-1) = 1.0D-2
        ATOL(NPDE) = 1.0D-1
        RTOL(NPDE) = 1.0D-4
        ATOL(2) = 1.0D-6
        RTOL(2) = 1.0D-1
      END IF

CC     End run when flame is very close to chamber wall.
      IF (frontB .GT. XB-0.0007D0) THEN
        WRITE(6,'(/A)')'Flame reached chamber wall. Simulation stopped.'
      END IF
      IF (frontB .GT. XB-0.0008D0) GOTO 999

CC     EXIT the loop and end cyccles because time steps are too small
      IF (TIME-dt .LT. 1.0D-20) GOTO 100

      MFLAG(1) = 1

      END DO

      GOTO 999

  100 CONTINUE
      WRITE(6,'(/A, E14.6)') 'Tout = ', TOUT
      WRITE(6,'(/A, I3)') 'NINT = ', NINT
      WRITE(6,'(A)') 'CANNOT PROCEED DUE TO ERROR FROM BACOL.'

  999 STOP
      END
C-----------------------------------------------------------------------
```

Listing D.2: Commented code for F subroutine

```
C-----------------------------------------------------------------------
      SUBROUTINE F(T, X, U, UX, UXX, FVAL, NPDE)
C-----------------------------------------------------------------------
C PURPOSE:
C       THIS SUBROUTINE DEFINES THE RIGHT HAND SIDE VECTOR OF THE
C       NPDE DIMENSIONAL PARABOLIC PARTIAL DIFFERENTIAL EQUATION
C                       UT = F(T, X, U, UX, UXX).
C
C-----------------------------------------------------------------------
        USE chemphys
C SUBROUTINE PARAMETERS:
C INPUT:
        INTEGER                 NPDE
C                               THE NUMBER OF PDES IN THE SYSTEM.
C
        DOUBLE PRECISION        T
C                               THE CURRENT TIME COORDINATE.
C
        DOUBLE PRECISION        X
C                               THE CURRENT SPATIAL COORDINATE.
C
        DOUBLE PRECISION        U(NPDE)
C                               U(1:NPDE) IS THE APPROXIMATION OF THE
C                               SOLUTION AT THE POINT (T,X).
C
        DOUBLE PRECISION        UX(NPDE)
C                               UX(1:NPDE) IS THE APPROXIMATION OF THE
C                               SPATIAL DERIVATIVE OF THE SOLUTION AT
C                               THE POINT (T,X).
C
        DOUBLE PRECISION        UXX(NPDE)
C                               UXX(1:NPDE) IS THE APPROXIMATION OF THE
C                               SECOND SPATIAL DERIVATIVE OF THE
C                               SOLUTION AT THE POINT (T,X).
C
C OUTPUT:
        DOUBLE PRECISION        FVAL(NPDE)
C                               FVAL(1:NPDE) IS THE RIGHT HAND SIDE
```

```
C                                VECTOR F(T, X, U, UX, UXX) OF THE PDE.
C
C                                Own parameters
C                        New input
C
C       -FUNCTIONS-
C
        DOUBLE PRECISION         avcp,avcv,HEATCAP,rate,HRXN,area
        DOUBLE PRECISION         LAMDA,DIF,VISC
        DOUBLE PRECISION         LAMDAD,DIFD,VISCD
        DOUBLE PRECISION         DD,DDD
C       summations
        DOUBLE PRECISION         sumr,sumra
C       counters
        INTEGER                  I,J
C-----------------------------------------------------------------------
C
C     ASSIGN FVAL(1:NPDE) ACCORDING TO THE RIGHT HAND SIDE OF THE PDE
C     IN TERMS OF U(1:NPDE), UX(1:NPDE), UXX(1:NPDE).
C
C
C     Calculate d(lamda)/dr and d(visc)/dr
C     where lamda represents the thermal conductivity
C     and visc the viscosity
      LAMDAD = 0.0D0
      VISCD = 0.0D0
      DO I = 1,NPDE
      LAMDAD = LAMDAD + LAMDA(U,NPDE,I)*UX(I)
      VISCD = VISCD + VISC(U,NPDE,I)*UX(I)
      END DO

C     Calculate each of the component conservation PDE's
      DO I=1,species
      DIFD = 0.0D0
        DO J = 1,NPDE
        DIFD = DIFD + DIF(U,NPDE,I,J)*UX(J)
        END DO

      FVAL(I) = -U(NPDE-1)*UX(I)-U(I)*UX(NPDE-1)-U(I)*U(NPDE-1)*area(X)
```

```
     &           +DIF(U,NPDE,I,0)*DDD(U,UX,UXX,NPDE,I,0,0)
     &           +DIF(U,NPDE,I,0)*DD(U,UX,NPDE,I,0,0)*area(X)
     &           +DD(U,UX,NPDE,I,0,0)*DIFD+rate(U,NPDE,I,0)

      END DO

C     Calulate the momentum conservation PDE
      sumr = 0.0D0
      DO I = 1,species
      sumr =  sumr + MW(I)*DIF(U,NPDE,I,0)*DD(U,UX,NPDE,I,0,0)
      END DO

      FVAL(NPDE-1)=(-U(NPDE)*spsum(UX,NPDE,0)-UX(NPDE)*spsum(U,NPDE,0)
     &       - 0.0D0*U(NPDE)*spsum(U,NPDE,0)*area(X))*R/rho(U,NPDE,0)
     &             -U(NPDE-1)*UX(NPDE-1)+sumr*UX(NPDE-1)/rho(U,NPDE,0)
     &             +(4.0D0/(3.0D0*rho(U,NPDE,0)))
     &             *(VISC(U,NPDE,0)*UXX(NPDE-1)+VISC(U,NPDE,0)
     &             *UX(NPDE-1)*area(X)+UX(NPDE-1)*VISCD)

C     Calculate the energy conservation PDE
      sumr = 0.0D0
      sumra = 0.0D0
      DO I = 1,species
      sumr= sumr+HEATCAP(U,NPDE,I,0)*DIF(U,NPDE,I,0)*DD(U,UX,NPDE,I,0,0)
      sumra = sumra + FVAL(I)
      END DO

      FVAL(NPDE)=(-avcp(U,NPDE,0)*U(NPDE-1)*UX(NPDE)+sumr*UX(NPDE)
     &           +LAMDA(U,NPDE,0)*UXX(NPDE)+UX(NPDE)*LAMDAD
     &           +LAMDA(U,NPDE,0)*UX(NPDE)*area(X)-HRXN(U,NPDE,0)
     &           +R*U(NPDE)*sumra)/avcv(U,NPDE,0)
C
C
      RETURN
      END
```

Listing D.3: Commented code for DERIVF subroutine

```
C-----------------------------------------------------------------------
      SUBROUTINE DERIVF(T, X, U, UX, UXX, DFDU, DFDUX, DFDUXX, NPDE)
C-----------------------------------------------------------------------
C PURPOSE:
C       THIS SUBROUTINE IS USED TO DEFINE THE INFORMATION ABOUT THE
C       PDE REQUIRED TO FORM THE ANALYTIC JACOBIAN MATRIX FOR THE DAE
C       OR ODE SYSTEM. ASSUMING THE PDE IS OF THE FORM
C                          UT = F(T, X, U, UX, UXX)
C       THIS ROUTINE RETURNS THE JACOBIANS D(F)/D(U), D(F)/D(UX), AND
C       D(F)/D(UXX).
C
C-----------------------------------------------------------------------
        USE chemphys
C SUBROUTINE PARAMETERS:
C INPUT:
        INTEGER                 NPDE
C                               THE NUMBER OF PDES IN THE SYSTEM.
C
        DOUBLE PRECISION        T
C                               THE CURRENT TIME COORDINATE.
C
        DOUBLE PRECISION        X
C                               THE CURRENT SPATIAL COORDINATE.
C
        DOUBLE PRECISION        U(NPDE)
C                               U(1:NPDE) IS THE APPROXIMATION OF THE
C                               SOLUTION AT THE POINT (T,X).
C
        DOUBLE PRECISION        UX(NPDE)
C                               UX(1:NPDE) IS THE APPROXIMATION OF THE
C                               SPATIAL DERIVATIVE OF THE SOLUTION AT
C                               THE POINT (T,X).
C
        DOUBLE PRECISION        UXX(NPDE)
C                               UXX(1:NPDE) IS THE APPROXIMATION OF THE
C                               SECOND SPATIAL DERIVATIVE OF THE
C                               SOLUTION AT THE POINT (T,X).
C
```

```
C OUTPUT:
      DOUBLE PRECISION        DFDU(NPDE,NPDE)
C                             DFDU(I,J) IS THE PARTIAL DERIVATIVE
C                             OF THE I-TH COMPONENT OF THE VECTOR F
C                             WITH RESPECT TO THE J-TH COMPONENT
C                             OF THE UNKNOWN FUNCTION U.
C
      DOUBLE PRECISION        DFDUX(NPDE,NPDE)
C                             DFDUX(I,J) IS THE PARTIAL DERIVATIVE
C                             OF THE I-TH COMPONENT OF THE VECTOR F
C                             WITH RESPECT TO THE J-TH COMPONENT
C                             OF THE SPATIAL DERIVATIVE OF THE
C                             UNKNOWN FUNCTION U.
C
      DOUBLE PRECISION        DFDUXX(NPDE,NPDE)
C                             DFDUXX(I,J) IS THE PARTIAL DERIVATIVE
C                             OF THE I-TH COMPONENT OF THE VECTOR F
C                             WITH RESPECT TO THE J-TH COMPONENT
C                             OF THE SECOND SPATIAL DERIVATIVE OF THE
C                             UNKNOWN FUNCTION U.
C
C                             Own parameters
C                     New input
C
C
C       -FUNCTIONS-
C
      DOUBLE PRECISION        TBE,avcp,pressure,heat,rate,HRXN
      DOUBLE PRECISION        LAMDA,DLAMDA,VISC,DVISC,DIF,DDIF,area
      DOUBLE PRECISION        DD,DDD
C       summations and constants
      DOUBLE PRECISION        sumr,dsumr,difsum,ddifsum,molsum,dmolsum
      DOUBLE PRECISION        frac
C       counters
      INTEGER                 I,J,K
C
C
C
C-----------------------------------------------------------------------
```

```
C-----------------------------------------------------------------------
C
C     ASSIGN DFDU(1:NPDE,1:NPDE), DFDUX(1:NPDE,1:NPDE), AND
C     DFDUXX(1:NPDE,1:NPDE) ACCORDING TO THE RIGHT HAND SIDE OF THE PDE
C     IN TERMS OF U(1:NPDE), UX(1:NPDE), UXX(1:NPDE).
C
C
      dsumr = 0.0D0
      sumr = 0.0D0
      difsum = 0.0D0
      ddifsum = 0.0D0
      molsum = 0.0D0
      dmolsum = 0.0D0

C-------------------DERIVATIVES TO SOLUTION VARIABLES-------------------

C     COMPONENTS
C     Calculate the derivative of each of the component conservation
C     PDE's to each of the solution variables.

      DO I=1,species
       DO J=1,NPDE
        molsum = 0.0D0
        dmolsum = 0.0D0
        DO K = 1,NPDE
         molsum = molsum + DDIF(U,NPDE,I,K,0)*UX(K)
         dmolsum = dmolsum + DDIF(U,NPDE,I,K,J)*UX(K)
        END DO
        IF (J .EQ. I) THEN
         DFDU(I,J) =-UX(NPDE-1)-U(NPDE-1)*area(X)
     &              +DIF(U,NPDE,I,J)*DDD(U,UX,UXX,NPDE,I,0,0)
     &              +DIF(U,NPDE,I,0)*DDD(U,UX,UXX,NPDE,I,J,0)
     &              +(DIF(U,NPDE,I,J)*DD(U,UX,NPDE,I,0,0)
     &              +DIF(U,NPDE,I,0)*DD(U,UX,NPDE,I,J,0))*area(X)
     &              +DD(U,UX,NPDE,I,0,0)*dmolsum
     &              +molsum*DD(U,UX,NPDE,I,J,0)+rate(U,NPDE,I,J)
        ELSE
         DFDU(I,J) =DIF(U,NPDE,I,J)*DDD(U,UX,UXX,NPDE,I,0,0)
```

```
     &               +DIF(U,NPDE,I,0)*DDD(U,UX,UXX,NPDE,I,J,0)
     &               +(DIF(U,NPDE,I,J)*DD(U,UX,NPDE,I,0,0)
     &               +DIF(U,NPDE,I,0)*DD(U,UX,NPDE,I,J,0))*area(X)
     &               +DD(U,UX,NPDE,I,0,0)*dmolsum
     &               +molsum*DD(U,UX,NPDE,I,J,0)+rate(U,NPDE,I,J)
        END IF
       END DO
C      The derivative to convective velocity
       DFDU(I,NPDE-1) = -UX(I)-U(I)*area(X)
       END DO


C      MOMENTUM
C      Calculate the derivative of the momentum conservation PDE's to
C      each of the solution variables.

       frac = 4.0D0/3.0D0
C      The derivative to each of the component concentrations
       DO J = 1,species

        difsum = 0.0D0
        ddifsum = 0.0D0
        DO K = 1,species
         difsum = difsum + DIF(U,NPDE,K,0)*MW(K)*DD(U,UX,NPDE,K,0,0)
         ddifsum = ddifsum + DIF(U,NPDE,K,J)*MW(K)*DD(U,UX,NPDE,K,0,0)
     &             + DIF(U,NPDE,K,0)*MW(K)*DD(U,UX,NPDE,K,J,0)
        END DO

        molsum = 0.0D0
        dmolsum = 0.0D0
        DO K = 1,NPDE
         molsum = molsum + VISC(U,NPDE,K)*UX(K)
         dmolsum = dmolsum + DVISC(U,NPDE,K,J)*UX(K)
        END DO

       DFDU(NPDE-1,J) =((-R*UX(NPDE)-R*U(NPDE)*area(X)*0.0D0
     &                  +ddifsum*UX(NPDE-1)
     &                  +frac*VISC(U,NPDE,J)*UXX(NPDE-1)
     &                  +frac*VISC(U,NPDE,J)*UX(NPDE-1)*area(X)
```

```
     &                +frac*UX(NPDE-1)*dmolsum)*rho(U,NPDE,0)
     &                -(-R*U(NPDE)*spsum(UX,NPDE,0)
     &                -R*UX(NPDE)*spsum(U,NPDE,0)
     &                -R*U(NPDE)*spsum(U,NPDE,0)*area(X)*0.0D0
     &                +difsum*UX(NPDE-1)
     &                +frac*VISC(U,NPDE,0)*UXX(NPDE-1)
     &                +frac*VISC(U,NPDE,0)*UX(NPDE-1)*area(X)
     &                +frac*UX(NPDE-1)*molsum)*rho(U,NPDE,J))
     &                /rho(U,NPDE,0)**2.0D0
      END DO

C     The derivative to convective velocity
      DFDU(NPDE-1,NPDE-1) = -UX(NPDE-1)

C     The derivative to temperature
      J = NPDE

       ddifsum = 0.0D0
       DO K = 1,species
        ddifsum = ddifsum + DIF(U,NPDE,K,J)*MW(K)*DD(U,UX,NPDE,K,0,0)
     &            + DIF(U,NPDE,K,0)*MW(K)*DD(U,UX,NPDE,K,J,0)
       END DO

       dmolsum = 0.0D0
       DO K = 1,NPDE
        dmolsum = dmolsum + DVISC(U,NPDE,K,J)*UX(K)
       END DO

      DFDU(NPDE-1,J) =(-R*spsum(UX,NPDE,0)
     &                -R*spsum(U,NPDE,0)*area(X)*0.0D0
     &                +ddifsum*UX(NPDE-1)
     &                +frac*VISC(U,NPDE,J)*UXX(NPDE-1)
     &                +frac*VISC(U,NPDE,J)*UX(NPDE-1)*area(X)
     &                +frac*UX(NPDE-1)*dmolsum)/rho(U,NPDE,0)


C     ENERGY
C     Calculate the derivative of the energy conservation PDE's to
C     each of the solution variables.
```

```
      sumr = 0.0D0
      difsum = 0.0D0
      DO I = 1,species
       dmolsum = 0.0D0
       DO K = 1,NPDE
        dmolsum = dmolsum + DIF(U,NPDE,I,K)*DD(U,UX,NPDE,K,0,0)
       END DO
       sumr= sumr-U(NPDE-1)*UX(I)-U(I)*UX(NPDE-1)-U(I)*U(NPDE-1)*area(X)
     &          +DIF(U,NPDE,I,0)*UXX(I)+DIF(U,NPDE,I,0)*UX(I)*area(X)
     &          +UX(I)*dmolsum+rate(U,NPDE,I,0)
       difsum = difsum + DIF(U,NPDE,I,0)*HEATCAP(U,NPDE,I,0)
     &                   *DD(U,UX,NPDE,I,0,0)
      END DO

      molsum = 0.0D0
      DO I = 1,NPDE
       molsum = molsum + LAMDA(U,NPDE,I)*UX(I)
      END DO

      DO J=1,NPDE

       ddifsum = 0.0D0
       dsumr = 0.0D0
       DO I=1,species
        ddifsum = ddifsum + DIF(U,NPDE,I,J)*HEATCAP(U,NPDE,I,0)
     &                      *DD(U,UX,NPDE,I,0,0)
     &         + DIF(U,NPDE,I,0)*HEATCAP(U,NPDE,I,J)*DD(U,UX,NPDE,I,0,0)
     &         + DIF(U,NPDE,I,0)*HEATCAP(U,NPDE,I,0)*DD(U,UX,NPDE,I,J,0)
        dsumr = dsumr + DFDU(I,J)
       END DO

       dmolsum = 0.0D0
       DO I = 1,NPDE
        dmolsum = dmolsum + DLAMDA(U,NPDE,I,J)*UX(I)
       END DO

      IF (J .EQ. NPDE) THEN
C      The derivative to temperature
```

```
        DFDU(NPDE,J) = ((-avcp(U,NPDE,J)*U(NPDE-1)*UX(NPDE)
     &                 +ddifsum*UX(NPDE)+LAMDA(U,NPDE,J)*UXX(NPDE)
     &                 +UX(NPDE)*dmolsum+LAMDA(U,NPDE,J)*UX(NPDE)*area(X)
     &                 -HRXN(U,NPDE,J)+R*U(NPDE)*dsumr+R*sumr)
     &                 *avcv(U,NPDE,0)
     &                 -(-avcp(U,NPDE,0)*U(NPDE-1)*UX(NPDE)
     &                 +difsum*UX(NPDE)+LAMDA(U,NPDE,0)*UXX(NPDE)
     &                 +UX(NPDE)*molsum+LAMDA(U,NPDE,0)*UX(NPDE)*area(X)
     &                 -HRXN(U,NPDE,0)+R*U(NPDE)*sumr)*avcv(U,NPDE,J))
     &                 /avcv(U,NPDE,0)**2.0D0

       ELSE IF (J .EQ. NPDE-1) THEN
C      The derivative to convective velocity
        DFDU(NPDE,J) = -avcp(U,NPDE,0)*UX(NPDE)/avcv(U,NPDE,0)
     &                 +UX(NPDE)*dmolsum/avcv(U,NPDE,0)
     &                 +U(NPDE)*R*dsumr/avcv(U,NPDE,0)

       ELSE
C      The derivative to each of the component concentrations
        DFDU(NPDE,J) = ((-avcp(U,NPDE,J)*U(NPDE-1)*UX(NPDE)
     &                 +ddifsum*UX(NPDE)+LAMDA(U,NPDE,J)*UXX(NPDE)
     &                 +UX(NPDE)*dmolsum+LAMDA(U,NPDE,J)*UX(NPDE)*area(X)
     &                 -HRXN(U,NPDE,J)+R*U(NPDE)*dsumr)*avcv(U,NPDE,0)
     &                 -(-avcp(U,NPDE,0)*U(NPDE-1)*UX(NPDE)
     &                 +difsum*UX(NPDE)+LAMDA(U,NPDE,0)*UXX(NPDE)
     &                 +UX(NPDE)*molsum+LAMDA(U,NPDE,0)*UX(NPDE)*area(X)
     &                 -HRXN(U,NPDE,0)+R*U(NPDE)*sumr)*avcv(U,NPDE,J))
     &                 /avcv(U,NPDE,0)**2.0D0
       END IF

       END DO

C
C--------------------DERIVATIVES TO FIRST ORDER SPATIAL------------------
C--------------------DERIVATIVES OF SOLUTION VARIABLES-------------------
C
C      COMPONENT
C      Calculate the derivative of each of the component conservation
C      PDE's to each of the first order spatial derivatives of the
```

```
C     solution variables.
      DO I=1,species
       molsum = 0.0D0
       DO K = 1,NPDE
        molsum = molsum + DIF(U,NPDE,I,K)*UX(K)
       END DO
       DO J=1,NPDE
        IF (J .EQ. I) THEN
         DFDUX(I,J) = -U(NPDE-1)
     &                +DIF(U,NPDE,I,0)*area(X)*DD(U,UX,NPDE,I,J,1)
     &                +DIF(U,NPDE,I,0)*DDD(U,UX,UXX,NPDE,I,J,1)
     &                +molsum*DD(U,UX,NPDE,I,J,1)
     &                +DD(U,UX,NPDE,I,0,1)*DIF(U,NPDE,I,J)
        ELSE IF (J .EQ. NPDE-1) THEN
C    The derivative to the first order spatial derivative of velocity
         DFDUX(I,J) = -U(I)+DIF(U,NPDE,I,0)*area(X)*DD(U,UX,NPDE,I,J,1)
     &                +DIF(U,NPDE,I,0)*DDD(U,UX,UXX,NPDE,I,J,1)
     &                +molsum*DD(U,UX,NPDE,I,J,1)
     &                +DD(U,UX,NPDE,I,0,1)*DIF(U,NPDE,I,J)
        ELSE IF (J .EQ. NPDE) THEN
C    The derivative to the first order spatial derivative of temperature
         DFDUX(I,J) = DIF(U,NPDE,I,0)*area(X)*DD(U,UX,NPDE,I,J,1)
     &                +DIF(U,NPDE,I,0)*DDD(U,UX,UXX,NPDE,I,J,1)
     &                +molsum*DD(U,UX,NPDE,I,J,1)
     &                +DD(U,UX,NPDE,I,0,1)*DIF(U,NPDE,I,J)
        ELSE
         DFDUX(I,J) = DIF(U,NPDE,I,0)*area(X)*DD(U,UX,NPDE,I,J,1)
     &                +DIF(U,NPDE,I,0)*DDD(U,UX,UXX,NPDE,I,J,1)
     &                +molsum*DD(U,UX,NPDE,I,J,1)
     &                +DD(U,UX,NPDE,I,0,0)*DIF(U,NPDE,I,J)
        END IF
       END DO
      END DO

C     MOMENTUM
C     Calculate the derivative of the momentum conservation PDE to each
C     of the first order spatial derivatives of the solution variables.

      difsum = 0.0D0
```

```
      DO K = 1,species
       difsum = difsum + DIF(U,NPDE,K,0)*MW(K)*DD(U,UX,NPDE,K,0,0)
      END DO

      molsum = 0.0D0
      DO K = 1,NPDE
       molsum = molsum + VISC(U,NPDE,K)*UX(K)
      END DO

      DO J = 1,NPDE

      ddifsum = 0.0D0
      DO K = 1,species
       ddifsum = ddifsum + DIF(U,NPDE,K,0)*MW(K)*DD(U,UX,NPDE,K,J,1)
      END DO

       IF (J .LE. species) THEN
C     The derivative to the first order spatial derivatives of
C     the component concentrations
         DFDUX(NPDE-1,J) = (-R*U(NPDE)+ddifsum*UX(NPDE-1)
     &                     +frac*UX(NPDE-1)*VISC(U,NPDE,J))
     &                     /rho(U,NPDE,0)
       ELSE IF (J .EQ. NPDE-1) THEN
C    The derivative to the first order spatial derivative of velocity
         DFDUX(NPDE-1,J) = -U(NPDE-1)+(difsum+ddifsum*UX(NPDE-1)+frac
     &                     *VISC(U,NPDE,0)*area(X)+frac*(molsum
     &                     +UX(NPDE-1)*VISC(U,NPDE,J)))/rho(U,NPDE,0)
       ELSE IF (J .EQ. NPDE) THEN
C    The derivative to the first order spatial derivative of temperature
         DFDUX(NPDE-1,J) = (-R*spsum(U,NPDE,0)+ddifsum*UX(NPDE-1)
     &                     +frac*UX(NPDE-1)*VISC(U,NPDE,J))/rho(U,NPDE,0)
       END IF

      END DO

C     ENERGY
C     Calculate the derivative of the energy conservation PDE to each
C     of the first order spatial derivatives of the solution variables.
```

```
      difsum = 0.0D0
      DO I = 1,species
       difsum= difsum
     &         + DIF(U,NPDE,I,0)*HEATCAP(U,NPDE,I,0)*DD(U,UX,NPDE,I,0,0)
      END DO

      molsum = 0.0D0
      DO I = 1,NPDE
       molsum = molsum + LAMDA(U,NPDE,I)*UX(I)
      END DO

      DO J = 1,NPDE

      ddifsum = 0.0D0
      DO K = 1,species
       ddifsum= ddifsum
     &         + DIF(U,NPDE,K,0)*HEATCAP(U,NPDE,K,0)*DD(U,UX,NPDE,K,J,1)
      END DO

       dsumr = 0.0D0
       DO K = 1,species
        dsumr = dsumr + DFDUX(K,J)
       END DO

       IF (J .LE. species) THEN
C      The derivative to the first order spatial derivatives of
C      the component concentrations
         DFDUX(NPDE,J)=(ddifsum*UX(NPDE)+UX(NPDE)*LAMDA(U,NPDE,J)
     &                 +R*U(NPDE)*dsumr)/avcv(U,NPDE,0)
       ELSE IF (J .EQ. NPDE-1) THEN
C     The derivative to the first order spatial derivative of velocity
         DFDUX(NPDE,J)=(ddifsum*UX(NPDE)+UX(NPDE)*LAMDA(U,NPDE,J)
     &                 +R*U(NPDE)*dsumr)/avcv(U,NPDE,0)
       ELSE IF (J .EQ. NPDE) THEN
C     The derivative to the first order spatial derivative of temperature
         DFDUX(NPDE,J)=(-avcp(U,NPDE,0)*U(NPDE-1)+difsum+ddifsum*UX(NPDE)
     &                 +UX(NPDE)*LAMDA(U,NPDE,J)+molsum
     &                 +LAMDA(U,NPDE,0)*area(X)+R*U(NPDE)*dsumr)
     &                 /avcv(U,NPDE,0)
```

```
       END IF
      END DO

C
C-------------------DERIVATIVES TO SECOND ORDER SPATIAL------------------
C--------------------DERIVATIVES OF SOLUTION VARIABLES-------------------
C
C     Calculate the derivative of each of the component conservation
C     PDE's to each of the first order spatial derivatives of the
C     solution variables.
      DO I=1,NPDE
        DO J=1,NPDE
        DFDUXX(I,J) = 0.0D0
        END DO
      END DO

C     Calculate the derivative of each of the component conservation
C     PDE's to each of the second order spatial derivatives of the
C     solution variables.
      DO I=1,species
        DO J=1,NPDE
        DFDUXX(I,J) = DIF(U,NPDE,I,0)*DDD(U,UX,UXX,NPDE,I,J,2)
        END DO
      END DO

C     Calculate the derivative of the momentum conservation PDE to each
C     of the second order spatial derivatives of the solution variables.
      DFDUXX(NPDE-1,NPDE-1) = (4.0D0/3.0D0)*VISC(U,NPDE,0)/rho(U,NPDE,0)

C     Calculate the derivative of the energy conservation PDE to each of
C     the second order spatial derivatives of the solution variables.
      DO J = 1,NPDE
      dsumr = 0.0D0
       DO I = 1,species
       dsumr = dsumr + DFDUXX(I,J)
       END DO
      DFDUXX(NPDE,J) = R*U(NPDE)*dsumr/avcv(U,NPDE,0)
      END DO
```

```
      DFDUXX(NPDE,NPDE) = DFDUXX(NPDE,NPDE)
     &                  + LAMDA(U,NPDE,0)/avcv(U,NPDE,0)


      RETURN
      END
```